UNIVERSITY OF SHEFFIELD

Nonlinear Model Predictive Control of Autonomous Surface Vehicle in Rough Seas

by

Daniel R. McCullough

A thesis submitted in partial fulfillment for the
degree of Doctor of Philosophy

in the
Faculty of Engineering
Department of Automatic Control and Systems Engineering

December 2021

ABSTRACT

Autonomous Surface Vehicles (ASVs) offer the potential of performing dirty, dull, and dangerous missions at sea, in an automated fashion. However, without consideration of the ocean environment and the risk of wave-induced damage, the use of conventional ASVs is restricted to relatively calm sea-states. Assuming a conventional underactuated ASV with only throttle and rudder inputs, this thesis addresses the problem of controlling an ASV in an optimal fashion, while maintaining headway towards a desired destination in any sea and with any sea state. This is a challenging problem owing to the coupled, nonlinear nature of the vessel-wave dynamics, along with multiple competing performance objectives, such as excessive motions, and actuation effort. The thesis shows that the optimal solution, obtained via nonlinear model predictive control (NMPC), involves tacking at two different timescales. This subsequently motivates the design of a two-degree of freedom controller, consisting of a tacking planner that generates a long-term, optimal, heading and velocity reference, and a feedback regulator that produce the optimal throttle and rudder commands to maintain this reference, whilst minimizing wave-induced effects with smaller tacks. This thesis represents the first work to formulate and solve the optimal control problem of navigating in rough seas, based upon a coupled dynamic model of a 6-DOF vessel excited by waves. Closed-loop simulation results from a high fidelity ocean-vessel model demonstrate significant reductions in excessive vessel motions and forces, compared to a conventional path following PID controller for head and beam seas. Further examinations show the superiority of the NMPC in a full sea state. The impact of the prediction horizon parameters on the performance is investigated with a view towards an adaptive prediction horizon. Lastly, the ability of the NMPC to use one set of Response Amplitude Operators (RAOs) in other wave conditions without loss of performance is shown.

Contents

List of Figures

List of Tables

List of Symbols

The following is a list of commonly appearing symbols. Single use symbols are defined in text at their use and are omitted from this table.

L	Length of the vessel
m	Mass of Vessel
X	Force in surge direction
Y	Force in sway direction
Z	Force in heave direction
K	Moment in roll direction
M	Moment in pitch direction
N	Moment in yaw direction
u	Velocity in surge direction
v	Velocity in sway direction
w	Velocity in heave direction
p	Velocity in roll direction
q	Velocity in pitch direction
r	Velocity in yaw direction
x_n	NED position in surge direction
x_c	Cartesian position in surge direction
y_n	NED position in sway direction
y_c	Cartesian position in sway direction
z_n	NED position in heave direction

ϕ	Position in roll direction
θ	Position in pitch direction
ψ	Position in yaw direction
$\boldsymbol{\eta}$	Vector of NED positions
$\boldsymbol{v}$	Vector of body fixed velocities
M	Vessel mass matrix
$\boldsymbol{v_r}$	Relative velcoties
$\boldsymbol{M_{RB}}$	Rigid body mass matrix
$\boldsymbol{M_A}$	Added mass matrix
$\boldsymbol{C_{RB}}$	Rigid body Coriolis matrix
$\boldsymbol{C_A}$	added mass Coriolis matrix
$\boldsymbol{D}$	Vessel damping matrix
$\boldsymbol{\mu}$	Memory fluid effects vector
$\boldsymbol{G}$	Restoring force matrix
$\boldsymbol{\tau}$	Vector of control actuation
$\boldsymbol{\tau}_{\text{wave}}$	Vector of wave forces
I_{yy}	Pitch Moment of Inertia
I_{zz}	Yaw Moment of Inertia
S	Wetted hull surface area
∇	Water displacement volume
A_{wp}	Water plane area at equilibrium
A_{fw}	Frontal projected area above waterline
A_{lw}	Lateral projected area above waterline
$G\bar{M}_T$	Transverse metacentric height
$G\bar{M}_L$	Frontal projected area below waterline
A_x	Water displacement volume
C_D^{2D}	Two-dimensional cross-flow drag coefficient
$L_{CG} - LCF$	Longitudinal distance between CG and CF
u_{max}	Maximum forward speed of vessel
$\boldsymbol{S}$	Skewed symmetric matrix
$\boldsymbol{I}$	Identity matrix
g	Acceleration due to gravity

$\boldsymbol{x}$	States vector
n_{p}	Propeller state
α_{r}	Rudder state
$\boldsymbol{u}$	Input vector
ω_e	Wave encounter frequency
ω_i	Wave frequency
β	Wave encounter angle
k	Wavenumber
$\boldsymbol{\mathcal{X}}_r$	Vector of future state references
$\hat{\boldsymbol{\mathcal{X}}}$	Vector of future state predictions
$\boldsymbol{\mathcal{U}}_r$	Vector of future input references
$\hat{\boldsymbol{\mathcal{U}}}$	Vector of future input predictions
$\bar{\boldsymbol{\mathcal{X}}}$	Vector of nominal future state predictions
$\bar{\boldsymbol{\mathcal{U}}}$	Vector of nominal future input predictions
$\boldsymbol{\mathcal{Y}}_r$	Vector of future output references
$\hat{\boldsymbol{\mathcal{Y}}}$	Vector of future output predictions
$\bar{\boldsymbol{\mathcal{Y}}}$	Vector of nominal output state predictions
$\boldsymbol{A}_k$	State sensitivity matrix
$\boldsymbol{B}_k$	Input sensitivity matrix
$\boldsymbol{\mathcal{G}}$	State to state prediction matrix
$\boldsymbol{\mathcal{H}}$	Input to state prediction matrix
$\boldsymbol{\mathcal{Q}}$	State penalization matrix
$\boldsymbol{\mathcal{R}}$	Input penalization matrix
$\boldsymbol{\mathcal{E}}$	Hessian matrix
$\boldsymbol{f}$	Gradient term
$\boldsymbol{\mathcal{M}}$	Constraint matrix
$\boldsymbol{\gamma}$	Constraint vector
$\delta\boldsymbol{x}_0$	Initial state mismatch
N_p	Prediction horizon
n_x	Number of states
n_u	Number of inputs
n_y	Number of outputs
N_s	Number of steps in shooting method

List of Acronyms

ASV	Autonomous surface vehicle
RAO	Response amplitude operator
NMPC	Nonlinear model predictive control
MPC	Model predictive control
PID	Proportional derivative integral
LOS	Line of sight
DOF	Degrees of freedom
SWEM	Sheffield Wave Environment Model
OCP	Optimal control problem
SQP	Sequential quadratic program
QP	Quadratic program
COLREG	Convention on the International Regulations for Preventing Collisions at Sea

Acknowledgements

Though conducted and written by me, a PhD is not a solitary endeavour. I owe a great deal of gratitude to the people who have helped me along the way. Thank you to Dr. Bryn Jones who got me started and guided me along this journey. You have been a supervisor, a mentor, a sounding board, and at times, therapist. Our pedantic talks on everything from results to grammar have made me a better researcher. To Dr. Anthony Rossiter, thank you for your immense knowledge in the field of predictive control and your helpful guidance with my sometimes inane questions. Thank you to Dr. Oscar Villarreal for the introduction and help in the world of nonlinear model predictive control. Thank you to Matthew Ham for all the work you do to help students get on with the task of researching, and our talks on American football.

Thanks also goes out to my family. To my wife for getting me out of the house and away from the computer to restore a bit of sanity during lockdown. To my parents for giving me a great mix of stubbornness (determination) to continue even after hitting roadblocks, and intelligence to ponder if I should try to avoid said roadblocks. I still prefer doing things the hard way. Thank you to my friend Leigh for your knowledge of the English language. And lastly, thank you to my dog Ryder who kept me company as I worked late into the night as the rest of the house slept.

Rough seas make good sailors.

Chapter 1

Introduction

To have a truly safe and capable autonomous surface vehicle (ASV) requires replicating the many skills used by a captain of a vessel. The captain must be cognizant of the other vessels in the immediate vicinity, along with their likely course headings to avoid collisions. They must also be aware of stationary or geographical hazards to avoid. In addition, captains must have knowledge of the prevailing sea and wind conditions, and how to effectively navigate these conditions while avoiding the other hazards. Neglect of any one of these presents a danger to the ASV, the other vessels, and the environment. Path planning for vehicle or obstacle avoidance and wave forecasting are their own research areas, and indeed many papers and theses have been written discussing these topics. This thesis seeks to build the backbone which connects these topics together with a controller that uses knowledge of future waves to improve the ability of the vessel to follow a predefined path, such as a course around an object, while mitigating the damaging effects of the waves, or in the case open water, plot a course which significantly reduces the damaging effects of the wave while still maintaining headway towards an objective.

Given that, this thesis sets out to construct a controller and subsequent architecture which can operate in all sea conditions that a crewed vessel can reasonably be expected to operate in. This means the controller must operate in waves which can cause structural damage or present a capsize danger. While mitigating these risks, the controller must still operate the craft towards a desired objective. This is a difficult task for both humans and machines. Firstly, the waves, especially in rough seas, can impart more force than the actuators, that is the propellers and rudders, can produce. This requires clever use of the vessel's momentum and maneuvering to counteract. Compounding this

is the fact that most marine vessels, including the one presented in this thesis, are underactuated. This means that there are more degrees of freedom (DOF), six, than there are actuators, two, with primary actuation in the forward (surge) direction, and heading (yaw) direction.

1.1 Motivation

Navigation on the sea requires more than just following a predefined path or trajectory. Waves and other disturbances do not only affect planar motions (surge, sway, and yaw), therefore, the controller should not consider solely planar motions when it comes to its performance index. Corrective actuation, such as a large rudder movement to counteract a wave pushing the vessel off course, could exacerbate the already present wave-induced rolling motion, leading to the vessel capsizing. Weather related accidents of human piloted vessels were studied in Zhang and Li (2017). Of the accident types, 5% were sinking, 14% were capsizing, and 25% were hull damage. The remaining were grounding or unclassified events. Half of the events occurred in sea states with a significant wave height of less than 3 meters, two-thirds occurred when the mean wave period was near 7 seconds, and almost all occurred offshore, but not in open ocean. The majority of these accidents were with larger vessels such as cargo or container ships. As the size of the vessel decreases, the effect of waves increases. For example, a 2 meter wave would hardly be noticed by an aircraft carrier, but a dinghy would struggle navigating a wave of that size. Additionally, as the threshold for the wave size necessary to cause an impact lowers, the likelihood of encountering those waves increases. Sea states with significant wave heights of 1-2 meters are quite common and, in fact, are the majority measured off the coast of India, (Mishra et al., 2014), and at various locations around Europe, (Smith et al., 2011). Figure 1.1 shows a global snapshot of the significant wave height of the oceans. Most of the coast of western Europe show a significant wave height of 2.5 to 5 meters and globally most coast show a minimum of 1 meter significant wave height. Larger waves can be easier to forecast as they require longer sustained winds and surges to develop such as when caused by a hurricane or tropical storm, while smaller waves can develop more rapidly and be due to the onset of a local storm or high wind event.

Failure to compensate for the presence of waves could also lead to bow diving, or other compromising positions which cause an ingress of water, which in turn could affect maneuverability, equipment

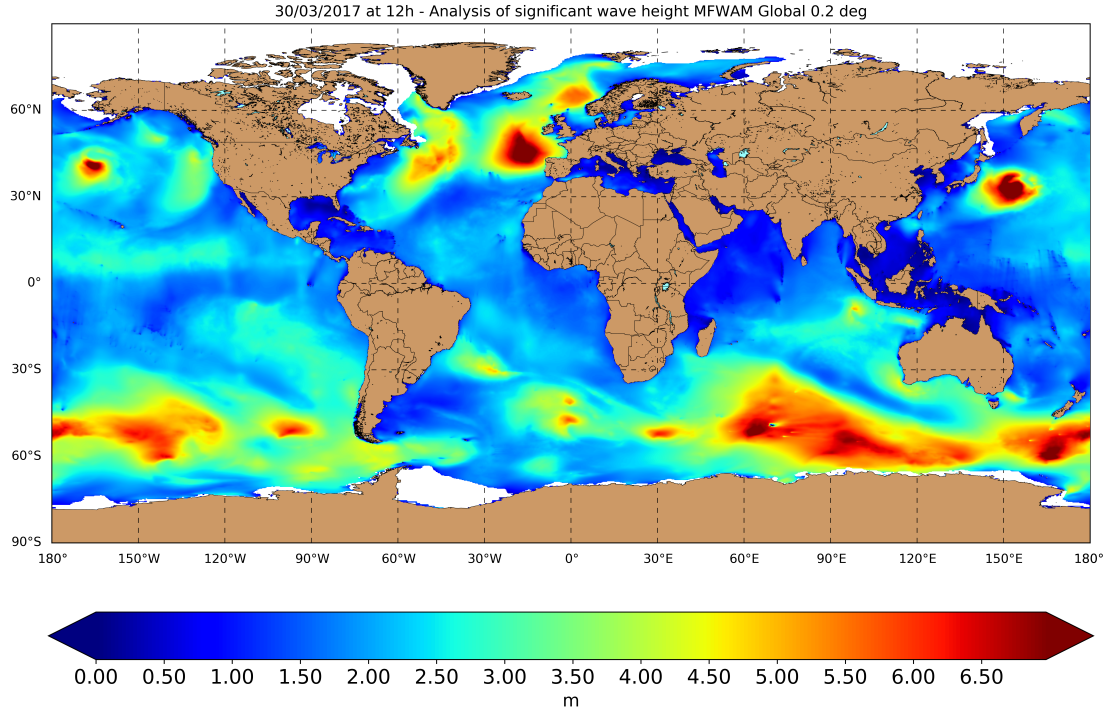

FIGURE 1.1: Global significant wave heights for 30 March 2017. Source: www.marine.copernicus.eu

damage, or in the case of too much water, sinking. This is shown in Jankowski and Laskowski (2006) where continued ingress of water over the gunwale, bow, or stern leads to capsizing. This is especially true in head seas whereby the higher frequency of the wave encounters results in more frequent events of water over the sides, and the higher differential speed between the vessel and the waves means more water is taken on in each event. When the water flowing in is greater than the water flowing out, the vessel begins to lose stability and capsizes or continues taking on water until buoyancy is lost. The U.S. Coast Guard's 2020 report on recreational boating accidents shows that flooding and swamping is the second most common accident type (U.S. Coast Guard, 2020). Inexperience and alcohol use are by far the largest primary contributing factors to accidents, but the second most is environmental causes such as weather, hazardous waters, and force of wave or wake. However, the report does not specify the percentage of each accident type caused by which contributing factor. Though capsizing was a small percentage of accident types examined by Krata (2008), it accounted for a large portion of deaths.

Though this thesis focuses on an unmanned ASV, passenger ASVs are also beginning to be used. In 2018, Rolls Royce, along with Finferries, launched the first autonomous car ferry (Rolls Royce, 2018). Control of a vessel which carries humans is even more difficult. Actuation in waves which

results in continued rolling or pitching oscillations can cause discomfort and sea-sickness in people. Roll-heave or pitch-heave motions can have the most dramatic effect, (Wertheim et al., 1998). The vessel does not need to sink or receive damage to be dangerous or life threatening. Large motions can cause people to fall over, run into objects, or if they are near the railings, they could fall overboard. For these reasons, whether it is the risk of loss of a vessel and equipment, or the loss of life, ASVs should to be designed to account for all 6 DOFs, especially if intended to operate in the presence of waves.

1.2 Background

This thesis uses a model of an ASV called Halcyon. Figure 1.2 shows the Halcyon, while Table 1.1 shows the basic parameters of the vessel. This is a medium-sized vessel intended to operate near or offshore. As just discussed, this is where most weather and wave induced accidents occur. Additionally, because it has been designed as a seafaring vessel, it is large enough and has enough actuation force to maneuver effectively through small and medium waves ranging from 0-1 meters. However, it is small enough that commonly occurring medium to large waves, 1-3 meters, requires additional mitigation strategies. The timescale for maneuvering the Halcyon, that is, the time it takes to significantly alter its velocity or heading, is typically shorter than the wave period for waves ranging from 1-3 meters. This makes Halcyon the ideal platform for developing wave force mitigation strategies for ASVs. With smaller vessels the frequency of the waves which require mitigation can be too high to provide enough time to navigate around them. For these, it is beneficial to have a design which provides a high level of stability such as Liquid Robotics Wave Glider (Liquid Robotics). Larger cargo and shipping vessels have such a large mass that maneuvering timescales are in minutes.

1.3 Aims and Objectives

It has just been shown that waves and other environmental effects can cause damage, capsizing, and loss of life for vessels, even when operated by skilled human pilots. Additionally, the increase in the use and operating environment of autonomous surface vessels, and the ever present waves in

FIGURE 1.2: A rendering of the Halcyon ASV.

TABLE 1.1: Basic Halcyon physical parameters

Parameter	Symbol	Value	Unit
Length	L	11.2	m
Beam	B	3.2	m
Height	H	2.9	m
Draft	T	.7	m
Mass	m	11000	kg
Top Speed		12.8	m/s
Number of engines		2	
Number of propellers		2	

a sea environment indicates the need to develop a controller which can navigate the waves. So the aim of this thesis is stated as:

Having knowledge of the sea-state, how can a controller be developed as to reduce wave forces and the potential of capsizing a boat?

Achieving this aim requires the following:

- Finding a suitable controller which can incorporate knowledge of the ocean disturbances into its control decisions. As it allows for mitigating future disturbances, predictive control is an ideal choice for this.

- Adapting the Sheffield Wave Environment Model and Halcyon ASV model so as to be conducive for use in the controller.
- Formulation of path following and wave induced motion mitigation as an optimal control problem, based upon the aforementioned coupled 6-DOF vessel and wave model.
- Investigating the optimal control behavior and devising of a method to produce a long time-scale optimal behavior.
- Implementing of these optimal behaviors, based upon a two degree-of-freedom controller design.
- Testing of the performance of the controller compared to a conventional path following controller in both, idealized conditions in which the controller has full knowledge of the waves, and in a fully developed sea where the controller has limited knowledge of the waves.
- Determining the practical aspects of the controller including prediction horizon length and step length based upon the ocean environment.

1.4 Notable Contributions

As stated, the aim of this research is the development of a control method for autonomous surface vehicles in rough seas. As this is an area of research that has not received much attention, much of the contributions center on the foundational understanding of optimal control and the control architecture in these conditions. The contributions of this work are as follows:

- Construction of path following problem to include mitigation of harmful wave induced motions using a 6 DOF vessel model. This is in contrast to the more typical 3 DOF motion controller which seeks to only minimize wave induced motions which affect path following performance. This is presented as an optimal control problem and solved using the Real Time Iteration Scheme method of Nonlinear Model Predictive Control.
- Numerical evidence that throttling and two-timescale tacking emerge as optimal control strategies via analysis of the solution to the above. There is a recognition that the longer time-scale tacking is intractable to the controller as devised for tacking upon individual waves. This

required the development of a two degree-of-freedom control architecture with an outer loop consisting of a novel tacking planner that is agnostic to the time dependent features of the wave harmonics.

- Numerical results that conclusively demonstrate the performance benefits of this controller, compared to conventional control designs that neglect the coupled vessel/wave dynamics in varied sea conditions and desired headings. Additional results which shows superior performance continues in full sea state, and with mismatch wave parameters.

1.5 Thesis Outline

The rest of the thesis is organized as follows:

- **Chapter 2** presents a literature review of ASV control. It starts with a brief history, discusses ASV types and uses, and presents various path following and trajectory tracking techniques used in the maritime field. This includes Line of Sight (LOS) path following with PID and MPC controllers as well as more recent research in energy optimized or COLREG compliant path planning.

- **Chapter 3** introduces the boat and wave model used in this thesis. This chapter also discusses simplifications made for the model used by the controller and changes to the simulation model to improve its accuracy for monochromatic environments.

- **Chapter 4** formulates the control problem and the NMPC controller. This includes a discussion on the Real Time Iteration (RTI) scheme. Formulation of the problem is given for both single and multiple shooting methods, both of which are implemented in this thesis.

- **Chapter 5** early methods are shown for incorporating the wave disturbance into the model by means of a wave state, along with results for a 1 DOF test. A modified method for modeling the wave disturbance is then shown along with initial tuning results for the NMPC in a head sea with large waves. Based on these results, it is shown that for navigation of the individual waves and long-term tacking along the desired path a two-timescale control architecture is needed

- **Chapter 6** a model-based tacking planner employing a cost function for head seas is introduced. Results for a variety of sea states, and desired heading and velocities are shown. Along with this testing is performed with a variety of prediction parameters, mismatched wave information, and in a full sea state.
- **Chapter 7** discusses the results of the combined tacking planner and NMPC controller in a head sea for various sea states. Additional tests showing the performance for differing prediction horizons and time steps are presented, along with the NMPC results in a full sea state.
- **Chapter 8** presents the changes to the tacking planner for both beam and following seas. The different design considerations for the different sea conditions are examined and the results are presented. Challenges in the simulation of following seas are also discussed.
- **Chapter 9** concludes the thesis with a review of the results along with future work considerations.

1.6 Publications

Much of work in this thesis is found in the following publications:

- Daniel R. McCullough, Bryn L. Jones, Oscar J.G. Villarreal, and J.A. Rossiter. Towards Control of Autonomous Surface Vehicles in Rough Seas. In *IFAC-PapersOnLine*, volume 53, pages 14692–14697. Elsevier Ltd, 2020.
- Daniel R. McCullough, Bryn L. Jones, and J.A. Rossiter. Optimal Control of Autonomous Surface Vehicles in Rough Seas. In *IEEE Oceanic Engineering* Submitted 2021.

1.7 Summary

This chapter introduced the reader to the trend of automating surface vessels, the dangers of the water for even skilled helmsmen, and the basic parameters of the vessel this thesis is based upon. The aim, objectives, and novel contributions of the thesis were discussed. Next we will look at the current research in the control of surface vessels.

Chapter 2

Literature Review

This chapter presents an overview and brief history of autonomous and unmanned surface vehicles and their uses. It follows with a literature review of recent and current literature on the challenges of ASVs with an emphasis on path and trajectory following. This chapter is intended to give a general understanding of the fields covered in this thesis, with later chapters providing further relevant literature and technical details on the control methods used for this research.

2.1 History and Development

Automatically controlled surface vessels (ASVs) have existed for hundreds, if not thousands, of years. Roberts and Sutton (2006) recounts how Sir Francis Drake used fire boats to help defeat the Spanish Armada in 1588. However, these early examples typically involved simply affixing the rudder or sail into locked position to maintain a course. The first vessel to actuate automatically to maneuver and maintain stability was the Whitehead torpedo in 1866. This was achieved with a pendulum and hydrostat controller, an early form of PD control (Briggs, 2002). Automatic piloting assistance devices began to regularly appear on human-piloted vessels throughout the early 20^{th} century to help maintain course in the presence of disturbances and currents. Unmanned controlled vessels continued to be developed in the 1940s. These were remote operated units, or automatically steering vessels, akin to the Whitehead torpedo, used for target practice or mine sweeping duty (U.S. Navy, 2007). Use in the private sector took off in the 1960s in the form of dynamic positioning vessels for use primarily in the oil and gas industry. With the advent of deep

sea drilling, traditional anchoring or other methods of mooring became infeasible due to the water depth, so dynamic positioning ships used azimuth thrusters to maintain its position in the water. This was done first manually by the *Cuss 1* and then later via a control system with the *Eureka* (Fay, 1989).

In the 1980s and 1990s, as computing continued its trend of becoming smaller, faster, and more affordable, relatively inexpensive microcontrollers saw wide adoption in all aspects of control research (Trevennor, 2012). No longer constrained to the large ships that were required to be able to carry the computer cabinets, autonomous surface vehicles began to rapidly increase in use. Starting in 1994, MIT developed a replica sea trawler ASV named *ARTEMIS* (Manley and Frey, 1994).This was quickly followed up with a small catamaran style ASV to be used for bathymetry called *ACES* (Manley, 1997). This vessel was redesigned to lighten it, improve transportability, and improve the maneuverability and control on the water. This redesigned vessel was renamed *AutoCat* (Manley et al., 2000). In Europe, the ASIMOV project spurred the development of the *DELFIM* ASV (Pascoal et al., 2000). The early 2000s saw a large number of ASVs developed by various research agencies and universities (Curcio et al., 2005; Alves et al., 2006; Ferreira et al., 2007b,a).

2.2 ASV Applications

Without the requirement of a vessel being constructed to carry a crew, it can reduce in size dramatically. This can greatly reduce the cost of building and maintaining the vessels and applies to both controlled and autonomous vessels. Autonomy has additional benefits of potential higher accuracies of metrics, such as path following without fatiguing as a human pilot would, and allows a single operator the ability to manage a fleet (U.S. Navy, 2007). These advantages make ASVs good candidates for scientific and environmental monitoring. Many of the early research vessels mentioned above were used for this monitoring, with ARTEMIS developed for bathymetric survey of inland coastal waterways, and subsequent improvement in the design of the ASVs moving further out into coastal waters (Manley, 1997; Manley et al., 2000). The DELFIM was designed for surveying and as a relay for underwater vehicles to communicate with above water researchers (Pascoal et al., 2000). Autonomous water samples were provided by Sesamo (Caccia et al., 2005). With many of these vehicles, they provide valuable data on waterways, as well as providing a useful platform with

which to test control techniques and sensing hardware (Vaneck et al., 1996; Ferreira et al., 2009; Kimball et al., 2015; Almeida et al., 2009; Larson et al., 2006; Caccia et al., 2008; Martins et al., 2007; Ferreira et al., 2012).

Another area of research, as highlighted above, is in military uses. Early developments were in torpedoes and drone target boats Roberts and Sutton (2006). It was recognized in the US Navy's Unmanned Surface Vehicle (USV) Master Plan (U.S. Navy, 2007), that full autonomy is necessary for future missions to act as a force multiplier. Full autonomy reduces necessary manpower, reduces communication bandwidth necessary for control, and extends the operational range and capabilities of the vehicles. Today, a US Congressional report shows the navy has a multitude of autonomous and semi-autonomous vessels ranging in size from less than a meter to over fifty meters, in various stages of development (O'Rourke, 2020). ASVs provide a method of continuous automated perimeter patrol Oleynikova et al. (2010), or area patrol Campbell et al. (2012) for security purposes. Additional roles in patrolling include mine countermeasures (Pastore and Djapic, 2010).

With the maturation of control techniques, ASVs are seeing deployment in passenger vessels. As mentioned above, Rolls Royce recently began operation of an autonomous car ferry (Rolls Royce, 2018). A small passenger research ferry has been in use for several years in Norway (Hegerland, 2018). Other small passenger ferries are in early stages of deployment, with an autonomous water taxi in Amsterdam called Roboat set to be launched widely in the next year (Wang et al., 2020). Hyundai also recently tested a passenger ferry in the Pohang canal in South Korea (Unmanned). The increasing use of ASVs to carry passengers has prompted an examination of the public's reaction and willingness to ride on these vessels (Mehta et al., 2021).

2.3 Vessel Modeling

Modeling and simulating marine structures and vessels uses a variety of methods and software. Computational Fluid Dynamics (CFD) programs solve the Navier-Stokes equations directly, resulting in an accurate representation of the dynamics of the system. The scale at which the turbulent flow is modeled varies from Direct Numerical Simulation (DNS) which models all the way down to the Kolmogorov scale, to Large Eddy Simulation (LES), to Reynolds Averaged Navier-Stokes (RANS), which averages the Navier-Stokes equations (Date, 2005). Beyond this there are methods

in which to deal with modeling the interaction of two fluids. For marine applications this is the sea and air. There are two common methods used, the Volume of Fluid method, and the Level Set method Katopodes (2018), however, this is beyond the remit of this thesis. One common area in which CFD is used is in ship design as it allows for testing and troubleshooting before costly prototyping is performed. The turbulence model used is often RANS as the computational power necessary for DNS and LES often far exceeds the benefit in resolution. CFD also allows for optimization methods to be applied to the design, accelerating the design time to finding a hull shape which meets performance specifications in maneuvering and fuel economy (Tahara et al., 2006). For use in control design, CFD models and simulations can help to understand highly nonlinear phenomena and dangerous situations, such as broaching in following seas. This topic is more thoroughly discussed in chapter 8, but this area is still being researched to further our understanding of the development of broaching, and methods of control to mitigate it (Carrica et al., 2012). This is an area where CFD excels as sea-trials would be prohibitively expensive as loss of the vessel is guaranteed.

However, just as there is not always a need for the high resolution of DNS, there are also times in which the mean effect of the fluid flow is sufficient. For most control strategy development, with the exception of following seas as mentioned, idealized flow can be used to estimate the hydrodynamic response of the vessel. This is done using potential flow theory in which several assumptions of the fluid are made. These are that the flow is constant, irrotational, incompressible, and inviscid. With these assumptions, the fluid dynamics reduce to a scalar function referred to as potential. Using this potential function, a boundary value problem can be obtained and solved for to find the pressure upon the hull (Newman, 1977). The establishment of the boundaries typically occur in one of two methods. The strip method, useful for slender bodies, assumes that the flow across the lateral sections of the vessel varies much more than the flow along the longitudinal sections, and thus the vessel is divided into lateral strips along the body (Chatjigeorgiou, 2018). A popular strip method software is ShipX Sintef (2022). The assumption of little longitudinal variation makes the strip method ill suited for more complex geometries Kara (2022). Instead, the panel method can be used in which the vessel is divided along both the longitudinal and lateral length resulting in a mesh of panels. Originally developed at MIT, WAMIT is a well known panel method software WAMIT (2013). While these methods provide some hydrodynamic data on the vessel, they do not calculate everything, such as the viscous damping terms. For a fully developed model, a seakeeping

model derived from one of the above methods can be combined with a maneuvering model with added nonlinearites such as memory fluid effects to obtain a good description of characteristics of the vessel. This is done in Skejic and Faltinsen (2008), and Heins et al. (2017) with sea-trials showing good agreement with maneuvering, and in Fossen (2005) & Perez and Fossen (2007).

Further, there has been much research in the applicability of the various methods in capturing the motion of vessels in the sea. For Smith and Silva (2017) which compared linear and nonlinear strip methods, it was found that the pitching due to waves was underestimated by the linear model as compared to the nonlinear model for higher wave heights. This was also found in Grigoropoulos et al. (2003), who looked at both strip and panel methods as they compare to live model testing, and it was found that pitching due to waves was underestimated compared to the model test. In Niklas and Karczewski (2020) it is noted that the strip method was insufficient to capture the nonlinearities in a vessel's ability to handle wave slamming or breaking. The panel method was not tested, so it is unknown if it would perform better as the front of the vessel, which is responsible for this behavior, is a complex shape which strip methods struggle with. In some studies, including Liu et al. (2021), stern overhangs can cause nonlinearities as only certain waves interact with this part of the vessel, and this in turn leads to disagreements with potential theory modeling methods. Additionally, there is some roll and sway forces in live model testing for head and following seas that do not appear in simulation. A simulation model of a Royal Lifeboat Severn Class is built using the MAESTRO software in Prini et al. (2015), with live model testing in Prini et al. (2016), and full scale sea-trials in Prini et al. (2018). The simulation model showed higher estimation of pitching at zero speed and high speed compared to the live model test and lower wave loads at high speeds compared to the sea-trials. This is most likely due to planing at higher velocities not being captured by the model. A maximum difference of 18% was found between the strip based numerical method and live model testing in Burlacu et al. (2018). These studies show that potential theory methods give a good estimation of vessel response in waves, however, their lack of ability to fully capture the nonlinearities means that edge cases of high or low velocities, or high waves may result in some model inaccuracies.

2.4 Control Techniques

There are a multitude of research areas in the control of ASVs. Dynamic positioning, detailed in the introduction for use in oil and gas exploration, uses multiple thrusters along the vessel and the main propellers to maintain a set position in the presence of disturbances (Sørensen, 2011) or even a defined orientation while traveling along a path at slow speeds (Martinsen et al., 2020). Operations in confined waters requires identification of obstacles to avoid (Larson et al., 2006). In traffic, manned and unmanned vessels must abide by the Convention on the International Regulation for Preventing Collisions at Sea (COLREGs), to avoid one another. This requires a high or mid-level path planning with knowledge of the paths of other vessels to safely navigate (Kuwata et al., 2014; Benjamin and Curcio, 2004; Allen, 2012; Eriksen and Breivik, 2017; Moe and Pettersen, 2017; Campbell et al., 2012; Naeem et al., 2006). Another task employed by path planners is efficient routing of the vessel for fuel conservation (Lee et al., 2015; Bitar et al., 2018; Kandel et al., 2020).

These high-level planners rely upon lower level controllers to follow the set references. Two primary controllers exist for this task, path following, and trajectory tracking controllers. Path following controllers adhere to a set of defined positions forming a path. Trajectory tracking is the path following problem with an additional temporal constraint to satisfy (Bibuli et al., 2007; Fossen, 2011). A third controller type is called a maneuvering controller, which is composed of two parts, the geomtric path following task, and a speed assignment task (Skjetne et al., 2004; Skjetne, 2005). In most of the literature, the speed assignment is assumed or is labeled path following with a speed assignment. A common approach to path following is using line-of-sight (LOS) based control. This is a kinematic approach in which the reference heading is determined based upon the crosstrack error and look-ahead distance. Yaw control is then typically handled by some form of PID controller (Fossen et al., 2003). Compensation for ocean currents can be provided by integral control as in (Caharija et al., 2014), or with an observer for both the straight line path (Paliotta and Pettersen, 2016) or curved path (Belleter et al., 2019). A prediction estimation is added in Liu et al. (2016a) for future sideslip angles to improve performance in LOS path following. An MPC controller replaces the PID to further improve path following performance (Liu and Geng, 2017). In Fossen et al. (2015), an adaptive integral slideslip compensation is embedded for LOS path following for Dubins paths. Time-varying disturbances are addressed in Wang et al. (2016) with an adaptive, robust finite time trajectory tracking which, employs a finite time disturbance observer. Ocean disturbances are

included to test observer estimation, and direct and indirect integral LOS in Fossen and Lekkas (2017). Additional collision avoidance is added to the task of ocean current mitigation in Moe and Pettersen (2017).

The lookahead distance has a large impact on the performance of the path following. A short lookahead distance provides fast convergence to the path but large overshoot, while a long lookahead distance provides a smooth convergence, but a long settling time. Several methods have been employed to combine the benefits of both while rejecting the consequences. Adaptive lookahead distance is added in Wiig et al. (2018) to provide appropriate lookahead distance for a given speed. In Pavlov et al. (2009), the LOS framework is used with an MPC controller to vary the look ahead distance to improve performance at all velocities without overshooting the path. A crosstrack error based speed assignment controller was used in Peymani and Fossen (2013) to increase the velocity of the vessel off path to improve convergence time. An additional positional constraint is added in Lekkas and Fossen (2014), to transform the LOS path following task into a trajectory tracking problem.

In path following a benefit of MPC in its use is the native ability of constraint handling. Using their Springer boat model, Annamalai et al. (2013) compares the performance of a typical LQG optimal controller with an MPC based optimal controller in a 7 waypoint tracking simulation on a calm surface with an omnidirectional current. The MPC controller showed an improvement in both crosstrack error, and actuator usage. Optimal and model predictive control have seen an increase in use recently due to an increase in computational power of computers, and the objectives of ASVs expanding beyond only path following. Model-based optimal control are used for trajectory planning about fixed obstacles (Bitar et al., 2019b). In Bitar et al. (2020), optimal control is used for planning the docking of an autonomous ferry utilizing dynamic positioning control. While a direct optimal control MPC based controller is employed to dock the ferry in Martinsen et al. (2019). A hybrid approach is used to incorporate COLREGs into energy optimized trajectory planning using MPC as a controller (Bitar et al., 2019a).

Model-based control, while requiring more effort in the devolopment of the model, once produced, can exhibit great performance. However, ASV's may vary their characteristics drastically during operation due to mass changes. This may occur when a military ASV launches missiles, a research ASV performs an automatic launch and recovery mission of an AUV, or a search and rescue ASV

picks up stranded sailors. An auto-regressive exogenous ARX model of the Springer vessel is used in Annamalai et al. (2015) in a new adaptive MPC controller. An initial model was established and then three methods were tested for parameter estimation of the model during a mass change of 50 percent; gradient descent, least squares, and weighted least squares. Though the standard weighted least squares showed good adaptability to the mass change, changes were made to the algorithm to improve accuracy. The covariance matrix was reinitialized every 25 seconds, while θ, the unknown parameters of the model, was kept constant, and more weighting was given to past values instead of current ones. Tests in both a mass change and a change in drag were done in Klinger et al. (2017) on their catamaran ASV. Using a traditional backstepping and an adaptive backstepping controller the team both dropped a 39 kg payload from the ASV and picked up a lightweight payload to induce drag. The adaptive backstepping controller displayed a much lower steady state speed error before and after the drop test and the increase in drag test compared to the standard backstepping controller, but had slightly higher error in heading both before and after compared to the standard backstepping controller.

All of these control strategies work well for their stated purpose of path following, and even more complex tasks of docking or obstacle avoidance, with stability proven in many of the papers. Additionally, with the LOS principle being kinematically based, detailed knowledge of a specific vessel's dynamics is unnecessary, which can be beneficial for application to real vessels. However, these papers do not include non-planar degrees of freedom (DOFs). That is, they only include surge, sway, and yaw motions. While these controllers are highly effective for path following, this may lead to bow diving and capsizing in severe weather.

As deployments of ASVs continues to increase, so too does their exposure to dangerous wave conditions. Waves can impart large forces upon vessels, with smaller vessels experiencing larger motions owing to their smaller masses. Path following performance is relevant to typical mission scenarios for ASVs such as bathymetric surveying, which require transitions from one waypoint to another (Kimball et al., 2015). However, control based primarily, or only on this metric risk damage or loss of vessel in rough seas. As noted in Liu et al. (2016b), much of the literature on ASV control focuses on 3 DOF models in calm seas. Few studies include actuator and yaw rate constraints in the controller design. Fewer still include constraints in the presence of environmental disturbances and rarely is the controller design based upon a 6 DOF model. As sea conditions deteriorate, the

requirement of good path following becomes superseded by survivability of the ASV. Human boat pilots balance path following with reductions in forces experienced by the crew or equipment, by adjustments in throttle or the encounter angle with waves (L3Harris, 2016). A key question that has motivated this thesis is whether or not such control behaviors applied by boat pilots are optimal and how to automate such behavior.

There are studies which take into consideration the other DOFs such as pitch and roll. For larger vessels which can handle larger waves, roll angles can still present a capsize issue. Using the LOS framework, MPC was used in Li et al. (2010) to constrain the roll angle of an S175 container ship while maneuvering in a path following scenario. Wave field and rudder constraints were added in Li et al. (2009), however, the controller had no knowledge of the waves and did not implement a predictive strategy to mitigate their effects. The waves were included to demonstrate the robustness of the controller in the presence of disturbances. It also should be noted that control strategies differ for larger vessels where their high centers of gravity mean that large rudder movements should be avoided. This pushes the timescale of the yaw response above that of individual encountered waves, hence making localized tacking maneuvers unviable. In Ono et al. (2014), Response Amplitude Operators (RAOs) were used to catalog maximum roll and pitch angles for a set of headings and velocities. Based upon predefined pitch and roll constraints, the set of headings and velocities were classed as safe or unsafe. A mixed integer MPC path planner was used to satisfy the control objectives and avoid unsafe headings and velocities. However, the transition between safe regions occurred in a discontinuous fashion, without constraints on the vessel input, nor with consideration of the dynamic coupling between the waves and the vessel. The latter point is important, since the response of a vessel depends upon its position on a wave and so the phasing of any controls requires careful consideration. In Reinhart et al. (2010), this coupling is considered in the design of an a priori differential evolution algorithm, which found that tacking led to reductions in bow diving. This led to the development of a tacking framework for a PID controller to reduce bow diving compared to a non tacking PID controller. However, all tacking was performed at the same heading angle, regardless of the desired destination. The offline nature of the DE method required a large number of simulations in order to generate a 'framework-scheduling' table; essentially a parametrization of the solution space. Using a framework developed for one wave condition resulted in worse performance when used on another wave condition, as seen when the original framework was used on smaller waves. Finally, as noted by the authors, the PID controller was unaware of

the local wave conditions. This meant that whilst tacking reduced bow diving, the PID controller was liable to respond in an adverse fashion to wave-induced disturbances, in a fashion that could be prevented through the use of predictive control.

A prediction of oncoming disturbances allows for mitigation of their effects in advance of them exciting the system, in contrast to the purely reactive nature of feedback control, alone. An NMPC controller was applied to the problem of trajectory tracking in a calm sea in Abdelaal et al. (2016). Collision avoidance and disturbances in the form of an arbitrary constant force in each DOF were included in Abdelaal et al. (2018), with the disturbances estimated with a nonlinear disturbance observer. However, and as in much of the preceding literature, the studies of Abdelaal et al. (2016) and Abdelaal et al. (2018) were restricted to 3 DOFs only, given their focus on trajectory tracking. The ability of a vessel to path follow in rough seas has been examined in Thakur et al. (2012). Parallel computing on a graphics processing unit was used to accelerate the time required to run, on board, a Monte Carlo simulation of a 6 DOF model using a PID controller, in rough seas, following a path between land masses. This was used to construct a state transition map and ultimately, determine if a path between the land masses, such as a narrow channel, was viably safe given the sea state and propose an alternative path if not. While the paper examined the effect of rough seas on the ability of a vessel to follow a path in dangerous areas, it did not directly address the problem of real-time path following when perturbed by waves instead relying on a more typical LOS PID controller for path following. This thesis relies upon, and assumes knowledge of, the wave conditions. Though the research into deterministic sea wave prediction is ongoing this assumption is justified by the ability to predict the wave forecast for several wave fronts ahead with measurements of oncoming wave profiles (Merigaud and Ringwood, 2019). Measurements of the wave profiles could be provided by LiDAR as in (Belmont et al., 2007; Blenkinsopp et al., 2012; Nouguier et al., 2014), or the encounter frequency could be estimated via an accelerometer and nonlinear observer as in (Belleter et al., 2015).

2.5 Summary

The literature review walked through a brief history of the control of ASVs. The controller structure and types of controllers used in path following were discussed, and it was shown that little literature

exists for a 6 DOF controller with mild disturbances, as well as adverse conditions. This, with the background in chapter 1, sets the motivation for the topics covered in this thesis. Next, we look to build a model of the vessel and the ocean surface.

Chapter 3

Boat and Wave Model

This chapter introduces the model and simulation environment used for this thesis. The simulation model, Sheffield Wave Environment Model (SWEM) was developed by Heins and Jones (2016) to enable rapid testing of guidance, navigation, and control (GNC) systems and reduce the need of sea-trials. It produces an approximate sea surface with a combination of several wave models. User controlled inputs, such as fetch area, swell height, and current speed allow for the creation of a wide range of sea states, from calm seas to storm surges. Though it produces a good replication of the sea surface elevation, SWEM is not a full fluid dynamics simulation. Solving the Navier-Stokes equations necessary for this would be too computationally demanding for practical use in devloping control strategies for ASVs. Owing to this, SWEM does not produce breaking waves, and the current velocity is constant, uniform, and surface only, i.e. it does not contain the orbital mechanics found in waves. This is discussed more in the following sea section.

Further work led to the development of an ASV dynamics model called Halcyon for use in SWEM (Heins et al., 2017). The Halcyon model employed in this study is based upon the C-Sweep vessel from L3Harris, a midsized minesweeper. The vessel is mono-hulled, with twin propellers, and twin rudders with the propellers and rudders operated as one, respectively. This vessel is ideal for the research presented here as it is large enough to be seagoing, with actuation forces sufficient enough to maneuver through waves, yet not so large that the timescale of actuation is longer than that of the wave periods. The rest of the chapter discusses modifications made for the controller model. This was necessary to make the model amenable to the controller. Some of the dynamics of the boat would be computationally burdensome for the controller to attempt to simulate, while other

dynamics are presented in a discontinuous state which is difficult for numerical solvers to solve. Additional changes were made to the simulation model to more accurately model a single harmonic environment. It is shown that these changes, while meaningful in a single harmonic environment, do not materially affect the simulation for full sea states.

3.1 Simulation Model

SWEM generates the wave environment by combining spectral wave models (SWMs) which account for ocean swell, wind conditions, water depth, and ocean currents. The Elfouhaily (EY) SWM, (Elfouhaily et al., 1997), calculates the higher energy, lower frequency spectrum of ocean swells which is then superimposed with the Texel-MARSEN-ARSLOE (TMA) SWM, (Bouws et al., 1985), a lower energy, higher frequency spectrum accounting for local wind direction and water depth. This produces a total wave energy spectrum that is then multiplied by the Nwogu SWM, which models the effect currents have on the waves, resulting in the final wave energy spectrum $\Psi_{\text{Final}}(\mathsf{k}, \vartheta)$, (Nwogu, 1993). This energy spectrum is used by SWEM to model the wave amplitudes using the following expression:

$$A_{\mathsf{k}_i,\vartheta_j} = \sqrt{2\Psi_{\text{Final}}(\mathsf{k}_i, \vartheta_j)\mathsf{k}_i\Delta_{\mathsf{k}}\Delta_{\vartheta}}, \tag{3.1}$$

where $\mathsf{k}_i \in \mathbb{R}$ is the spatial wave number, $\vartheta_j \in \mathbb{R}$ is the direction, $\Delta_{\mathsf{k}} \coloneqq |\mathsf{k}_{i+1} - \mathsf{k}_i|$, and $\Delta_{\vartheta} \coloneqq |\vartheta_{j+1} - \vartheta_j|$, where i and j are integers. The mean of the one-third largest waves is defined as the significant wave height H_s, where the height of a wave is double its amplitude. Figure 3.1 shows an example of a wave environment produced by SWEM.

This amplitude is used by the Halcyon model to calculate the first-order forces the waves impart on the vessel by:

$$\tau_{\text{wave}}^{\{\text{dof}\}} = \sum_{i=1}^{N}\sum_{j=1}^{M} \rho_{\text{w}} g \left| F_{\text{wave}}^{\{\text{dof}\}}\big(\omega_i, \beta_j, U(t)\big)\right| A_{\mathsf{k}_i,\vartheta_j} \cos\Big(\omega_e\big(\omega_i, \beta_j, U(t)\big)t + \angle F_{\text{wave}}^{\{\text{dof}\}}\big(\omega_i, \beta_j, U(t)\big) + \epsilon_{k_i}\Big), \tag{3.2}$$

where $\text{dof} \in \{1, 2, 3, 4, 5, 6\}$ indicates a particular degree of freedom, $\rho_{\text{w}} = 1025\,\text{kg/m}^3$ is the density of seawater, $g = 9.81\,\text{m/s}^2$ is the acceleration due to gravity, $F_{\text{wave}}^{\{\text{dof}\}} \in \mathbb{R}$ is the force RAO, $\omega_i \in \mathbb{R}$ is the wave frequency number, $\beta_i \in \mathbb{R}$ is the wave direction with respect to the vessel, $\angle F_{\text{wave}}^{\{\text{dof}\}} \in \mathbb{R}$

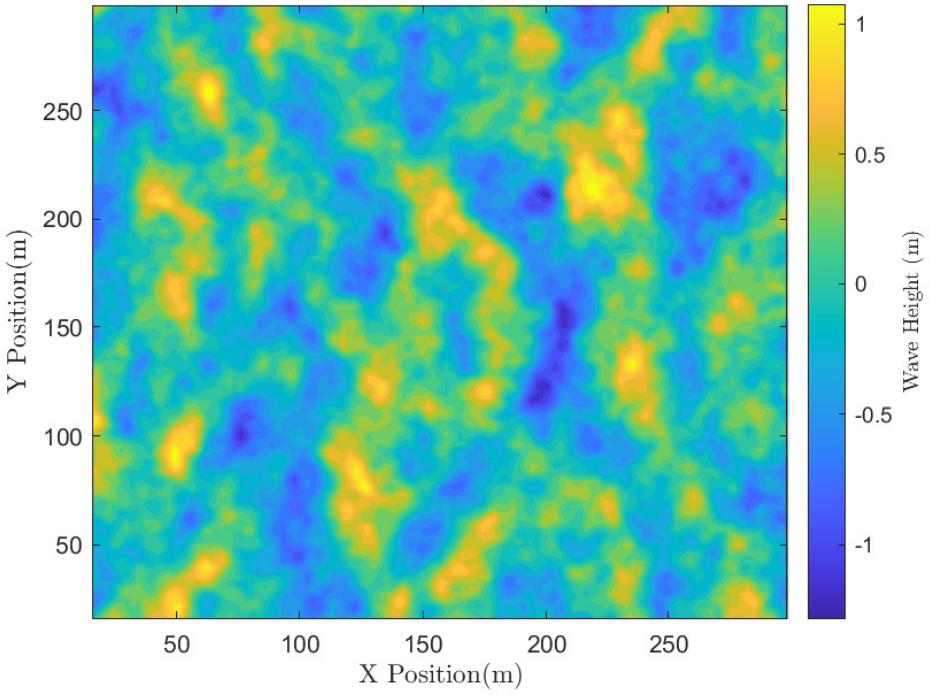

FIGURE 3.1: Example of a SWEM produced wave environment.

is the phase shift RAO, $\epsilon_{k_i} \in [0, 2\pi]$ is a random added phase component, and $\omega_e \in \mathbb{R}$ is encounter frequency which is defined as:

$$\omega_e\big(\omega_i, \beta_j, U(t)\big) \coloneqq \omega_i - \frac{\omega_i^2}{g} U(t)\cos(\beta_j), \tag{3.3}$$

where $U(t) = \sqrt{u(t)^2 + v(t)^2}$ is the forward speed, $u \in \mathbb{R}$ is the surge velocity, and $v \in \mathbb{R}$ is the sway velocity. The angular frequency, ω_i is defined as:

$$\omega_i \coloneqq \sqrt{g k_i \tanh(k_i d)}, \tag{3.4}$$

where $d \in \mathbb{R}$ is the water depth. Equation (3.2) shows the dependency of the wave forces upon the wave encounter frequency and the force/phase RAOs. In turn, these are each dependent upon throttle and steering inputs, hence establishing a causal relationship from these inputs to the wave force responses.

With respect to the force RAO in (3.2), figure 3.2 shows the force RAO plots, that is, $\rho_{\mathrm{w}} g \left| F_{\mathrm{wave}}^{\{\mathrm{pitch}\}}\big(\omega_i, \beta_j, U(t)\big) \right| A_{k_i,\theta_j}$, for the pitch degree of freedom for 2.5 m and 0.25 m wave heights.

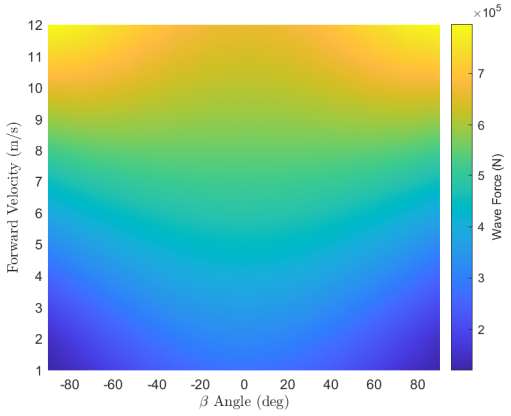

(a) The RAO force plot of 2.5m waves as a function of encounter angle and velocity.

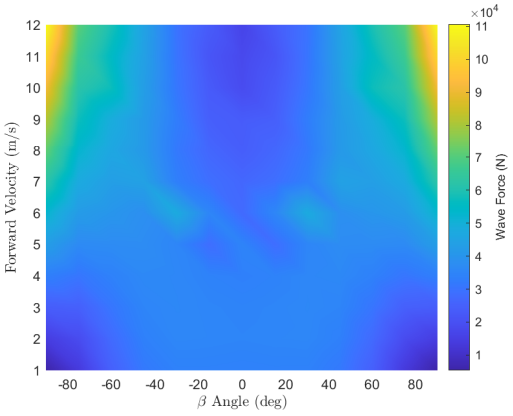

(b) The RAO force plot of 0.25m waves as a function of encounter angle and velocity.

FIGURE 3.2: These figures show the force RAO plots for 2.5m and 0.25m wave heights in the pitch DOF. An angle β of 0 indicates the vessel encountering the wave head on in a head sea.

In 2.5 m waves and below 8 m/s, lower wave force is experienced in the pitch direction as the encounter angle moves away from zero. In 0.25 m waves, the wave force is a magnitude lower, with lowest force experienced at high forward velocity heading directly into the waves. As can be inferred from the figure, manipulating the velocity and heading will alter the wave induced forces imparted upon the vessel, as described by (3.2). Hence, the wave induced forces can be controlled, to some extent, by the throttle and rudder inputs. However, the exact nature of the 'best' form of control is far from obvious, not least given the additional nonlinear dependency of the vessel forces upon the phase-shift RAOs, as described in (3.2).

3.2 Boat Model

Before discussing the vessel dynamics it is important to first establish the reference frames in which the various dynamics are defined. The first reference frame is the body-fixed frame (b-frame). This is a moving frame affixed to the vessel. The origin of this frame is usually chosen to be at the midship point at the waterline (CO). Choosing this point requires careful attention to be paid to transform the equations of motion about the center of gravity (CG) to the CO, or from the center of flotation (CF) to the CO. The CF is the point about which the vessel rolls and pitches. The advantage of using a geometrically fixed point, is the center of gravity can change depending on the loading of the vessel. Next is the sea keeping, or s-frame. The s-frame is fixed at the equilibrium state of the vessel while moving in waves. Lastly, there is the North-East-Down frame or n-frame.

TABLE 3.1: SNAME notation

Description	DOF	Forces & Moments	Velocities	Positions
Motion in x (surge)	1	X	u	x_{n}
Motion in y (sway)	2	Y	v	y_{n}
Motion in z (heave)	3	Z	w	z_{n}
Rotation about x (roll)	4	K	p	ϕ
Rotation about y (pitch)	5	M	q	θ
Rotation about z (yaw/-heading)	6	N	r	ψ

This is a reference plane tangential to the surface of the earth. The axis point to true North, East, and down, normal to the surface. The positions of the vessel are normally defined in this frame.

As discussed in the literature review, most research occurs on 3 DOF models. These models are based on what is known as Maneuvering theory, whereby the vessel is assumed to be operating in calm waters and therefore the dynamics are frequency independent due to the lack of waves. For wave environments, seakeeping theory models the frequency dependent dynamics, such as natural oscillating harmonics of the vessel as well as the motion due to wave excitation. Maneuvering theory is usually developed in the b-frame while seakeeping theory is developed in the s-frame. A unified theory for maneuvering and seakeeping combines the two methods and allows for a time-domain representation of the vessel in most sea-states. Note that the seakeeping dynamics are linearized about the s-frame, which is assumed to move at a constant speed and heading. Large disturbances which move the vessel far from the equilibrium point might affect the accuracy of the linearizations. The hydrodynamic parameters of the Halcyon model were computed using University of Southampton's hydrodynamic program THARBM (Hudson, 2000). The Society of Naval Architects and Marine Engineers (SNAME) notation used for the motions and rotations in the six degrees of freedom (SNAME The Society of Naval Architects and Marine Engineers, 1950) are listed in Table 3.1.

The kinematic equation of the vessel in the inertial n-frame is described by:

$$\dot{\boldsymbol{\eta}} = \mathbf{J}_{\boldsymbol{\Theta}}(\boldsymbol{\eta})\boldsymbol{v}, \tag{3.5}$$

where:

$\boldsymbol{\eta} \coloneqq [x_{\mathrm{n}},\ y_{\mathrm{n}}\ , z_{\mathrm{n}},\ \phi,\ \theta,\ \psi]^T$ are the positions and Euler angles in the n-frame,

$\boldsymbol{v} \coloneqq [u,\ v,\ w,\ p,\ q,\ r]^T$ are the linear and angular velocities in the *b*-frame,

and where $\mathbf{J}_\Theta(\boldsymbol{\eta}) \in \mathbb{R}^{6\times6}$ is the Euler transformation matrix between the b-frame and n-frame defined as:

$$\mathbf{J}_\Theta = \begin{bmatrix} \boldsymbol{R}_b^n(\boldsymbol{\eta}) & \mathbb{O} \\ \mathbb{O} & \boldsymbol{T}_\Theta(\boldsymbol{\eta}) \end{bmatrix}, \tag{3.6}$$

where,

$$\boldsymbol{R}_b^n(\boldsymbol{\eta}) = \begin{bmatrix} c(\psi)c(\theta) & -s(\psi)c(\phi) + c(\psi)s(\theta)s(\psi) & s(\psi)s(\phi) + c(\psi)c(\phi)s(\theta) \\ s(\psi)c(\theta) & c(\psi)c(\phi) + s(\phi)s(\theta)s(\psi) & -c(\psi)s(\phi) + s(\theta)s(\psi)c(\phi) \\ -s(\theta) & c(\theta)s(\phi) & c(\theta)c(\phi) \end{bmatrix},$$

$$\boldsymbol{T}_\Theta(\boldsymbol{\eta}) = \begin{bmatrix} 1 & s(\phi)t(\theta) & c(\phi)t(\theta) \\ 0 & c(\phi) & -s(\phi) \\ 0 & s(\phi)/c(\theta) & c(\phi)/c(\theta) \end{bmatrix},$$

where c, s, and t (not to be confused with time, in this instance) denote cosine, sine and tangent respectively. The following equation describes the motion of the vessel in the b-frame:

$$\boldsymbol{M}\dot{\boldsymbol{v}} + \boldsymbol{C_{RB}}(\boldsymbol{v})\boldsymbol{v} + \boldsymbol{C_A}(\boldsymbol{v_r})\boldsymbol{v_r} + \boldsymbol{D}(\boldsymbol{v_r})\boldsymbol{v_r} + \boldsymbol{\mu} + \boldsymbol{G\eta} = \boldsymbol{\tau} + \boldsymbol{\tau}_{\text{wave}}, \tag{3.7}$$

where:

$\boldsymbol{v_r} \coloneqq \boldsymbol{v} - \boldsymbol{v_c} \in \mathbb{R}^6$ are the relative velocities and $\boldsymbol{v_c}$ is the current velocity in the *b*-frame,

$\boldsymbol{M} \coloneqq \boldsymbol{M_{RB}} + \boldsymbol{M_A} \in \mathbb{R}^{6\times6}$, where $\boldsymbol{M_{RB}} \in \mathbb{R}^{6\times6}$ is the rigid-body mass matrix, and $\boldsymbol{M_A} \in \mathbb{R}^{6\times6}$ is the hydrodynamic added mass matrix,

$\boldsymbol{C_{RB}}(\boldsymbol{v}) \in \mathbb{R}^{6\times6}$ is the rigid-body Coriolis-centripetal matrix,

$\boldsymbol{C_A}(\boldsymbol{v_r}) \in \mathbb{R}^{6\times6}$ is the hydrodynamic added mass Coriolis-centripetal matrix,

$\boldsymbol{D}(\boldsymbol{v_r}) \coloneqq \boldsymbol{D} + \boldsymbol{D_n}(\boldsymbol{v_r}) \in \mathbb{R}^{6\times6}$, where $\boldsymbol{D} \in \mathbb{R}^{6\times6}$ is the linear damping matrix, and $\boldsymbol{D_n}(\boldsymbol{v_r}) \in \mathbb{R}^{6\times6}$ is the nonlinear damping matrix,

$\boldsymbol{\mu} \in \mathbb{R}^6$ is a vector of the fluid memory effects,

TABLE 3.2: Halcyon physical parameters

Parameter	Symbol	Value	Unit
Mass	m	11000	kg
Roll Moment of Inertia	I_{xx}	6982	kg·m^2
Pitch Moment of Inertia	I_{yy}	39077	kg·m^2
Yaw Moment of Inertia	I_{zz}	36062	kg·m^2
Length	L_{pp}	11.2	m
Beam	B	3.2	m
Height	H	2.9	m
Draft	T	.7	m
Wetted hull surface area	S	36.4	m^2
Water displacement volume	∇	10.7	m^3
Water plane area at equilibrium	A_{wp}	27.4	m^2
Frontal projected area above waterline	A_{fw}	2.4	m^2
Lateral projected area above waterline	A_{lw}	16.5	m^2
Transverse metacentric height	$G\bar{M}_T$	1.7	m
Longitudinal metacentric height	$G\bar{M}_L$	20.6	m
Frontal projected area below waterline	A_x	2.1	m^2
Two-dimensional cross-flow drag coefficient	C_D^{2D}	0.63	m
Longitudinal distance between CG and CF	$L_{CG} - LCF$	-0.37	-
Maximum forward speed of vessel	u_{max}	12.8	m/s

$\boldsymbol{G} \in \mathbb{R}^{6\times6}$ is a matrix that accounts for gravity and buoyancy effects,

$\boldsymbol{\tau} \in \mathbb{R}^6$ is a vector of control actuation forces,

$\boldsymbol{\tau}_{\text{wave}} \in \mathbb{R}^6$ is a vector of wave-induced forces.

3.2.1 Dynamic definitions

This section provides further definitions of the vessel terms in (3.7). Table 3.2 contains the physical parameters of the Halcyon. The rigid body mass matrix is defined as:

$$\boldsymbol{M_{RB}} \coloneqq \begin{bmatrix} m\boldsymbol{I}_{3x3} & -m\boldsymbol{S}(\boldsymbol{r}_g^b) \\ m\boldsymbol{S}(\boldsymbol{r}_g^b) & \boldsymbol{I}_b \end{bmatrix}, \tag{3.8}$$

where m is the mass of the vessel, $\boldsymbol{I}_{3x3}$ is an identity matrix, $\boldsymbol{S}$ is a skewed symmetric matrix, $\boldsymbol{r}_g^b$ is a displacement vector between the vessel's center of gravity CG and center of origin CO, in this case they are the same so $\boldsymbol{r}_g^b = 0$, $\boldsymbol{I}_b$ is the moments of inertia about CG. The skewed symmetric

matrix is defined as:

$$\boldsymbol{S}(\boldsymbol{\lambda}) = -\boldsymbol{S}^{\mathrm{T}}(\boldsymbol{\lambda}) = \begin{bmatrix} 0 & -\lambda_3 & \lambda_2 \\ \lambda_3 & 0 & -\lambda_1 \\ -\lambda_2 & \lambda_1 & 0 \end{bmatrix}, \quad \boldsymbol{\lambda} = \begin{bmatrix} \lambda_1 \\ \lambda_2 \\ \lambda_3 \end{bmatrix}. \tag{3.9}$$

The added mass accounts for the extra energy required for a moving vessel to move the surrounding water. It is defined as:

$$\boldsymbol{M}_A \approx \begin{bmatrix} A_{11}(0) & 0 & & & & & 0 \\ 0 & A_{22}(0) & & \cdots & & & A_{26}(0) \\ & & A_{33}(\omega_{\text{heave}}) & 0 & 0 & & \\ & \cdots & 0 & A_{44}(\omega_{\text{roll}}) & 0 & \cdots & \\ & & 0 & 0 & A_{55}(\omega_{\text{pitch}}) & & \\ 0 & A_{62}(0) & & \cdots & & & A_{66}(0) \end{bmatrix} \tag{3.10}$$

where $A(\omega)$ is a frequency dependent potential added mass and where a 0 indicates the zero frequency value while ω indicates the natural frequency of the vessel in the axis labeled. Rotation of the b-frame in the n-frame results in Coriolis and centripetal forces. The Coriolis-centripetal matrices are defined as:

$$\boldsymbol{C}(\boldsymbol{\nu}) \coloneqq \begin{bmatrix} 0 & -\boldsymbol{S}(\boldsymbol{M}_{11}\boldsymbol{\nu}_1 + \boldsymbol{M}_{12}\boldsymbol{\nu}_2) \\ -\boldsymbol{S}(\boldsymbol{M}_{11}\boldsymbol{\nu}_1 + \boldsymbol{M}_{12}\boldsymbol{\nu}_2) & -\boldsymbol{S}(\boldsymbol{M}_{21}\boldsymbol{\nu}_1 + \boldsymbol{M}_{22}\boldsymbol{\nu}_2) \end{bmatrix} \tag{3.11a}$$

For the rigid body Coriolis-centripetal matrix $\boldsymbol{C}_{\mathrm{RB}(\boldsymbol{\nu})}$:

$$\boldsymbol{M}_{\mathrm{RB}} = \begin{bmatrix} \boldsymbol{M}_{11} & \boldsymbol{M}_{12} \\ \boldsymbol{M}_{21} & \boldsymbol{M}_{22} \end{bmatrix}, \quad \boldsymbol{\nu} = \begin{bmatrix} \boldsymbol{\nu}_1 \\ \boldsymbol{\nu}_2 \end{bmatrix}, \tag{3.11b}$$

and for the added mass Coriolis-centripetal matrix $\boldsymbol{C}_{\mathrm{A}}(\boldsymbol{\nu}_{\boldsymbol{r}})$:

$$\boldsymbol{M}_{\mathrm{A}} = \begin{bmatrix} \boldsymbol{M}_{11} & \boldsymbol{M}_{12} \\ \boldsymbol{M}_{21} & \boldsymbol{M}_{22} \end{bmatrix}, \quad \boldsymbol{\nu}_{\boldsymbol{r}} = \begin{bmatrix} \boldsymbol{\nu}_1 \\ \boldsymbol{\nu}_2 \end{bmatrix}. \tag{3.11c}$$

The linear damping can be defined as:

$$\boldsymbol{D} = \boldsymbol{D_p} + \boldsymbol{D_v} \tag{3.12a}$$

where the forward speed-dependent damping is:

$$\boldsymbol{D_p} \coloneqq \begin{bmatrix} X_u & 0 & 0 & 0 & 0 & 0 \\ 0 & Y_v & 0 & Y_p & 0 & Y_r \\ 0 & 0 & Z_w & 0 & Z_q & 0 \\ 0 & K_v & 0 & K_p & 0 & K_r \\ 0 & 0 & M_w & 0 & M_q & 0 \\ 0 & N_v & 0 & N_p & 0 & N_r \end{bmatrix}, \tag{3.12b}$$

and where the linear viscous damping is defined as:

$$\boldsymbol{D}_v = \text{diag}\{\boldsymbol{D}_{v_{11}}, \boldsymbol{D}_{v_{22}}, \boldsymbol{D}_{v_{33}}, \boldsymbol{D}_{v_{44}}, \boldsymbol{D}_{v_{55}}, \boldsymbol{D}_{v_{66}}\} \tag{3.12c}$$

The following equations are used to calculate the values of $\boldsymbol{D}_v$:

$$\boldsymbol{D}_{v_{11}} = \frac{m + A_{11}(0)}{T_{\text{surge}}}, \tag{3.12d}$$

$$\boldsymbol{D}_{v_{22}} = \frac{m + A_{22}(0)}{T_{\text{sway}}}, \tag{3.12e}$$

$$\boldsymbol{D}_{v_{33}} = 2\Delta\zeta_{\text{heave}}\omega_{\text{heave}}[m + A_{33}(\omega_{\text{heave}})], \tag{3.12f}$$

$$\boldsymbol{D}_{v_{44}} = 2\Delta\zeta_{\text{roll}}\omega_{\text{roll}}[I_{zz} + A_{44}(\omega_{\text{roll}})], \tag{3.12g}$$

$$\boldsymbol{D}_{v_{55}} = 2\Delta\zeta_{\text{pitch}}\omega_{\text{pitch}}[I_{yy} + A_{55}(\omega_{\text{pitch}})], \tag{3.12h}$$

$$\boldsymbol{D}_{v_{66}} = \frac{I_{zz} + A_{66}(0)}{T_{\text{yaw}}}, \tag{3.12i}$$

where T is the time constant in the indicated axis, and $\Delta\zeta$ denotes additional damping that can be added to the indicated axis. T and ω were determined through sea trail data. The $\Delta\zeta$'s were adjusted so that the linear model behaved similarly to the nonlinear model. The additional off diagonal terms of the damping matrix was calculated using the University of Southampton's THARBM software.

The nonlinear surge resistance is defined as:

$$X_{D_n}(\boldsymbol{\nu}_r) = -\frac{1}{2}\rho_{\text{w}} S C_f^*(u_r)|u_r|u_r, \tag{3.13a}$$

where

$$C_f^* = C_f(u^{\max}) + \left(\frac{A_x}{S}C_x - C_f(u^{\max})\right)\exp(-\alpha u_r^2), \tag{3.13b}$$

and

$$C_f(u_r) = \frac{0.075}{(\log_{10} Re - 2)^2} + C_R, \quad Re \coloneqq \frac{u_r L_{pp}}{\nu}, \tag{3.13c}$$

where ρ_w is the density of seawater, S is the static wetted surface area of the hull, C_f^* is modified resistance curve to ensure high enough damping levels at low speeds, u_r is the relative surge velocity, $u^{\max}$ is the maximum surge speed, A_x is the frontal projected area of the hull below the waterline, Re is the Reynolds number, ν is the kinematic viscosity of seawater, $C_f(u_r)$ is the normal resistance curve, C_R is the residual resistance, C_x is the current coefficient, and $\alpha > 0$ is a weighting constant. C_R, C_x, and α were determined through sea trial data. The nonlinear resistance in the sway direction is calculated as:

$$Y_{D_n}(\boldsymbol{\nu}_r) = -\frac{1}{2}\rho_{\text{w}} F C_d^{2D} \int_{-L_{pp}/2}^{L_{pp}/2} |v_r + xr|(v_r + xr)dx, \tag{3.13d}$$

and in the yaw direction:

$$N_{D_n}(\boldsymbol{\nu}_r) = -\frac{1}{2}\rho_{\text{w}} F C_d^{2D} \int_{-L_{pp}/2}^{L_{pp}/2} x|v_r + xr|(v_r + xr)dx, \tag{3.13e}$$

where T is the vessel's draft, v_r is the relative sway velocity, and r is the yaw rate.

For intermediate Stokes number, when the viscosity can neither be assumed negligible nor dominant as in the case for added mass or added damping, time dependent terms remain in the momentum balance equation between the vessel and fluid. This means the forces imparted on the vessel by the fluid is not instantaneous, but occurs over time. These forces known as memory fluid effects is modeled by:

$$\boldsymbol{\mu} \coloneqq \int_0^t \boldsymbol{K}(t-\tau)\left[\boldsymbol{\nu}_r(\tau) - U\boldsymbol{e}_1\right] d\tau, \tag{3.14a}$$

where,

$$\boldsymbol{K}(t) = \frac{2}{\pi}\int_0^\infty \left[\boldsymbol{B}_{\text{Total}}(\omega) - \boldsymbol{B}_{\text{Total}}(\infty)\right] \cos(\omega t)\, d\omega, \tag{3.14b}$$

and where,

$$\boldsymbol{B}_{\text{Total}}(\omega) \coloneqq \boldsymbol{B}_{\text{Total}}(\omega, U=0) + \boldsymbol{D}_V. \tag{3.14c}$$

In the above equations $\boldsymbol{K}(t)$ is a matrix of retardation functions, U is the forward speed, $\boldsymbol{e}_1$ is a unit vector aligned with the axis x_b, $\boldsymbol{B}(\omega, U)$ is the forward speed-dependent hydrodynamic potential damping coefficient matrix, and $\boldsymbol{D}_V$ is the viscous damping matrix. Using frequency-domain identification a transfer function is fitted to (3.14a) which is converted to second order time-domain state-space model using the MSS FDI toolbox (Perez and Fossen, 2009).

The linear restoring matrix is defined as:

$$\boldsymbol{G} \coloneqq \begin{bmatrix} 0 & 0 & 0 & 0 & 0 & 0 \\ 0 & 0 & 0 & 0 & 0 & 0 \\ 0 & 0 & G_{33} & 0 & G_{35} & 0 \\ 0 & 0 & 0 & G_{44} & 0 & 0 \\ 0 & 0 & G_{53} & 0 & G_{55} & 0 \\ 0 & 0 & 0 & 0 & 0 & 0 \end{bmatrix}, \tag{3.15a}$$

where,

$$G_{33} = \rho_{\text{w}} g A_{wp}, \tag{3.15b}$$

$$G_{44} = \rho_{\text{w}} g \overline{GM_T} \nabla, \tag{3.15c}$$

TABLE 3.3: Halcyon propeller and engine parameters

Parameter	Symbol	Value	Unit
Diameter	D	0.6	m
Number of blades	Z	5	-
Pitch to diameter ratio	P/D	1.14	-
Blade area ratio	A_e/A_o	0.9	-
Engine-propeller gear ratio	G_E	2.5	-
Engine idle speed	E_{idle}	700	RPM

TABLE 3.4: Halcyon rudder parameters

Parameter	Symbol	Value	Unit
Aspect Ratio	AR	0.19	-
Planform area	A_r	0.19	m^2
Vertical distance between rudders and CG	V_{CG}	1	m
Longitudinal distance between rudders and CG	L_{CG}	-4.71	m

$$G_{55} = \rho_{\mathrm{w}} g \overline{GM_L} \nabla, \tag{3.15d}$$

$$G_{35} = G53 = \rho_{\mathrm{w}} g A_{wp} (L_{cg} - LCF), \tag{3.15e}$$

where A_{wp} is the area of the water plane at equilibrium, g is the acceleration due to gravity, $\overline{GM_T}$ is the transverse metacentric height, ∇ is the displaced water volume at equilibrium, $\overline{GM_T}$ is the longitudinal metacentric height, and L_{CG} is the longitudinal location of the center of gravity while L_{CF} is the longitudinal location of the center of flotation.

3.2.2 Actuation

The vessel is under-actuated with only two actuation controls for all 6 DOF. The actuation for the vessel is achieved by the rudders and propellers:

$$\boldsymbol{\tau} = \boldsymbol{\tau}_{\mathrm{rudder}} + \boldsymbol{\tau}_{\mathrm{prop}}. \tag{3.16}$$

The two rudders are similar to the wing of a plane and produces forces and moments in the surge (X_r), sway (Y_r), roll (K_r), and yaw (N_r) directions shown as:

$$\tau_{\mathrm{rudder}} = [\ X_{\mathrm{r}} \quad Y_{\mathrm{r}} \quad 0 \quad K_{\mathrm{r}} \quad 0 \quad N_{\mathrm{r}}\ ]^{\mathrm{T}} \tag{3.17a}$$

The drag induced in the surge direction is modeled by:

$$X_{\mathrm{r}} = -\left[\frac{(\frac{\partial C_L}{\partial \alpha}\alpha_e)^2}{\pi AR} + C_{D0}\right]\frac{1}{2}\rho_{\mathrm{w}} A_r (u_r^2 + v_r^2), \tag{3.17b}$$

where $\frac{\partial C_L}{\partial \alpha}$ is the linear lift coefficient-angle of attack gradient, α_e is the effective angle of attack of the rudders defined as:

$$\alpha_e = \alpha - \mathrm{atan2}(v_r, |u_r|). \tag{3.17c}$$

AR is the rudder aspect ratio, C_{D0} is the zero-lift drag coefficient, and A_r is the planform area of the rudders. The force of the rudders in the sway direction is modeled as:

$$Y_{\mathrm{r}} = -\left(\frac{\partial C_L}{\partial \alpha}\alpha_e\right)\frac{1}{2}\rho_{\mathrm{w}} A_r (u_r^2 + v_r^2), \tag{3.17d}$$

while multiplying by the vertical, V_{CG}, and longitudinal, L_{CG} distances results in the moments in the roll and yaw directions respectively shown as:

$$K_{\mathrm{r}} = -Y_{\mathrm{r}} V_{CG}, \tag{3.17e}$$

$$N_{\mathrm{r}} = -Y_{\mathrm{r}} L_{CG}. \tag{3.17f}$$

The propellers produce a force in the surge direction, and a moment in the pitching direction shown as:

$$\tau_{\mathrm{prop}} = [\, X_{\mathrm{p}} \quad 0 \quad 0 \quad 0 \quad M_{\mathrm{p}} \quad 0 \,]\,. \tag{3.18a}$$

The thrust in the surge direction is the result of two propellers, $X_{\mathrm{p}} = 2T_{\mathrm{p}}$ where the thrust from a single propeller is defined as:

$$T_{\mathrm{p}} = K_T(J)\rho_{\mathrm{w}} n_{\mathrm{p}} |n_{\mathrm{p}}| D^4, \tag{3.18b}$$

where,

$$K_T(J) = K_T^{\{1\}} J^2 K_T^{\{2\}} J + K_T^{\{3\}}, \quad J = \frac{V_a}{n_{\mathrm{p}} D}, \quad V_a = |u_r|. \tag{3.18c}$$

The speed of the propellers, n_{p} is in revolutions per second, D is the diameter of the propeller, J is the advance coefficient, V_a is the advance speed, and $K_T^{\{i\}}$ are the thrust polynomial coefficients defined as:

$$K_T^{\{1\}} = 0.0041, \quad K_T^{\{2\}} = -0.5002, \quad K_T^{\{3\}} = 0.6008. \tag{3.18d}$$

Table 3.5: Halcyon constraint parameters

Parameter	Value	Unit
Maximum Surge Velocity	12	m/s
Minimum Surge Velocity	1	m/s
Maximum Roll Angle	±15	degrees
Maximum Propeller Speed	22	rps
Minimum Propeller Speed	0	rps
Maximum Propeller Acceleration	±2.2	rps/s
Propeller Time Constant	5	s
Maximum Rudder Angle	±32	degrees
Maximum Rudder Rate	±40	degrees/s
Rudder Time Constant	0.1	s

The term, M_{p}, shows that the propeller can influence pitch motions by inducing a pitching moment, $M_{\mathrm{p}} = X_{\mathrm{p}} V_{CG}$, though it is marginal.

3.3 Controller Model

The simulation model outlined in the previous section is not directly amenable to controller design and so the purpose of this section is to define a simplified state-space representation. The model of the coupled wave and ASV dynamics is:

$$\dot{\boldsymbol{x}}(t) = f\big(\boldsymbol{x}(t), \boldsymbol{u}(t), t\big) \tag{3.19a}$$

$s.t.$

$$\boldsymbol{x}_{\min}(t) \leq \boldsymbol{x}(t) \leq \boldsymbol{x}_{\max}(t) \tag{3.19b}$$

$$\boldsymbol{u}_{\min}(t) \leq \boldsymbol{u}(t) \leq \boldsymbol{u}_{\max}(t) \tag{3.19c}$$

where the state vector $\boldsymbol{x}$ is defined as:

$$\boldsymbol{x} \coloneqq [x_{\mathrm{c}}, u, y_{\mathrm{c}}, v, z_{\mathrm{n}}, w, \phi, p, \theta, q, \psi, r, n_{\mathrm{p}}, \alpha_{\mathrm{r}}]^T, \tag{3.19d}$$

This includes additional states that account for the dynamics of the thrust, n_{p}, and rudder actuators, α_{r}, both of which are approximated as first-order systems with linear rate constraints. This also includes x_{c} and y_{c}, which are the respective x and y positions in Cartesian coordinates. Table 3.5 lists the state and input constraints of the vessel. The detailed description of the state-space model is included at the end of this chapter in section 3.6. With the exception of the terms relating to

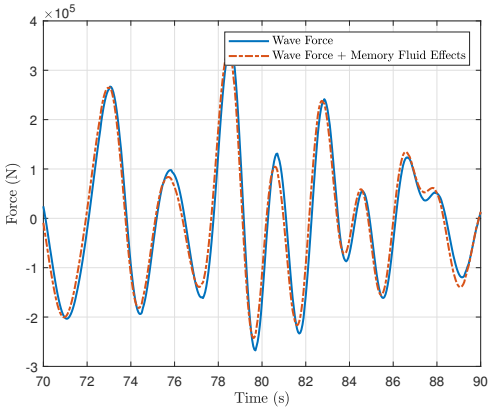

(a) Pitch wave force and pitch wave force + memory fluid effects.

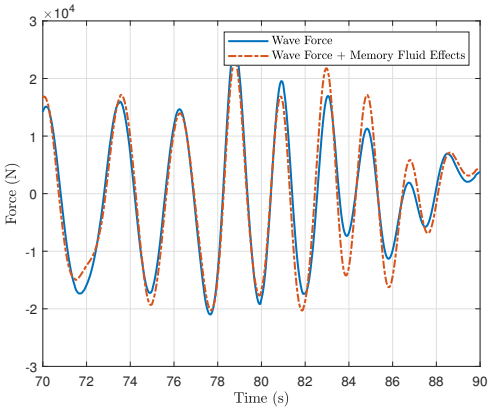

(b) Yaw wave force and yaw wave force + memory fluid effects.

FIGURE 3.3: These figures plot the wave force and the wave force + memory fluid effects in the pitch and yaw directions for a full sea state. These figures justify the exclusion of the memory fluid effects from the controller model.

the x and y positions in (3.6) which are dependent on the yaw angle, the off diagonal terms reduce to zero when roll and pitch angles are zero. Though the roll and pitch angles are not zero in the presence of waves, as shown in the results chapters of this thesis, they are typically small enough to justify the small model mismatch in order to reduce the computational burden they impose with their inclusion. With roll and pitch presumed zero, (3.5) can be approximated as:

$$\dot{\boldsymbol{\eta}} \approx \boldsymbol{v}, \tag{3.20a}$$

with the yaw angle increasing in the counter-clockwise direction as is standard in Cartesian coordinates, the derivative x_c and y_c positions are calculated as:

$$\dot{x}_c(t) = u(t)\cos\big(\psi(t)\big) + v(t)\sin\big(\psi(t)\big), \tag{3.20b}$$

and

$$\dot{y}_c(t) = u(t)\sin\big(\psi(t)\big) - v(t)\cos\big(\psi(t)\big). \tag{3.20c}$$

The translation between the n-frame and b-frame is handled outside the controller by the simulation. The state space model of the ASV and wave dynamics is then discretized with respect to time and simulated using the forward Euler method.

Another simplification made to reduce the computational power required for the controller is the

omission of the memory fluid effects. In the time domain, these consist of three second order state space models for each degree of freedom which would require 36 extra states to fully capture the dynamics. Neglecting these effects represents a trade-off between model accuracy for a reduction in model complexity and hence controller synthesis. Figure 3.3 plots both the wave force only and the wave force with the memory fluid effects in a full sea state for both the pitch and yaw DOF. The memory fluid effects in the pitch DOF, figure 3.3(a), are minimal relative to the wave force and represent the smallest deviation of the 6 DOFs. The memory fluid effects in the yaw DOF, figure 3.3(b), are the largest relative to the wave force. The other DOFs are somewhere in between these results. These two figures show, however, that the model accuracy remains high despite not modeling the memory fluid effects.

Most of the parameters used by the simulation model, such as the drag resistance curve, and the force and phase RAOs, such as those shown in Fig. 3.2, are presented as look-up tables. The functional dependence of this data upon the independent variables was approximated by polynomial interpolants, so as to enable tractable numerical solution in the next section. However, many of these parameters are represented in a discontinuous nature. Whether this is because of convention or the result of the output format of hydrodynamic programs, this can pose a significant challenge for numerical solvers. When numerical solvers attempt to find a minimum value using something such as a gradient method, as they encounter a discontinuity they can fail if the solver is not robust, or continue decreasing its step size until the solution is found or a maximum number of iterations is met. None of these outcomes are ideal, especially when a solver is intended to run online for control purposes. Figure 3.4 shows one such occurrence of a discontinuity. This shows the wave force and phase RAO for the surge direction when encountering a 1.5 meter wave at a fixed velocity of 5 m/s for all possible encounter angles. The wave force as seen in (3.2) is usually represented as the magnitude of the force RAO, with the phase RAO shifting by 180 degrees to denote a change in "direction" of the wave force. What is meant by direction is imagine encountering a wave in a head sea. There is a point on that wave in which the harmonic component, cosine, of (3.2) is a positive 1 and with the magnitude of the force RAO, the equation indicates a force in the positive surge direction. If, in that instant, the boat changes its heading by 180 degrees to a following sea, the phase RAO causes a phase shift of 180 degrees in the harmonic component, with the equation now indicating the wave force in the negative surge direction. To alleviate the issue of discontinuity, the

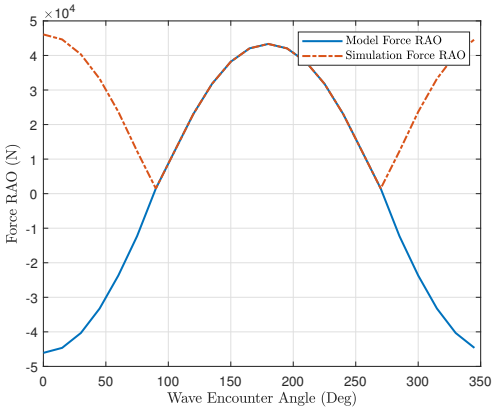

(a) The original representation of the force RAO plotted with the controller model representation.

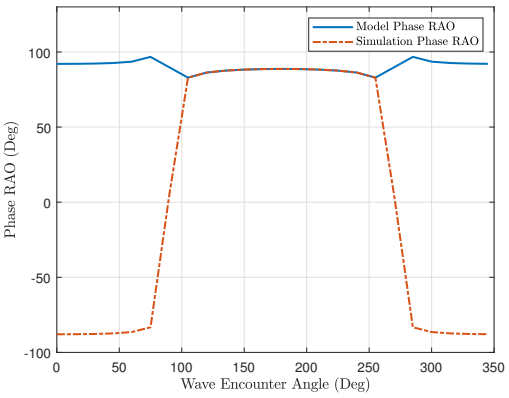

(b) The original representation of the phase RAO plotted with the controller model representation.

FIGURE 3.4: These figures show the surge force and phase RAO for a 1.5 meter wave. Typically, the force RAO is given as the magnitude of force, while the phase RAO determines "directionality" of the force.

force RAO is changed to allow negative values to indicate direction changes, while the phase RAO is unshifted to indicate only where on the wave the force is experienced.

3.4 Modifications To Simulation Model

The previous changes were only carried out on the controller model, with the simulation model retaining its original data. There can be a slight model mismatch in the transition between one phase extreme and the other such as between a heading of 75 degrees and 105 degrees in figure 3.4(b), though this occurs when the force RAO is at or near zero so the effects are minimal. However, when the transition occurs because the output data from the hydrodynamic program is bounded, the model mismatch can be large due to the simulation interpolating the wrong value. Figure 3.5 shows the phase RAO for the pitch direction in a following wave for all velocities. The output data for the phase RAO's is bounded to ± 180 degrees. The bounding causes the first three velocities to have a negative phase value. These values produce the correct output, however, in between 3 m/s and 4 m/s the value jumps dramatically. During simulation, if the velocity of the vessel is in between these two velocities, the simulation will interpolate between the two values which produces the wrong output. Worse, if the vessel is accelerating from 3 m/s to 4 m/s, the phase RAO will cause the vessel to experience 300 degrees of a wave cycle, even if the position of the vessel on the wave changes little. This can be especially pronounced in following seas where

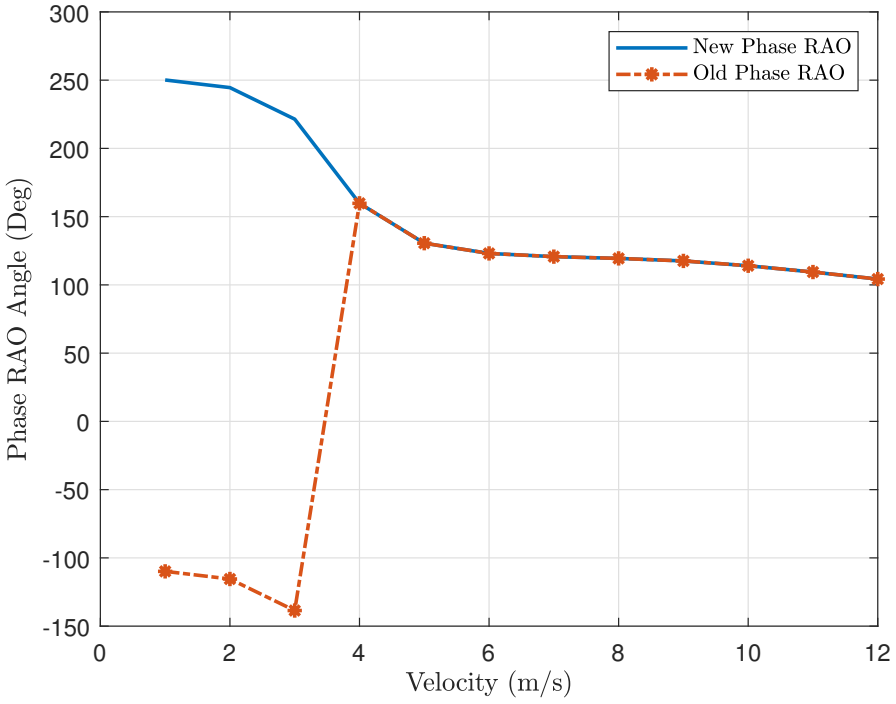

FIGURE 3.5: An example where the bounded output of hydrodynamic data can cause issue when interpolating between integer velocity values.

the differential velocity of the wave and vessel can be negligible. The fix is similar to before, only now the RAO mapping is shifted 360 degrees to produce a more continuous curve, and is allowed to have values beyond ±180 degrees.

The interpolation of figure 3.5 was not originally an issue for the Halcyon model. Figure 3.6(a) shows how the Halcyon handled the interpolation. Outside of the RAO data tables, both the velocity, and heading are rounded both up and down to the nearest integers. The force and phase RAO values for these integers are then outputted. This avoids the incorrect interpolation between the integer values shown previously. These integer RAO values are then interpolated to produce a total output value. However, this interpolation introduces its own errors. Figure 3.6(b) shows a simplified example of what can occur. Because the output phase RAOs are from two different integers, they can have largely different values. In this example, the plotted output of two velocities, 5 m/s and 6 m/s, have the same magnitude of 1 N. Their phase differs by 30 degrees though, and the resultant final magnitude is less than the expected value of 2 N because of the phase interference. As figure 3.5 shows, the phase RAO value of neighboring integer velocities can vary by 50 degrees or more, with the RAO value of neighboring integer headings, further increasing the difference. Figure 3.7 shows

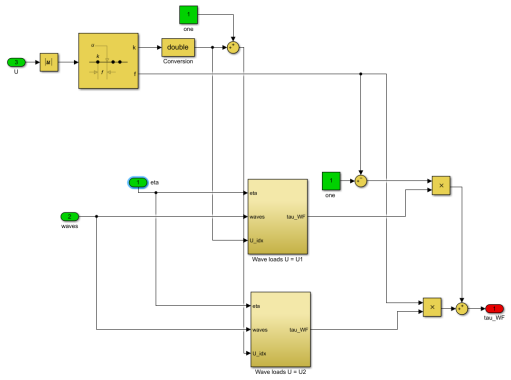

(a) The original Halcyon method of interpolating between velocity and heading integers outside of the data table.

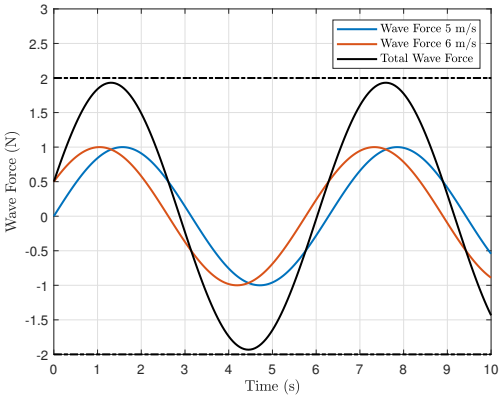

(b) An example of the phase interference that can occur with the original Halcyon method of interpolation.

FIGURE 3.6: These figures show the original Halcyon method for interpolation and the resultant phase interference that occurs.

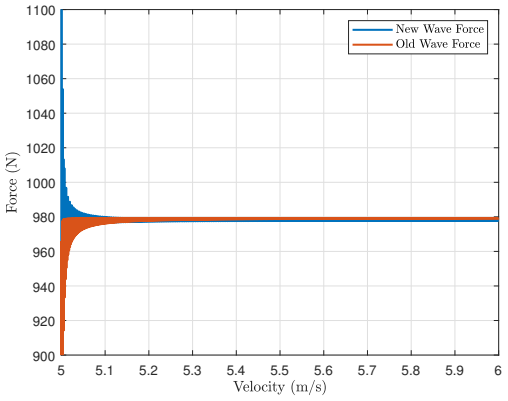

(a) Continuous RMS value of the wave force in the surge direction for the old and new interpolation method as the vessel accelerates from 5 to 6 m/s.

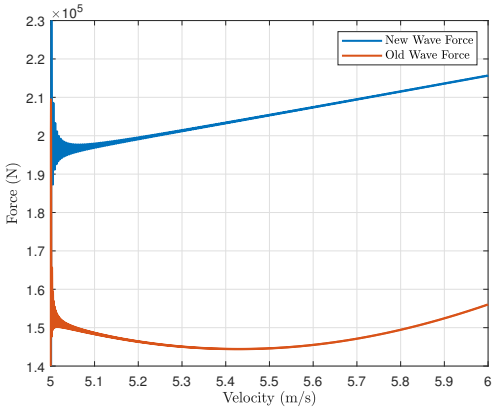

(b) Continuous RMS value of the wave force in the pitch direction for the old and new interpolation method as the vessel accelerates from 5 to 6 m/s.

FIGURE 3.7: These plots show how the interpolation method employed by the Halcyon model can result in a phase interference due to varying phase RAO values of the different integer velocities and ultimately result in a lower wave force than what is expected.

what this interference can cause. These two figures plot the continuous RMS value of the wave force in the surge and pitch DOFs for a single wave harmonic. The heading is held constant as the velocity is increased from 5 to 6 m/s. The original output is compared with the new method which interpolates inside the data tables while applying the fix highlighted in figure 3.5. The force in the surge DOF is shown in 3.7(a). Both methods show a similar force because the phase RAO for surge is mostly constant in respect to both velocity and heading. The pitch force for both methods vary considerably, however. The magnitude of the pitch force generally increases as velocity increases for a given heading. This can be seen with the new method in figure 3.7(b). The method used

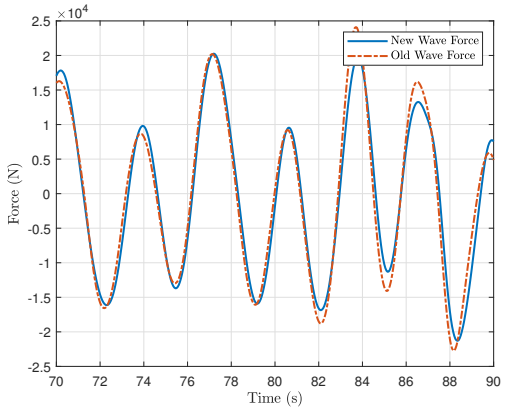

(a) The original and new wave force in the surge direction.

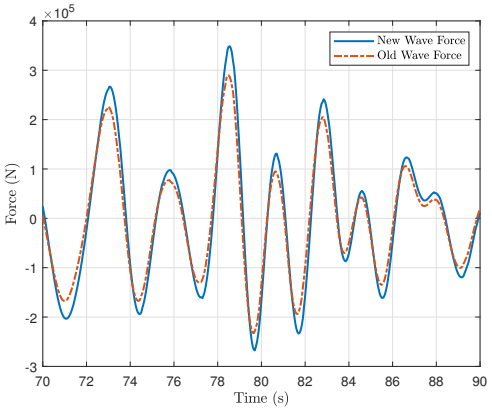

(b) The original and new wave force in the surge direction.

FIGURE 3.8: These figures show the results of the changes made in this section on the overall wave force experienced in a full sea state.

originally by the Halcyon has a much lower starting value, and decreases as the velocity increases until about 5.4 m/s.

Figure 3.8 shows the result of the changes presented in this chapter on a full sea state. As before with the individual harmonic, little change is seen with the surge force in figure 3.8(a) but the pitch force sees slightly higher peak forces in figure 3.8(b) as it did previously. The overall effect of the changes on the wave forces is minimal.

3.5 Linear Seakeeping Model

The vessel modeled is a Nonlinear Unified Seakeeping and Maneuvering Model with Memory Fluid Effects. In other words, this is a linear seakeeping model combined with a maneuvering model which includes nonlinear damping and Coriolis forces with added memory fluid effects to express frequency dependent functions in a time domain model. That means that the seakeeping response, i.e. the response to wave excitation forces, should be linear for all wave heights with the same frequency. More preciously, the response should be the same for the same encounter frequency, because, as was shown previously, the response varies with the velocity of the vessel encountering the wave.

To test this, the vessel was simulated going directly into the wave with a reference velocity of 4 m/s. The wave was composed of a single harmonic with a frequency of 1.3 rad/s, and the wave height

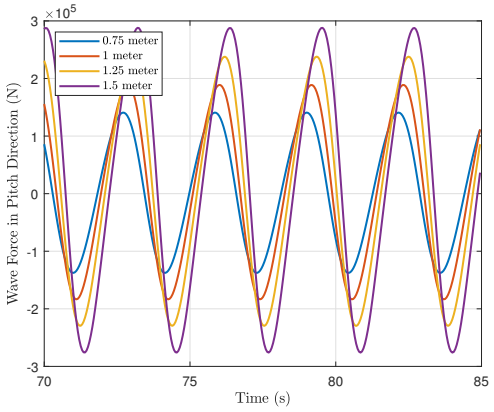

(a) Wave force in the pitch direction for the 4 wave heights.

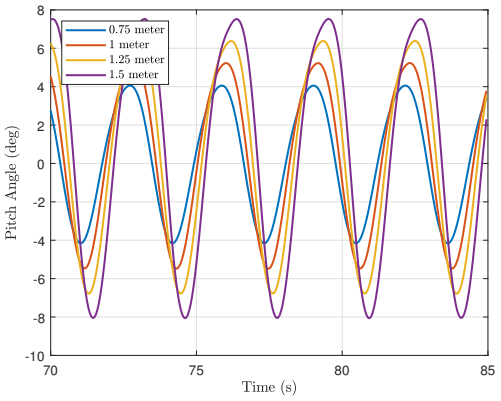

(b) Pitch angle for the 4 wave heigths.

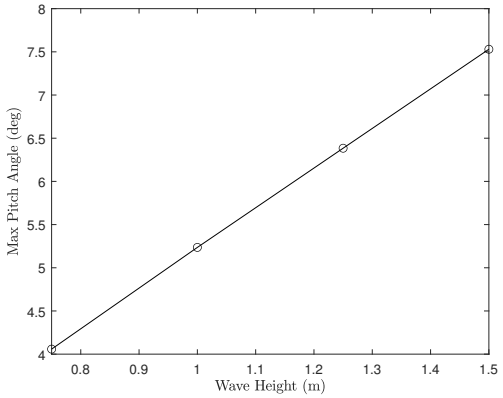

(c) The maximum pitch angles for the 4 waves.

FIGURE 3.9: These figures show the wave force in the pitch direction, the pitch angles, and the maximum pitch angles for a wave height of 0.75, 1, 1.25, and 1.5 meter waves with a wave frequency of 1.3 rad/s.

was set a 0.75, 1, 1.25, and 1.5 meters to test the linearity. The velocity was achieved by actuation from the propellers controlled by a PID controller. As the vessel is heading directly into the waves, there is no wave force in the sway, roll, or yaw so pitch was chosen as the direction to test. Figure 3.9(a) shows the wave force in the pitch direction for the 4 wave heights, while figure 3.9(b) shows the resulting pitch angle. As can be seen with these, the larger waves have a slight temporal offset of their peaks. This is due to the wave having a larger effect on the surge velocity, and therefor the encounter frequency of the vessel. Figure 3.9(c) shows that the response is still affine, with the maximum pitch angles of the 4 wave heights plotted in a straight line, however, note that the pitch angle for the 0.75 meter wave is 4 degrees, while the pitch angle for double that height of 1.5 meters is only 7.5 degrees.

To remove this variable, the wave force in the surge direction is neglected. The PID is then able to

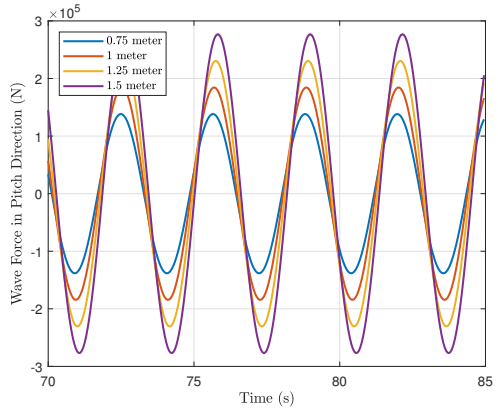

(a) [Wave force in the pitch direction for the 4 wave heights.

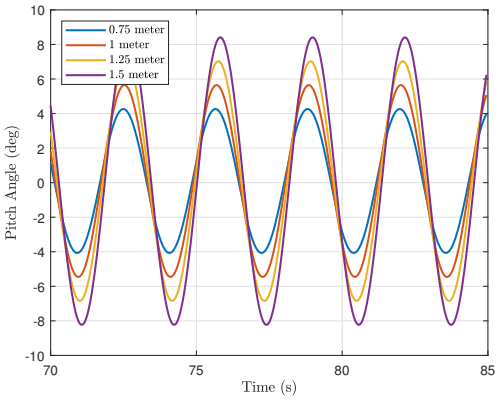

(b) Pitch angle for the 4 wave heigths.

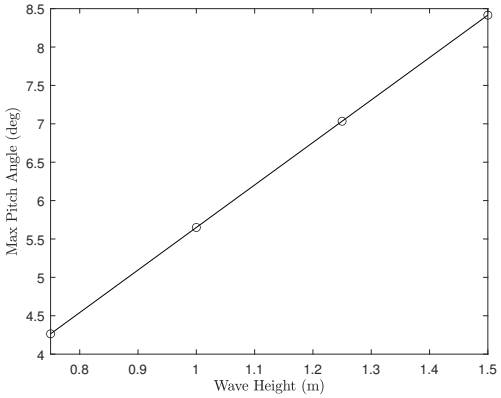

(c) The maximum pitch angles for the 4 waves.

FIGURE 3.10: These figures show the wave force in the pitch direction, the pitch angles, and the maximum pitch angles for a wave height of 0.75, 1, 1.25, and 1.5 meter waves with a wave frequency of 1.3 rad/s.

keep a more constant 4 m/s through the waves. This removes the temporal shift in figures 3.10(a) and 3.10(b) and produces a linear response amongst the 4 wave heights. This can be seen in figure 3.10(c) where the pitch angle for the 0.75 meter wave is half that of the 1.5 meter wave at 4.2 degrees to 8.4 degrees.

3.6 Detailed definition of controller model

Finally, before the detailed controller model, the reader is presented with Table 3.6. This table presents a generalized description of the force and phase RAO for each DOF, so that the reader has an understanding of the characteristics of the vessel in waves. These descriptions are for waves 0.5 meters and higher, as the response of the vessel to these waves have a very similar characteristic

TABLE 3.6: Generalized RAO descriptions

Degree of freedom	Description
Surge	Surge wave force is typically dependent only on vessel heading with the maximum force experienced in a head or following sea, and no force experienced in a beam sea. The surge phase is typically near constant for all headings and velocities.
Sway	Sway wave force is heavily dependent on the heading while only slightly dependent on the velocity. Sway force is highest in beam seas and zero for head and following seas. Sway increases slightly with an increase in velocity. The sway phase is typically near constant for all headings and velocities.
Heave	Heave is not heavily dependent on velocity or heading, and its phase is constant.
Roll	Roll wave force is heavily dependent on the heading while only slightly dependent on the velocity. Roll force is highest in beam seas and zero for head and following seas. Roll increases slightly with an increase in velocity. The roll phase is typically near constant for all headings and velocities.
Pitch	Pitch wave force is heavily dependent on the heading and velocity. The higher forces are seen at higher velocities with the highest occurring in a beam wave. Conversely, at lower velocities, the lowest force is also seen in a beam wave. Pitch phase varies widely between wave heights and with changes in heading and velocity.
Yaw	Yaw wave force is heavily dependent on the heading while only slightly dependent on the velocity. Yaw force is highest in beam seas and zero for head and following seas. Yaw increases slightly with an increase in velocity. The yaw phase is typically near constant for all headings and velocities.

and vary only in magnitude of the values. And lastly, the following is a full derivation of the vessel

model from (3.19a).

$$\dot{x}_{\mathrm{c}}(t) = u(t)\cos\big(\psi(t)\big) + v(t)\sin\big(\psi(t)\big), \tag{3.21a}$$

$$\dot{u}(t) = \boldsymbol{C}_{11}(\boldsymbol{\nu}) + X_{D_n}(\boldsymbol{\nu}) + \boldsymbol{D}_{v_{11}}u(t) + \boldsymbol{D}_{p_{11}}u(t) + \tau_{\mathrm{prop}}^{\{\mathrm{surge}\}}(t) + \tau_{\mathrm{rudder}}^{\{\mathrm{surge}\}}(t) + \tau_{\mathrm{wave}}^{\{\mathrm{surge}\}}(t), \tag{3.21b}$$

$$\dot{y}_{\mathrm{c}}(t) = u(t)\sin\big(\psi(t)\big) - v(t)\cos\big(\psi(t)\big), \tag{3.21c}$$

$$\dot{v}(t) = \boldsymbol{C}_{22}(\boldsymbol{\nu}) + Y_{D_n}(\boldsymbol{\nu}) + \boldsymbol{D}_{v_{22}}v(t) + \boldsymbol{D}_{p_{22}}v(t) + \boldsymbol{D}_{p_{24}}p(t) + \boldsymbol{D}_{p_{26}}r(t) + \tau_{\mathrm{rudder}}^{\{\mathrm{sway}\}}(t) + \tau_{\mathrm{wave}}^{\{\mathrm{sway}\}}(t), \tag{3.21d}$$

$$\dot{z}_{\mathrm{n}}(t) = w(t), \tag{3.21e}$$

$$\dot{w}(t) = \boldsymbol{C}_{33}(\boldsymbol{\nu}) + \boldsymbol{D}_{v_{33}}w(t) + \boldsymbol{D}_{p_{33}}w(t) + \boldsymbol{D}_{p_{35}}q(t) + \boldsymbol{G}_{33}w(t) + \boldsymbol{G}_{35}q(t) + \tau_{\mathrm{wave}}^{\{\mathrm{heave}\}}(t), \tag{3.21f}$$

$$\dot{\phi}(t) = p(t), \tag{3.21g}$$

$$\dot{p}(t) = \boldsymbol{C}_{44}(\boldsymbol{\nu}) + \boldsymbol{D}_{v_{44}}p(t) + \boldsymbol{D}_{p_{42}}v(t) + \boldsymbol{D}_{p_{44}}p(t) + \boldsymbol{D}_{p_{46}}r(t) + \boldsymbol{G}_{44}p(t) + \tau_{\mathrm{rudder}}^{\{\mathrm{roll}\}}(t) + \tau_{\mathrm{wave}}^{\{\mathrm{roll}\}}(t), \tag{3.21h}$$

$$\dot{\theta}(t) = q(t), \tag{3.21i}$$

$$\dot{q}(t) = \boldsymbol{C}_{55}(\boldsymbol{\nu}) + \boldsymbol{D}_{v_{55}}q(t) + \boldsymbol{D}_{p_{53}}w(t) + \boldsymbol{D}_{p_{55}}q(t) + \boldsymbol{G}_{53}w(t) + \boldsymbol{G}_{55}q(t) + \tau_{\mathrm{prop}}^{\{\mathrm{pitch}\}}(t) + \tau_{\mathrm{wave}}^{\{\mathrm{pitch}\}}(t), \tag{3.21j}$$

$$\dot{\psi}(t) = r(t), \tag{3.21k}$$

$$\dot{r}(t) = \boldsymbol{C}_{66}(\boldsymbol{\nu}) + N_{D_n}(\boldsymbol{\nu}) + \boldsymbol{D}_{v_{66}}r(t) + \boldsymbol{D}_{p_{62}}v(t) + \boldsymbol{D}_{p_{64}}p(t) + \boldsymbol{D}_{p_{66}}r(t) + \tau_{\mathrm{prop}}^{\{\mathrm{yaw}\}}(t) + \tau_{\mathrm{rudder}}^{\{\mathrm{yaw}\}}(t) + \tau_{\mathrm{wave}}^{\{\mathrm{yaw}\}}(t), \tag{3.21l}$$

$$\dot{n}_{\mathrm{p}}(t) = \frac{1}{\tau_{n_{\mathrm{p}}}}\left(u_{n_{\mathrm{p}}}(t) - n_{\mathrm{p}}(t)\right), \tag{3.21m}$$

$$\dot{\alpha}_{\mathrm{r}}(t) = \frac{1}{\tau_{\alpha_r}}\left(u_{\alpha_{\mathrm{r}}}(t) - \alpha_{\mathrm{r}}(t)\right). \tag{3.21n}$$

3.7 Summary

This chapter laid out the model of the wave environment and vessel dynamics used in the thesis. The model was shown to be highly nonlinear, but some simplifications, including the elimination of the Euler transformation, or the memory fluid effects, can reduce the complexity without much loss in model accuracy. It was also shown how the previous implementation of the simulation could

cause wave phase cancellation, which does not readily present itself in a full sea state, but becomes obvious for a single harmonic. The change to correct this then introduces an interpolation error for the phase RAOs, which also required correction. The next chapter discusses the controller used in the thesis.

Chapter 4

NMPC Controller

This chapter introduces the nonlinear model predictive controller architecture and initial results. This chapter starts with section 4.1 which discusses why nonlinear control was necessary. Then section 4.2 opens with why the method in the thesis was chosen and then presents the NMPC problem formulation and Real Time Iteration (RTI) scheme.

4.1 Linear Model

Initial attempts to discern an optimal control strategy for the ASV in rough seas began with linearization of the Halcyon model. It was hoped that an expression, like an algebraic Riccati equation, could be derived which would provide a fundamental understanding for future control strategies. A 1 DOF surge model was developed. Surge was ideal for this because it is dynamically decoupled from the other states, and the actuation in the surge direction, the propeller, is dependent upon only the surge velocity and propeller speed. The surge dynamics are mostly affine for much of the operating range. However, the inclusion of the wave disturbances proved intractable to a linear framework. To understand why, it is necessary to reexamine and modify (3.2) & (3.3), shown here with the random phase removed:

$$\cos\Big(\omega_e\big(\omega_i, \beta_j, U(t)\big)t + \angle F_{\text{wave}}^{\{\text{dof}\}}\big(\omega_i, \beta_j, U(t)\big)\Big). \tag{4.1}$$

Besides the force RAO, the estimation of the expected wave force requires two elements: the phase of the physical wave, i.e. where on the wave the vessel is located, and the phase of when the wave force is experienced relative to the physical wave, i.e. the phase RAO. For example a phase RAO of zero means that the wave force imparted to the vessel, coincides with the wave elevation such that the maximum wave force is experienced at the crest, and the minimum (negative) wave force is experienced in the trough. For a linear model, the phase RAO poses little difficulty for all DOFs except pitch because most phase RAOs are relatively constant. To describe the phase of the physical wave, Airy Wave Theory, also known as Linear Wave Theory replaces the description of the instantaneous encounter frequency in (4.1). For a 1 degree case the phase of the wave can be described by:

$$\omega_i t - k x_c \tag{4.2}$$

where $k = \frac{\omega_i^2}{g}$ is the wave number. This formulation now accounts for the accumulation of differences in the position due to a variable velocity, because x_c is the integral of the velocity. While the encounter frequency and wave state can still be estimated using the average velocity in a linear state space model such as:

$$\begin{bmatrix} \dot{\eta} \\ \ddot{\eta} \end{bmatrix} = \begin{bmatrix} 0 & 1 \\ -\omega_{\text{ave}}^2 & 0 \end{bmatrix} \begin{bmatrix} \eta \\ \dot{\eta} \end{bmatrix}, \tag{4.3}$$

this can prove inaccurate, especially in high sea states where the velocity can vary greatly. The controller has no knowledge of the coupling of the vessel and wave states and, therefore, its solution can be sub-optimal. This shows that for a complete solution, even for simple problems that can mostly be linearized, nonlinear control is required.

4.2 NMPC Controller

The need now is to find a suitable nonlinear controller which would provide the performance necessary while meeting certain criteria. The aim of this study is to find an “optimal” course of navigation so the problem should be presented as such. This study is also conducted under the premise that the wave disturbance can be effectively predicted which naturally motivates the choice of predictive control. NMPC also provides a means to handle the constraint limitations of the vessel, such as the actuation inputs, or a user-defined state constraint such as a maximum roll angle. As discussed

in the literature review, there are many methods for solving an NMPC problem. Because of the application based nature of this thesis, the appeal of the Real Time Iteration scheme is its ability to be used on systems which require quick solving of the optimal control problem. Though the controller presented in this work was coded by the author, based on the work of Oscar Julian Gonzalez Villarreal, the RTI method is provided by the ACADO toolkit allowing the methods presented here to be implemented and improved upon in academia and industry with relative ease (Houska et al., 2011).

4.2.1 NMPC Problem Formulation

Pitch and roll are the primary concerns for capsizing or water ingress. Wave force in the pitch direction is non zero for any wave encounter angle, while wave force in the roll direction is zero in head and following seas and roll angles can be large due to rudder actuation only. For these reasons, the pitch angle is considered an optimizing variable while the roll angle is treated as a constraint. Considering a discrete-time representation of the general nonlinear system (3.19a), the objective then is to find the propeller and rudder inputs, $\boldsymbol{u}_k$ which minimize the pitch angles while adhering to a desired surge velocity and heading, subject to the input, and state constraints. This is mathematically stated as follows:

$$\min_{\hat{\boldsymbol{\mathcal{U}}},\hat{\boldsymbol{\mathcal{X}}}} J = (\boldsymbol{\mathcal{X}}_r - \hat{\boldsymbol{\mathcal{X}}})^T \boldsymbol{\mathcal{Q}} (\boldsymbol{\mathcal{X}}_r - \hat{\boldsymbol{\mathcal{X}}}) + (\boldsymbol{\mathcal{U}}_r - \hat{\boldsymbol{\mathcal{U}}})^T \boldsymbol{\mathcal{R}} (\boldsymbol{\mathcal{U}}_r - \hat{\boldsymbol{\mathcal{U}}}), \tag{4.4a}$$

$$s.t.$$

$$\boldsymbol{x}_k = \boldsymbol{x}_0, \quad k = 0, \dots N_p - 1, \tag{4.4b}$$

$$\boldsymbol{x}_{k+1} = f(\boldsymbol{x}_k, \boldsymbol{u}_k), \tag{4.4c}$$

$$\boldsymbol{\mathcal{U}}_{\min} \leq \hat{\boldsymbol{\mathcal{U}}} \leq \boldsymbol{\mathcal{U}}_{\max}, \tag{4.4d}$$

$$\boldsymbol{\mathcal{X}}_{\min} \leq \hat{\boldsymbol{\mathcal{X}}} \leq \boldsymbol{\mathcal{X}}_{\max}, \tag{4.4e}$$

where $\boldsymbol{x}_k \in \mathbb{R}^{n_x}$ are the states of the system (3.19d). The number of states is n_x, $\boldsymbol{x}_0 \in \mathbb{R}^{n_x}$ are the initial conditions, and $\boldsymbol{u}_k \in \mathbb{R}^{n_u}$ is a vector of the two actuator inputs, propeller and rudder servo signals. Additionally, $\boldsymbol{\mathcal{Q}} \geq 0 \in \mathbb{R}^{N_p n_x \times N_p n_x}$ is a positive semi-definite matrix to penalize state errors with N_p the prediction horizon, and $\boldsymbol{\mathcal{R}} > 0 \in \mathbb{R}^{N_p n_u \times N_p n_u}$ is a positive definite matrix for

penalizing input errors; $\boldsymbol{\mathcal{X}}_r, \hat{\boldsymbol{\mathcal{X}}}, \boldsymbol{\mathcal{U}}_r, \hat{\boldsymbol{\mathcal{U}}}$ are column-vectors containing future state references, state predictions, input references and input predictions, respectively.

The optimization problem (4.4) is in the form of a Nonlinear Programming problem (NLP), which is generally difficult to solve (Bradley, Stephen P., Hax, Arnoldo C., Magnanti, 1977). A well used approach to solving is the use of Sequential Quadratic Programming (SQP) methods which form a linearized convex Quadratic Program to find an optimal search direction to drive the solution towards a local optimum (Boggs and Tolle, 1995). Since the dynamics of the system are linearized about the input and state trajectories, the linearization is only defined after the future inputs and states trajectories are calculated. To address this, shooting methods employ an initially guessed nominal input trajectory $\bar{\boldsymbol{\mathcal{U}}} = [\bar{\boldsymbol{u}}_k^T, \bar{\boldsymbol{u}}_{k+1}^T, \cdots, \bar{\boldsymbol{u}}_{k+N_p-1}^T]^T$ for which in single-shooting can be used to obtain the nominal state trajectories, $\bar{\boldsymbol{\mathcal{X}}} = [\bar{\boldsymbol{x}}_{k+1}^T, \bar{\boldsymbol{x}}_{k+2}^T, \cdots, \bar{\boldsymbol{x}}_{k+N_p}^T]^T$, by propagating the input through the state dynamics (4.5), or in the case of multiple-shooting, the nominal state trajectory can be chosen independently, such as using a known parameterized path for trajectory tracking (Diehl et al., 2005a).

4.2.2 Single Shooting

The early results and the results in chapter 7 were obtained using single shooting, while later results were obtained with multiple shooting. As such, the NMPC prediction models are first formulated for single shooting, with the modifications necessary for multiple shooting derived after. The general form of the nonlinear system from (4.4) is repeated here:

$$\boldsymbol{x}_{k+1} = f(\boldsymbol{x}_k, \boldsymbol{u}_k), \tag{4.5}$$

A first order Taylor series approximation of (4.5) is:

$$\begin{aligned} \hat{\boldsymbol{x}}_{k+1} &= f(\bar{\boldsymbol{x}}_k, \bar{\boldsymbol{u}}_k) + \frac{\partial f(\hat{\boldsymbol{x}}_k, \hat{\boldsymbol{u}}_k)}{\partial \hat{\boldsymbol{x}}_k}\delta\boldsymbol{x}_k + \frac{\partial f(\hat{\boldsymbol{x}}_k, \hat{\boldsymbol{u}}_k)}{\partial \hat{\boldsymbol{u}}_k}\delta\boldsymbol{u}_k, \\ &= \bar{\boldsymbol{x}}_{k+1} + \boldsymbol{A}_k\delta\hat{\boldsymbol{x}}_k + \hat{\boldsymbol{B}}_k\delta\boldsymbol{u}_k, \end{aligned} \tag{4.6}$$

where $\delta\hat{\boldsymbol{x}}_k = \hat{\boldsymbol{x}}_k - \bar{\boldsymbol{x}}_k$ and $\delta\hat{\boldsymbol{u}}_k = \hat{\boldsymbol{u}}_k - \bar{\boldsymbol{u}}_k$ represent the deviation of the states and inputs from their respective nominal points at time step $t = kT$, where

$$\boldsymbol{A}_k = \left.\frac{\partial f(\hat{\boldsymbol{x}}_k, \hat{\boldsymbol{u}}_k)}{\partial \hat{\boldsymbol{x}}_k}\right|_{\substack{\hat{\boldsymbol{x}}_k=\bar{\boldsymbol{x}}_k \\ \hat{\boldsymbol{u}}_k=\bar{\boldsymbol{u}}_k}}, \quad \boldsymbol{B}_k = \left.\frac{\partial f(\hat{\boldsymbol{x}}_k, \hat{\boldsymbol{u}}_k)}{\partial \hat{\boldsymbol{u}}_k}\right|_{\substack{\hat{\boldsymbol{x}}_k=\bar{\boldsymbol{x}}_k \\ \hat{\boldsymbol{u}}_k=\bar{\boldsymbol{u}}_k}}. \tag{4.7}$$

represent the partial derivatives of the state equation (4.5). The deviation $\delta\hat{\boldsymbol{x}}_{k+1} = \hat{\boldsymbol{x}}_{k+1} - \bar{\boldsymbol{x}}_{k+1}$ at time instant $k+1$ can then approximated by;

$$\delta\hat{\boldsymbol{x}}_{k+1} = \boldsymbol{A}_k\delta\hat{\boldsymbol{x}}_k + \boldsymbol{B}_k\delta\hat{\boldsymbol{u}}_k. \tag{4.8}$$

Simulating forward the next time step is calculated as:

$$\delta\hat{\boldsymbol{x}}_{k+2} = \boldsymbol{A}_{k+1}\delta\hat{\boldsymbol{x}}_{k+1} + \boldsymbol{B}_{k+1}\delta\hat{\boldsymbol{u}}_{k+1}, \tag{4.9}$$

substituting (4.8) in for $\delta\hat{\boldsymbol{x}}_{k+1}$ results in:

$$\begin{aligned}\delta\hat{\boldsymbol{x}}_{k+2} &= \boldsymbol{A}_{k+1}(\boldsymbol{A}_k\delta\hat{\boldsymbol{x}}_k + \boldsymbol{B}_k\delta\hat{\boldsymbol{u}}_k) + \boldsymbol{B}_{k+1}\delta\hat{\boldsymbol{u}}_{k+1}, \\ &= \boldsymbol{A}_{k+1}\boldsymbol{A}_k\delta\hat{\boldsymbol{x}}_k + \boldsymbol{A}_{k+1}\boldsymbol{B}_k\delta\hat{\boldsymbol{u}}_k + \boldsymbol{B}_{k+1}\delta\hat{\boldsymbol{u}}_{k+1}.\end{aligned} \tag{4.10}$$

This is continued for all inputs up to the prediction horizon, N_p. The deviations from the predicted nominal state trajectory can be represented in matrix form.

$$\begin{aligned}\hat{\boldsymbol{\mathcal{U}}} &= \bar{\boldsymbol{\mathcal{U}}} + \delta\hat{\boldsymbol{\mathcal{U}}}, \\ \hat{\boldsymbol{\mathcal{X}}} &= \bar{\boldsymbol{\mathcal{X}}} + \delta\hat{\boldsymbol{\mathcal{X}}} = \bar{\boldsymbol{\mathcal{X}}} + \boldsymbol{\mathcal{G}}\delta\boldsymbol{x}_0 + \boldsymbol{\mathcal{H}}\delta\hat{\boldsymbol{\mathcal{U}}},\end{aligned} \tag{4.11}$$

where $\delta\boldsymbol{x}_0$ is the initial state mismatch which the RTI scheme uses for feedback control. Matrices $\boldsymbol{\mathcal{G}}$ and $\boldsymbol{\mathcal{H}}$ are defined as:

$$\boldsymbol{\mathcal{G}} := \begin{bmatrix} \boldsymbol{A}_0 \\ \boldsymbol{A}_1\boldsymbol{A}_0 \\ \vdots \\ \boldsymbol{A}_{N_p-1}\cdots\boldsymbol{A}_1\boldsymbol{A}_0 \end{bmatrix}, \tag{4.12a}$$

$$\boldsymbol{\mathcal{H}} \coloneqq \begin{bmatrix} \boldsymbol{B}_0 & \mathbb{O} & \cdots & \cdots \\ \boldsymbol{A}_1\boldsymbol{B}_0 & \boldsymbol{B}_1 & \mathbb{O} & \cdots \\ \boldsymbol{A}_2\boldsymbol{A}_1\boldsymbol{B}_0 & \boldsymbol{A}_2\boldsymbol{B}_1 & \boldsymbol{B}_2 & \cdots \\ \vdots & \vdots & \vdots & \ddots \\ \boldsymbol{A}_{N_p-1}\cdots\boldsymbol{A}_1\boldsymbol{B}_0 & \boldsymbol{A}_{N_p-2}\cdots\boldsymbol{A}_2\boldsymbol{B}_1 & \cdots & \cdots \end{bmatrix}. \tag{4.12b}$$

For compactness the notation is changed slightly so $\boldsymbol{A}_k = \boldsymbol{A}_0$, $\boldsymbol{A}_{k+1} = \boldsymbol{A}_1$ and so forth. Substituting input and state linearized prediction models from (4.11) in the original cost function (4.4), and rearranging the cost in terms of the decision variable $\delta\hat{\boldsymbol{\mathcal{U}}}$ results in the standard QP form:

$$\min_{\delta\hat{\boldsymbol{\mathcal{U}}}} J = \frac{1}{2}\delta\hat{\boldsymbol{\mathcal{U}}}^T\boldsymbol{\mathcal{E}}\delta\hat{\boldsymbol{\mathcal{U}}} + \delta\hat{\boldsymbol{\mathcal{U}}}^T\boldsymbol{f}, \tag{4.13a}$$

s.t.

$$\boldsymbol{\mathcal{M}}\delta\hat{\boldsymbol{\mathcal{U}}} \leq \boldsymbol{\gamma}, \tag{4.13b}$$

$$\boldsymbol{\mathcal{E}} = \boldsymbol{\mathcal{H}}^T\boldsymbol{\mathcal{Q}}\boldsymbol{\mathcal{H}} + \boldsymbol{\mathcal{R}}, \tag{4.13c}$$

$$\boldsymbol{f} = -\left[\boldsymbol{\mathcal{H}}^T\boldsymbol{\mathcal{Q}}(\boldsymbol{\mathcal{X}}_r - \bar{\boldsymbol{\mathcal{X}}} - \boldsymbol{\mathcal{G}}\delta\boldsymbol{x}_0) - \boldsymbol{\mathcal{R}}(\bar{\boldsymbol{\mathcal{U}}} - \boldsymbol{\mathcal{U}}_r)\right], \tag{4.13d}$$

$$\boldsymbol{\mathcal{M}} = \begin{bmatrix} \boldsymbol{\mathcal{I}} \\ -\boldsymbol{\mathcal{I}} \\ \boldsymbol{\mathcal{H}} \\ -\boldsymbol{\mathcal{H}} \end{bmatrix}, \quad \boldsymbol{\gamma} = \begin{bmatrix} \boldsymbol{\mathcal{U}}_{max} - \bar{\boldsymbol{\mathcal{U}}} \\ -(\boldsymbol{\mathcal{U}}_{min} - \bar{\boldsymbol{\mathcal{U}}}) \\ \boldsymbol{\mathcal{X}}_{max} - \bar{\boldsymbol{\mathcal{X}}} - \boldsymbol{\mathcal{G}}\delta\boldsymbol{x}_0 \\ -(\boldsymbol{\mathcal{X}}_{min} - \bar{\boldsymbol{\mathcal{X}}} - \boldsymbol{\mathcal{G}}\delta\boldsymbol{x}_0) \end{bmatrix}. \tag{4.13e}$$

Having defined this, any QP solver of choice can be used to solve (4.13). Once the optimal input deviation, $\delta\hat{\boldsymbol{\mathcal{U}}}^\star$, is obtained, (4.11) is used to recover the actual input.

4.2.3 Multiple Shooting

In multiple shooting, the state trajectory is discretized along the intervals of the prediction horizon, and simulated independently at each initial state value of the interval. As previously stated, these initial state values $\boldsymbol{x}_k$ can be chosen, such as desired states along a trajectory path, where previously, the initial state value was dependent upon the simulation from the previous interval i.e. $\boldsymbol{x}_k = f(\boldsymbol{x}_{k-1}, \boldsymbol{u}_{k-1})$. This change also has the benefit of allowing the initial state values for each interval to be decision variable in the NLP (Bock and Plitt, 1985). The simulated end state at each interval in multiple shooting may not match the initial state value of the next interval. This difference,

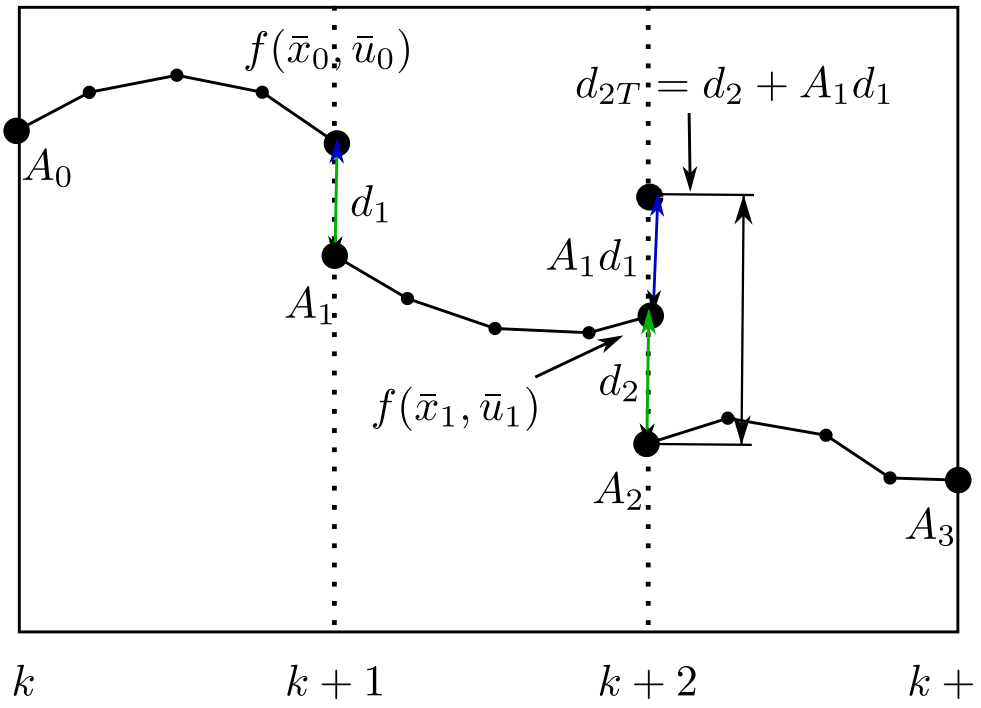

FIGURE 4.1: Graphical representation of the multiple shooting method. Defects are indicated by 'd'.

sometimes known as defects, is shown in figure 4.1. A continuity constraint is imposed in the NLP to create continuous trajectory. Briefly shown here is how the defects are propagated through the system dynamics and how it changes (4.11), and (4.13). Looking at figure 4.1 it can be seen that:

$$\boldsymbol{d}_1 = f(\bar{\boldsymbol{x}}_0, \bar{\boldsymbol{u}}_0) - \bar{\boldsymbol{x}}_1. \tag{4.14}$$

Inserting this into (4.8) results in:

$$\delta\hat{\boldsymbol{x}}_1 = \boldsymbol{A}_0\delta\hat{\boldsymbol{x}}_0 + \boldsymbol{B}_0\delta\hat{\boldsymbol{u}}_0 + \boldsymbol{d}_1. \tag{4.15}$$

Simulating the next time step gives results in (4.9) with the second defect added:

$$\delta\hat{\boldsymbol{x}}_2 = \boldsymbol{A}_1\delta\hat{\boldsymbol{x}}_1 + \boldsymbol{B}_1\delta\hat{\boldsymbol{u}}_1 + \boldsymbol{d}_2 \tag{4.16}$$

Again, inserting (4.15) in (4.16) gives:

$$\begin{aligned} \delta\hat{\boldsymbol{x}}_2 &= \boldsymbol{A}_1(\boldsymbol{A}_0\delta\hat{\boldsymbol{x}}_0 + \boldsymbol{B}_0\delta\hat{\boldsymbol{u}}_0 + \boldsymbol{d_1}) + \boldsymbol{B}_1\delta\hat{\boldsymbol{u}}_1 + \boldsymbol{d}_2, \\ &= \boldsymbol{A}_1\boldsymbol{A}_0\delta\hat{\boldsymbol{x}}_0 + \boldsymbol{A}_1\boldsymbol{B}_0\delta\hat{\boldsymbol{u}}_0 + \boldsymbol{B}_1\delta\hat{\boldsymbol{u}}_1 + \boldsymbol{A}_1\boldsymbol{d}_1 + \boldsymbol{d}_2. \end{aligned} \tag{4.17}$$

The last two terms are grouped together to create the total defect $\boldsymbol{d}_{2T}$. The vector of defects, $\boldsymbol{D} = [\boldsymbol{d}_1, \boldsymbol{d}_{2T}, \boldsymbol{d}_{3T}, \cdots, \boldsymbol{d}_{NpT}]^T$, subsequently appears in the predicted nominal state trajectory,

$$\hat{\boldsymbol{\mathcal{X}}} = \bar{\boldsymbol{\mathcal{X}}} + \delta\hat{\boldsymbol{\mathcal{X}}} = \bar{\boldsymbol{\mathcal{X}}} + \boldsymbol{\mathcal{G}}\delta\boldsymbol{x}_0 + \boldsymbol{\mathcal{H}}\delta\hat{\boldsymbol{\mathcal{U}}} + \boldsymbol{D}, \tag{4.18}$$

and in the QP equation:

$$\min_{\delta\hat{\boldsymbol{\mathcal{U}}}} J = \frac{1}{2}\delta\hat{\boldsymbol{\mathcal{U}}}^T\boldsymbol{\mathcal{E}}\delta\hat{\boldsymbol{\mathcal{U}}} + \delta\hat{\boldsymbol{\mathcal{U}}}^T\boldsymbol{f}, \tag{4.19a}$$

s.t.

$$\boldsymbol{\mathcal{M}}\delta\hat{\boldsymbol{\mathcal{U}}} \leq \boldsymbol{\gamma}, \tag{4.19b}$$

$$\boldsymbol{\mathcal{E}} = \boldsymbol{\mathcal{H}}^T\boldsymbol{\mathcal{Q}}\boldsymbol{\mathcal{H}} + \boldsymbol{\mathcal{R}}, \tag{4.19c}$$

$$\boldsymbol{f} = -\left[\boldsymbol{\mathcal{H}}^T\boldsymbol{\mathcal{Q}}(\boldsymbol{\mathcal{X}}_r - \bar{\boldsymbol{\mathcal{X}}} - \boldsymbol{\mathcal{G}}\delta\boldsymbol{x}_0 - \boldsymbol{D}) - \boldsymbol{\mathcal{R}}(\bar{\boldsymbol{\mathcal{U}}} - \boldsymbol{\mathcal{U}}_r)\right], \tag{4.19d}$$

$$\boldsymbol{\mathcal{M}} = \begin{bmatrix} \boldsymbol{\mathcal{I}} \\ -\boldsymbol{\mathcal{I}} \\ \boldsymbol{\mathcal{H}} \\ -\boldsymbol{\mathcal{H}} \end{bmatrix}, \quad \boldsymbol{\gamma} = \begin{bmatrix} \boldsymbol{\mathcal{U}}_{max} - \bar{\boldsymbol{\mathcal{U}}} \\ -(\boldsymbol{\mathcal{U}}_{min} - \bar{\boldsymbol{\mathcal{U}}}) \\ \boldsymbol{\mathcal{X}}_{max} - \bar{\boldsymbol{\mathcal{X}}} - \boldsymbol{\mathcal{G}}\delta\boldsymbol{x}_0 - \boldsymbol{D} \\ -(\boldsymbol{\mathcal{X}}_{min} - \bar{\boldsymbol{\mathcal{X}}} - \boldsymbol{\mathcal{G}}\delta\boldsymbol{x}_0 - \boldsymbol{D}) \end{bmatrix}. \tag{4.19e}$$

4.2.4 Real Time Iteration Scheme

The nominal input and state trajectories that the optimization is linearized about are important for the performance of the optimization. A poorly chosen input and state trajectory can require longer to converge to the optimal solution or provide poor results if iteration time is limited. Usually in optimal control, during the run time the optimal solution should not vary by much from one time step to the next. For this reason, the RTI method is employed in this work. The RTI uses the fact that in a system, the successive optimal control problems are related and iterates towards the optimal solution during the runtime of the process (Diehl et al., 2005b). The following is a brief explanation of the RTI procedure.

Initial Value Embedding (IVE)

After the first time step, IVE uses the previous solution found to obtain the nominal trajectory over which the formulation will linearize and optimise, warm-starting the next optimization.

Single SQP

To further reduce the computational burden and achieve predictable timings, only a single step of the SQP is performed. This is reasonable given that the solution is warm-started from the previous solution, which is expected to be close to the optimal solution.

Computation Separation

Separates the computations into preparation and feedback phases to avoid the computation delay related to the preparation of the QP (Gros et al., 2016).

- Preparation Phase: In between sampling times, the preparation phase uses a predicted nominal state for the next sampling time $\bar{\boldsymbol{x}}_0 = \hat{\boldsymbol{x}}_{k|k-1}$ as a starting point obtained from the last state $\boldsymbol{x}_{k-1|k-1}$ and last input $\boldsymbol{u}_{k-1|k-1}$ which allows the preparation of the QP main matrices $\boldsymbol{\mathcal{H}}, \boldsymbol{\mathcal{M}}, \boldsymbol{\mathcal{G}}$,etc., and partially, vectors $\boldsymbol{f}$ and $\boldsymbol{\gamma}$.
- Feedback Phase: Once the current state measurement becomes available the feedback phase calculates the state mismatch $\delta \boldsymbol{x}_0 = \boldsymbol{x}_0 - \bar{\boldsymbol{x}}_0$, finishes the calculation of $\boldsymbol{f}$ and $\boldsymbol{\gamma}$, and solves the QP.

The previously defined linearized matrices, $\boldsymbol{A}_k$ & $\boldsymbol{B}_k$, called sensitivities, are computed with a discretize then linearize method (Gros et al., 2016). This differs from the linearize then discretize commonly used in linear MPC whereby the continuous system dynamics are linearized about an operating point, then discretized for computation in the MPC. Depending on the level of nonlinearity the valid region for the linearization in linear MPC can be small and, therefore, the MPC can only effectively operate in this region. By contrast, when the system is linearized about the nominal state at each time step the linearization need only be valid for the region between the nominal states at each time step.

This describes that linearized matrices are obtained, but not how. The simulation of the system is performed via numerical integration methods. For this thesis, the method employed is Explicit Euler, that is:

$$\boldsymbol{x}_k = \boldsymbol{x}_0 + Tf(\boldsymbol{x}_0, \boldsymbol{u}_0), \tag{4.20}$$

where T is the sample time of the prediction horizon. To obtain the sensitivity matrices, the integration method, 4.20 is differentiated as:

$$\boldsymbol{A}_0 = I + T\frac{\partial f(\boldsymbol{x}_o, \boldsymbol{u}_o)}{\partial \boldsymbol{x}_0}, \quad \boldsymbol{B}_0 = T\frac{\partial f(\boldsymbol{x}_0, \boldsymbol{u}_0)}{\partial \boldsymbol{u}_0}. \tag{4.21}$$

For the most straight forward implementation, the sample time of the Euler method can be the same as the sample time of the controller, meaning there is one Euler step per time step in the prediction horizon. However, this can often be undesirable because the simulation accuracy is directly effected by the size of the step. To improve accuracy smaller Euler steps are used in an inner loop between the prediction horizon time steps. The sensitivity matrices are computed via forward accumulation automatic differentiation recursively for N_s steps of the inner loop, with the $\boldsymbol{A}_k$ initialized as an identity matrix and $\boldsymbol{B}_k$ initialized as $\mathbb{O}$:

$$\begin{aligned} \boldsymbol{A}_k &= \left[I + \frac{T}{N_s}\frac{\partial f(\boldsymbol{x}_k, \boldsymbol{u}_0)}{\partial \boldsymbol{x}_k}\right]\boldsymbol{A}_k, \\ \boldsymbol{B}_k &= \left[I + \frac{T}{N_s}\frac{\partial f(\boldsymbol{x}_k, \boldsymbol{u}_0)}{\partial \boldsymbol{x}_k}\right]\boldsymbol{B}_k + \frac{T}{N_s}\frac{\partial f(\boldsymbol{x}_k, \boldsymbol{u}_0)}{\partial \boldsymbol{u}_0}. \end{aligned} \tag{4.22}$$

The system dynamics are then simulated forward by $\frac{T}{N_s}$ to compute the next states:

$$\boldsymbol{x}_{k+1} = \boldsymbol{x}_k + \frac{T}{N_s}f(\boldsymbol{x}_k, \boldsymbol{u}_k), \tag{4.23}$$

before (4.22) is then repeated to continue the cycle. Note that for the inner loop, $\boldsymbol{u}_0$ remains the same. Changes in the actuation input only occur at the prediction horizon steps with a zero order hold and therefore in the inner loop it is held constant. Relatedly, the SQP and therefore the optimization is performed for the larger prediction horizon steps and has no knowledge of inner steps.

4.3 Summary

In this chapter, first the linearization efforts were discussed and it was shown, in conjunction with the previous chapter, how the vessel-wave interaction is not amenable to linearization without loss of this information. This then sets up the introduction to the NMPC. The OCP problem is constructed to be solved via SQP methods. Single and multiple shooting derivations are shown. However, this alone is not sufficient to readily implement in a real system owing to potential long computation times necessary to solve the SQP, motivating the use of the RTI method. By shifting the previous SQP solution forward and using computation separation, the RTI method provides quick optimal control and in previous studies shown to be self-converging over the course of the simulation.

Chapter 5

Initial Results

The previous chapter introduced the concept of the RTI NMPC. This chapter shows the initial results of its implementation on the task of optimally maneuvering the vessel through waves. The first section of this chapter formulates the control problem of reducing hull impact forces for a 1 DOF vessel in a head sea. This work by the author was first published in (McCullough et al., 2020). This simplified problem shows interesting results in how the optimal solution is related to the encounter frequency of the wave harmonic. It also serves to hopefully better the understanding of the reader of the implementation of the RTI NMPC.

The second section of the chapter discusses the expansion of the controller to a 6 DOF model. Simulations were carried out to ascertain the optimal trajectory in a head sea given a certain reference. The early results in the second section helped inform the development of the remaining thesis.

5.1 Single Degree of Freedom Example

The goal in this example is the reduction of the wave force in the surge direction while maintaining a desired average velocity. The ASV model is based upon a simplified description of the Halcyon ASV presented previously. For the purpose of developing initial control strategies this section examines the 1 DOF scenario, with the changes and simplifications from the full model noted below. The simplification is based upon the following assumptions:

- The model degrees of freedom are restricted to forwards (surge) motion only.
- There are no water-current or wind-induced forces.
- Actuation is restricted to the propeller input only (no steering).
- The wave induced forces arise from a single wave harmonic.
- The vessel is heading directly into the oncoming waves.

The equations of motion of the boat in the surge direction are as follows:

$$\dot{x}(t) = u(t), \tag{5.1a}$$

$$\dot{u}(t) = \frac{D(u(t)) + \tau_{\mathrm{p}}(u(t), n_{\mathrm{p}}(t)) + \tau_{\mathrm{w}}^{\mathrm{u}}(u(t), \eta(t))}{m}, \tag{5.1b}$$

$$\dot{n_{\mathrm{p}}} = \frac{-1}{\tau_{n_{\mathrm{p}}}} n_{\mathrm{p}}(t) + \frac{1}{\tau_{n_{\mathrm{p}}}} u_{n_{\mathrm{p}}}(t). \tag{5.1c}$$

The system has four states, $\boldsymbol{x} = [x, u, n_{\mathrm{p}}, \eta]^T$, with $x(t)$ being the position in the boat reference frame at time t, $u(t)$ is the surge velocity of the boat, $n_{\mathrm{p}}(t)$ is the propeller speed, and $\eta(t)$ is a wave state defined in the following section. In the above equations $D(u(t))$ is the drag term, $\tau_{\mathrm{p}}(u(t), n_{\mathrm{p}}(t))$ is the propulsion from the propellers, $\tau_{\mathrm{w}}^{u}(u(t), \eta(t))$ is the wave force in the surge direction.

5.1.1 Wave Environment and Forces

In the case of the surge direction, the force RAO is appoximately an affine function of the surge velcoity and wave frequency, as shown in 5.1. The phase RAO is assumed to be constant for all vessel velocities. For the force RAO, the force is linearly dependent on the velocity, as well as linearly dependent on the wave frequency. In this case study the wave frequency, ω, is 0.5 rad/s, giving a force RAO, $F^{u}(u(t))$, as a function of velocity only. Presented here is a formulation of the wave itself. As first highlighted in section 4.1, the vessel-wave coupling is nonlinear and attempts at linearization loses this knowledge of the coupling. The force imparted on the boat from the wave is subject to the wave height and boat position. For a single harmonic traveling in the negative surge direction and the vessel in a head sea the wave elevation is defined as:

$$\eta(x, t) = a_h \cos(\omega t + kx), \tag{5.2}$$

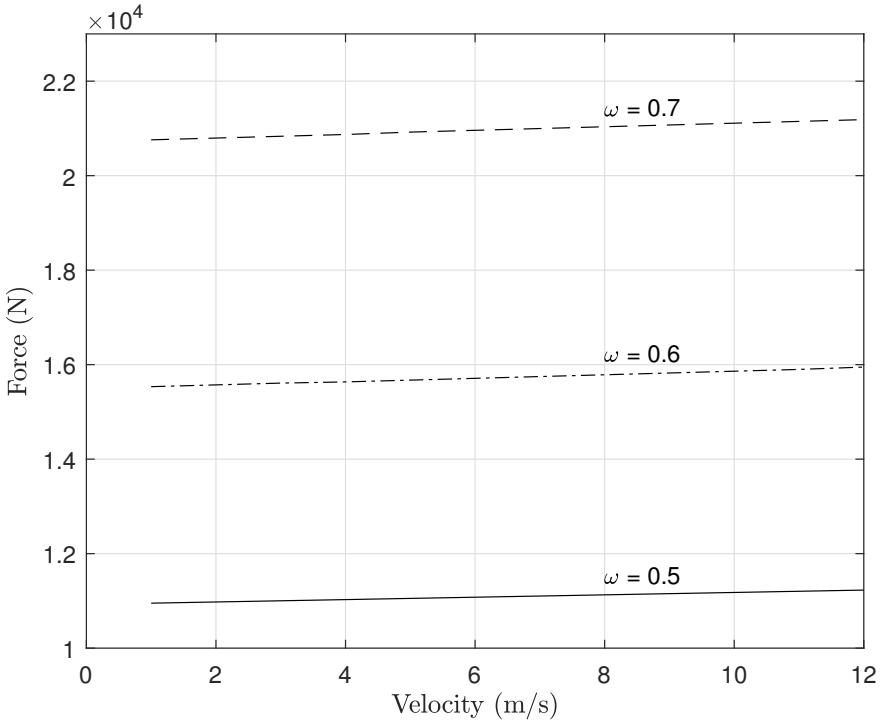

FIGURE 5.1: Surge force RAOs at various frequencies and velocities.

where a_h is the wave amplitude, changed from the earlier notation to avoid confusion with the linearized prediction matrix, $k = \omega^2/g$ is the wave number, and x is the boat's position along the surge axis. Inserting the definition of the wave elevation (5.2) in to the expression for the wave force (3.2) leads to:

$$\tau_{\mathrm{w}}^{\mathrm{u}}(u(t), \eta(t)) = \rho g F^{u}\left(u(t)\right) a_h \cos\left(\omega t + \frac{\omega^2}{g} x(t) + \phi_{\mathrm{RAO}}\right), \tag{5.3}$$

where ϕ_{RAO} is the phase RAO which is assumed constant.

Next, the wave harmonic, now with the effect of the phase RAO added, is decoupled from the height and force RAO to simplify use in state space form:

$$\eta(t) := \cos\left(\omega t + \frac{\omega^2}{g} x(t) + \phi_{\mathrm{RAO}} + \epsilon\right). \tag{5.4}$$

The dynamics of of $\eta(t)$ are obtained by differentiating 5.4 with respect to time. The resulting expressions are somewhat involved, but can be simplified significantly by performing an order of magnitude analysis to retain only the leading-order terms under the assumption that $\frac{\omega^2}{g}\dot{u}(t)$ is

negligible. The results of the assumption for the first derivative is:

$$\dot{\eta}(t) \approx -\left(\omega + \frac{\omega^2}{g}u(t)\right)\sin\left(\omega t + \frac{\omega^2}{g}x(t) + \phi_{\mathrm{RAO}}\right), \tag{5.5}$$

and the second derivative is:

$$\ddot{\eta}(t) \approx -\left(\omega + \frac{\omega^2}{g}u(t)\right)^2 \eta(t). \tag{5.6}$$

The wave force can now be expressed as a function of the force RAO and wave state as:

$$\tau_{\mathrm{w}}^{\mathrm{u}}(u(t), \eta(t)) = \rho g F^u\left(u(t)\right) a_h \eta(t). \tag{5.7}$$

The inside term of $\eta(t)$, $\omega + \frac{\omega^2}{g}u(t)$ is the encounter frequency of the boat to a wave in a head sea. This is the nonlinear term that describes how the encounter frequency changes with changes in the vessel velocity and with the $\frac{\omega^2}{g}x(t)$ term relates how the velocity and position of the vessel determine its position on the wave at a given time t. The combined surge and wave dynamics are shown in (5.8) where the dependence of the magnitude of the force RAO on the velocity can also be seen. These couplings motivate the use of nonlinear control.

$$\begin{bmatrix} \dot{x}(t) \\ \dot{x}(t) \\ \dot{n_{\mathrm{p}}}(t) \\ \dot{\eta}(t) \\ \ddot{\eta}(t) \end{bmatrix} = \begin{bmatrix} 0 & 1 & 0 & 0 & 0 \\ 0 & -\frac{D(u(t))}{m} & \frac{\tau_{\mathrm{p}}(u(t),n_{\mathrm{p}}(t))}{m} & -\frac{\rho g|F^u(u(t))|a_h}{m} & 0 \\ 0 & 0 & -\frac{1}{\tau_{n_{\mathrm{p}}}} & 0 & 0 \\ 0 & 0 & 0 & 0 & 1 \\ 0 & 0 & 0 & -\left(\omega + \frac{\omega^2}{g}u(t)\right)^2 & 0 \end{bmatrix} \begin{bmatrix} x(t) \\ u(t) \\ n_{\mathrm{p}}(t) \\ \eta(t) \\ \dot{\eta}(t) \end{bmatrix} + \begin{bmatrix} 0 \\ 0 \\ \frac{1}{\tau_{n_{\mathrm{p}}}} \\ 0 \\ 0 \end{bmatrix} u_{n_{\mathrm{p}}}(t) \tag{5.8}$$

5.2 Controller Design

The controller used is the same one as described in the previous chapter. However, difficulty arises in penalization for the 1 DOF case. Typically, to minimize wave-induced motion, one would penalize deviations from a reference position or velocity. For example, a penalization on the pitch angle to reduce overly large angles would result in the controller modifying the velocity and heading of the vessel to reduce the wave force and subsequent resulting pitch angle, while meeting the other

objectives of the cost function. In this scenario, the cost function balances the cost of the pitch angle with the cost of deviating from a desired velocity to reduce the pitch angle. In the 1 DOF case, the states can not be penalized as a proxy to the wave force. Unless created as a trajectory tracking problem, there is not a reference x position to track and penalizing deviations from a reference velocity will cause the controller to modulate the actuation to maintain the velocity and minimize the effects of wave force, but not the wave force itself. In order to minimize the wave force in the 1 DOF case, the wave force itself must appear in the cost function. However, the force imparted on the vessel by the wave is itself not a state. In order to penalize large wave forces in the cost function the outputs must be used. The prediction trajectory is modified from the state to output form as:

$$\hat{\boldsymbol{\mathcal{Y}}} = \bar{\boldsymbol{\mathcal{Y}}} + \delta\hat{\boldsymbol{\mathcal{Y}}} = \bar{\boldsymbol{\mathcal{Y}}} + \boldsymbol{\mathcal{G}}\delta\boldsymbol{x}_0 + \boldsymbol{\mathcal{H}}\delta\hat{\boldsymbol{\mathcal{U}}}, \tag{5.9}$$

Matrices $\boldsymbol{\mathcal{G}}$ and $\boldsymbol{\mathcal{H}}$ are similarly redefined as:

$$\boldsymbol{\mathcal{G}} \coloneqq \begin{bmatrix} \boldsymbol{C}_1\boldsymbol{A}_0 \\ \boldsymbol{C}_2\boldsymbol{A}_1\boldsymbol{A}_0 \\ \vdots \\ \boldsymbol{C}_{N_p}\boldsymbol{A}_{N_p-1}\cdots\boldsymbol{A}_1\boldsymbol{A}_0 \end{bmatrix}, \tag{5.10a}$$

$$\boldsymbol{\mathcal{H}} \coloneqq \begin{bmatrix} \boldsymbol{C}_1\boldsymbol{B}_0 & \mathbb{O} & \cdots & \cdots \\ \boldsymbol{C}_2\boldsymbol{A}_1\boldsymbol{B}_0 & \boldsymbol{C}_2\boldsymbol{B}_1 & \mathbb{O} & \cdots \\ \boldsymbol{C}_3\boldsymbol{A}_2\boldsymbol{A}_1\boldsymbol{B}_0 & \boldsymbol{C}_3\boldsymbol{A}_2\boldsymbol{B}_1 & \boldsymbol{C}_3\boldsymbol{B}_2 & \cdots \\ \vdots & \vdots & \vdots & \ddots \\ \boldsymbol{C}_{N_p}\boldsymbol{A}_{N_p-1}\cdots\boldsymbol{A}_1\boldsymbol{B}_0 & \boldsymbol{C}_{N_p}\boldsymbol{A}_{N_p-2}\cdots\boldsymbol{A}_2\boldsymbol{B}_1 & \cdots & \cdots \end{bmatrix}. \tag{5.10b}$$

With the resultant QP problem being:

$$\min_{\boldsymbol{\delta\hat{\mathcal{U}}}} J = \frac{1}{2}\delta\hat{\boldsymbol{\mathcal{U}}}^T \boldsymbol{\mathcal{E}}\delta\hat{\boldsymbol{\mathcal{U}}} + \delta\hat{\boldsymbol{\mathcal{U}}}^T \boldsymbol{f}, \tag{5.11a}$$

s.t.

$$\boldsymbol{\mathcal{M}}\delta\hat{\boldsymbol{\mathcal{U}}} \leq \boldsymbol{\gamma}, \tag{5.11b}$$

$$\boldsymbol{\mathcal{E}} = \boldsymbol{\mathcal{H}}^T \boldsymbol{\mathcal{Q}}\boldsymbol{\mathcal{H}} + \boldsymbol{\mathcal{R}}, \tag{5.11c}$$

$$\boldsymbol{f} = -\left[\boldsymbol{\mathcal{H}}^T \boldsymbol{\mathcal{Q}}(\boldsymbol{\mathcal{Y}}_r - \bar{\boldsymbol{\mathcal{Y}}} - \boldsymbol{\mathcal{G}}\delta\boldsymbol{x}_0) - \boldsymbol{\mathcal{R}}(\bar{\boldsymbol{\mathcal{U}}} - \boldsymbol{\mathcal{U}}_r)\right], \tag{5.11d}$$

$$\boldsymbol{\mathcal{M}} = \begin{bmatrix} \boldsymbol{\mathcal{I}} \\ -\boldsymbol{\mathcal{I}} \\ \boldsymbol{\mathcal{H}} \\ -\boldsymbol{\mathcal{H}} \end{bmatrix}, \quad \boldsymbol{\gamma} = \begin{bmatrix} \boldsymbol{\mathcal{U}}_{max} - \bar{\boldsymbol{\mathcal{U}}} \\ -(\boldsymbol{\mathcal{U}}_{min} - \bar{\boldsymbol{\mathcal{U}}}) \\ \boldsymbol{\mathcal{Y}}_{max} - \bar{\boldsymbol{\mathcal{Y}}} - \boldsymbol{\mathcal{G}}\delta\boldsymbol{x}_0 \\ -(\boldsymbol{\mathcal{Y}}_{min} - \bar{\boldsymbol{\mathcal{Y}}} - \boldsymbol{\mathcal{G}}\delta\boldsymbol{x}_0) \end{bmatrix}. \tag{5.11e}$$

Since the wave force is dependent on both the boat velocity and the wave state, η, the output selection matrix, C, is constructed to reflect this. In this paper, the boat velocity and wave force are the two variables to be regulated giving rise to:

$$\boldsymbol{C} = \begin{bmatrix} 0 & 1 & 0 & 0 \\ 0 & \frac{\partial\tau_{\mathrm{w}}(\bar{u}_k,\bar{\eta}_k)}{\partial u_k} & 0 & \frac{\partial\tau_{\mathrm{w}}(u_k,\eta_k)}{\partial\eta_k} \end{bmatrix}, \tag{5.12}$$

With the linearized wave force (5.7) at time k is defined as:

$$\tau_{\mathrm{w}} = \frac{\partial\tau_{\mathrm{w}}(\bar{u}_k,\bar{\eta}_k)}{\partial u_k}u_k + \frac{\partial\tau_{\mathrm{w}}(u_k,\eta_k)}{\partial\eta_k}\eta_k. \tag{5.13}$$

One other change is needed to achieve the stated goal of simultaneous wave force reduction and average velocity. The cost function as currently formulated minimizes the cost of the summation of deviations from the reference velocity and wave force at each time step in the prediction horizon, respectively. This does not, however, account for the average velocity over the prediction horizon. For instance, when the vessel is at a point on the wave where the wave force is zero, the minimal cost is to travel at the desired velocity. At another point, when the wave force is higher, the minimal cost might involve a slight reduction in velocity, for a reduction in wave force. At no point, will the cost be minimal by going above the desired velocity, as the wave force will also be higher. This means the maximum velocity will be the desired velocity, and an average velocity lower than the

desired. To rectify this, the prediction matrices and QP problem are modified to include the average velocity. To show how, let us look at the $\boldsymbol{\mathcal{G}}$ and $\boldsymbol{\mathcal{H}}$ matrices again. Now:

$$\boldsymbol{\mathcal{G}} \coloneqq \begin{bmatrix} \boldsymbol{\mathcal{G}}_u \\ \boldsymbol{\mathcal{G}}_{\mathrm{W}} \end{bmatrix} \tag{5.14}$$

and

$$\boldsymbol{\mathcal{H}} \coloneqq \begin{bmatrix} \boldsymbol{\mathcal{H}}_u \\ \boldsymbol{\mathcal{H}}_{\mathrm{W}}, \end{bmatrix} \tag{5.15}$$

where $\boldsymbol{\mathcal{G}}_{\mathrm{W}}$ and $\boldsymbol{\mathcal{H}}_{\mathrm{W}}$ have the same form as before with the W indicating that it only contains the wave force output, that is they were formed with:

$$\boldsymbol{C} = \begin{bmatrix} 0 & \frac{\partial \tau_{\mathrm{w}}(\bar{u}_k, \bar{\eta}_k)}{\partial u_k} & 0 & \frac{\partial \tau_{\mathrm{w}}(u_k, \eta_k)}{\partial \eta_k} \end{bmatrix}. \tag{5.16}$$

The matrices $\boldsymbol{\mathcal{G}}_u$ and $\boldsymbol{\mathcal{H}}_u$ are the output prediction matrices for surge velocity, that is:

$$\boldsymbol{C} = \begin{bmatrix} 0 & 1 & 0 & 0 \end{bmatrix}. \tag{5.17}$$

However, to obtain the average values, the columns of $\boldsymbol{\mathcal{G}}_u$ and $\boldsymbol{\mathcal{H}}_u$ are summed and divided by the prediction horizon length shown as:

$$\boldsymbol{\mathcal{G}_u} \coloneqq \left[\tfrac{1}{N_p} \sum \boldsymbol{C}_1 \boldsymbol{A}_0 + \boldsymbol{C}_2 \boldsymbol{A}_1 \boldsymbol{A}_0 + \ldots + \boldsymbol{C}_{N_p} \boldsymbol{A}_{N_p - 1} \ldots \boldsymbol{A}_1 \boldsymbol{A}_0 \right], \tag{5.18}$$

and:

$$\boldsymbol{\mathcal{H}_u} \coloneqq \Bigg[\frac{1}{N_p} \sum \boldsymbol{C}_1 \boldsymbol{B}_0 + \ldots + \boldsymbol{C}_{N_p} \boldsymbol{A}_{N_p - 1} \ldots \boldsymbol{A}_1 \boldsymbol{B}_0, \\ \frac{1}{N_p} \sum \boldsymbol{C}_2 \boldsymbol{B}_1 + \ldots + \boldsymbol{C}_{N_p} \boldsymbol{A}_{N_p - 2} \ldots \boldsymbol{A}_2 \boldsymbol{B}_1, \frac{1}{N_p} \sum \boldsymbol{C}_{N_p} \boldsymbol{B}_{N_p - 1} \Bigg]. \tag{5.19}$$

With these new definitions, the size of $\boldsymbol{\mathcal{G}} \in \mathbb{R}^{N_p ny \times nx}$ and $\boldsymbol{\mathcal{H}} \in \mathbb{R}^{N_p ny \times N_p}$ now change to $\boldsymbol{\mathcal{G}} \in \mathbb{R}^{N_p (ny-1) \times nx}$ and $\boldsymbol{\mathcal{H}} \in \mathbb{R}^{N_p (ny-1) \times N_p}$. A similar treatment is performed for $\boldsymbol{\mathcal{Q}}$, $\boldsymbol{\mathcal{Y}}_r$, & $\bar{\boldsymbol{\mathcal{Y}}}$ to ensure correct calculation and application of the reference deviations and penalty weights respectively.

Finally, before discussion of the results, when discretizing and simulating the system, (5.8), the

states can be reduced from 5 to 4 without losing the information on the vessel-wave coupling. Discretizing the system using Explicit Euler results in:

$$x_{k+1} = x_k + Tu_k \tag{5.20a}$$

$$u_{k+1} = u_k + \frac{T}{m}(D(u_k) + T(u_k, n_{p_k}) + W(u_k)) \tag{5.20b}$$

$$n_{p_{k+1}} = n_{p_k} + \frac{T}{\tau_{n_p}}\left(-n_{p_k} + u_{n_{p_k}}\right) \tag{5.20c}$$

$$\eta_{k+1} = \eta_k - T(\omega_k + \frac{\omega_k^2}{g}u_k)\cos(\omega_k t + \frac{\omega_k^2}{g}x_k + \phi_{RAO}), \tag{5.20d}$$

where T is the sample time, and $W(u_k) = \rho g F^u(u_k)\, a_h$. Note that the dependence on the velocity in the wave encounter frequency and the dependence on the x position for the position of the vessel on the wave are both present. With that the sensitivity matrices can be shown to be:

$$A_k = \begin{bmatrix} 1 & T & 0 & 0 \\ 0 & a_{2,2} & a_{2,3} & a_{2,4} \\ 0 & 0 & 1 - \frac{T}{\tau_p} & 0 \\ a_{4,1} & a_{4,2} & 0 & 1 \end{bmatrix} \qquad B_k = \begin{bmatrix} 0 \\ 0 \\ \frac{T}{\tau_p} \\ 0 \end{bmatrix} \tag{5.21a}$$

where,

$$a_{2,2} = 1 + \left(\frac{T}{m}\right)\left(\frac{\partial D(\hat{u}_k)}{\partial \hat{u}_k} + \frac{\partial T(\hat{u}_k, \hat{n}_{p_k})}{\partial \hat{u}_k} + \frac{\partial W(\hat{u}_k, \hat{\eta}_k)}{\partial \hat{u}_k}\right)\Bigg|_{\hat{u}_k=\bar{u}_k, \hat{n}_{p_k}=\bar{n}_{p_k}, \hat{\eta}_k=\bar{\eta}_k} \tag{5.21b}$$

$$a_{2,3} = \left(\frac{T}{m}\right)\frac{\partial T(\hat{u}_k, \hat{n}_{p_k})}{\partial \hat{n}_{p_k}}\Bigg|_{\hat{u}_k=\bar{u}_k, \hat{n}_{p_k}=\bar{n}_{p_k}} \tag{5.21c}$$

$$a_{2,4} = \left(\frac{T}{m}\right)\frac{\partial W(\hat{u}_k, \hat{\eta}_k)}{\partial \hat{\eta}_k}\Bigg|_{\hat{u}_k=\bar{u}_k, \hat{\eta}_k=\bar{\eta}_k} \tag{5.21d}$$

$$a_{4,1} = \frac{\partial \hat{\eta}_{k+1}}{\partial x_k}\Bigg|_{\hat{x}_k=\bar{x}_k, \hat{u}_k=\bar{u}_k} \tag{5.21e}$$

$$a_{4,2} = \frac{\partial \hat{\eta}_{k+1}}{\partial u_k}\Bigg|_{\hat{x}_k=\bar{x}_k, \hat{u}_k=\bar{u}_k} \tag{5.21f}$$

Again, note the coupling between the vessel and wave in $a_{2,4}$, $a_{4,1}$, & $a_{4,2}$.

5.3 Simulation Results

5.3.1 Surge Only

The boat was simulated heading directly into oncoming waves with the propellers being the only actuation. The simulation was performed on the same model as the controller, i.e. not in the SWEM simulation environment, albeit at a lower step size than the controller. This means the only errors between the simulation and the controller prediction are from the difference in simulation step size. The wave was a single harmonic with a wave height of 1 meter and a frequency of 0.5 rad/s. The NMPC controller had a prediction horizon of 200 steps ahead, with the sample period 0.08 seconds resulting in a prediction window of 16 seconds which captures just over one complete harmonic. The simulation was run for 30 seconds. Because of the limited difference in the wave force in the surge direction relative to velocity, see figure 5.1, the time constant on the propeller for this case study was artificially reduced to 1.8 seconds. The following shows a comparison between a constant propeller input, which on a calm sea, produces an average 5 m/s velocity and the NMPC controller with a desired average velocity of 5 m/s. Figure 5.2(a) shows the velocity profiles of the open loop controller and the NMPC controller compared to the wave state, η. A clear difference in the velocity profiles can be seen. The open loop controller has an oscillating, single harmonic velocity resulting from changes only in the wave force, while the NMPC scenario has a more complex velocity profile. A global minimum of velocity for the NMPC controller occurs when the wave state is at its maximum, while a local minimum velocity for the NMPC controller occurs at the minimum of the wave state, and both the local and global maximum velocity occurs when the wave state is at zero, and therefore wave force is minimum.

The resulting surge force on the boat can be seen in Figure 5.2(b). The base force, that which the boat would experience at 0 m/s, is subtracted from this figure to better show the difference in the two scenarios.

Figure 5.2(c) shows the input for both controllers as it compares to the wave state. The NMPC input frequency appears to be twice that of the wave. This double harmonic is confirmed when looking at Figure 5.2(d). This figure shows the amplitude spectrum of the input control to the propeller for the NMPC controller. In the simulation, with an average velocity of 5 m/s the average encounter frequency of the boat is 0.628 rad/s, which has a small peak in the amplitude spectrum

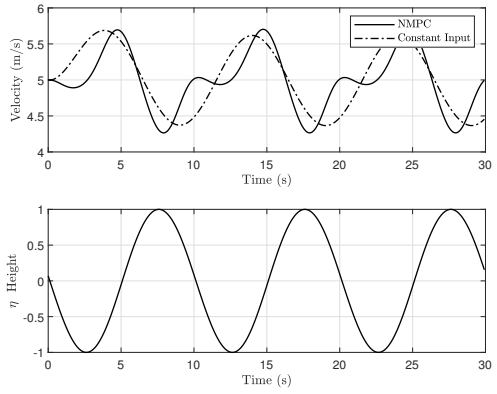

(a) Top plot contains the velocity profiles of the two controllers. The bottom plot shows the wave state η. The velocity profile shows a global minimum for the NMPC controlled boat when η is maximum and a local minimum when η is minimum.

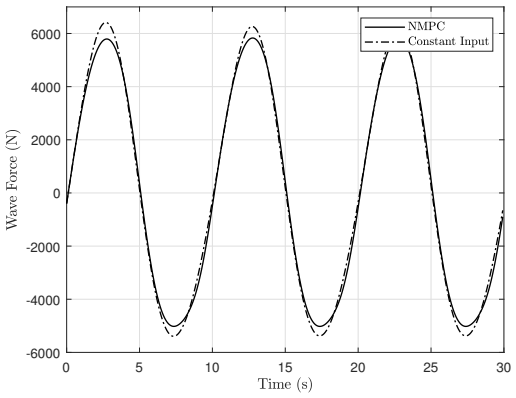

(b) Wave force comparison between the two controllers. Note: The base wave force is subtracted to better show the difference in the two controllers.

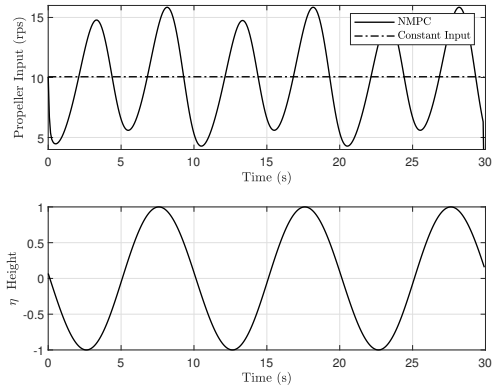

(c) Top plot contains the propeller input profiles of the two controllers. The bottom plot shows the wave state η.

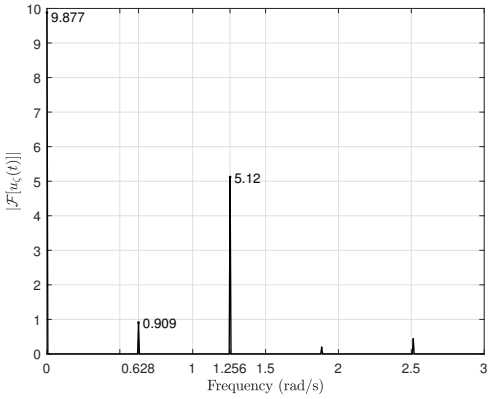

(d) An amplitude spectrum of the NMPC controller input

FIGURE 5.2: These figures show the results of the surge only case.

while a much larger peak in seen at 1.256 rad/s or double the average encounter frequency. This can be explained by the fact that for each wave period, the minimal wave force occurs twice. The NMPC controller exploits this by having the velocity profile shown in Figure 5.2(a), with peaks during the minimal wave force time.

5.3.2 Surge, Heave, and Pitch

This brief section is to discuss the surge, heave, and pitch results. The results are not much improved from the previous surge only results because the vessel is still limited to propeller actuation, but interesting behaviors emerge as a result of penalizing wave force in the pitch direction versus pitch

angle. We start with (5.22) showing the continuous time state space representation of the system.

$$\begin{bmatrix} \dot{x}(t) \\ \dot{u}(t) \\ \dot{z}(t) \\ \dot{w}(t) \\ \dot{\theta}(t) \\ \dot{q}(t) \\ \dot{n_{\mathrm{p}}}(t) \\ \dot{\eta}_u(t) \\ \ddot{\eta}_u(t) \\ \dot{\eta}_w(t) \\ \ddot{\eta}_w(t) \\ \dot{\eta}_q(t) \\ \ddot{\eta}_q(t) \end{bmatrix} = \begin{bmatrix} 0 & 1 & 0 & 0 & 0 & 0 & 0 & 0 & 0 & 0 & 0 & 0 & 0 \\ 0 & -\frac{D_{1,1}}{M_{1,1}} & 0 & 0 & 0 & 0 & \frac{\tau_p}{M_{1,1}} & \frac{F^u}{M_{1,1}} & 0 & 0 & 0 & 0 & 0 \\ 0 & 0 & 0 & 1 & 0 & 0 & 0 & 0 & 0 & 0 & 0 & 0 & 0 \\ 0 & 0 & -\frac{G_{3,3}}{M_{3,3}} & -\frac{D_{4,4}}{M_{3,3}} & -\frac{G_{3,5}}{M_{3,3}} & -\frac{D_{4,6}}{M_{3,3}} & 0 & 0 & 0 & \frac{F^w}{M_{3,3}} & 0 & 0 & 0 \\ 0 & 0 & 0 & 0 & 0 & 1 & 0 & 0 & 0 & 0 & 0 & 0 & 0 \\ 0 & 0 & -\frac{G_{5,3}}{M_{5,5}} & -\frac{D_{6,4}}{M_{5,5}} & -\frac{G_{6,5}}{M_{5,5}} & -\frac{D_{6,6}}{M_{5,5}} & \frac{\tau_p}{M_{5,5}} & 0 & 0 & 0 & 0 & \frac{F^q}{M_{5,5}} & 0 \\ 0 & 0 & 0 & 0 & 0 & 0 & -\frac{1}{\tau_{n_{\mathrm{p}}}} & 0 & 0 & 0 & 0 & 0 & 0 \\ 0 & 0 & 0 & 0 & 0 & 0 & 0 & 0 & 1 & 0 & 0 & 0 & 0 \\ 0 & 0 & 0 & 0 & 0 & 0 & 0 & -\omega_e^2 & 0 & 0 & 0 & 0 & 0 \\ 0 & 0 & 0 & 0 & 0 & 0 & 0 & 0 & 0 & 1 & 0 & 0 & 0 \\ 0 & 0 & 0 & 0 & 0 & 0 & 0 & 0 & 0 & -\omega_e^2 & 0 & 0 & 0 \\ 0 & 0 & 0 & 0 & 0 & 0 & 0 & 0 & 0 & 0 & 0 & 0 & 1 \\ 0 & 0 & 0 & 0 & 0 & 0 & 0 & 0 & 0 & 0 & 0 & -\omega_e^2 & 0 \end{bmatrix} \begin{bmatrix} x(t) \\ u(t) \\ z(t) \\ w(t) \\ \theta(t) \\ q(t) \\ n_{\mathrm{p}}(t) \\ \eta_u(t) \\ \dot{\eta}_u(t) \\ \eta_w(t) \\ \dot{\eta}_w(t) \\ \eta_q(t) \\ \dot{\eta}_q(t) \end{bmatrix} + \begin{bmatrix} 0 \\ 0 \\ 0 \\ 0 \\ 0 \\ 0 \\ \frac{1}{\tau_{n_{\mathrm{p}}}} \\ 0 \\ 0 \\ 0 \\ 0 \\ 0 \\ 0 \end{bmatrix} u_{n_{\mathrm{p}}}(t), \tag{5.22}$$

Note that for compactness, similar notation to that shown in (3.21) is used, and that the ω_e^2 is not the average encounter frequency, but the full nonlinear encounter frequency, $\omega + \frac{\omega^2}{g}u(t)$. Also note the 6 extra states required to calculate the wave states for the wave force for the 3 vessel states. This is due to phase RAO for the 3 states being unique and requiring their own wave state to track it. This adds 12 extra states to the state matrix for a full 6 DOF representation, so a simplification is made to eliminate it which is discussed in the next section.

The vessel was simulated as before, by heading directly into the wave, with only propeller actuation. Besides the constant input control, the vessel was simulated with the NMPC controller having 3 penalization methods. As discussed earlier, the resulting pitch angles are not much improved and are thus not shown because propeller only actuation for wave force mitigation is such a restricted method. Shown in figure 5.3, the solid blue line shows the penalization of the average surge velocity, as before, and the pitch angle. The dashed blue line shows penalization of the average surge velocity and the wave force in the pitch direction, derived using the same method as in the surge only case. The third method, shown in the dashed black line has penalization of the average surge velocity, wave force in the pitch direction, and pitch angle. An interesting result occurs among these 3 methods. The penalization of the pitch force only shows a harmonic at double the encounter frequency as before with the surge only case, but now, the local maximum velocities, when the wave force in the pitch direction is at zero, are roughly equal. Additionally, the local minimum velocities at both the maximum and minimum wave force period are roughly the same as well. As the controller only has one penalization term at that phase of the wave, remember the average surge velocity is penalized as well, but those forces occur out of phase to the pitch forces, it is able make the response to the wave symmetrical. The penalizing of both the wave force in the pitch direction and the pitch

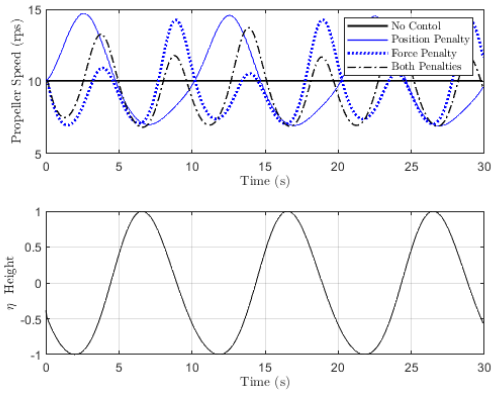

(a) A plot of the propeller speed of the vessel with a constant input, when the NMPC controller penalizes just the pitch position shown in solid blue, penalizes just the wave force in the pitch direction shown in dashed blue, and when both are penalized shown in dashed black.

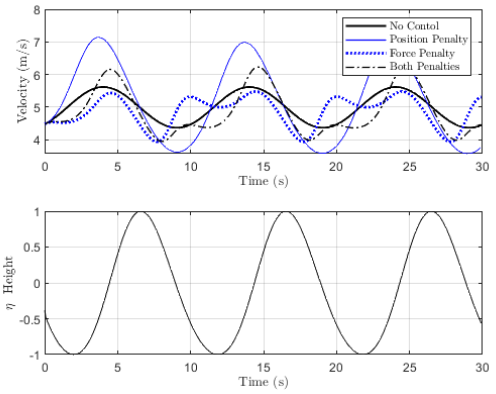

(b) A plot of the surge velocity of the vessel with a constant input, when the NMPC controller penalizes just the pitch position shown in solid blue, penalizes just the wave force in the pitch direction shown in dashed blue, and when both are penalized shown in dashed black.

FIGURE 5.3: These figures show the propeller speed and surge velocity of the vessel with a constant input, when the NMPC controller penalizes just the pitch position shown in solid blue, penalizes just the wave force in the pitch direction shown in dashed blue, and when both are penalized shown in dashed black.

angle results in a similar behavior to the surge only case. There are still local velocity maximums during periods of low wave force, and local velocity minimums during high wave force periods, but they are asymmetrical. The reason this response is similar to the surge only case is that in both instances, the controller is trying to balance both a state and the respective wave force in that direction i.e. surge velocity and wave force in the surge direction or pitch angle and wave force in the pitch direction. The double harmonic behavior is lost when only penalizing the pitch angle. As wave force is not a concern, the controller focuses on only the resulting pitch angle and thus increases actuation when the wave force causes the bow of the vessel downwards, and decreases when the wave force causes the bow of the vessel upwards, resulting in an actuation signal that is largely the inverse of the wave force signal.

5.4 Initial NMPC Behaviour in Rough Seas

5.4.1 Elimination of Wave State

Building upon the previous simulations, changes were made while creating the 6 DOF model. Rather than have η be a wave state dependent on surge position and velocity, which in turn affects the surge acceleration, the wave is modeled directly as a disturbance that is dependent on surge position and

velocity, which affects the surge acceleration. This is more similar to how other state dependent disturbances are modeled, such as a current disturbance if one is included. The change reduces the previous surge only model from 4 to 3 states where $W(u_k, x_k) = \rho g F^u(u_k)\, a_h \cos(\omega_k t + \frac{\omega_k^2}{g} x_k + \phi_{RAO})$, now includes the harmonic wave state. The linearized matrices then become:

$$A_k = \begin{bmatrix} 1 & T & 0 \\ a_{2,1} & a_{2,2} & a_{2,3} \\ 0 & 0 & 1 - \frac{T}{\tau_p} \end{bmatrix} \qquad B_k = \begin{bmatrix} 0 \\ 0 \\ \frac{T}{\tau_p} \end{bmatrix} \tag{5.23a}$$

where,

$$a_{2,1} = \left(\frac{T}{m}\right) \left.\frac{\partial W(\hat{u}_k, \hat{x}_k)}{\partial \hat{x}_k}\right|_{\hat{u}_k = \bar{u}_k, \hat{x}_k = \bar{x}_k} \tag{5.23b}$$

$$a_{2,2} = 1 + \left(\frac{T}{m}\right) \left.\left(\frac{\partial D(\hat{u}_k)}{\partial \hat{u}_k} + \frac{\partial T(\hat{u}_k, \hat{n}_{p_k})}{\partial \hat{u}_k} + \frac{\partial W(\hat{u}_k, \hat{x}_k)}{\partial \hat{u}_k}\right)\right|_{\hat{u}_k = \bar{u}_k, \hat{n}_{p_k} = \bar{n}_{p_k}, \hat{x}_k = \bar{x}_k} \tag{5.23c}$$

$$a_{2,3} = \left(\frac{T}{m}\right) \left.\frac{\partial T(\hat{u}_k, \hat{n}_{p_k})}{\partial \hat{n}_{p_k}}\right|_{\hat{u}_k = \bar{u}_k, \hat{n}_{p_k} = \bar{n}_{p_k}}, \tag{5.23d}$$

where it can be seen that the sensitivity matrices still contain the knowledge of the dependence of the wave force on both the position and velocity. Figure 5.4 shows that there is no difference in the response when the surge only case is reduced to 3 states. The full 6 DOF model was then developed as expressed in (3.21).

5.4.2 Full Model Testing

With a full model, testing was carried out to gain an understanding of the optimal control strategy in the presence of waves. The test involved the vessel starting on and following a reference heading directly into a head sea with monochromatic waves with wave height of 2.5 m and a wave frequency of 0.9 rad/s. As with the previous 1 DOF simulation, the simulation and controller model were the same. This was done to ensure any behavior seen was the result of the NMPC and optimization and not a model mismatch. With penalizations on deviations from the reference heading, from the reference velocity, and from a zero degree pitch angle, a two-timescale tack behavior emerged from the NMPC. The penalization on the heading, Q_ψ, was decreased from 1 to 0.1 in order to investigate the influence of this penalization to the resulting tacking behavior. This is shown in Fig. 5.5(a). Two tacking behaviors can be seen in this figure, firstly a large overall angle away from

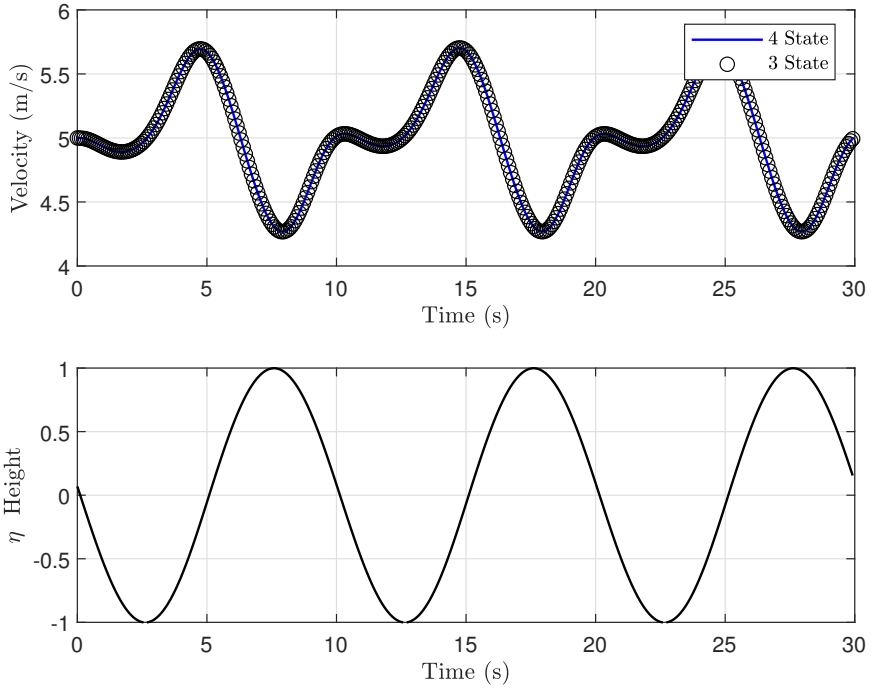

FIGURE 5.4: The velocity response profile of the surge only case with and without the wave state.

the reference heading angle and secondly, a small amplitude, high frequency tack. The larger tack enables an average encounter angle that is larger than the reference heading. This angle increases as the penalization on the heading angle decreases. The smaller tacking allows even larger encounter angles during the period of the wave cycle when selected wave forces are highest. This smaller tacking occurs at the encounter frequency of the wave and with higher harmonics. This coupling of the wave encounter frequency and actuation is similar to the one discussed in the 1 DOF case study, though for rudder actuation instead. This high frequency tacking is not solely the result of the wave force in the yaw direction. In fact, in figures 5.5(e) and 5.5(f) it can be seen that magnitude of the actuation and the changes in heading for the lowest Q_ψ penalty is lower than the highest Q_ψ penalty. Instead, these figures show that the large changes in rudder angle are a response to mitigate surge and pitch forces and are responsible for the high-frequency tacking, while the smaller rudder actuation is to neglect the influence of the wave in the yaw direction. The rudder actuation of the lower Q_ψ penalty shows that more actuation is needed at a larger heading angle because of the larger wave forces in the yaw direction. The propeller actuation in Fig. 5.5(b) also shows a coupling between the wave encounter frequency, however, it does not have the higher harmonics seen in the previous section. This is for two reasons; in the previous section, the penalty

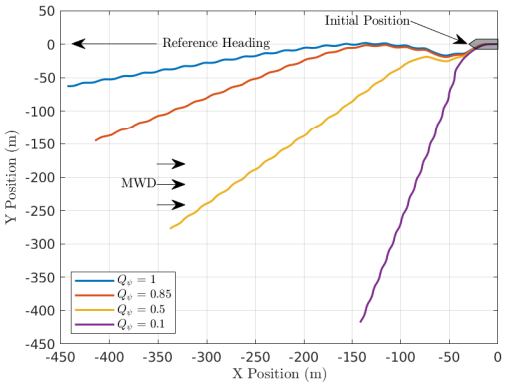

(a) This plot shows the large and small, high frequency tacks of the vessel when heading directly into the major wave direction.

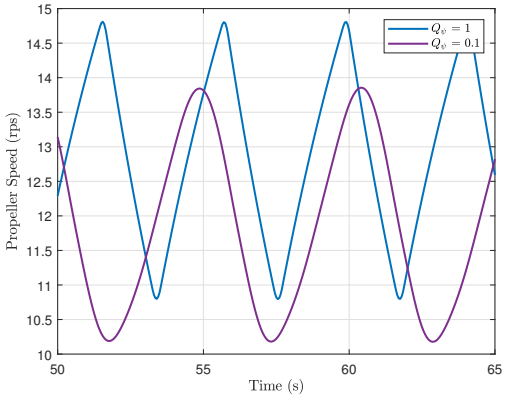

(b) Propeller speed of the largest and smallest tack. Larger tacking requires less actuation in both mean and amplitude.

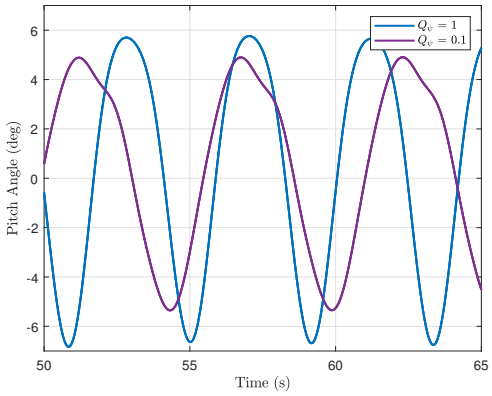

(c) Pitch angle of the largest and smallest tack. Larger tacking results in less wave force in the pitch direction helping to reduce the overall pitch angle.

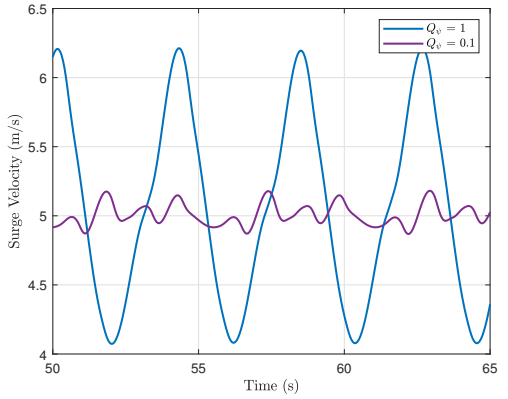

(d) Surge velocity response of the largest and smallest tack. Larger tacking results in less wave force in the surge direction and therefore better adherence to the reference velocity.

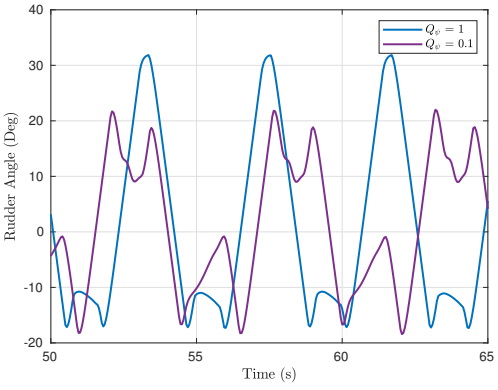

(e) Rudder angle of the largest and smallest tack. Larger tacking results in larger wave force in the yaw direction.

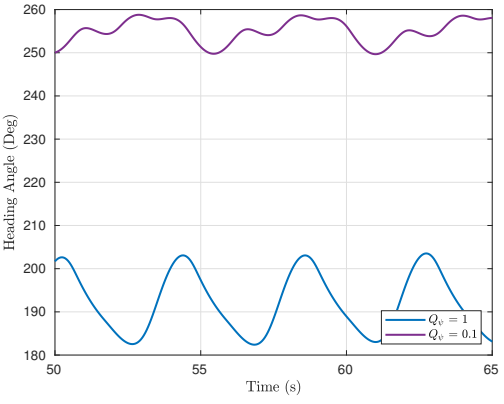

(f) Heading angle response of the largest and smallest tack. The larger wave force in the yaw direction means more actuation is needed to maintain course for the larger tack.

FIGURE 5.5: These figures show the double harmonic velocity, resulting wave force, required input, and amplitude spectrum of a vessel in a head sea with only propeller control.

term was on the wave force in the surge direction, not the surge velocity, and in this study the waves are much larger, requiring the focus of the actuation to be maintaining the reference velocity. Fig. 5.5(d) shows how large of an impact the waves have upon the surge velocity when encountering them head on. The higher peak velocity seen in the higher Q_ψ penalty case can in turn cause higher wave forces in the other DOFs. Also of note in Fig. 5.5(d) is the higher harmonics of the velocity for the lower Q_ψ due to the drag from the rudder. This appears for the lower Q_ψ case due to higher relative drag force to the wave force in the surge direction. Both high and low frequency tacking, along with the more moderate surge velocity can measurably reduce the pitching angle of the vessel as seen in Fig. 5.5(c), along with accelerations in some of the other DOFs. This is discussed in detail in the results chapter 7. This result arises from the fact that wave forces in the surge and pitch directions are highest when encountering a wave head on. Tacking, while increasing the wave force in the yaw direction and the necessary actuation on the rudder to maintain heading, reduces the necessary actuation in the propeller to maintain a desired velocity, and reduces the forces in the pitch direction.

This shows that given a desired heading directly into the waves, the optimal heading is at an angle to it. While this is shown to reduce wave-induced motions in the surge and pitch direction, the NMPC is not following a path to a desired destination. The larger drift tack is doing just that, drifting. The act of tacking about a desired path is a binary operation in which the transition from one tack to the next should be completed as quickly as is safe to do so. This binary behavior can not be achieved through a path deviation penalty term. A tacking boundary constraint can be used to complete a quick tack, however, in rough seas there is no guarantee that the constraint will not be violated. Additionally, in a head or following sea, the tacking should be symmetrical about the major wave direction, while in a beam sea it should be symmetrical about an axis perpendicular to the major wave direction. When a desired heading which is not directly into the wave direction, or perpendicular to it, penalizations for deviations on the heading will occur symmetrically about the desired heading angle and not the wave direction. Lastly, the time scale for the tacking would require a sufficiently large prediction horizon and correspondingly large time steps for the computation to be feasible. The reliability of predictions of the waves also diminishes greatly for long time scales. These time steps are then too large for the NMPC to navigate the individual waves. This motivates the use of a two degree of freedom controller, consisting of a tacking planner described in the next chapter, which uses the ocean environment and vessel dynamics to provide an optimal long-term

surge velocity and heading reference and an NMPC controller. The NMPC controller uses the tacking planner references and provides smaller actuation signals over a shorter horizon to further reduce motions on a per wave basis.

5.5 Summary

The initial 1 DOF results were presented in this chapter. This was then expanded to include heave and pitch to show how the actuation transitions from a double harmonic when penalizing just wave force, to a single harmonic when penalizing just position. Further simplifications of the model were made, along with changes to the NMPC, to output form so as to enable calculation of the wave force, which is not a state. Here was the first look at what the optimal behavior in the presence of waves is. By producing a double harmonic input, the desired average velocity is maintained, while reducing the peak wave force experienced by the vessel. The problem was then expanded to the 6 DOF model and investigated. The same harmonic responses remained, however, now it was primarily in the rudder response. These results showed that small tacking is implemented to reduce pitching motion and necessary propeller actuation on a per wave basis, with a larger tack reducing these even further. The two time scale tacking serves as the basis of the tacking planner discussed in the next chapter.

Chapter 6

Tacking Planner

As highlighted in the previous chapter, the task of maneuvering over individual waves and the task of creating an optimal path to make headway in rough seas occur on two different time-scales. An NMPC controller is well suited to maneuver in an optimal fashion over individual waves given a reference path to follow, however, it is not suited to also generate that path. A novel contribution of this thesis comes from the construction and use of a tacking planner as an optimal reference signal.

The tacking planner finds the optimal velocity, u_{r}, and heading, ψ_{r}, reference to tack with dependent on the input desired velocity, u_{d}, heading, ψ_{d}, and ocean environment. These reference signals guide the previously described NMPC controller in a large tacking course while the NMPC controller actuates on the individual waves to further mitigate their impact. This allows for the two time scale tacking seen in Fig. 5.5, but with the large tacking occurring along the desired direction and handled by the tacking planner. Fig. 6.1 shows the structure of the closed-loop simulation model. This NMPC is the same in structure as that of the previous chapter, and the one formulated in chapter 4, with slight adjustment on the weights of the penalties. Ideally, the tacking planner would run at set intervals in the range of minutes to tens of minutes or if large disturbances were detected. Then it would update the references in accordance with changes in the ocean environment. In this thesis the tacking planner is run only once at the beginning of the simulation as the wave environment is assumed to remain constant, and the simulation is carried out over a 1 kilometer path. Also, note that the tacking planner is not a full path planner, and as such is not designed to plot a course to a specific final destination or position, x, y, but rather provide tacking maneuvers to allow the vessel, as safely as possible, to make headway towards calmer waters, a harbor, or a

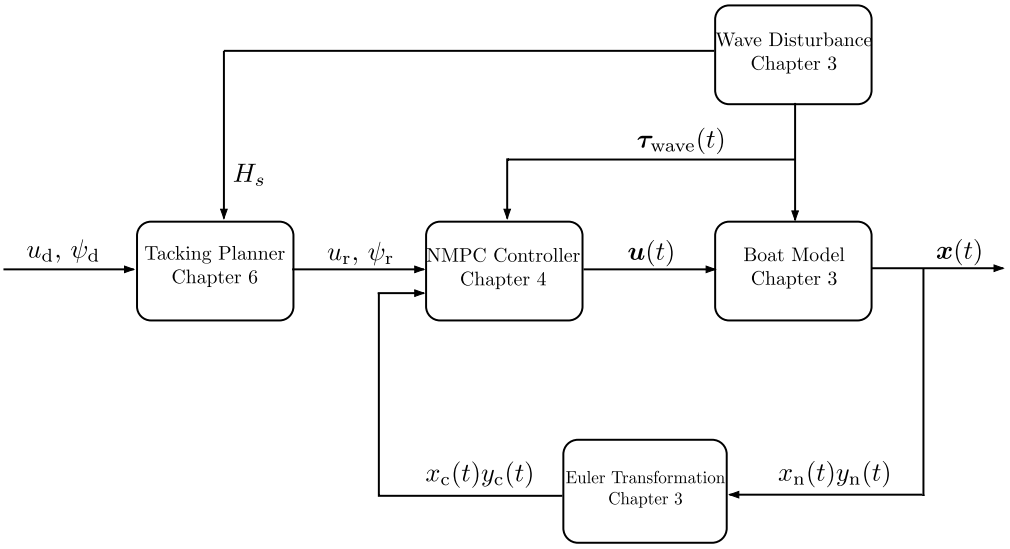

FIGURE 6.1: The structure of the closed-loop simulation model. Note the tacking planner uses the significant wave height of the ocean and not the time dependent wave heights.

rendezvous area. Once out of rough seas, the vessel can return to more typical path planning and following.

In a human piloted vessel that is performing a tacking maneuver, the pilot quickly determines the tacking angle based on a number of criteria. This can include the maximum distance from the path that a tack can venture which may be determined by geographical constraints, the severity of the waves, the angle of the major wave direction compared to the desired heading angle, or fuel remaining on board. The tacking planning imbues these same criteria. The tacking planner seeks to minimize the effect of potentially damaging waves while balancing the need to stay within a set distance of the desired path, and consider the time required to arrive at the destination. The optimization starts with identifying in which of the four predefined quadrants the desired final location lies. These quadrants can broadly be described as a head/bow sea, beam sea, and following/quartering sea. In a head and bow sea, the wave forces of concern are in the surge and pitch directions. In a beam sea, the difficulty lies with larger wave forces in the roll direction, a still present wave force in the pitch direction, and the asymmetrical RAOs between a beam/bow sea and a beam/quartering sea. This requires asymmetrical tacking in a beam sea. For following and quarter seas, the challenge lies in wave speed matching and risk of broaching when being overtaken by a wave. The tacking planner introduced here in this chapter focuses on the head/bow sea. With slight modification to the presented methodology, the tacking planning will be designed for beam sea and following/quartering seas in later chapters.

TABLE 6.1: Parameters used in the tacking planner

Parameter	Symbol	Value	Unit
Direct Path Length	d_{D}	1000	m
Width Constraint	d_{C}	200	m
Desired Velocity	u_{d}	4	m/s
Kappa Time Penalty	κ_{time}	1.00001	$1/\mathrm{s}^2$

The head/bow sea covers a 120° segment heading into the major wave direction. The major wave direction is the direction in which the average velocity of the waves travel. Owing to the symmetrical nature of the vessel dynamics relative to the encounter angle of the wave in a head sea, the quadrant is further divided in half. Which half of the quadrant is used in the optimization is dependent on which half of the quadrant the desired destination lies. Alternatively if the desired destination is directly into the major wave direction, the optimization is done in the bottom half of the quadrant. For this chapter, all of the tacking planning will take place in the bottom half of the quadrant for consistency. This is highlighted in blue in Fig. 6.2.

The tacking planner consists of two main terms. The first is geometric, which considers the geometry of the tacking path as it relates to the desired destination. This includes the amount of turning needed to complete the path, time to destination, and estimated fuel required for the tacking path. The second is force and actuation, which considers the wave forces expected to be experienced for a given heading and velocity as well as the corresponding actuation needed to maintain said heading and velocity. The forces considered are surge, roll, and pitch since these pose the greatest threat to damage and capsizing. Yaw force is also considered indirectly with the rudder actuation term. The parameters used in the tacking planner are listed in Table 6.1. The optimal speed and tacking angle which minimize the total cost are calculated by solving the following optimization problem:

$$\min_{u,\psi} J_{\mathrm{Total}} = \frac{A_k^{\max} - A_k}{A_k^{\max}} \boldsymbol{J}_{\mathrm{Geometric}}(u,\psi) + \frac{A_k}{A_k^{\max}} \boldsymbol{J}_{\mathrm{Force}}(u,\psi), \tag{6.1a}$$

$$s.t.$$

$$u \in [1, 12], \tag{6.1b}$$

$$\psi \in \left[\frac{\pi}{2}, \frac{4\pi}{3}\right], \tag{6.1c}$$

where A_k is the current wave amplitude and $A_k^{\max}$ is the maximum assumed survivable wave amplitude which, for this thesis corresponds to a wave height of 2.5 meters. The tacking planner

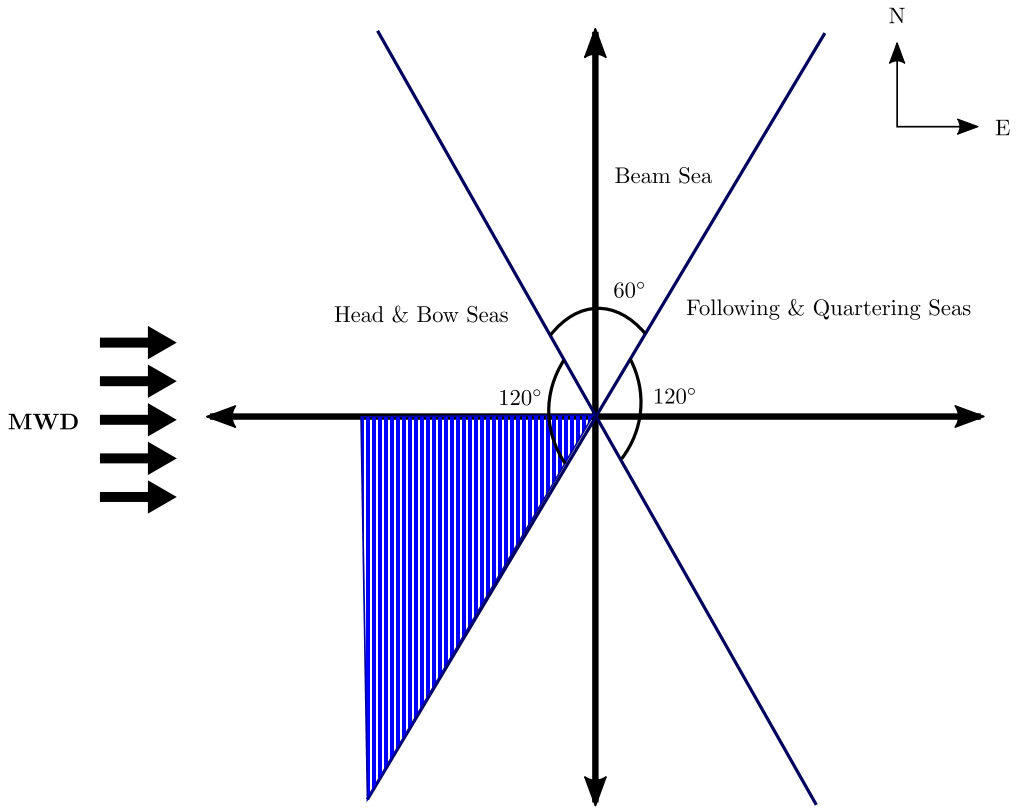

FIGURE 6.2: The general encounter angles of a vessel. This thesis is concerned with only the head and bow seas in general, and specifically within the area shaded in blue.

and its equations are defined in the Cartesian plane with the major wave direction being $\frac{pi}{2}$, while the results of the tacking planner, and the other result chapters are presented in the North East Down frame with the equivalent major wave direction of 270° W. The disparate units of the cost terms, such as (l/km) for fuel efficiency or (n) for wave force require a non-dimensionalization and normalization for use in the cost function. All cost terms are non-dimensionalized and normalized to a range of 0 to 1, making each cost term equivalent with respect to weighting. Owing to this procedure, the wave force terms no longer reflect the absolute increase in force that occurs with an increase in wave height. To compensate for this, the fraction in front of the force term increases with an increase in wave height while the geometric term decreases. The disparate units also mean that a unifying function that represents the total cost can not be described a priori, and a minimum finding algorithm used to find the minimizing heading and velocity. Since each term needs to be non-dimensionilized and normalized, a surface of each term is created, representing the value at each heading and velocity pair, first. Then the procedure is done to reduce its values to a range between 0 and 1.

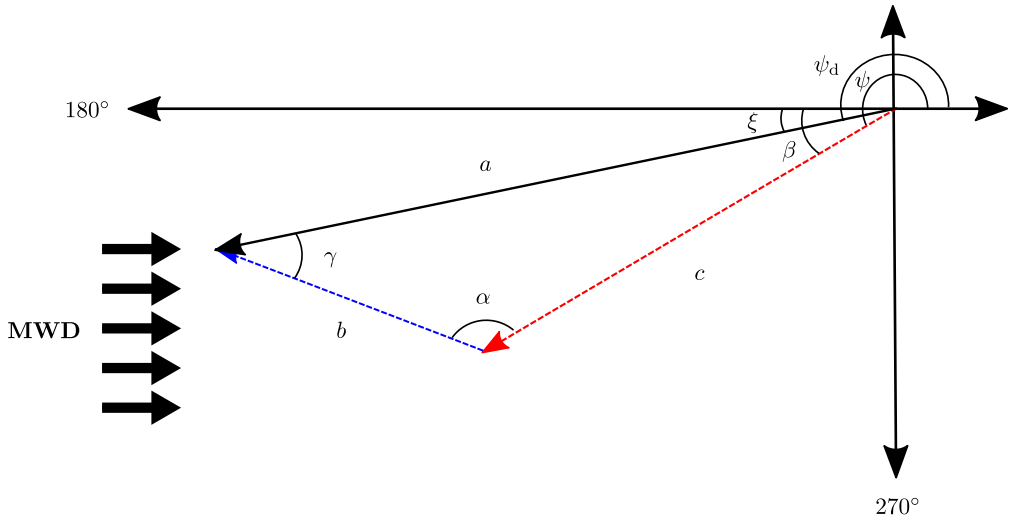

FIGURE 6.3: The tacking in the planner is estimated as a single large tack. This figure shows the angles used in the tacking planner.

6.1 Geometric

The geometric term consists of three parts, the amount of tacking needed to reach the destination, the fuel cost, and the time to destination cost:

$$\boldsymbol{J}_{\text{Geometric}}(u,\psi) = \boldsymbol{J}_{\text{fuel}}(u,\psi) + \boldsymbol{J}_{\text{time}}(u,\psi) + \boldsymbol{J}_{\text{turn}}(\psi), \tag{6.2a}$$

Since these terms have non related units, they are non-dimensionalized and normalized by first subtracting the minimum cost value in the operating region of $u \in [1, 12]$ and $\psi \in \left[\frac{\pi}{2}, \frac{4\pi}{3}\right]$, then dividing by the maximum cost in the operating region. This results in the cost of each term retaining its functional behavior, but ranging from 0 to 1. The cost for the time-to-destination and the fuel cost both use the estimated total path length as shown in Fig. 6.3. The total path length is calculated by:

$$d_{\text{T}} = b + c, \tag{6.2b}$$

the law of sines gives the length of b:

$$b = \frac{a \sin(|\beta - \xi|)}{\sin(\alpha)}, \tag{6.2c}$$

where $\beta = |\psi - \psi_{\text{MWD}}|$, and $\xi = |\psi_{\text{d}} - \psi_{\text{MWD}}|$. Here, $\psi_{\text{MWD}} = 180°$, is defined as the heading angle which results in going against the major wave direction, ψ is the potential tacking angle, and ψ_{d} is the desired heading angle. The length of a is the same as the direct path length d_{D}, and the angle α, due to the symmetrical tacking, is defined as:

$$\alpha \coloneqq 180° - 2\beta. \tag{6.2d}$$

Similarly, the length of c is calculated as:

$$c = \frac{a \sin(\gamma)}{\sin(\alpha)}, \tag{6.2e}$$

where γ is,

$$\gamma = \psi + \psi_{\text{d}} - 2\psi_{\text{MWD}}, \tag{6.2f}$$

With all lengths defined, the normalized time to reach the destination cost is defined as:

$$\boldsymbol{J}_{\text{time}}(u, \psi) = 1 - \kappa_{\text{time}}^{-\left(\frac{d_{\text{D}}}{u_{\text{d}}} - \frac{d_{\text{T}}(\psi)}{u}\right)^2}, \tag{6.2g}$$

where u_{d} is the desired velocity, u is the velocities used to construct the cost surface, and $\kappa_{\text{time}} > 1$. The squaring ensures the value inside the parentheses is positive. This cost term quantifies the difference between the time to reach the desired destination when traveling the direct path at the desired velocity and when tacking the total path length at a different velocity. This allows for a user-defined desired velocity and heading to be set and no penalty to be incurred for tacking when compensated with an appropriate velocity increase. This calculation is performed for each possible velocity and heading in the search region to construct a cost surface. Fig. 6.4(a) shows the plot of the cost surface of $\boldsymbol{J}_{\text{time}}$ for a desired velocity of 4 m/s and a desired heading of 270 degrees NED. The red line indicates headings and velocities which achieve the same time to destination as the desired heading and velocity and therefore incur no penalty. The difference in the value of the time-to-destination term, $\left(\frac{d_{\text{D}}}{u_{\text{d}}} - \frac{d_{\text{T}}}{u}\right)$, increases more quickly when going slower than the desired velocity than it does going faster. The exponential term is used to slow this growth rate. This is shown in figure 6.4(b), whereby large tacking angles at slow velocities take proportionally longer to reach the destination the vast majority of the cost surface is near zero. This does not provide any useful information to the tacking planner, hence using it as an exponential term. The next

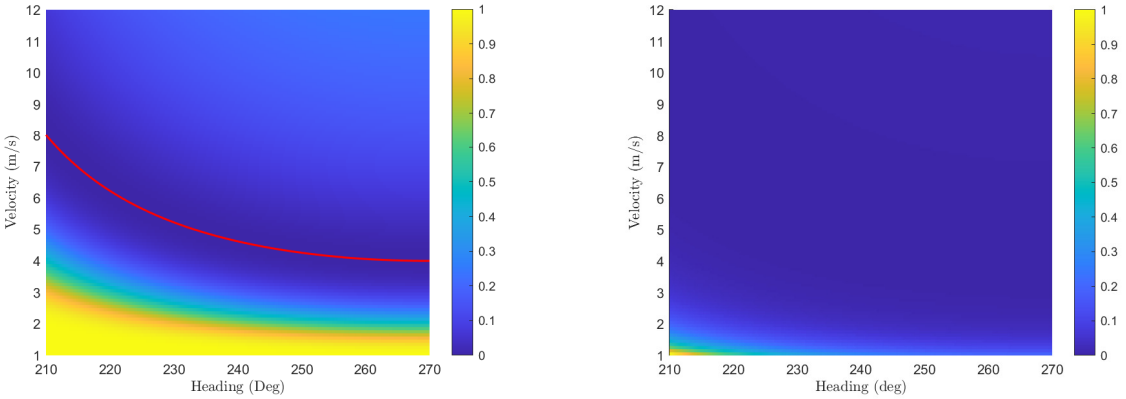

(a) A plot of the time-to-destination term defined in the text. Note that by doubling the velocity to 8 m/s, tacking with a heading of 210 degrees has the same time to destination as the desired heading and velocity, i.e. both are points on the red isocline.

(b) A plot of the an unmodified time-to-destination calculation.

FIGURE 6.4: These figures show a plot of the time-to-destination term of the tacking planner for a desired velocity of 4 m/s and a desired heading of 270 degrees for the method defined in the text and the original time to destination calculation.

geometric term quantifies the fuel cost required to reach the destination. This is simply the fuel consumption rate per distance traveled multiplied by the total path length:

$$\boldsymbol{J}_{\text{fuel}}(u, \psi) = \frac{d_{\text{T}}(\psi)\, G(u)}{u}, \tag{6.2h}$$

where $G(u)$ is a function relating the fuel consumption per meter traveled to vessel velocity. Again, as with all of the cost terms, this is calculated for all possible velocities and headings in the search area to construct a cost surface.

During rough seas, if it is deemed prudent to travel at an angle to the waves to minimize forces, then it follows that the number of times the vessel needs to tack should also be minimized, since this requires briefly heading into the major wave direction. This, and the roll moment induced by the rudders coupled with the wave force in the roll direction could be enough to capsize the vessel. The final geometric term quantifies this with an estimation of the number of tacks required to reach the destination calculated as:

$$\boldsymbol{J}_{\text{turn}}(\psi) = \frac{\tan(|\psi - \psi_{\text{d}}|) d_{\text{D}}}{d_{\text{C}}}, \tag{6.2i}$$

where d_{C} is the width constraint on the tacking i.e. the furthest from the straight line path the vessel can go before it must tack back. This is an estimation of the number of tacks the vessel must complete not an exact count, as that would make it an integer problem. Though an exact count

could be calculated and the surface interpolated, no value would be gained from this, as this, and the cost as presented above have the same characteristic; larger tacking angles, and smaller width constraints require more tacking.

6.2 Force and Actuation

Large waves can compromise the structural integrity of the vessel and pose a capsize risk. They also require larger amounts of actuation to maintain a steady course and can even impart larger forces than can be produced by the actuators of the vessel. The rudder can only actuate when there is a relative velocity between the vessel and the ocean, therefore, it is important for the vessel to travel at a velocity and heading which minimizes the wave force, but also enables a forwards velocity to be maintained for rudder control. The force and actuation cost function accounts for the force from the waves in the surge, roll, and pitch directions since these are the most likely to compromise the vessel, as well as the actuation effort required by the rudders and propellers to maintain course. Heave force is not considered because it is relatively equal for all headings and velocities. Sway and yaw forces are not considered since they are not likely to cause damage or present a capsize danger, they only affect path following behavior. Yaw is also already partially considered in the rudder actuation effort. The force and actuation cost function is defined as:

$$\boldsymbol{J}_{\text{Force}}(u,\psi) = \Big\{ \big(\boldsymbol{\tau}_{\text{surge}}(u,\psi)\big)^2 + \big(\boldsymbol{\tau}_{\text{roll}}(u,\psi)\big)^2 + \big(\boldsymbol{\tau}_{\text{pitch}}(u,\psi)\big)^2 + \big(\boldsymbol{\Delta}\tau_{\text{prop}}(u,\psi)\big)^2 + \big(\boldsymbol{\Delta}_{\text{vel}}(u,\psi)\big)^2 + \big(\boldsymbol{\Delta}\tau_{\text{rudder}}(u,\psi)\big)^2 \Big\}^{(1/2)}, \quad (6.3a)$$

where the superscript, ^{2}, indicates the piecewise Hadamard product of the elements of the $\boldsymbol{\tau}$ and $\boldsymbol{\Delta}$ cost matrices, defined below. Long term tacking is concerned not with periodic nature of the wave force, but the magnitude of said force. Accordingly, the harmonic component of (3.2) is removed along with dimensionalizing (scaling) terms leaving:

$$\boldsymbol{\tau}_{\text{dof}}(u,\psi) = |F^{\text{dof}}(u,\psi)|, \quad (6.3b)$$

where the force RAO surface is that of a wave for the current significant wave height. The wave angle used is that of the major wave direction. With the sway velocity assumed negligible, the force

RAO reduces down to being dependent upon the surge and heading angle of the vessel. This is normalized from 0 to 1 like all other terms. The quantification of propeller actuation proceeds from equating thrust (3.13a) to drag (3.18b) on a calm sea:

$$0 = \boldsymbol{\tau}_{\text{prop}}(u, n_{\text{p}}) + \boldsymbol{X}_{D_n}(u), \tag{6.3c}$$

this is solved for, $\boldsymbol{n}_{\text{p,nom}}$, at a constant nominal velocity, $\boldsymbol{u}_{\text{nom}}$. Next the wave force in the surge direction is added to (6.3c). Since the goal is to find a constant value, only the magnitude of the wave force is added:

$$0 = \boldsymbol{\tau}_{\text{prop}}(u, n_{\text{p}}) + \boldsymbol{X}_{D_n}(u) - \boldsymbol{\tau}_{\text{surge}}(u, \psi), \tag{6.3d}$$

which results in a new, higher propeller speed, $\boldsymbol{n}_{\text{p,wave}}$. Finally, the propeller speed difference is calculated as:

$$\boldsymbol{\Delta}\tau_{\text{prop}}(u, \psi) = \boldsymbol{n}_{\text{p,wave}}(u, \psi) - \boldsymbol{n}_{\text{p,nom}}(u). \tag{6.3e}$$

When the wave force is pushing the vessel in the positive surge direction, the excess velocity caused by the wave force is calculated similar to that in (6.3d). Using the nominal propeller speed, $\boldsymbol{n}_{p,\text{nom}}$, from (6.3c) a new constant velocity, $\boldsymbol{u}_{\text{wave}}$ is found in from (6.3d). The excess velocity is then calculated by:

$$\boldsymbol{\Delta}_{\text{vel}} = \boldsymbol{u}_{\text{wave}}(n_{\text{p}}, \psi) - \boldsymbol{u}_{\text{nom}}(n_{\text{p}}). \tag{6.3f}$$

The rudder angle necessary to maintain heading is calculated in a similar manner, using (6.3b) and (3.17f). The rudder angle necessary to maintain heading is calculated from:

$$0 = \boldsymbol{\tau}_{\text{rudder}}(u, \alpha_{\text{r}}) + \boldsymbol{\tau}_{\text{yaw}}(u, \psi). \tag{6.3g}$$

The rudder angle used, α_{r}, is the actual rudder angle and not the effective rudder angle because the sway velocity does not appear in this equation. Since the nominal rudder angle is zero, assuming no currents, the necessary rudder angle to maintain heading is simply the root of (6.3g). Finally, on some occasions, the optimal heading of the force term may be near enough to the optimal heading of the geometric term that total optimal heading is only slightly different than the geometric optimal. Note that the desired heading and geometric heading are always the same, though the desired velocity and the geometric velocity can be different. On these occasions, the heading angle difference

may be small enough that over the course of the entire path, the vessel would not encounter the path constraint. In this instance, it is deemed that the deviation from the path, and the subsequent required tack back across the major wave direction is not justified by the small reduction in the force cost. When this occurs the optimal heading is the desired heading according to:

$$\psi^{\star} = \begin{cases} \psi_{\mathrm{d}}, & \text{if } \tan(\beta - \xi) < \dfrac{d_{\mathrm{C}}}{d_{\mathrm{D}}} \\ \min\limits_{u,\psi} J_{\mathrm{Total}}, & \text{else.} \end{cases} \tag{6.4}$$

Figure 6.5 shows the force and geometric surfaces, and then the total cost for the tacking planner. This example is for a significant wave height of 2 meters, with a desired heading of 270°. Though from the proportional weighting factors of (6.1), the geometric term does not have a large bearing on the total cost for a sea state with a 2 meter significant height, it still influences the total cost slightly.

6.3 Tacking Planner Results

For the tacking planner, a variety of different desired heading angles and significant wave heights were used to assess behavior in differing sea states. The desired velocity in (6.2g) was set to 4 m/s. Fig. 6.6 shows the optimal headings and velocities for desired headings of 270, 255, 240, and 225 degrees in the North East Down frame. What is evident is the optimal heading and desired heading are the same for up to and including 1 meter of significant wave height, indicating that these wave conditions are not sufficient to warrant tacking, and instead follow a traditional path following procedure. This is shown by the marker lining up with the desired heading. The optimal velocities for a calm sea and significant wave height of 0.25 meters are below the desired velocity of 4 m/s, driven down by the cost of the fuel efficiency term, where the most fuel efficient velocity is roughly 2.8 m/s. For a calm sea, the force and actuation term is zero in (6.1), with the optimal cost being driven solely by the geometric term. At 0.5 meters, the optimal velocity is the desired velocity of 4 m/s for most headings. Above this wave height, at 1 m, the optimal velocity increases above the desired velocity. This appears counter-intuitive to the goal of reducing wave forces, but it is due to the actuation cost terms of (6.3e), (6.3f), and (6.3g). With higher wave heights, a higher reference velocity is needed to ensure forward momentum is retained, and has a lower relative

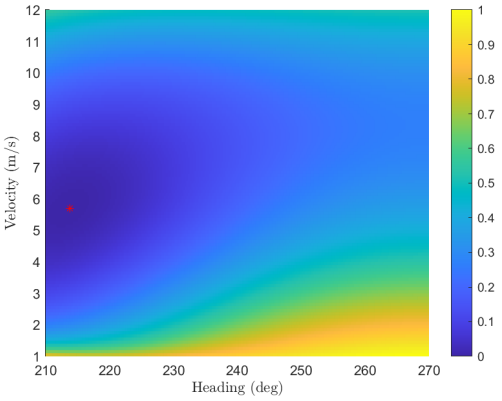

(a) Force cost surface of the tacking planner.

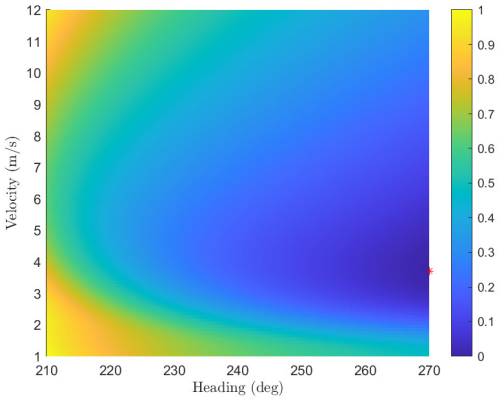

(b) Geometric cost surface of the tacking planner.

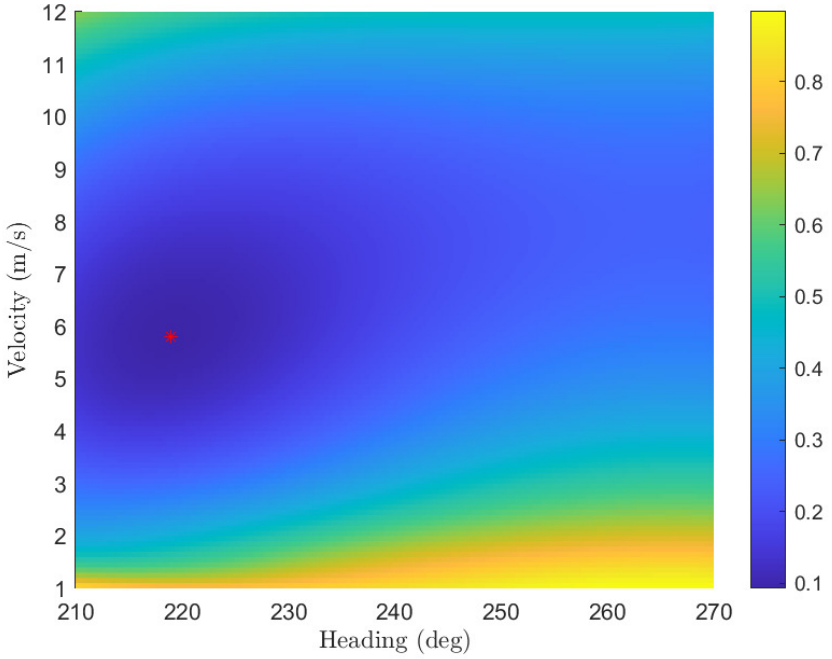

(c) Total cost surface of the tacking planner.

FIGURE 6.5: These figures show the force, geometric, and the combined total cost surface of the tacking planner for a 2 meter significant wave height with a desired heading of 270°. The red $*$ indicates the minimum point.

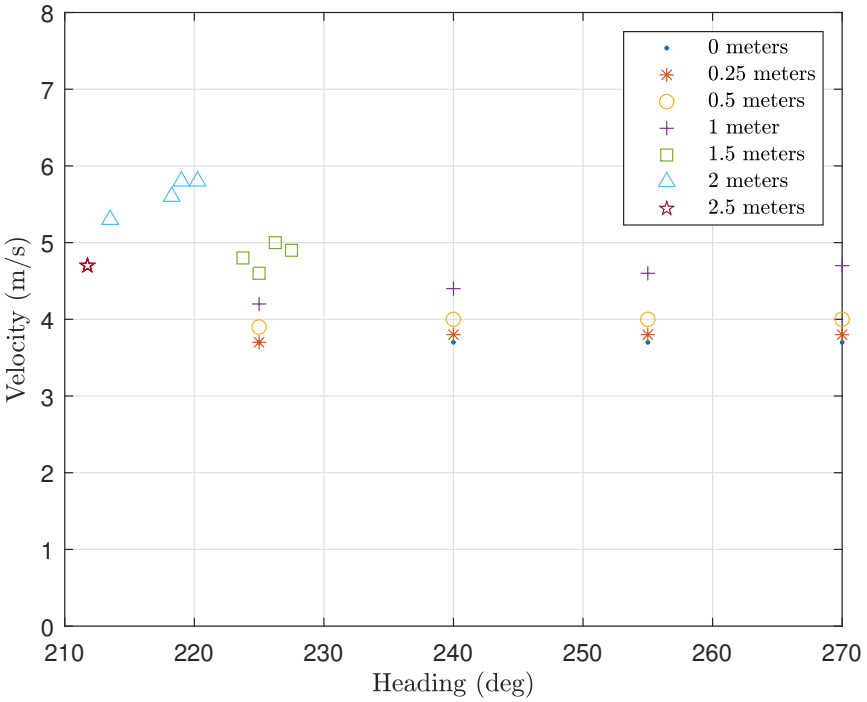

FIGURE 6.6: This figure shows the optimal heading and velocity for a given desired heading and a desired velocity of 4 m/s according to the tacking planner. The desired headings are 270 degrees, which is directly into the major wave direction, 255, 240, and 225 degrees. The different shapes indicate the different significant wave heights. Note that for waves above 1 meter, tacking is deemed necessary, i.e. the optimal heading is not the same as the desired heading. Also note that at 2.5 meters the tacking planner is concerned only with the force cost (6.3a) and therefore the optimal is found to be the same regardless of desired heading. This can be seen with the 4 red stars being plotted on one another.

velocity increase with a positive wave force. This can also be seen in the decrease of the optimal velocity as the desired heading angles increasingly move away from the major wave direction. There is less force in the surge direction, and therefore the surge actuation cost is lower.

Above 1 meter, the tacking planner begins to prescribe tacking as the optimal path. For 1.5 meter waves, the optimal tacking angle is roughly 225 degrees with an even slightly higher velocity than the cost function sets out for 1 meter waves at that same heading. For the desired heading of 225 degrees, the cost function activates the logic of (6.4), and sets the optimal heading as the desired heading. For 2 meter waves, the optimal tacking angle increases, as well as the velocity. This is shown by the triangles clustering further to the left, around 218 degrees, for all four desired headings. Finally for the 2.5 meter waves, the tacking angle again increases, but it can be seen that the wave forces are growing large enough to temper the influence of the actuation forces, as the optimal velocity prescribed is lower than that of the 2 meters waves. Also, at this wave height, the

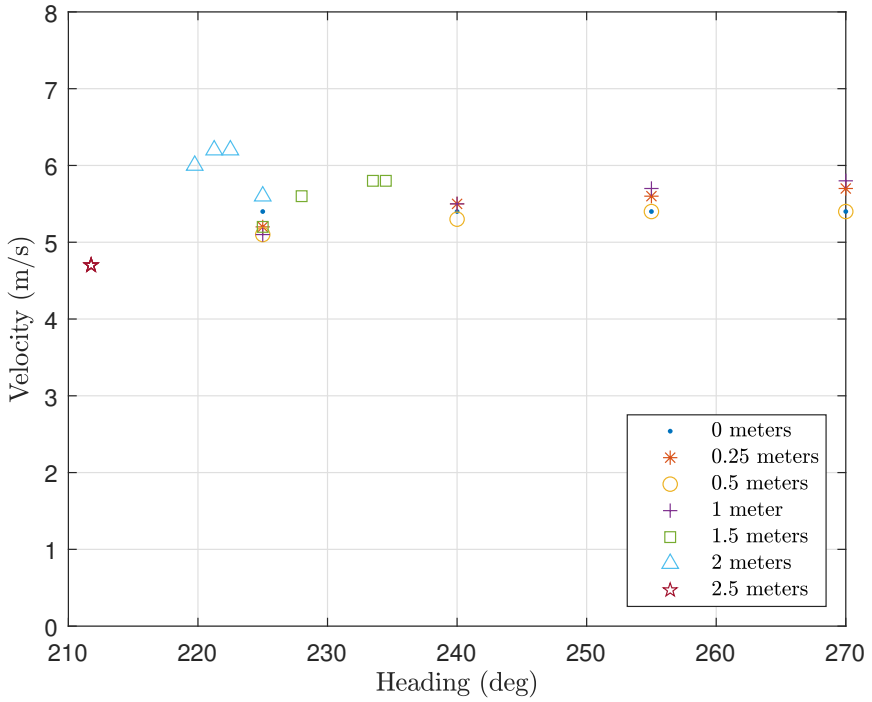

FIGURE 6.7: This figure shows the optimal heading and velocity for a given desired heading and a desired velocity of 8 m/s according to the tacking planner. Again the desired headings are 270, 255, 240, and 225 degrees. The different shapes indicate the different significant wave heights. Note that for waves above 1 meter, tacking is deemed necessary. Also note that at 2.5 meters the tacking planner is concerned only with the force cost (6.3a) and therefore the optimal is found to be the same regardless of desired heading. This can be seen with the 4 red stars being plotted on one another.

geometric term is zero in (6.1), so there is no longer a time-to-destination penalty to increase the velocity at this heading angle. This results in all of the reference heading and velocities to be the same.

The tacking planner was also run with a desired velocity of 8 m/s to investigate the influence of differing desired velocities on the outcome. The results have some of the same characteristics as before, such as tacking being prescribed above 1 meter of significant wave height, and the 2.5 meter waves having the same optimal heading and velocity owing to the fact they are driven solely by the force cost. However, some of the positions have shifted. For both 1.5 and 2 meter waves, tacking is still the optimal course, but their tacking angles have been reduced by up to 10°. They also have slightly higher optimal velocities. The non-tacking results have also changed slightly. The results are much closer together with the optimal velocity of the 0.25 meter results higher than that of the 0.5 meter results. This is due to the shape of the force RAOs for pitch and surge at small waves sizes. This was shown in figure 3.2(b), where the lowest wave force is experienced at higher

velocities. Also of note is the influence of the fuel consumption term. Before, the geometric cost, which can be seen in the 0 meter results, was close to the desired velocity. This was due to the desired velocity being near the optimal velocity for fuel efficiency. Now, with a desired velocity of 8 m/s, the optimal velocity calculated by the geometric cost is 5.4 m/s which is the average of the desired velocity and the velocity for optimal fuel efficiency.

Finally, the implementation of the tacking planner during simulation. For the head sea results, during the simulation, the last predicted location is used to check if it violates the path boundary, and if it does, the final reference heading of the prediction horizon is changed to the opposite heading angle. This creates a soft constraint at the path boundary which is preferred due to the large disturbances. This method is not ideal for the NMPC though, as with the RTI method, the references of the system should be free of large changes. For the beam and following seas, the tacking planner uses the optimal velocity to calculate the turn rate of the vessel. This turn rate is then used with the tacking angle differential to calculate the time required to turn, and the heading reference is updated with a smooth turning trajectory for the tacking.

6.4 Summary

The larger tacking angles in the previous chapter showed that they can greatly reduce the pitching motion, but the NMPC can not operate in a binary fashion necessary to producing a tacking behavior about a desired path on its own. This chapter saw the introduction of the tacking planner to produce a tacking reference for the NMPC to follow. This novel method uses the dynamics stripped of their harmonics, and the tacking path to calculate the optimal tacking angle and velocity based upon the sea state and user-defined desired heading and velocity. Next chapter looks at the results of this control method in head seas.

Chapter 7

Head Sea Navigation

With the model and controller defined, and the tacking planner crafted, testing can begin. To provide context for the performance of the NMPC, the results are compared to the LOS PID controller found in (Fossen, 2011). This controller is robust and easy to implement, and because of this, forms the basis of many of the controllers found in use, as highlighted in the literature review. The the chapter begins with the formulation of the PID and the listing of the parameters used for the NMPC and PID. Initial testing of the controllers in their ability to path follow with no or minimal disturbances is shown. Next, the results are shown for the NMPC both path following and tacking for each of the desired headings and wave heights shown previously in the tacking planner chapter. This is compared to the results of the PID in the same conditions with a highlight of the 2.5 meter wave condition. Lastly, additional tests were performed to ascertain the robustness of the NMPC in a full sea state, as well as examining the results of other tests which implement wave forecast uncertainty and hardware restrictions to better simulate the difficulties that may be encountered when deploying the controller in real-world tests. Note that for the remainder of the thesis, the major wave direction travels from 270 degrees west to 90 degrees east in the NED frame. That means that a heading of 270 degrees indicates traveling directly into the waves. This chapter covers head and bow sea operation with headings from 270 to 210 degrees. The next chapter covers beam sea with headings from 210 to 150 degrees, and quartering and following seas with headings from 150 degrees to 90 degrees.

Table 7.1 list the wave parameters used this thesis. The wave heights are the same as those in the tacking planner. To gather the other parameters, SWEM was simulated with the wind vectors

TABLE 7.1: Wave parameters

	Wave Height					
Parameter	0.25 m	0.5 m	1.0 m	1.5 m	2.0 m	2.5 m
Wave Frequency	2.2 rad/s	1.7 rad/s	1.3 rad/s	1.1 rad/s	1 rad/s	0.9 rad/s
Wave Velocity	4.46 m/s	5.77 m/s	7.55 m/s	8.92 m/s	9.81 m/s	10.9 m/s
Wave Length	12.74 m	21.33 m	36.49 m	50.95 m	61.64 m	76.10 m

aligned, and the swell and fetch areas were increased until the desired significant wave height was reached. This produced a sea in which most wave components were traveling in a uniform direction creating a definable major wave direction. The first n-number of largest wave components whose amplitudes totaled to the desired wave heights were tabulated with their frequencies averaged. The vessel-wave dynamic tables in the simulation are indexed by wave frequencies rounded to the nearest tenth while the wave amplitude is simply a scaling factor of the output. Owing to this after all values were tabulated, the wave parameters were interpolated to calculate their values at the discrete wave frequencies. The resulting values are near those produced by the deep water theory with the parameters in table 7.1 having a slightly slower wave frequency than deep water theory suggest. The effort was made to calculate the wave components this way with a view towards future research in which only the largest wave components could be measured reliably, in which the research presented here could provide a baseline of performance for when a full sea state was implemented.

7.1 NMPC and PID Controller Tuning Parameters

This section details the LOS PID used in this thesis for comparison to the NMPC controller. The LOS PID used is that found in Fossen (2011) . For straight line paths where the heading error is:

$$\tilde{\psi} = \psi - \mathcal{X}_d + \beta_s, \tag{7.1}$$

where $\mathcal{X}_d$ is the course angle defined as:

$$\mathcal{X}_d(e) = \psi_d + \mathcal{X}_r(e), \tag{7.2}$$

and

$$\mathcal{X}_r(e) \coloneqq \arctan \frac{-e}{\Delta} \tag{7.3}$$

where e is the cross-track error and Δ is the lookahead distance. The sideslip angle of the is calculated as:

$$\beta_s = \arcsin \frac{v}{u} \tag{7.4}$$

The NMPC, because of the nature of the cost function, increases its velocity when there is a high cross-track error, to return to the path as quickly as possible. To create a similar behavior the PID was also tested with a cross-track error based speed compensator modeled as:

$$\tilde{u} = u - \big(u_d + (u_{\max} - u_d)(1 - \kappa_{\text{PID}}^{-|e|})\big), \tag{7.5}$$

where $\kappa_{\text{PID}} > 1$ is the tuning parameter to determine how quickly the reference velocity increases with increases in the cross-track error. This is a simplified method of Peymani and Fossen (2013).

The vessel was simulated with an initial condition away from the desired path for the smallest two wave heights, 0.25 m and 0.5 m and on a calm sea, to test the ability to reach the path. For this, the vessel starts with an initial cross-track error of 75 m with a heading that is parallel to the desired path. The path begins at (0,0) with an angle of ξ. With this the cross-track error for the NMPC is calculated as:

$$\tilde{y} = y_{\text{d}} - y, \tag{7.6}$$

where $y_{\text{d}} = x_d \tan(\xi)$. The 0.25 m waves were accompanied by a 1 m/s current in the major wave direction, while the 0.5 m waves had a 2 m/s current. Simulations were also conducted with an initial starting point at (0,0). These path following simulations were conducted to tune the PID controller and establish the baseline performance of the PID and NMPC controllers in a typical path following procedure, seen in most literature where there is no or minimal environmental disturbances. Table 7.2 shows the tuning weights used for the NMPC, as well as the PID tuning parameters. More details of the dual PID controller on the propellers can be found in (Heins et al., 2017).

As discussed in chapter 4, roll is not included in the cost function. Because the rudders can impart a larger moment in the roll direction than the waves in some cases, penalizing roll directly affects rudder actuation. Roll is a consequence of turning, even on a calm sea, and is not itself considered a negative effect. Though it is not included, roll is still an important consideration in regards to preventing capsizing, therefore a constraint of 15 degrees was imposed on the roll state to prevent excessive roll angles, but allow full rudder use.

TABLE 7.2: NMPC and PID tuning parameters

NMPC		PID		
Parameter	Value	Parameter	Symbol	Value
Surge Velocity Weight	1	Look Ahead Distance	LAD	20 m
Y position Weight (no tacking)	1	Heading Proportional	K_{P_H}	0.8
Y position Weight (tacking)	0	Heading Integral	K_{I_H}	0.01
Pitch Angle Weight	38.2	Heading Derivative	K_{D_H}	0.05
Yaw Position (no tacking)	2	Propeller Proportional 1	$K_{P_{P1}}$	4000
Yaw Position (tacking)	10	Propeller Integral 1	$K_{I_{P1}}$	500
Propeller State Weight	0.35	Propeller Derivative 1	$K_{D_{P1}}$	1500
Propeller Actuation Weight	0.001	Propeller Proportional 2	$K_{P_{P2}}$	1
Rudder Actuation Weight	0.1	Propeller Integral 2	$K_{I_{P2}}$	50
Heading Positive Constraint	360° N	Propeller Derivative 2	$K_{D_{P2}}$	0
Heading Negative Constraint	180° S	κ_{PID}		1.01
Prediction Time Step	0.05s	-	-	-
Prediction Horizon	300 steps	-	-	-
Prediction Length	15s	-	-	-

Figure 7.1 shows the performance of the PID controller, PID controller with speed compensator (PID_{sc}), and NMPC controller in a calm sea with no disturbances and with a single harmonic wave with a height of 0.25 m and a current of 1 m/s. The desired path is along the y-axis and the desired velocity is 4 m/s. With the knowledge that later testing would be performed exclusively with wave disturbances, the PID controller and PID_{sc} controller were tuned in the simulation with 0.25 m and a current of 1 m/s. This can be seen with no overshoot and quicker settling time in the 0.25 m wave case, however, both the calm sea and the 0.25 m wave sea have similar rise times for the PID controllers. The NMPC controller performs the same in both sea conditions and has a quicker settling time, 15 seconds, due to the higher overall velocity. While a larger κ_{PID} weight for the PID_{sc} controller can achieve a similar rise time to the NMPC controller, a κ_{PID} larger than 1.01 results in a constant oscillation around the path. This is a consequence of having the velocity change with the crosstrack error, which in turn directly affects the turning performance. This also shows the benefit of model based control on a multi-input multi-output system in which the performance of the actuation and the states of the system are tightly coupled. Figure 7.2 shows a zoomed in plot of the PID and NMPC controllers in a sea with 0.5 m wave and 2 m/s current, with a desired heading of 225 degrees. The PID controller has an RMS path error of 0.2602 meters, while the NMPC has a path error of 0.1434.

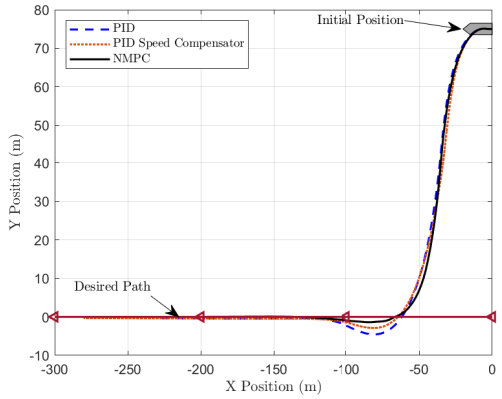

(a) Path following of the three controllers on a calm sea

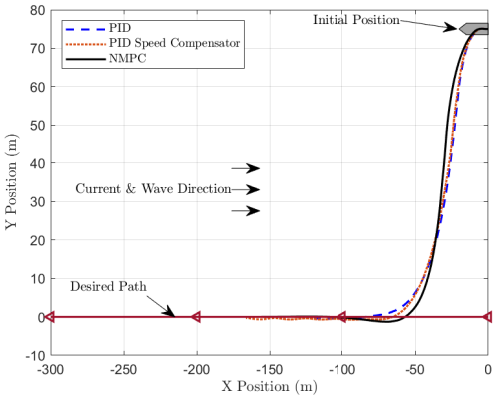

(b) Path following of the three controllers with 0.25m waves & 1 m/s current

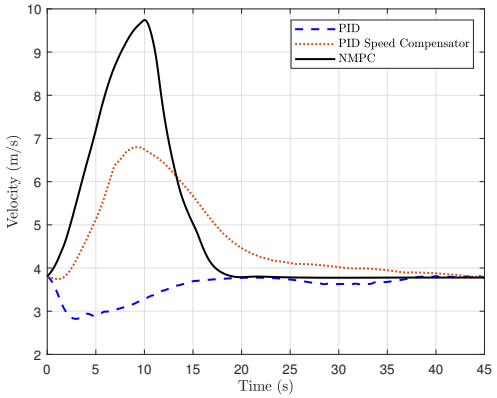

(c) Velocity of the three controllers on calm sea

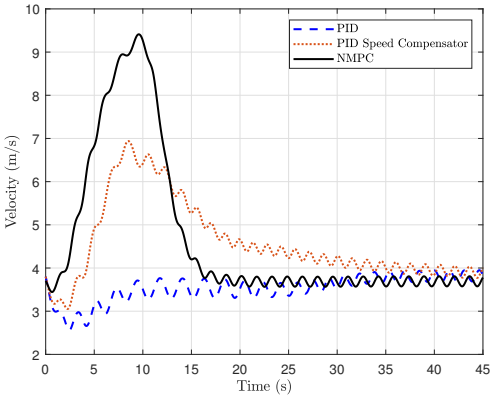

(d) Velocity of the three controllers with 0.25m waves & 1 m/s current

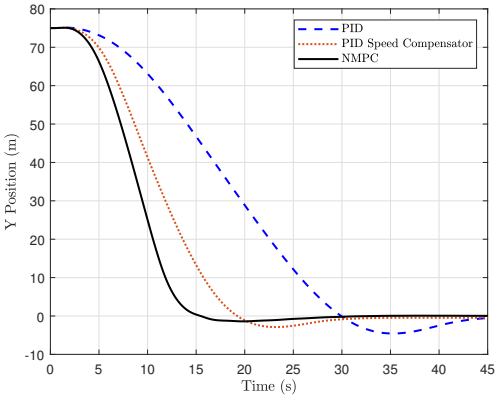

(e) Y position of the three controllers on calm sea

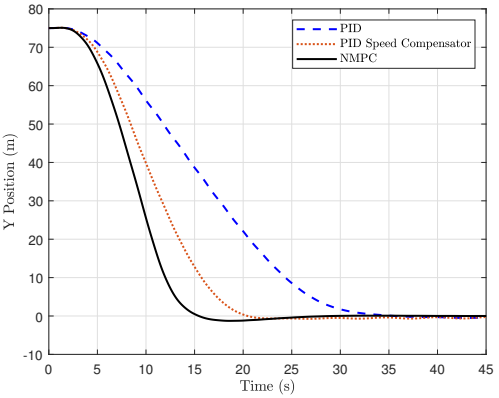

(f) Y position of the three controllers with 0.25m waves & 1 m/s current

FIGURE 7.1: Path following for NMPC and PID controllers on a calm sea and with 0.25m waves and 1 m/s current.

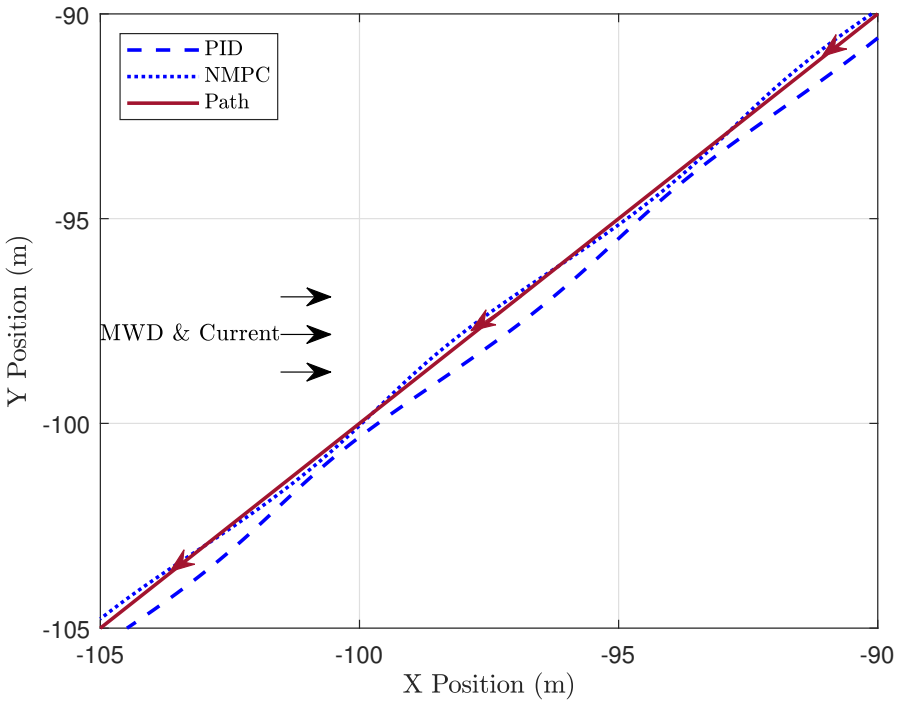

FIGURE 7.2: The path adherence of the PID and NMPC with 0.5 m waves and a 2 m/s current with a desired heading of 225 degrees.

7.2 Rough Sea Tests

To test the ability of the tacking planner and the NMPC controller to reduce wave-induced motions in rough seas, the vessel was simulated at each of the significant wave heights and desired headings presented in the previous section. The sea surface was comprised of a single harmonic with a wave height equal to that of the significant wave heights of the previous chapter. Current and wind forces are assume negligible. For the three highest wave heights, the vessel was simulated with the NMPC controller following the prescribed tacking angle, reaching the tacking boundary and tacking back, as well as without the tacking planner, where the NMPC controller followed the direct path. This was compared to the baseline PID control case approach which followed the direct path. The speed compensated PID controller was not used in these tests. All controllers use the same reference velocity of that calculated by the tacking planner. This is to test the ability of the controllers in similar scenarios. The prediction steps were 0.05 seconds with a prediction horizon of 300 steps, resulting in a prediction time of 15 seconds. To ensure more equitable comparison of the results, the additional propeller state penalty seen in Table 7.2 was added to keep the average velocity of the PID controller and NMPC similar. Without it, the average NMPC velocity may deviate from

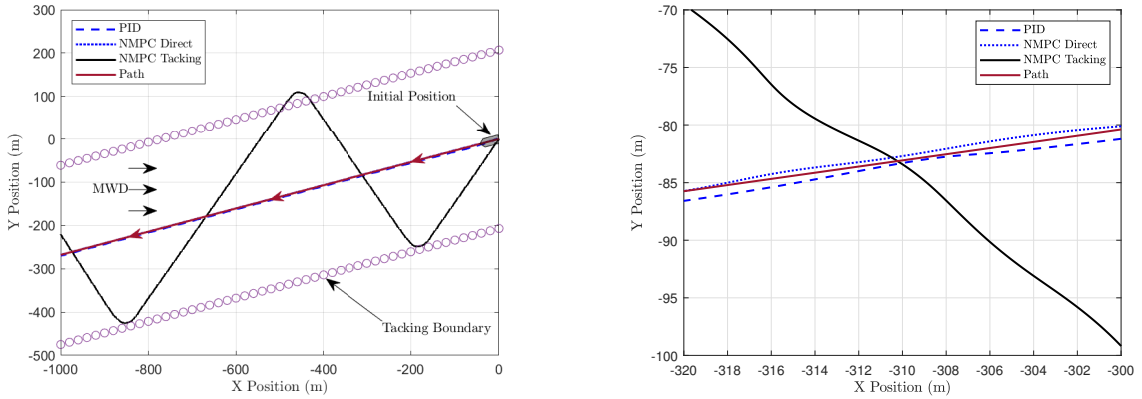

(a) The path of all three controllers with a desired heading of 255 degrees. Note that the tacking boundary is not a hard constraint and therefore the NMPC controller may go beyond these bounds during tacking.

(b) A zoomed plot of the three controllers showing the high frequency tacking of the NMPC tacking controller.

FIGURE 7.3: These figures show the PID and NMPC direct controllers following the tack, while the NMPC tacking controller tacks about the path.

the desired velocity in order to satisfy other terms of the cost function. This is a different approach than with the 1 DOF problem where the surge velocity was averaged over the prediction horizon. This penalty has the effect of worse performance in some aspects, such as pitch angle and reference velocity adherence, but with improvements in actuation effort reduction. It is the author's belief that the trade offs are worth the cost and are representative of how the system would be implemented on actual hardware where the performance reduction is justified by the improvement to the long-term durability of the engine.

Figure 7.3(a) shows the paths taken by the three controllers. For this figure, the desired heading was 255 degrees with a 2.5 meter wave. The vessel starts at the position (0,0), with the NMPC direct and PID controllers following the path, while the NMPC tacking controller tacks about the path. The tacking is handled by detecting if the final position of the vessel in the prediction horizon is beyond the tacking boundary. If it is, the final heading reference is changed to the opposite tacking angle. There is no constraint set at the boundary because the large wave forces could cause the vessel to violate them. This can be seen in the figure whereby the vessel moves past the boundary during tacking due to the larger angle between the boundary and the tacking path in one direction versus the other. Figure 7.3(b) shows a zoomed plot of the three controllers to highlight the small, high-frequency tacking of the NMPC tacking controller.

Figures 7.4-7.5 show the results for the three controllers in which the desired heading is 270 degrees,

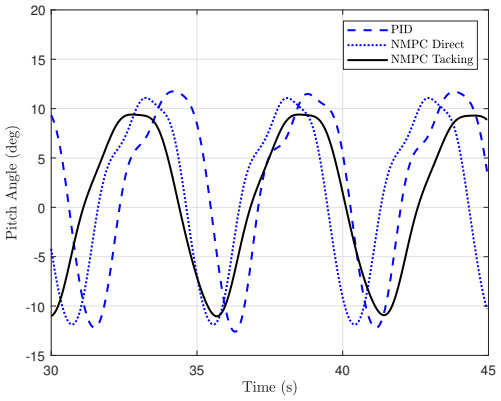

(a) The pitch angle of the 3 controllers with a desired heading of 270 degrees and 2.5 meter waves. Closed-loop pitch angle responses show reductions in pitching amplitude from both the NMPC tacking and NMPC direct controllers. The NMPC tacking controller is able flatten the pitch peak.

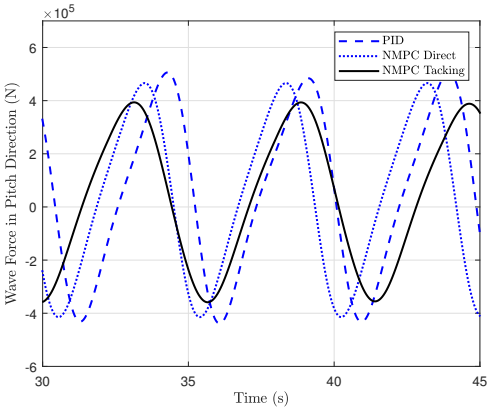

(b) The wave force in the pitch direction for the 3 controllers with a desired heading of 270 degrees and 2.5 meter waves. The NMPC tacking controller sees the lowest wave forces in the pitch direction.

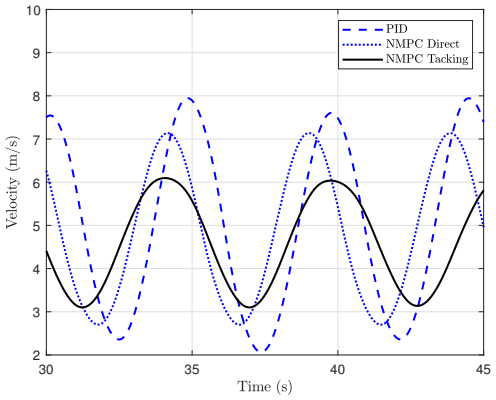

(c) The velocity profiles of the 3 controllers with a desired heading of 270 degrees and 2.5 meter waves. The lower wave force in the surge direction for the NMPC tacking controller allows for better adherance to the 4.7 m/s reference velocity.

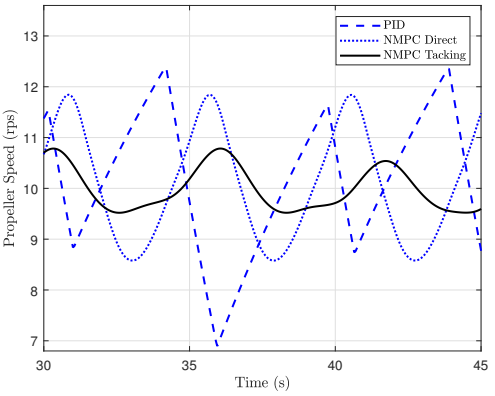

(d) The propeller speed of the 3 controllers with a desired heading of 270 degrees and 2.5 meter waves. The NMPC tacking controller is able to acheive better adherance to the reference velocity with lower actuation effort.

FIGURE 7.4: These figures show the performance of the three controllers in 2.5 meter waves.

which is directly into the waves, and a wave height of 2.5 meters. Figure 7.4(a) is the pitch angle for the three controllers. While following the direct path, the NMPC direct controller is still able to lower the pitching of the vessel compared to the PID controller. The tacking NMPC controller reduces the pitching further with a 20% reduction in the maximum pitch angle and a 12% reduction in minimum pitch angle. Part of the improvement of the pitch angle is due to the lower wave forces experienced in the pitch direction shown in figure 7.4(b). However, other factors such as propeller actuation in the pitch direction and the strong coupling with heave can have an effect on the pitch angle. Besides the higher encounter angle, the NMPC tacking controller has a lower peak velocity, shown in figure 7.4(c), to help achieve lower peak wave forces in the pitch direction. The

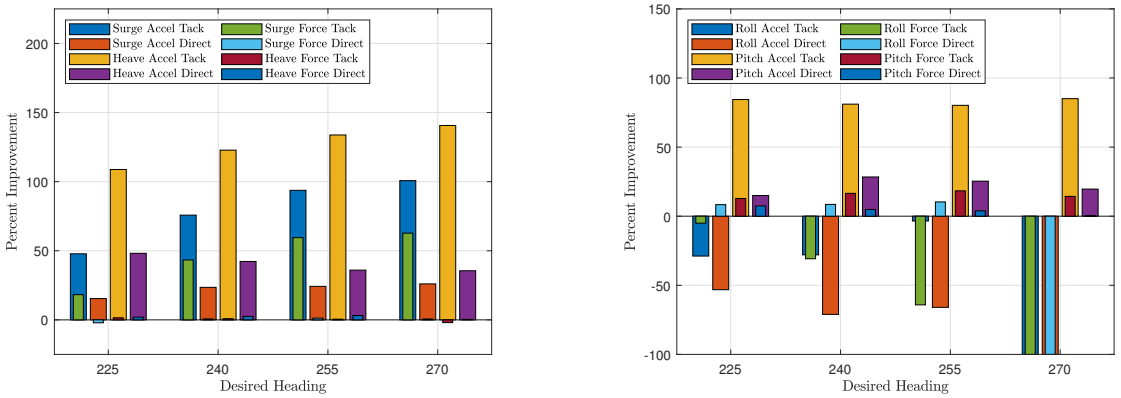

(a) Percent improvement in the surge and heave directions of the NMPC controllers over the PID controller in 2.5 meter waves.

(b) Percent improvement in the roll and pitch directions of the NMPC controllers over the PID controller in 2.5 meter waves.

FIGURE 7.5: Percent improvement of the NMPC controllers over the PID controller for force and acceleration in surge, heave, roll, and pitch.

NMPC direct controller also achieves a lower peak velocity compared to the PID controller. The PID controller experiences the largest range of velocities traveling through the waves with range of 6m/s. Having the lowest minimum velocity would seem to be a benefit for the PID controller in the goal of reducing the wave force in the pitch direction. However, the minimum velocity of the PID controller is achieved after the trough of the pitch wave force has passed. The PID controller actually has the highest velocity of the three when experiencing its peak pitch wave force in the negative direction. Figure 7.4(d) shows that the NMPC tacking controller is able to achieve these improvements with much lower actuation effort. Because of the higher wave forces in the surge direction when traveling directly into the waves, the NMPC direct controller needs to increase the actuation effort to try to maintain the desired velocity and reduce pitching. The large wave forces and reactionary nature of the PID controller sees it hitting the maximum slew rate of the engine. This type of actuation can damage the engine, worsen fuel consumption, and should be avoided.

Figure 7.5(a) includes the percent improvement over the PID controller of the root mean square of the accelerations and wave forces in the surge and heave directions. The percent improvement is calculated as:

$$\text{Percent Improvement} = \frac{\text{PID}_{\text{RMS}} - \text{NMPC}_{\text{RMS}}}{\text{NMPC}_{\text{RMS}}} \times 100 \tag{7.7}$$

Wave force is plotted because of the potential to cause damage either directly by the wave force imparted on the structure of the vessel or as a result of the wave-induced motions. There is a correlation between the wave forces and vessel accelerations, however, the vessel can actuate in

most DOFs directly, and in all of the DOFs indirectly through the dynamic couplings of the vessel, which can mitigate these accelerations. There are the fluid memory effects which can also mitigate the effects of the wave force, though these are unknown to the controller. These other forces mean that while the vessel may experience near identical wave forces with the different controllers, the accelerations can be vastly different.

Note that for the 2.5 meter wave height case, the reference heading and velocity of the NMPC tacking controller is the same, so the the results for all four headings are roughly similar. This means that changes in the percent improvement for the NMPC tacking controller are driven solely by the changes in the PID controller performance. In figure 7.5(a), as expected, the heave force is broadly similar for all three controllers so there is minimal, if no change, in the percent improvement for heave force with both the NMPC tacking and direct controllers. In spite of this, the NMPC tacking controller manages to see a reduction in heave accelerations of roughly 140% compared to the PID controller when the desired heading is 270 degrees, which trends down to 110% at 225 degrees. The surge accelerations follows the same pattern from 100 to 50%, though this is directly related to the reduction in wave force in the surge direction. The NMPC direct controller decreases its heave accelerations more than the PID controller, as the desired heading goes from 270 to 225 degrees resulting in a larger percentage improvement. Surge accelerations for the NMPC direct controller is more mixed with the improvements over the PID controller remaining at 20-25%.

Figure 7.5(b) shows the percent improvement for the roll and pitch DOFs. Improvements in accelerations in the pitch direction for the NMPC tacking controller are similar throughout. Again, the reference velocity and heading, and therefore results for all cases of the NMPC tacking, controller are the same. What this lack of change in relative performance shows then, is the PID controller does not reduce pitch accelerations as it increases its heading relative to the wave direction. There is also not an appreciable reduction in wave forces in the pitch direction for the PID controller. Similarly, the NMPC direct controller does not decrease its accelerations in the pitch direction as a result of its change in heading direction, and in fact decreases in relative performance at 225 degrees despite decreasing its relative wave force. For the NMPC direct controller, the necessity to also mitigate other reference errors, namely path following, is why pitch accelerations do not decrease. The increase in wave force in the sway and yaw directions requires more actuation to mitigate this. The NMPC tacking controller is less affected by this since heading adherence is less restrictive

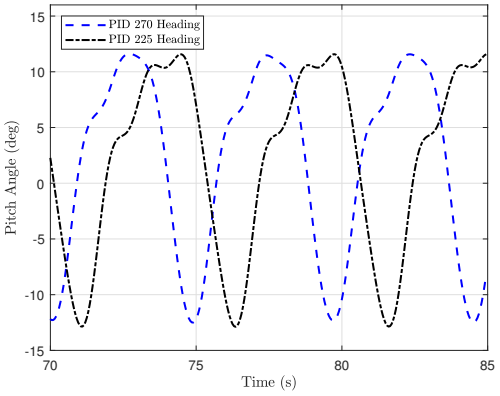

(a) The pitch angle of the PID controller with a heading of 270 and 255 degrees.

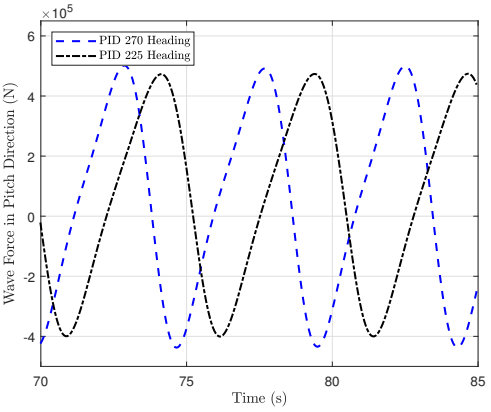

(b) The wave force in the pitch direction of the PID controller with a heading of 270 and 255 degrees.

FIGURE 7.6: Comparison of the pitch angles and wave force in the pitch direction for the PID controller with a heading of 270 and 225 degrees.

than path adherence. In the roll direction, both NMPC controllers have a 100% deterioration in acceleration and force RMS values at 270 degrees; that is they give rise to greater accelerations and forces compared to the PID controller, which does not experience any when heading directly into the waves. Roll is an interesting motion because it is the only one in which the actuation force from the vessel can far exceed the force from the waves at 2.5 meters. For these simulations, the maximum wave force in the roll direction is around 1.5 kn/m while the rudders can potentially produce 2 kn/m at 5m/s, and 5 kn/m at 8 m/s. Both NMPC controllers show this disparity. At 255 degrees, the NMPC tacking controller experiences a significantly greater wave force in the roll direction. However, it does not experience noticeably more acceleration in the roll direction. In contrast, the NMPC direct controller sees a reduction in wave force, but a much higher amount of roll acceleration because of the small tacks it performs on the individual waves.

As previously stated, the NMPC tacking controller has near identical performance for each desired heading, owing to the controller having the same reference heading and velocity. With this in mind, the lack of change in pitch accelerations by the PID controller seen in figure 7.5(b) means the PID controller does not improve with a larger wave encounter angle. The plots in figure 7.6 expand upon this with the pitch angle and wave force of the PID controller with a 2.5 meter wave and a heading of 270 and 225 degrees. In figure 7.6(a), the PID controller achieves marginally higher peak pitch angles as well as lower trough pitch angles when traveling at 225 degrees. This is in spite the fact that traveling at this angle reduces wave forces in the pitch direction. This again shows the benefit of predictive control, and having a controller with knowledge of the coupled dynamics.

TABLE 7.3: Average percent improvement for various parameters for both the direct and tacking NMPC over the PID. D=Direct, T=Tacking

Controller & Wave Cond.	Pitch Peak (%)	Pitch Trough (%)	Fuel Consumption (%)	Surge Accel. (%)	Heave Accel. (%)	Roll Accel. (%)	Pitch Accel. (%)	Time (%)
0.25m D	3.43	3.47	-0.85	11.37	4.53	66.16	3.40	-3.68
0.5m D	4.57	3.81	-2.61	12.72	5.52	-39.71	4.38	-3.24
1m D	4.48	6.74	2.17	20.82	16.35	-67.05	10.86	-3.45
1.5m T	11.31	8.52	-16.00	55.10	38.81	-73.96	27.35	-20.85
1.5m D	1.42	8.83	2.88	23.96	22.75	-77.72	12.39	0.23
2m T	10.00	6.56	-23.47	47.50	40.05	-65.70	28.82	-31.81
2m D	3.09	4.78	-1.79	1.66	11.56	-70.90	5.12	-3.95
2.5m T	16.04	12.25	-44.74	79.57	126.80	-39.97	82.70	-40.10
2.5m D	2.93	6.78	-20.40	22.63	39.92	-75.21	21.81	0.56

Table 7.3 shows the performance of the controllers for each wave height, averaged over the four desired heading angles. The 'D' represents the direct controller and the 'T' represents the tacking controller. The pitch peak refers to the average maximum pitch angle and the pitch trough refers to the average minimum pitch angle. The pitch angle is separated like this instead of using RMS, because as shown in figure 7.4(a), the two values can differ. Generally speaking, the improvements in the accelerations in the surge, heave, and pitch directions increase as the wave height increases. The roll accelerations, as mentioned earlier, are driven largely by the rudder actuation and, therefore, there is no discernible trend, though the NMPC controllers use more rudder actuation and as a result have higher motions in that direction. There is more improvement in the pitch peak angles throughout, than there is in the pitch trough angles for the tacking NMPC, while the reverse is true for the direct NMPC. The biggest improvement is with 2.5 meter waves, where the wave force is highest. Not surprisingly, fuel consumption for the tacking NMPC controller was 15-45% worse than the PID controller along the path. This trend tracks largely with the increased time required by the tacking NMPC controller to make the same progress along the path as the path following controllers. This increase is directly correlated with cosine of the tacking angle and, as such, there is a doubling of the extra time required when tacking at 58 degrees for the 2.5 meter wave case versus tacking at 45 degrees for the 1.5 meter wave case. Though the total time for the tacking NMPC is longer, the temporal fuel rate is lower with the percentage of additional fuel consumption lower than that of the percentage of additional time for the 1.5 and 2 meter waves. The NMPC direct controller had similar fuel consumption and time performance to the PID controller, with the

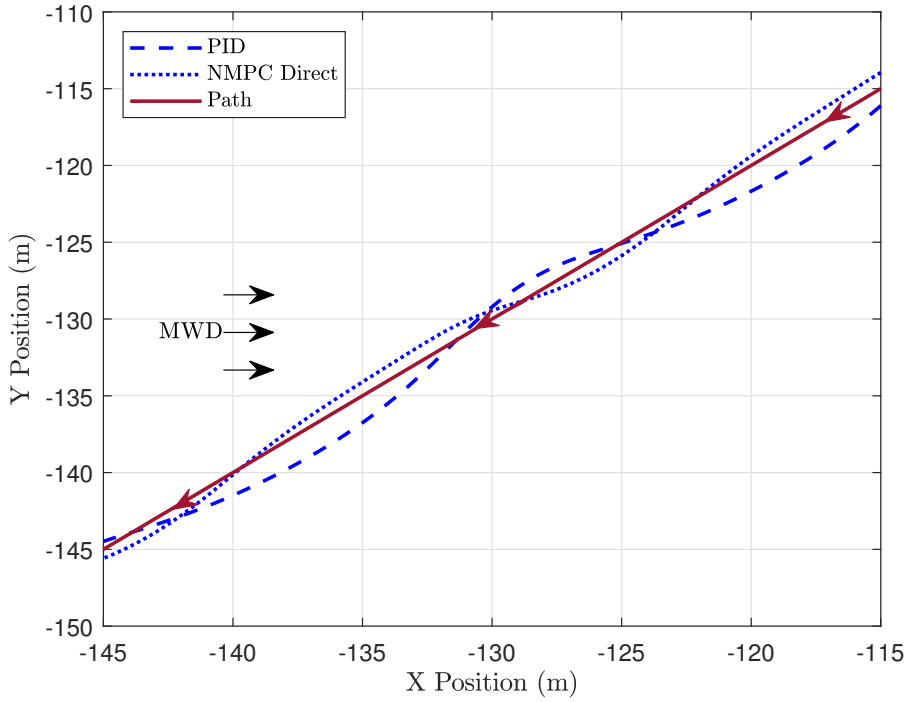

FIGURE 7.7: The path adherence of the NMPC and PID controllers in 2.5 meter waves with a desired heading of 225 degrees.

exception of the fuel consumption for the 2.5 meter case. The expression for fuel consumption was calculated using fuel rate data at steady engine speeds, and as with figure 7.4(d), the large changes in the engine speed could cause excessive fuel consumption so the PID controller may have higher fuel consumption than calculated.

Though the focus of this section is on mitigating wave forces and its resulting motions, the NMPC direct controller is still designed to follow a path. Though tacking with the NMPC controller provides the largest reduction in many of the wave forces and motions, situations may still arise in which tacking is not allowable, such as collision avoidance of a ship or object, or traveling in a busy shipping area. In these situations, the NMPC direct controller provides the benefits previously shown, while also providing better path adherence over the PID controller. Figure 7.7 shows the NMPC direct and PID controller following a path with 2.5 meter waves and a desired heading of 225 degrees. The NMPC controller has an RMS path error of 0.8 meters while the PID controller has an RMS path error of 1.5 meters. This follows the the trend seen earlier in figure 7.2 with the NMPC controller having half the path error as the PID.

Table 7.4 contains the results for all of the simulations to provide full context for the reader. One

TABLE 7.4: Percent improvement for various parameters for both the direct and tacking NMPC over the PID. D=Direct, T=Tacking

Controller & Wave Cond.	Pitch Peak (%)	Pitch Trough (%)	Fuel Consumption (%)	Surge Accel. (%)	Heave Accel. (%)	Roll Accel. (%)	Pitch Accel. (%)	Time (%)
0.25m 270° D	0.80	1.12	-2.92	8.44	-0.44	-100	-0.32	2.41
0.25m 255° D	4.04	4.32	-1.31	11.30	4.65	216.20	4.51	0.56
0.25m 240° D	3.89	3.71	0.38	4.58	6.97	133.58	5.52	-3.88
0.25m 225° D	4.99	4.76	0.46	19.61	12.73	14.47	6.54	-13.80
0.5m 270° D	4.23	3.53	-4.15	10.47	1.19	-100	3.06	2.81
0.5m 255° D	4.27	3.42	-3.66	10.64	3.07	-46.81	3.43	2.06
0.5m 240° D	4.16	3.78	-1.33	12.06	8.83	-28.97	4.75	-2.25
0.5m 225° D	5.62	4.52	-1.33	18.78	12.87	-2801	7.97	-15.58
1m 270° D	5.58	3.07	2.16	15.69	16.87	-100	9.49	-1.83
1m 255° D	6.32	3.72	0.51	17.75	19.96	-65.04	10.51	-1.76
1m 240° D	4.78	7.93	2.94	22.44	14.30	-55.98	10.57	-1.66
1m 225° D	1.23	12.25	3.06	30.60	13.99	-53.57	13.80	-8.52
1.5m 270° T	19.25	6.59	-28.67	69.39	39.09	-100	27.53	-27.21
1.5m 255° T	14.63	7.35	-22.67	60.73	39.05	-63.59	24.83	-22.87
1.5m 240° T	7.42	7.89	-17.13	57.68	44.52	-61.15	29.98	-21.21
1.5m 225° T	3.94	12.06	4.45	31.94	32.40	-67.94	27.22	-12.10
1.5m 270° D	3.60	3.75	1.36	18.75	18.41	-100	6.26	1.15
1.5m 255° D	0.97	6.24	3.64	19.82	22.06	-69.36	9.25	2.16
1.5m 240° D	-1.5	10.16	3.87	26.89	24.72	-76.01	13.52	2.46
1.5m 225° D	2.58	15.16	2.64	34.02	26.71	-73.61	22.34	-4.85
2m 270° T	16.24	4.67	-33.73	56.92	38.15	-100	34.79	-32.17
2m 255° T	13.7	3.33	-25.68	44.89	34.89	-45.86	24.71	-29.38
2m 240° T	7.87	6.73	-16.91	39.67	36.91	-63.6	23.03	-26.62
2m 225° T	2.2	11.51	-17.57	48.73	53.73	-42.37	33.29	-39.07
2m 270° D	10.01	9.58	-8.67	-2.26	16.32	-100	5.37	-4.02
2m 255° D	5.42	-0.37	4.62	-3.16	9.44	-52.24	2.57	-3.88
2m 240° D	2.39	3.73	5.86	0.02	11.67	-68.64	8.17	-2.86
2m 225° D	-5.46	6.18	-8.98	18.17	8.52	-63.2	4.66	-5.06
2.5m 270° T	19.23	11.11	-45.16	100.75	140.66	-100	85.06	-47.8
2.5m 255° T	17.15	11.45	-44.14	93.73	133.77	-3.46	80.24	-45.9
2.5m 240° T	13.94	13.39	-46.81	75.79	122.8	-27.97	81.1	-39.69
2.5m 225° T	13.85	13.05	-42.84	47.78	108.79	-28.84	84.42	-27.02
2.5m 270° D	4.36	4.38	-18.91	26.02	35.52	-100	19.62	0.92
2.5m 255° D	3.14	5.8	-17.7	24.24	35.99	-65.95	25.37	1.92
2.5m 240° D	1.7	9.78	-20.59	23.53	42.27	-71.05	28.39	2.17
2.5m 225° D	2.52	7.15	-24.41	15.39	48.17	-53.18	14.97	-2.78

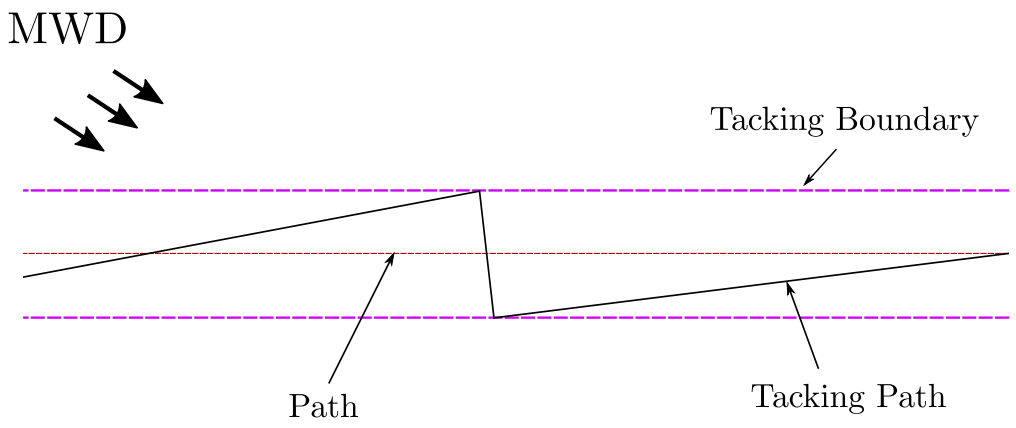

FIGURE 7.8: The tacking path for a desired heading with a large angle to the major wave direction.

note of interest is the decrease in the fuel consumption and time-to-destination for the tacking NMPC as the desired path moves from 270 to 225 degrees. This is in spite of the fact that as the angle between the desired path and the major wave direction increases, the angle between the opposite tack angle and the path increases. Figure 7.8 shows an example of this. With extreme tacking and path angles, the opposite tack back across the path can actually regress along the path. It would, at first, seem that this would drastically increase fuel consumption and time, however, as can be seen in figure 7.8, the steep angle across the path for the opposite tack means only a small proportion of the total travel time is spent moving in this direction.

7.2.1 Additional Position and Acceleration Plots

With the general performance of the 3 controllers discussed, we move on to more closely examine the acceleration of the vessel, as well as the roll angle. The biggest improvement of the tacking NMPC over the PID controller was in heave acceleration. This is more surprising given that the wave force experience in the heave direction is nearly identical for all headings and velocities as shown in figure 7.5(a), and there is no actuation force in the heave direction. Figure 7.9(a) shows the heave acceleration over time for the 3 controllers for the 2.5 meter waves with a desired heading of 270 degrees. While the NMPC tacking controller sees acceleration of ± 1 m/s^2, the PID controller experiences upwards of -3.5 m/s^2 with a change in acceleration, known as jerk, of up to 0.5 m/s^3. The primary driver for the differential in the heave acceleration is the coupling between heave, and the pitch position and velocity as seen in (3.21). Though actuation can not be achieved in the heave direction, and the wave force in the heave direction can not be mitigated by manipulation of the

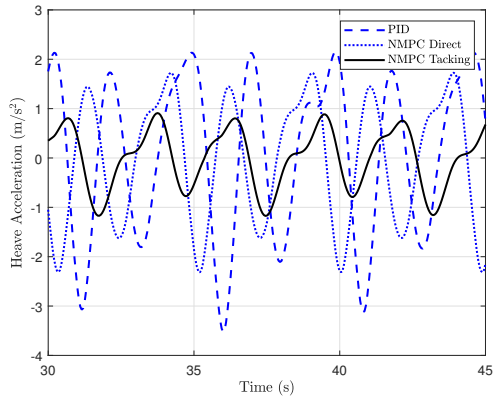

(a) Heave acceleration for 2.5 m waves and desired heading of 270 degrees.

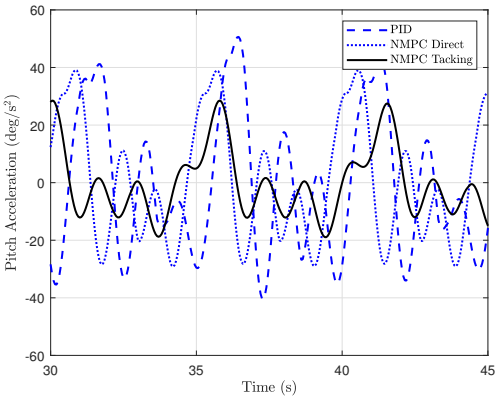

(b) Pitch acceleration for 2.5 m waves and desired heading of 270 degrees.

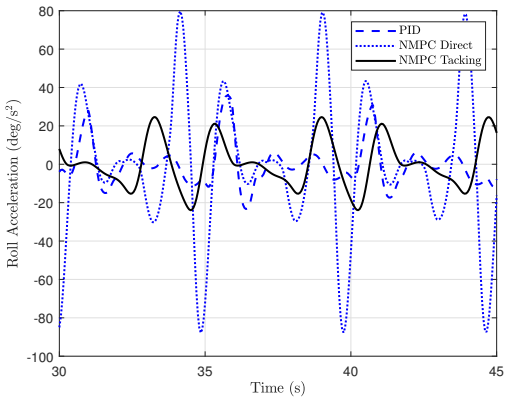

(c) Roll acceleration for 2.5 m waves and desired heading of 255 degrees.

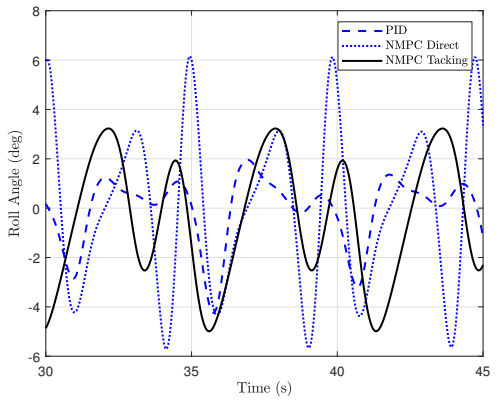

(d) Roll angle for 2.5 m waves and desired heading of 255 degrees.

FIGURE 7.9: Plot of heave and pitch accelerations for 2.5 m waves and a desired heading of 270 degrees. The roll plots depict the results for a desired heading of 255 degrees.

velocity or heading, heave accelerations benefit greatly from the reduction in the pitch position and velocity. The pitch accelerations are included in figure 7.9(b), where the NMPC tacking controller has the lowest acceleration as well.

For figures 7.9(c), and 7.9(d), the results from the 255 degree desired heading simulations were used. This is to show results in which the PID controller actuates the rudder. Figure 7.9(c) plots the roll acceleration of the 3 controllers with the NMPC direct controller showing the highest roll accelerations as it tacks quickly over each wave to reduce the pitch angle. The PID and NMPC tacking have similar roll accelerations, with the PID experiencing higher positive accelerations and the NMPC tacking experiencing higher negative accelerations. The roll angles in figure 7.9(d) follows the same pattern with the higher roll accelerations of the NMPC direct controller resulting in higher roll angles. The NMPC tacking controller has slightly higher roll angles than the PID,

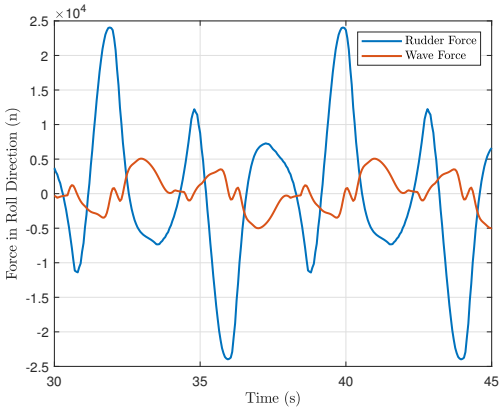

(a) Roll force from rudder actuation compared to wave force at 255 degrees for the NMPC direct controller.

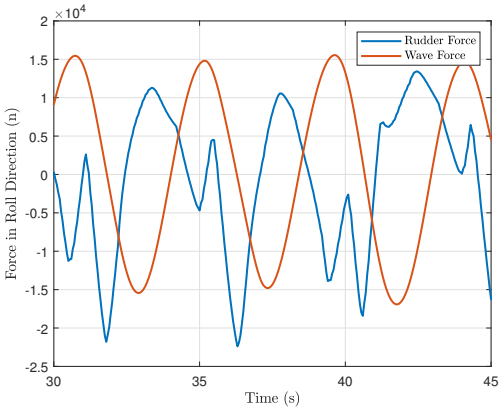

(b) Roll force from rudder actuation compared to wave force at 212 degrees for the NMPC tacking controller.

FIGURE 7.10: A comparison of the roll force from the rudder versus the wave for the NMPC direct controller at 255 degrees and the NMPC tacking controller at 212 degrees.

despite similar roll accelerations due to the increased wave force in the roll direction at 270 degrees versus the PID heading of 255 degrees. Despite the high roll accleration for the NMPC direct controller and the higher wave force in the roll direction from the wave for the NMPC tacking controller, all roll angles are well below the roll constraint of 15 degrees.

Despite having a shallow angle to the major wave direction and, therefore, a relatively small wave force in the roll direction, the NMPC direct controller has the highest roll accelerations in figure 7.9(c). Figure 7.10(a) shows that the cause is the rudder actuation. The high-frequency tacking that the NMPC direct controller performs in order to increase the encounter angle to the wave results in a roll force from the rudder that is 500% higher than from the wave itself. For the NMPC tacking controller traveling with a heading of roughly 212 degrees, with less aggressive rudder action, the rudder and wave impart nearly equivalent force to the vessel in the roll direction as seen in figure 7.10(b). The rudder force in the roll direction for the NMPC direct controller is higher even than the wave force experienced by the NMPC tacking controller. This becomes more pertinent in the next chapter when wave force in the roll direction increases in beam seas.

7.3 Full Sea State

The previous simulations were conducted in a wave environment containing a single wave harmonic, with full information of this made available to the controller. However, the wave spectrum is

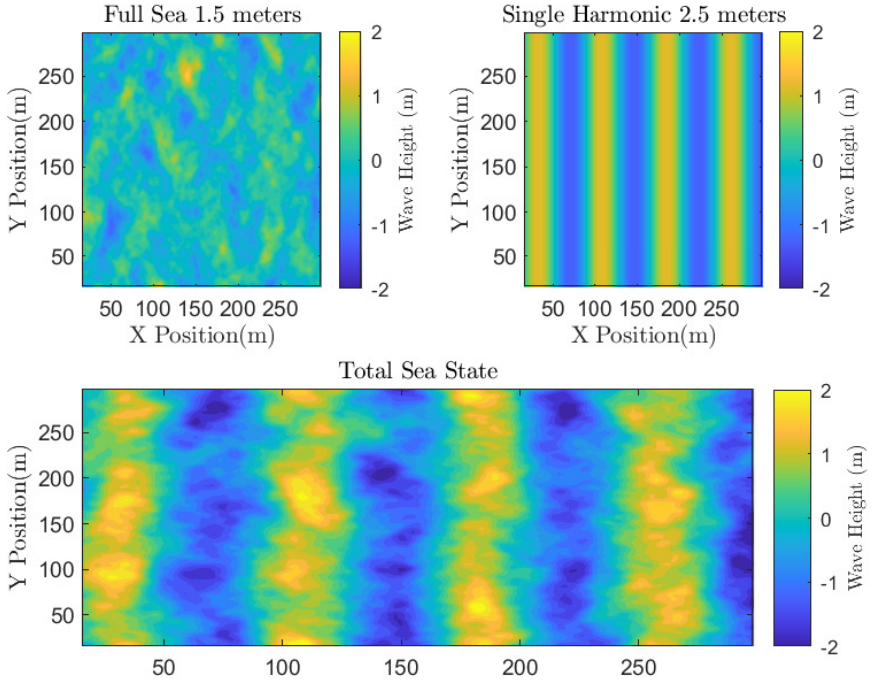

FIGURE 7.11: A full SWEM sea state at 1.5 meters and a single harmonic at 2.5 meters. The bottom figure shows the resulting combination of these two.

panchromatic. In principle, the controller methodology outlined in this thesis could be extended to include all of the wave harmonics, although this would come at the price of increasing numerical complexity for the extra terms. Additionally, this would assume availability of information of these harmonics from available sensing and deterministic sea-wave predictions - which is clearly a more challenging problem than identifying the waves in a monochromatic sea. It is nonetheless a valid question to ask to what extent the single-wave controllers assumed in this thesis will perform upon more realistic sea states. To test the effect of unmodeled waves on the ability of the NMPC controller to reduce the pitch angle of the vessel as before, a full sea state of various significant wave heights was superimposed on the single 2.5 meter wave harmonic. The highest of these was a sea state with a significant wave height of 1.5 meters. Figure 7.11 shows the superposition of this sea state with the single harmonic 2.5 meter wave. The resulting sea state still bears much of the characteristics of the single wave harmonic, though the added full sea causes the total sea state to occasionally produce waves which measure roughly 4 meters. Note that this is not the same full sea states as produced to gather the wave parameters discussed at the beginning of the chapter. This is a confused sea state as can be seen in figure 7.11.

TABLE 7.5: Pitch angle averages in full sea state

Parameter	NMPC Tacking (deg)	NMPC Direct (deg)	PID (deg)
Average Pitch Peak Angle	10.36	14.78	18.17
Average Pitch Trough Angle	9.97	15.32	17.65
Pitch Peak Max Angle	12.69	20.78	23.72
Pitch Trough Max Angle	15.82	21.76	21.86

The 3 controllers were simulated in this environment with a desired heading of 270 degrees. The reference heading and velocity of the controllers were the same as those for the monochromatic 2.5 meter wave environment. The resulting pitch angles of the three controllers are shown in figure 7.12(a). As before the NMPC tacking controller has the lowest magnitude pitch angles of the three. The added full sea state means that the NMPC tacking controller, with its tacking path, does not experience precisely the same wave conditions as the PID and NMPC direct controllers. While this makes it more difficult to make a direct comparison on a per wave basis, it is worthy to note the maximum and minimum pitch angles of the NMPC tacking controller are much lower of not only the maximum and minimum pitch angles but also the average maximum pitch angles and average minimum pitch angles of the PID controller as seen in Table 7.5. In figure 7.12(a), the NMPC direct controller is a few seconds advanced of the PID controller, but shows generally lower pitch angles. This is seen in Table 7.5 where the NMPC direct controller has lower maximum and average angles compared to the PID controller, though the trough minimum angles are similar.

The roll angles of the three controllers are shown in figure 7.12(b). Though the desired heading is 270 degrees, which usually sees the PID controller experience no rolling, the full sea state results in wave forces in all directions which in turn results in the PID controller experiencing roll from the wave force, but also from the rudder actuation needed to maintain its course. Both NMPC controllers have much higher roll angles as they have large rudder actuations to maneuver around the larger waves, though neither violate the roll constraint. Figures 7.12(c) and 7.12(d) show the pitch and heave accelerations the vessel had. Again, the NMPC tacking controller had the lowest acceleration of the three for both pitch and heave. What is notable is the magnitude of the accelerations of the NMPC direct and PID controllers compared to the NMPC tacking controller. The NMPC direct controller has the highest heave acceleration at -10 m/s^2, with the PID closely behind at -9 m/s^2. For humans, these accelerations are not near the damage inducing ones seen in Hodgson et al. (1963), but they are close to encroaching on some recommended limits for human-ridden

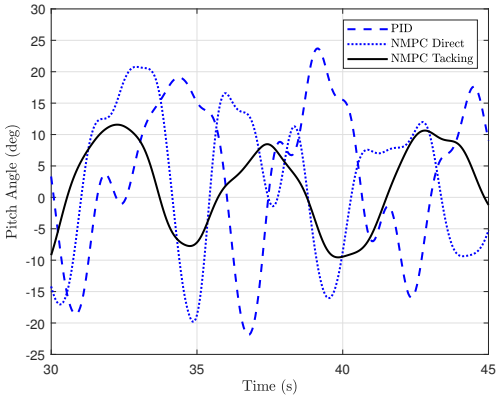

(a) The pitch angles of the three controllers for the 1.5 meter SWEM sea imposed on the 2.5 meter single harmonic.

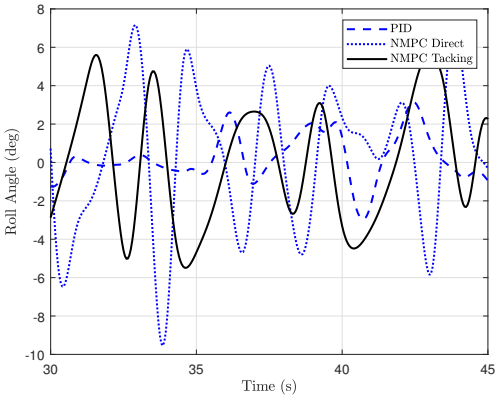

(b) The roll angles of the three controllers for the 1.5 meter SWEM sea imposed on the 2.5 meter single harmonic.

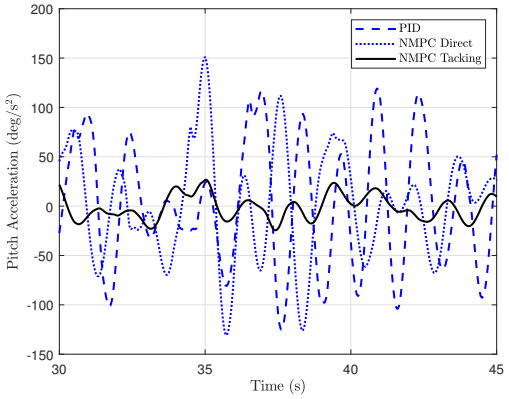

(c) The pitch accelerations of the three controllers for the 1.5 meter SWEM sea imposed on the 2.5 meter single harmonic.

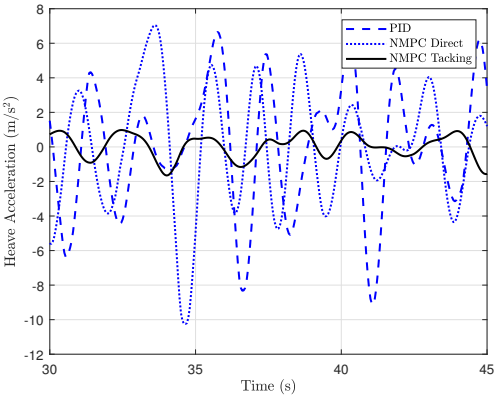

(d) The heave accelerations of the three controllers for the 1.5 meter SWEM sea imposed on the 2.5 meter single harmonic.

FIGURE 7.12: Plot of angles and accelerations of the vessel with a 1.5 meter full sea state imposed on a 2.5 meter harmonic.

equipment, such as roller coasters, set in ISO standard 17929, as discussed in (Eager et al., 2016; Pendrill and Eager, 2020).

Besides the pitch angle and pitch and heave accelerations, another aspect the PID controller had difficulty in for the full sea state simulations was surge velocity management. Figure 7.13 highlights this. First with figure 7.13(a), we can see the PID controlled vessel dipping below 0 m/s, while the NMPC controllers maintain a positive velocity. The NMPC controllers have a constraint to maintain forward velocity and positive propeller speeds. Further investigation shows what appears to be integral windup of the PID controller in the propeller plots in figure 7.13(b). Again, the NMPC controllers maintain their velocities with sensible propeller actuation, despite waves occasionally being twice as large as predicted. Figure 7.13(c) shows the PID controlled vessel being forced

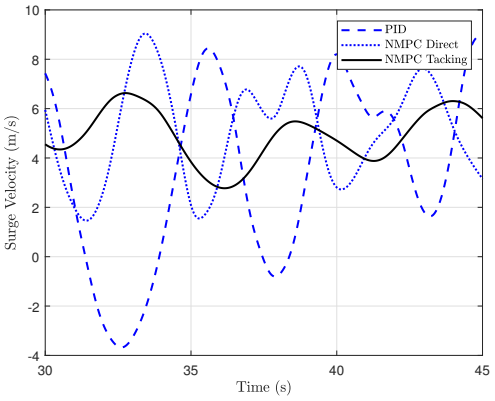

(a) Surge velocity of the three controllers for the 1.5 meter SWEM sea imposed on the 2.5 meter single harmonic.

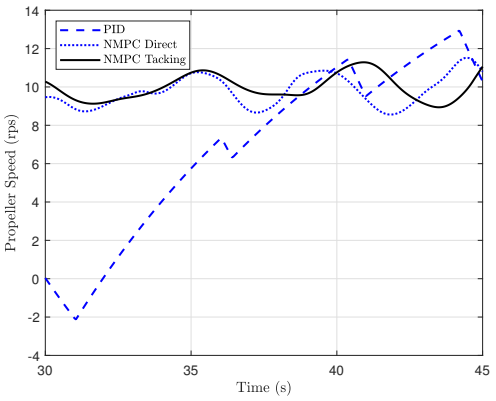

(b) Propeller speed of the three controllers for the 1.5 meter SWEM sea imposed on the 2.5 meter single harmonic.

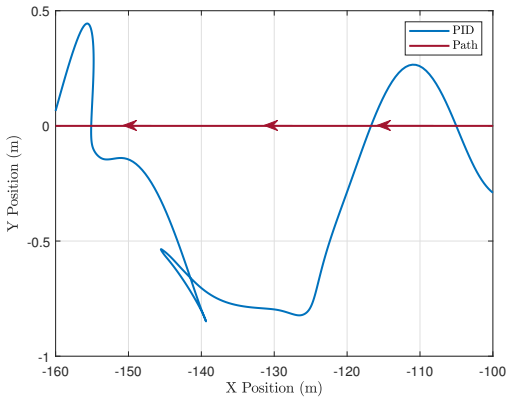

(c) Position of the PID controller for the 1.5 meter SWEM sea imposed on the 2.5 meter single harmonic.

FIGURE 7.13: Plots showing the difficulties the PID controller had in maintaining a positive surge velocity in a sea state composed of a 1.5 meter SWEM sea imposed on a 2.5 meter single harmonic.

back about 7 meters. This backwards motion occurred a few times on this simulation. This is a dangerous scenario and is why the tacking planner includes estimation on the effect of the waves on surge velocity. Larger waves require higher average surge velocity to maintain momentum. Most surface vessels are not designed to move backwards at these velocities. They are shaped to move forwards through the water. Vessels with low sterns run the risk of water ingress, and rudder effectiveness is dependent on the vessel velocity.This means after the vessel is forced backwards, it may not have enough time to accelerate forward to regain steering and avoid the next wave.

Gain scheduling for the PID controller may improve the performance of the PID in rough seas, as it was originally tuned for 0.25 meter waves. This still presents the problem that the PID is effectively blind to the disturbances. Linear MPC has been increasing in use, as noted in the literature review, though often limited to 3 DOF. To test how a controller with knowledge of the waves, but not

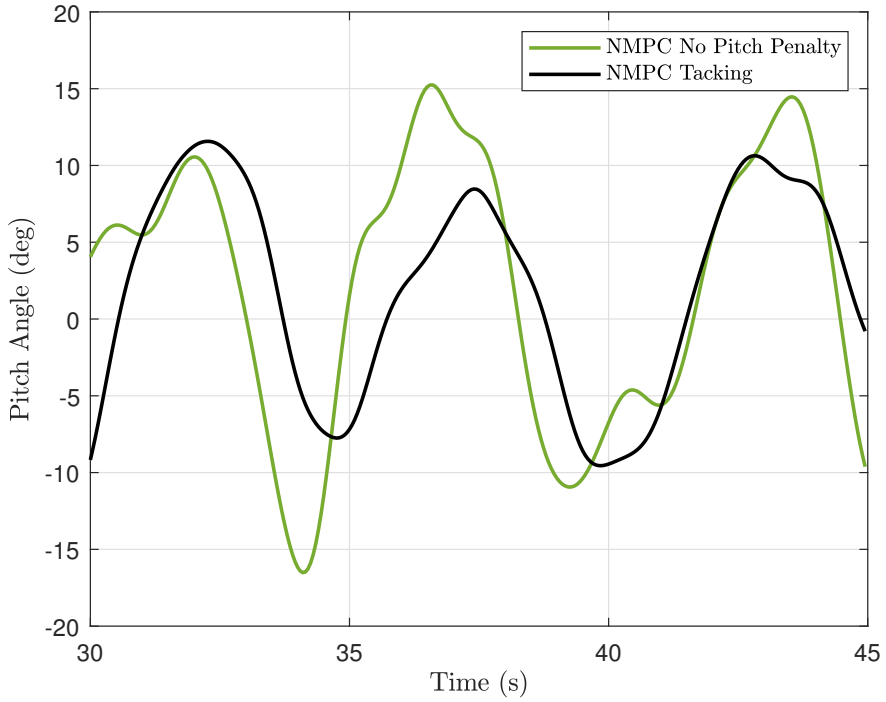

FIGURE 7.14: Comparison of the NMPC tacking controller with and without a penalty on the pitch angle term, simulated in a sea state composed of the 2.5 meter single harmonic and 1.5 meter full sea state.

designed to limit pitch angles would fare, the pitch angle penalization weighting term was removed. The controller retained knowledge of all 6 DOF. This controlled vessel was then simulated in the same 2.5 meter single harmonic with a 1.5 meter full sea state scenario. Figure 7.14 shows that without prioritizing for it, the NMPC can have worse performance in the pitch angle. Knowledge of the waves is not sufficient, if the controller is not designed to penalize large pitch angles. It should be noted, however, that wave force in the surge and pitch direction share the same characteristic, that larger encounter angles decrease the magnitude of the force. A 3 DOF MPC controller adhering to a reference velocity may show a similar tacking maneuver, as seen through this thesis, to reduce wave force in the surge direction in a head sea, and as a consequence, may benefit from reduced pitch angles.

These results show that with only knowledge of the larger harmonic behavior of the sea, the NMPC direct controller still provides a benefit over the PID controller. Further, the pitch results reinforce the earlier results of the monochromatic seas that the tacking planner, in conjunction with the NMPC controller provides a superior method of traversing in a rough sea state.

7.4 Towards Implementation

The first simulations assumed perfect knowledge of the wave harmonic, while further testing added a full sea state to better simulate actual sea surface conditions. Other questions remain as to effective implementation of the controller on hardware where further constraints can affect performance. One of these is modeling and predicting the wave harmonics. Even in simulations, such as SWEM, there are hundreds of wave harmonics simulated. Most of these are higher frequency, low amplitude waves, which have little effect on the vessel and are unlikely to be fully captured by sensing hardware. However, this still leaves a large number of wave harmonics that can affect the performance of the vessel. It was shown previously that even without knowledge of the 1.5 meter full sea state, the NMPC still outperforms the PID controller, but it is easy to speculate that had the NMPC had knowledge of the higher wave peaks and troughs, it could maneuver to avoid these and reduce the pitch angles further. Fully modeling each of these larger wave harmonics would be computationally burdensome because of the inclusion of the high-order polynomial surfaces describing the force and phase RAO imposed by each harmonic. Many of these force and phase RAOs share similar surface characteristics between the various wave heights, so the question is: can the sea surface harmonics be modeled separately to provide a description of the anticipated wave heights over the course of the prediction horizon with the effect of the wave heights being described by only one set of force and phase RAOs? The amplitude of the waves for the prediction horizon is calculated as the sum total of all of the wave amplitudes shown as:

$$A_{\text{Total}} = \sum_{i=1}^{N} \sum_{j=1}^{M} A_{\mathsf{k}_i,\vartheta_j} \cos\Big(\omega_e\big(\omega_i, \beta_j, U(t)\big)t\Big). \tag{7.8}$$

The total wave force in each DOF is now calculated as:

$$\tau_{\text{Total}}^{\text{dof}} = \rho_{\text{w}} g \Big| F_{\text{wave}}^{\{\text{dof}\}}\big(\omega_{\text{C}}, \beta, U(t)\big)\Big| A_{\text{Total}} \cos\Big(\omega_e\big(\omega, \beta, U(t)\big)t + \angle F_{\text{wave}}^{\{\text{dof}\}}\big(\omega_{\text{C}}, \beta, U(t)\big)\Big), \tag{7.9}$$

where the force and phase RAO surfaces are constant as denoted by the 'C' subscript and are chosen a priori.

To test this, the vessel was simulated with a 2.5 meter single harmonic wave using the RAOs for a 1 meter wave, with a 1.5 meter single harmonic wave using RAOs for a 1 meter wave, and with

a 1 meter single harmonic wave using the RAOs for a 2.5 meter wave. First is the simulation of the NMPC controller in a 2.5 meter wave harmonic using the 1 meter wave RAOs. The RAOs are multiplied by the 2.5 meter amplitude to estimate the 2.5 meter wave force. The NMPC controller was simulated with a desired heading of 270 degrees and compared to the original tacking NMPC using the correct 2.5 meter RAOs. The pitch angles in figure 7.15(a) look promising, with only a slight increase in the maximum angle, but as can be observed, the results are out of phase. This is because the NMPC controller with the 1 meter RAOs is taking a larger average tacking angle than the original seen in figure 7.15(b). This leads to a large discrepancy in the path compared to the NMPC tacking controller with the 2.5 meter RAOs in figure 7.15(c). The RAO surface shapes and magnitude differ slightly for the different wave heights, causing the predictions in this case to be lower than the actual wave force. This underestimation results in lower predicted actuation necessary to maintain course, and coupled with the corrective feedback resulting from the underestimated pitch angles has the combined effect of a larger average tack. Figure 7.16 has the results of the NMPC controller using the RAOs for 1 meter waves simulated over 1.5 meter waves. The same phenomenon seen in the figure 7.15 also appears here, though to a lesser degree. The pitch angles in 7.16(a) are similar in magnitude with a smaller phase difference than seen previously. The heading angles in figure 7.16(b) are near identical in magnitude, resulting in a similar path in figure 7.16(c). So the NMPC controller using the 1 meter RAOs has similar performance in 1.5 meter waves to that of the NMPC controller using the correct 1.5 meter RAOs. To determine whether using the RAOs for a certain wave height are only valid for a small range of wave heights near it, we now look at the reverse of the first example.

Using the RAOs for 2.5 meter waves, the NMPC controller is simulated with a 1 meter wave harmonic. The phase difference in figure 7.17(a) is smaller than in the first two examples. Overestimated yaw force results in higher magnitudes for the heading angles in figure 7.17(b), though only by a couple of degrees, and this has no effect on the resulting path that the NMPC controller takes in figure 7.17(c). These initial results suggest that using the RAOs of a single wave height to give a good estimation of future wave forces is possible. They also suggest that using a RAOs which slightly over estimate the predicted wave force fare better than ones which underestimate, though these are only initial findings and thorough testing of all the RAOs at each wave height would be needed to confirm it.

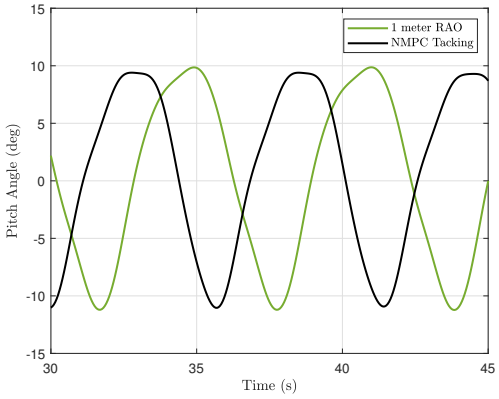

(a) Pitch position in a 2.5 meter wave with the RAOs for a 1 meter wave.

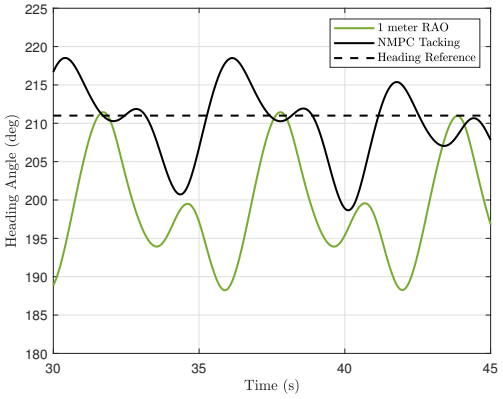

(b) Heading angle in a 2.5 meter wave with the RAOs for a 1 meter wave.

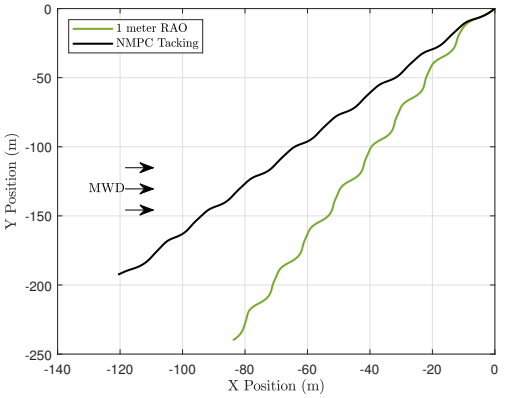

(c) Position in a 2.5 meter wave with the RAOs for a 1 meter wave.

FIGURE 7.15: These figures show the NMPC controller with the RAO surfaces for 1 meter waves simulated over 2.5 meter waves as compared to the NMPC controller with the correct 2.5 meter wave RAOs

Besides efficiently estimating the waves and subsequent wave forces, another question for the practical implementation of the controller is the required step size and total length of the prediction horizon. The typical requirements predictive control of the prediction horizon is that it should be long enough to fully capture the entirety of the major dynamics, in this case a complete harmonic cycle, and the step size should be sufficiently small as to provide effective actuation points over the course of the major dynamics. A step size significantly larger than the span of a wave harmonic means a constant input for several wave harmonics, rendering the controller unable to actuate about them. Conversely, too small of step sizes, or overly long prediction horizons prevent the necessary computations to be completed before the next iteration. Two wave conditions were used to test these requirements, the 2.5 meter wave harmonic with the NMPC tacking controller to provide an example of a long wave harmonic, but low frequency, and the 0.5 meter wave harmonic with the

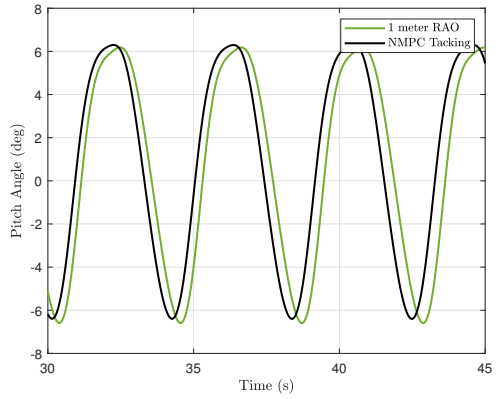

(a) Pitch position in a 1.5 meter wave with the RAOs for a 1 meter wave.

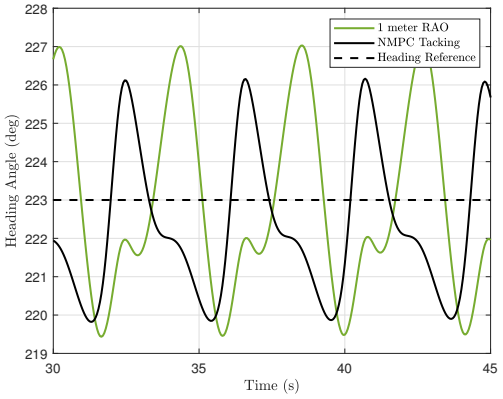

(b) Heading angle in a 1.5 meter wave with the RAOs for a 1 meter wave.

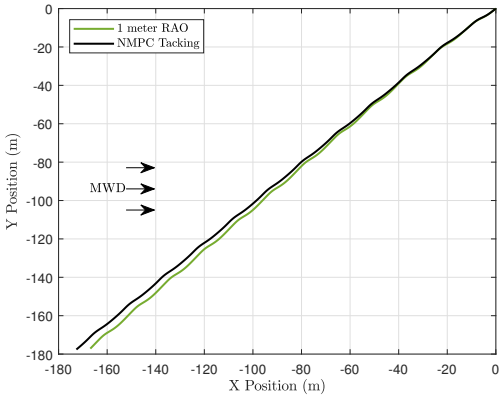

(c) Position in a 1.5 meter wave with the RAOs for a 1 meter wave.

FIGURE 7.16: These figures show the NMPC controller with the RAO surfaces for 1 meter waves simulated over 1.5 meter waves as compared to the NMPC controller with the correct 1.5 meter wave RAOs

NMPC tacking controller for a short wave harmonic, but high frequency. These were both tested with a step size of 0.05 seconds for a prediction horizon length of 12, 10, 7.5, 5, and 2.5 seconds. This was compared to the original 15 second horizon. Then they were tested with a prediction horizon length of 15 seconds, but step sizes of 0.1, 0.15, 0.2, 0.25, 0.3, 0.35, 0.4, 0.45, and 0.5 and compared to the original step size of 0.05 seconds.

First Table 7.6 has computation times for the various horizon lengths and step sizes. This thesis is not concerned with efficient implementation of the RTI NMPC, for that readers are encouraged to look at other sources such as (Kirches et al., 2012; Villarreal, 2021; Gonzalez Villarreal and Rossiter, 2020). The table is provided to give the reader context on the effect horizon length and step size have on the iteration time. Figure 7.18 shows the perfomance of the NMPC tacking controller in

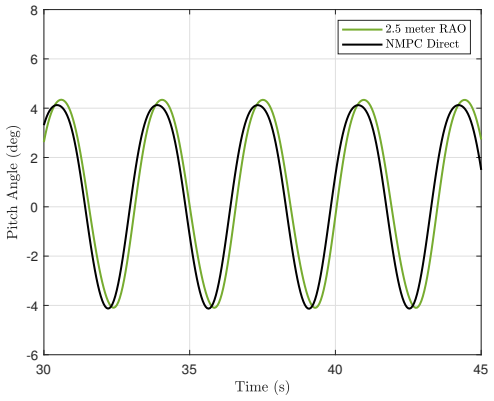

(a) Pitch position in a 1 meter wave with the RAOs for a 2.5 meter wave.

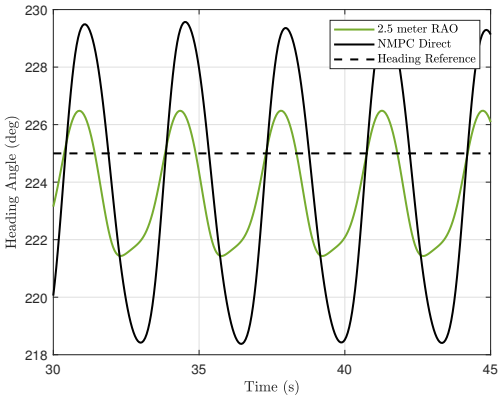

(b) Heading angle in a 1 meter wave with the RAOs for a 2.5 meter wave.

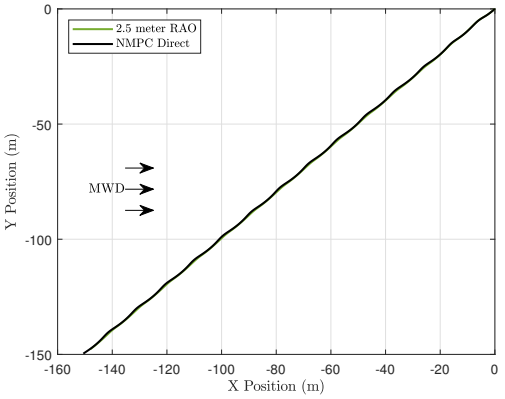

(c) Position in a 1 meter wave with the RAOs for a 2.5 meter wave.

FIGURE 7.17: These figures show the NMPC controller with the RAO surfaces for 2.5 meter waves simulated over 1 meter waves as compared to the NMPC controller with the correct 2.5 meter wave RAOs

TABLE 7.6: Effect of prediction step size and length on computation time

Horizon Length	Total Steps	Iteration Time	Step Size	Total Steps	Iteration Time
15s	300	3.26s	0.05s	300	3.26s
12.5s	250	2.36s	0.1s	150	1.11s
10s	200	1.63s	0.15s	100	0.68s
7.5s	150	1.10s	0.2s	75	0.49s
5s	100	0.66s	0.25s	60	0.38s
2.5s	50	0.31s	0.3s	50	0.31s
-	-	-	0.35s	43	0.27s
-	-	-	0.4s	38	0.23s
-	-	-	0.45s	33	0.21s
-	-	-	0.5s	30	0.19s

2.5 meter waves with a desired heading of 270 degrees, for the various prediction horizon lengths mentioned above. For these simulations the vessel has an average wave encounter frequency of 1.10 rad/s or 5.70 second period. With that there appears to be slight degradation to the performance with a prediction length of 7.5 seconds with larger degradation occurring at shorter prediction lengths. This is about 1.3 times the period of the encountered harmonic. The heading angles in figure 7.18(a) for these shorter prediction lengths drift below the reference heading angle causing larger tacking angles in 7.18(b).

For various step sizes, the performance of the controller in 2.5 meter waves begins to drop off at 0.25 seconds. Again, the heading for the controller with larger step sizes falls below the heading reference and the vessel drifts from the original tacking path. At this step size and encounter frequency, the controller has roughly 23 steps per encountered period, or 23 discrete inputs it can use to minimize the cost function.

Figure 7.20 looks the the effect of the controller horizon length on the performance of the vessel in 0.5 meter waves. For these simulations the vessel has a desired heading of 225 degrees and is using the direct NMPC controller. For these parameters, the average encounter frequency is 2.48 rad/s with a encounter period of 2.54 seconds. The effect of this shorter encounter period is apparent, with all of the prediction lengths giving good performance. Only the 2.5 seconds horizon shows slight degredation of the heading in figure 7.20(a), though it has no effect of the path following in figure 7.20(b). The 2.5 second horizon is 0.98 times the encounter period.

The last figures in 7.4 show the effect of step size on the 0.5 meter wave case. Degradation begins to appear at a time step of 0.2 seconds in figure 7.21(a). The loss of performance here is much greater than in the 2.5 meter case, with the controller appearing unstable as the paths begin to diverge in figure 7.21(b). With a step size of 0.2 seconds, the controller has only 13 steps per harmonic period.

What can be deduced from these plots is that the ideal prediction horizon length is one that is at least as long as the encounter harmonic, and the step size should provide at least 23 input points for the controller per encounter harmonic period. This is of course a generalization and the effect of shorter prediction horizons with larger steps sizes has yet to be tested on this system, but it points to an interesting problem; with large range of wave frequencies and the influence of the heading and velocity on the encounter frequency what is the optimal prediction horizon length, and step size?

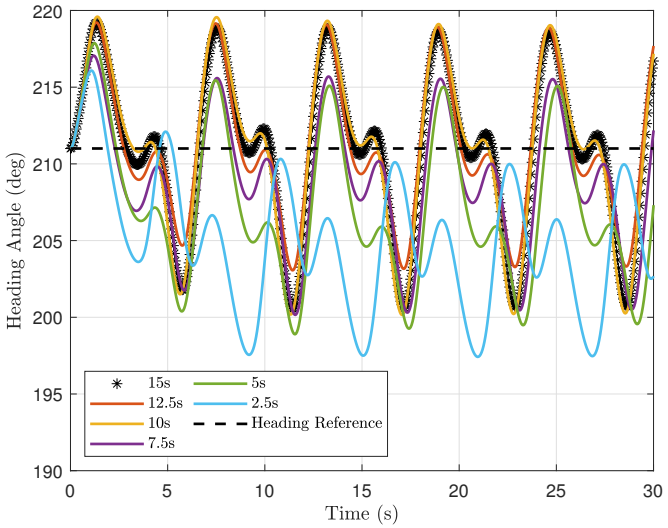

(a) Heading angle for various prediction horizon lengths in 2.5 meter waves. Original indicated by the '∗'.

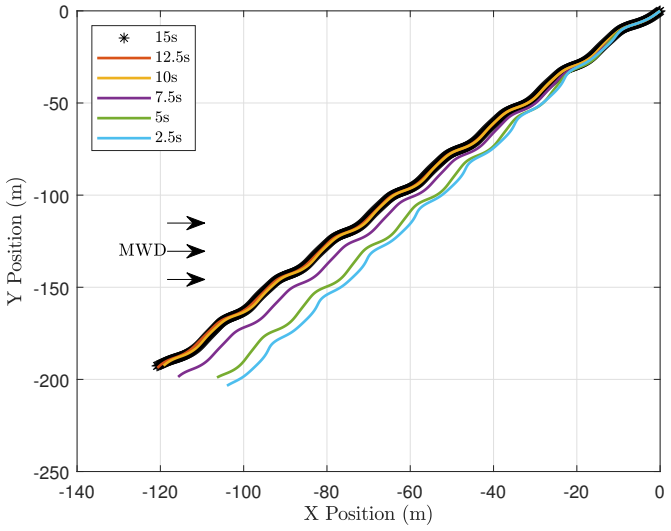

(b) Position for various prediction horizon lengths in 2.5 meter waves. Original indicated by the '∗'.

FIGURE 7.18: These figures show the performance of the NMPC in 2.5 meter waves with various prediction horizon lengths.

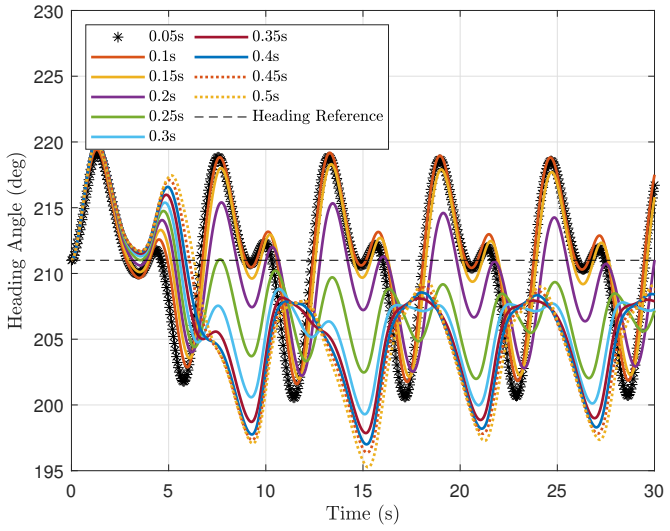

(a) Heading angle for various prediction horizon step sizes in 2.5 meter waves. Original indicated by the '∗'.

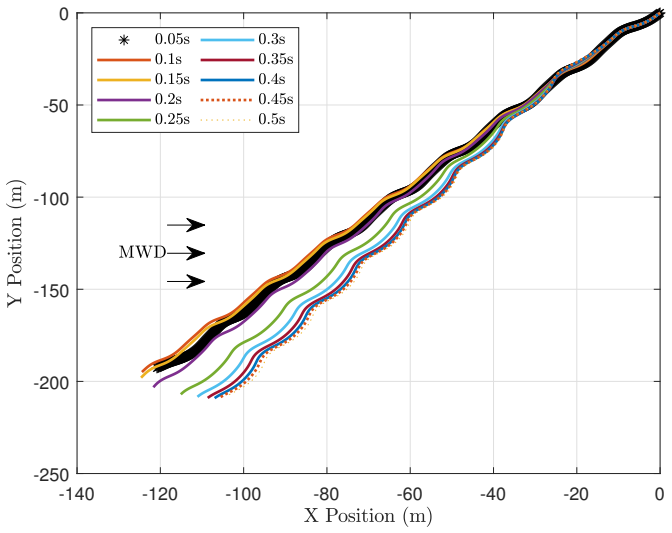

(b) Position for various prediction horizon step sizes in 2.5 meter waves. Original indicated by the '∗'.

FIGURE 7.19: These figures show the performance of the NMPC in 2.5 meter waves with various prediction horizon step sizes.

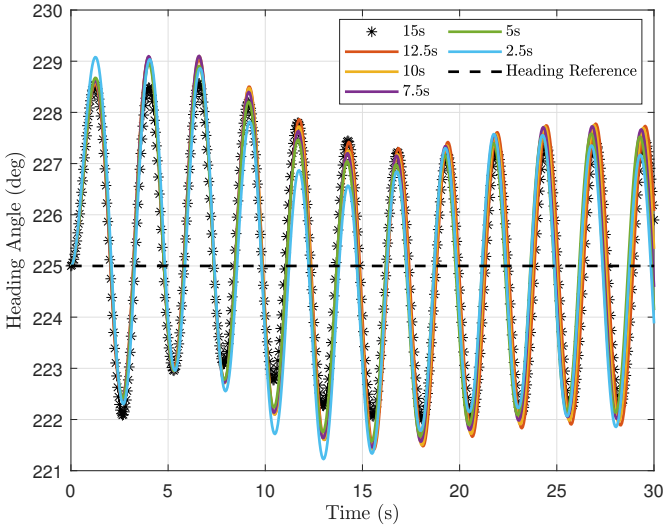

(a) Heading angle for various prediction horizon lengths in 0.5 meter waves. Original indicated by the '∗'.

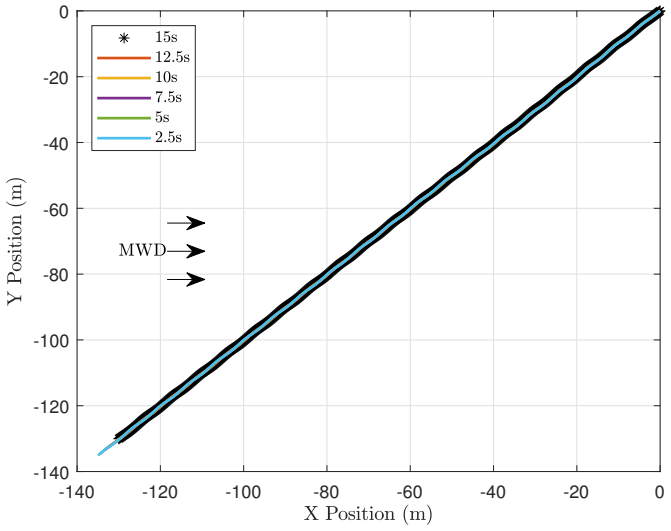

(b) Position for various prediction horizon lengths in 0.5 meter waves. Original indicated by the '∗'.

FIGURE 7.20: These figures show the performance of the NMPC in 0.5 meter waves with various prediction horizon lengths.

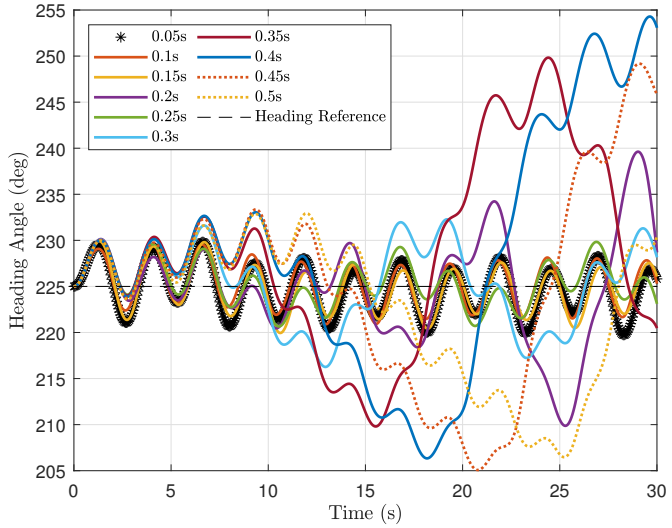

(a) Heading angle for various prediction horizon step sizes in 0.5 meter waves. Original indicated by the '∗'.

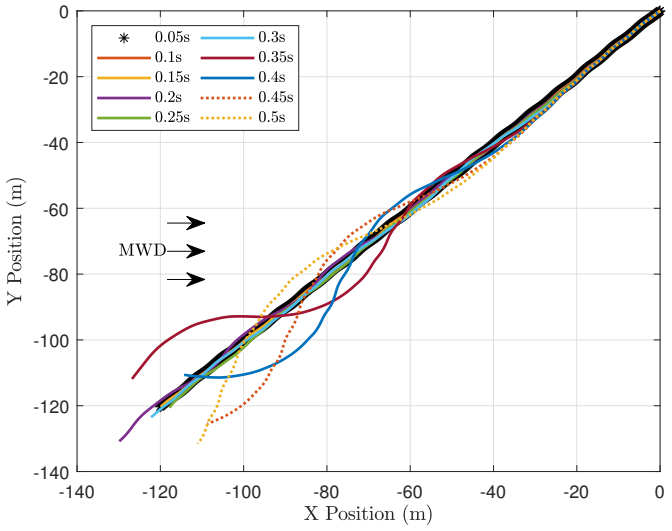

(b) Position for various prediction horizon step sizes in 0.5 meter waves. Original indicated by the '∗'.

FIGURE 7.21: These figures show the performance of the NMPC in 0.5 meter waves with various prediction horizon step sizes.

This is not too different from the issue in Zhang et al. (2019), in which some conditions require small step sizes for better path tracking in wheeled autonomous vehicles, and other conditions require long prediction horizons for stability. The proposed solution is an adaptive prediction horizon. A similar method could work for ASVs with a form of prediction horizon scheduling dependent on wave conditions and desired heading and velocity.

7.5 Summary

This chapter introduced the LOS PID used in the thesis, with the initial tuning of the PID and NMPC. It was shown that in reaching the path the NMPC was quicker with less overshoot and consistent in all wave conditions. The results of the tacking planner was applied to the NMPC controlled vessel in this chapter. This was compared to the PID controller and NMPC controller following the path set out by the desired heading. The results showed that the NMPC tacking controller in 2.5 meter waves greatly reduced many of the wave-induced motions. Heave accelerations saw a decrease of up to 140% and pitch angles saw an average reduction of 16% for the tacking NMPC. These results were achieved with little propeller actuation effort compared to the PID controller. Even when traveling along the same path, the NMPC direct controller managed to reduce the pitch angle, and accelerations in the surge, heave, and pitch directions. This was while having better path adherence than the PID controller. The only consequences of both NMPC controllers were increased rolling due to the rudder actuation, and increased time and fuel for the tacking NMPC.

The benefits of the NMPC tacking controller extended to environments with a full sea state. Here, the controller continued to reduce both angles and accelerations. The NMPC direct controller was still able to reduce the pitch angles of the vessel, but saw no improvement to the accelerations, as compared to the PID. The full sea state also showed the limits of the PID controller as it was tuned, seeing it go backwards in large waves. The benefits of the NMPC tacking controller come not only from the prediction of the wave-induced forces, but a penalization on the resulting motions. Without this penalization, performance is worsened. These results were predicated on the assumption of knowledge of the waves, but modeling every wave component in a sea state is computationally burdensome for the controller, so a potential method of only calculating the total

wave height, and using a single set of RAOs to calculate forces, was investigated. Using the RAOs for a 2.5 meter wave saw little degradation in performance. This chapter also introduced the impact of prediction horizon length and step size on the performance of the controller. The results indicate that future controllers, to remain efficient, should adopt prediction horizon parameters so that, depending on the sea state, heading, and velocity, the horizon length extends to at least 1.3 wave harmonics, and there are at least 20 steps per harmonic.

Chapter 8

Beam and Following Sea Navigation

The following chapter saw the introduction of the LOS PID controller and the tuning of the PID and NMPC controllers in mild conditions. It then established the performance of the controllers in a variety of headings for a multitude of sea conditions, and later examined the effect of unmodeled sea states and differing controller parameters. This chapter will look at the PID and NMPC controllers in first beam seas with its modified tacking planner. Then the controllers will be simulated in the various sea states as before to gain an understanding of the performance of the controllers, followed by additional testing to gather further insight. After, the task of control in following seas is presented. The tack planner is retained for following seas, but only for certain scenarios, as following seas present a trajectory tracking problem.

8.1 Beam Sea

A beam sea is a sea in which the heading of the vessel is perpendicular to the major wave direction, with the waves impacting on the side of the vessel. In these conditions, shown in figure 8.1, wave forces in the sway, roll, and yaw directions are highest while wave force in the pitch direction is still present, and wave force in the heave direction is little changed. Little wave force in the surge direction exists in these conditions. These changes from the head/bow sea require modification to the tacking planner introduced in chapter 6. In this chapter a heading of 180 degrees is a pure beam sea while larger headings such as 210 degrees are heading slightly into the waves and angles smaller than 180 degrees are heading with the waves.

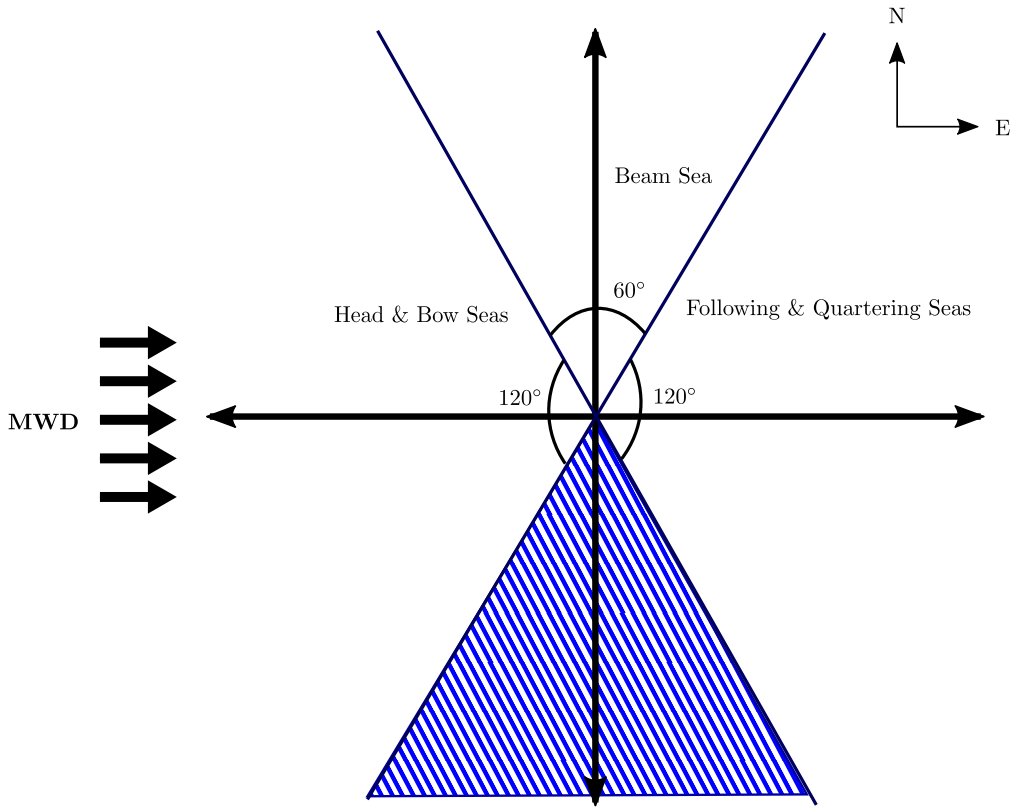

FIGURE 8.1: Beam sea is defined as the shaded blue region.

8.1.1 Beam Sea Tacking Planner

Tack planning in the beam seas present some interesting challenges. The vessel-wave dynamics are similar in head and bow seas, and are similar in following and quartering seas. However, bow and quartering seas are not, and this creates vessel-wave dynamics which are asymmetrical across the perpendicular travel axis, referred to herein as the beam axis. The tacking planner can no longer make tacking decisions on only half of the decision area. Figure 8.2(a) shows the terms used in the beam sea tacking planner. The terms are the same as the previous tacking planner with the exception that they are defined about the beam axis. The tacking is also performed about this axis as opposed to tacking about the major wave direction. The equations used in the beam sea tacking planner are the same as defined in chapter 6 with the exceptions noted here. The weightings of some of the force terms are changed. Owing to the negligible effect of the wave in the surge direction, and the loss of the scaling of the wave force due to the non-dimensionalization and normalization of the terms, the surge force, propeller actuation, and excess velocity terms need to be manually adjusted. The surge force term is not included in the beam sea tacking planner, and the propeller actuation and excess velocity terms are reduced to 0.25 of their values, closely aligned to the actual decrease

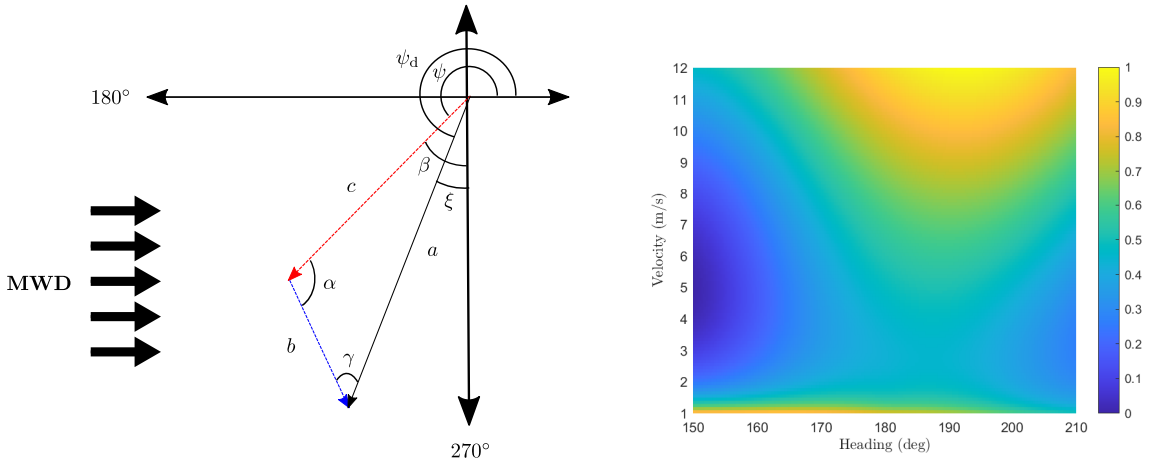

(a) Tacking angles and path terms for the beam sea tacking planner.

(b) Force cost surface in beam seas for 2.5 meter waves.

FIGURE 8.2: The beam sea tacking planner terms, and the force cost surface for 2.5 meter waves show the asymmetrical nature of the wave force in beam waves. Note the disparate angle values are due to the tacking planner calculations 8.2(a) being performed in the Cartesian plane and the results 8.2(b) and subsequent navigation are in NED coordinates.

in their values before normalization as compared to in head seas. Figure 8.2(b) plots the resultant force cost surface for a 2.5 meter beam sea. The asymmetry can be seen in this figure. The path lengths and tacking angle equations (6.2b)-(6.2f) are no longer driven by the initial tacking angle. Because of the asymmetry, the tacking angle and lengths are determined from the optimal tack in each direction.

The asymmetric nature of the force cost surface requires the tacking planner to iterate to determine the appropriate course of action. First finding what the opposite tacking angle and velocity are, then using this information to determine the near side tacking angle and velocity. This is explained fully below. Starting with a desired heading in zone 1 as defined in figure 8.3, the following is the iterative procedure used by the beam tacking planner:

1. The force cost surface for both zones is calculated.

2. The minimum of the force cost surface for zone 1 is found. The geometric term is excluded at this point because if tacking is determined to be optimal, the force term is likely to have more influence on the optimal heading and velocity. The logic term, $\tan(\beta - \xi) < \frac{d_C}{d_D}$, is used to determine if the force cost minimum heading is near to the desired heading. If it is, then the desired heading is determined to be optimal, the minimizing velocity is found, and no tacking occurs.

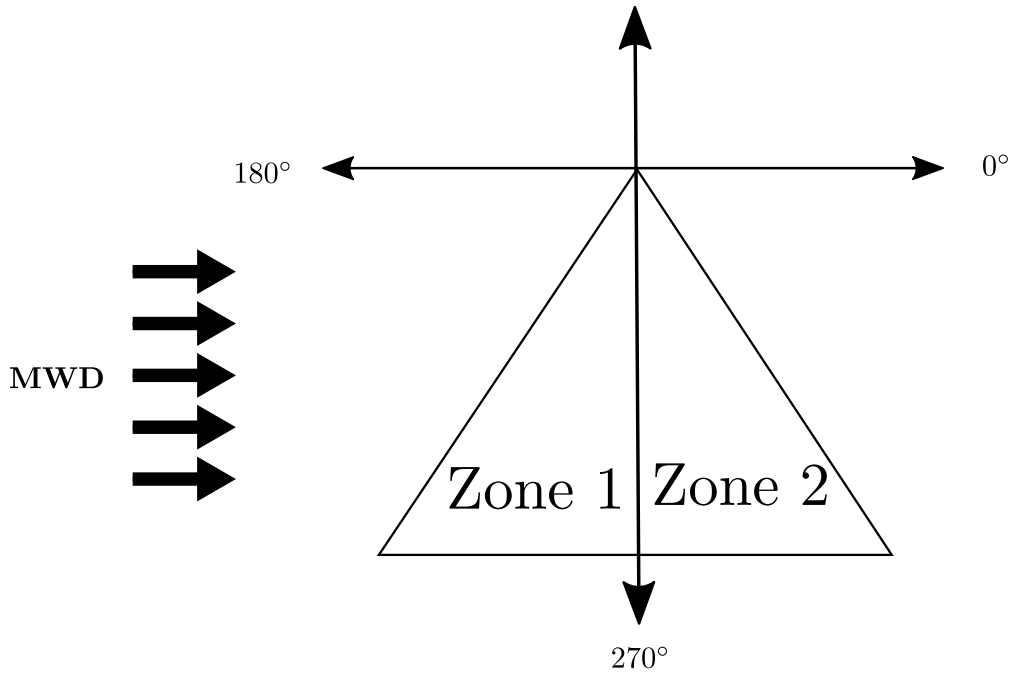

FIGURE 8.3: The beam sea area divided into two zones for the tacking planner. Note that this is in Cartesian coordinates.

3. Using the optimal tacking angle and velocity values found for zone 1, the optimal tacking angle and velocity are found for zone 2. Since tacking may no longer be symmetrical, the angle α is now calculated as $\alpha = 180 - (\beta_{Z1} + \beta_{Z2})$, where Z refers to the zone of the angles. With tacking performed about the beam axis, the desired heading for zone 2 is aligned with this axis. Calculating γ is then simply, $\gamma = 180 - (\beta_{Z2} + \alpha)$. The subsequent path lengths can be determined with these angles. With the optimal tacking angle and velocity for zone 2 calculated, the force cost value at this tacking angle and velocity is checked against the minimum force cost along the original heading angle in zone 1. If the force cost in zone 2 is higher than zone 1, then the best course is path following along the desired heading at the optimal velocity.

4. With the optimal tacking and velocity determined for zone 2, the optimal tacking angle and velocity is calculated for zone 1. This time the geometric cost is included in the calculation. The angle α is calculated the same as in step 3, but because the desired path lies in zone 1, γ is calculated as $\gamma = 180 - ((\beta_{Z1} - \epsilon) + \alpha)$. With the optimal tacking angle and velocity for zone 1, a last logic check is made to verify that the optimal angle is sufficiently different to the desired heading.

The results of the tacking planner are presented in table 8.1 in lieu of the plot in the chapter 6 because the differing tacking angles and velocities are difficult to indicate on a plot. The number of wave states are reduced from the previous six, down to three: 0.5 meters, 1.5 meters, and 2.5 meters. The desired headings tested are 210°, 195°, 180°, 165°, and 150°. Note that the bounds of the tacking planner are 210° and 150°, so these desired headings will always produce a path following result.

The lack of the surge force term and the reduction of the propeller and excess velocity terms in the force cost function leads to a lower prescribed velocity for 0.5 meter waves. The loss of influence from these terms also leads to velocities at 1.5 meters that are lower than they are at 0.5 meters. This reflects the higher pitch wave force at higher velocities, particularly for 210° to 180°. At 1.5 meters we begin to see the diverging minimums for the extremes of the beam sea area. At a heading of 210°, the vessel is traveling at the boundary of a beam and bow sea, so the characteristics of the wave force are similar to that of the previous chapter, chiefly, higher pitch and yaw wave forces at higher velocities. Higher wave forces in the yaw direction require more rudder actuation so the force cost goes up. The resulting optimal velocity is then lower than the optimal velocity at 150° where the lowest wave force in the pitch direction is actually near 5 m/s. This difference can be seen in figure 8.2(b). The tacking planner does not prescribe tacking at 1.5 meters, but cost difference between tacking and direct path following for a desired heading of 180° was less than 1%, so tacking was added for comparison. This is indicated by the * in the table. In 2.5 meter waves with a desired heading of 165°, tacking at 150° reduces the force cost, however, the logic check of the tacking planner found that the opposite tacking angle of 210° has a higher force cost than traveling at 165° at 4.3 m/s, so path following is prescribed. The different tacking velocities pose a challenge on what velocity the equivalent path follow simulations for the PID and NMPC direct controllers should use to provide an equitable comparison. Ultimately, to determine the velocity, the proportional time spent at each tack angle was used to weight the averaging of the velocities. With a desired heading of 195°, the path length of the 210° tack is longer than the path length of the 150° tack and, therefore, was weighted down to a slower velocity than compared to a desired heading of 180° where the path lengths are equal.

Table 8.1: Beam sea tacking planner results

Wave Cond. & Type	210°	195°	180°	165°	150°
0.5 m Direct	3.6 m/s	3.5 m/s	3.5 m/s	3.5 m/s	3.6 m/s
1.5 m Direct	3.4 m/s	3.2 m/s	3.2 m/s	3.7 m/s	4.9 m/s
1.5 m Tacking*	-	-	2.9@210° & 4.7@150°	-	-
2.5 m Direct	3.1 m/s	3.4 m/s	3.7 m/s	4.3 m/s	4.9 m/s
2.5 Tacking	-	3.1@210° & 4.9@150°	3.1@210° & 4.9@150°	-	-

8.1.2 Beam Sea Results

Simulations of the NMPC were carried out for the velocities and headings described in table 8.1 and compared to the PID controller. A few changes were made to the NMPC tuning parameters. Following the testing done on the effect of the step size in the previous chapter, and with the expected encounter frequency to decrease, the step size was increased from 0.05 seconds to 0.1 seconds. Also, due to the higher wave force in the roll direction and the focus on minimizing roll angles in beam seas, a roll angular velocity and angular position weighting term, along with a pitch angular velocity term, were added to the cost function of the NMPC. The controller was also changed from single shooting to multiple shooting. The results are shown in table 8.3 and

Table 8.2: NMPC beam sea tuning parameters

NMPC			
Parameter	Value	Parameter	Value
Surge Velocity Weight	1	Yaw Position (no tacking)	2
Y position Weight (no tacking)	1	Yaw Position (tacking)	10
Y position Weight (tacking)	0	Propeller State Weight	0.35
Roll Angular Velocity Weight	38.2	Propeller Actuation Weight	0.001
Roll Angle Weight	38.2	Rudder Actuation Weight	0.1
Pitch Angular Velocity Weight	38.2	Heading Positive Constraint	270° W
Pitch Angle Weight	38.2	Heading Negative Constraint	0° E
Prediction Horizon	150 steps	Prediction Time Step	0.1s
Prediction Length	15s	-	

they are mixed. For 0.5 meter waves, the NMPC direct controller largely improves upon the PID controller, but at this wave height, most wave forces are generally low, so the magnitude of the gains are minimal. For the 1.5 and 2.5 meter wave cases, the best performance by the NMPC direct controller is found for a desired heading of 180°. The tacking NMPC controller for 1.5 and 2.5 meter waves actually has worse performance than the PID or NMPC direct controllers. The middling outcome for the NMPC controllers is for two reasons: for both it is the low magnitude of the wave force in the roll direction, and for the NMPC tacking controller, it is the difficulty in

TABLE 8.3: NMPC improvements over PID in beam seas. (Note: D=Direct, T=Tacking)

Controller & Wave Cond.	Pitch Peak (%)	Pitch Trough (%)	Roll Peak (%)	Roll Trough (%)	Heave Accel. (%)	Roll Accel. (%)	Roll Force (%)	Pitch Accel. (%)
0.5m 210° D	38.02	-3.18	-12	-12.44	-2.69	-19.89	-0.81	3.11
0.5m 195° D	-11.16	20.33	19.96	10.35	6.12	8.27	-0.83	32.96
0.5m 180° D	4.98	20.06	31.79	1.45	-1.51	-38.57	101.87	41.33
0.5m 165° D	71.58	13.72	235.89	193.64	2.93	-38.34	19.92	88.2
0.5m 150° D	11.52	42.48	82.88	564.39	-8.9	30.75	-2.97	17.35
1.5m 210° D	-4.6	13.89	-12.77	-22.03	34.29	-73.53	-0.63	33.47
1.5m 195° D	-4.21	3.68	-9.83	-26.22	8.96	-38.55	-0.28	13.51
1.5m 180° D	-2.62	12.33	12.22	20.99	1.58	23.17	-0.16	15.27
1.5m 165° D	-12.07	8.34	-21.03	32.23	5.04	-29.26	-0.22	-5.86
1.5m 150° D	-0.43	10.48	-29.03	2.7	-8.74	-73.87	-2.81	-4.49
1.5m 180° T	-28.89	-12.03	-21	22.76	-2.28	-40.63	10.38	-22.4
2.5m 210° D	12.12	9.6	7.59	34.09	-11.31	-50.86	-13.18	-16.7
2.5m 195° D	-5.04	3.56	42.01	-16.79	6.74	-6.63	0.94	13.2
2.5m 180° D	-0.94	15.82	58.23	45.87	-0.33	46.73	-0.24	12.56
2.5m 165° D	-5.02	10.08	14.57	37.72	20.79	25.42	-1.13	13.43
2.5m 150° D	-2.26	12.24	-46.55	41.94	-19.34	-52.21	-2.4	-27.62
2.5m 195° T	-9.5	-2.2	4.88	0.29	-5.5	-34.24	6.09	0.18
2.5m 180° T	-17.23	-7.06	1.63	17.57	-22.96	-31.55	9.83	-14.21

TABLE 8.4: Average pitch and roll angles of the PID and NMPC direct controllers.

Wave Cond. & Controller	Pitch Peak Ave.	Pitch Trough Ave.	Roll Positive Ave.	Roll Negative Ave.
0.5 m PID	1.90	2.36	2.98	2.49
0.5 m NMPC	1.79	2.08	2.30	2.00
1.5 m PID	4.46	5.26	2.44	2.65
1.5 m NMPC	4.68	4.79	2.86	2.61
2.5 m PID	8.28	9.09	3.48	4.21
2.5 m NMPC	8.29	8.25	3.51	3.28

comparing the tacking controller to the direct controllers. Looking at the roll force improvement for the NMPC tacking controller it can be seen that roll force is reduced and for 2.5 meter waves the average roll angles are reduced as well. The pitch angles for the tacking NMPC are worse for both 1.5 and 2.5 meter waves. Though efforts were made to try and balance the velocities at which the controllers were tested, discrepancies still exist. The other reason for lower performance is the wave force in the roll direction does not have a large effect on the vessel. To see this, table 8.4 shows the average positive and negative pitch and roll angles for the PID and NMPC direct controllers. The pitch angles approximately double for each increase in wave height while the roll angles see a very mild increase. The overall magnitude of the roll angle is low, even lower than the many of the roll angles experienced in a head sea. To understand why, we first examine figure 8.1.2.

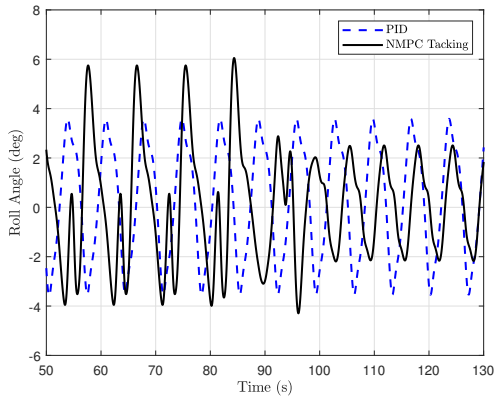

(a) The roll angle of the NMPC tacking and PID controller with a desired heading of 180° in 2.5 meter waves.

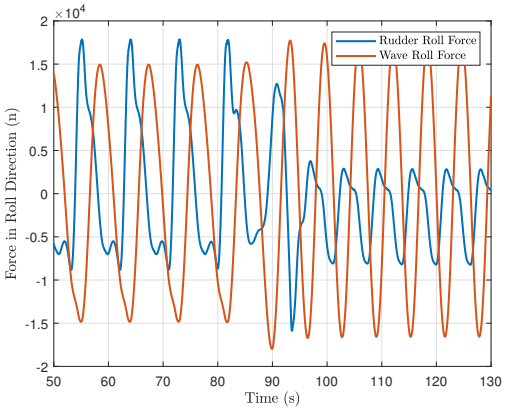

(b) The rudder and wave force in the roll direction before and after a tack with the NMPC tacking controller in 2.5 meter waves.

FIGURE 8.4: Plots showing the rudder responsible for the large change in roll angle for the NMPC tacking controller.

These figures show the NMPC tacking and PID controllers for a desired heading of 180° with 2.5 meter waves. Figure 8.4(a) plots the roll angle of the two controllers, with a tack change occurring around the 85 second mark for the NMPC tacking controller. Before the tack change, the NMPC controller is traveling at 4.9 m/s with a heading of 150°. The negative roll angles are similar for the NMPC and PID controllers, while the NMPC has a higher positive roll angle. After the tack, the NMPC is traveling at 3.1 m/s with a heading of 150°. In this new direction, the roll angle of the NMPC are significantly reduced for both positive and negative values. This reduction is not caused by a reduction in wave force in the roll direction, in fact, figure 8.4(b) shows that the wave force is about 16% lower. The primary driver for the roll angle is the rudder, even in beam seas. The rudder force in the positive roll direction is larger than the wave force. The reduction in the rudder force is a result of the lower surge velocity as the rudder force is proportional to the surge velocity.

The magnitude of the wave force in the roll direction is low enough that wave height is not a good indicator for roll performance in beam seas. Figure 8.5(a) illustrates this point with the NMPC direct controller for 0.5 and 2.5 meter waves with a heading of 180°. This is the heading in which the wave force in the to direction is highest for any wave height, and yet, the positive roll angle is 1 degree lower for the 2.5 meter waves compared to the 0.5 meter waves. In this scenario, the rudder force remains below the wave force in the roll direction for the 0.5 meter wave in figure 8.5(b), as well as for the 2.5 meter wave in figure 8.5(c). For both, the rudder force is approximately half of the

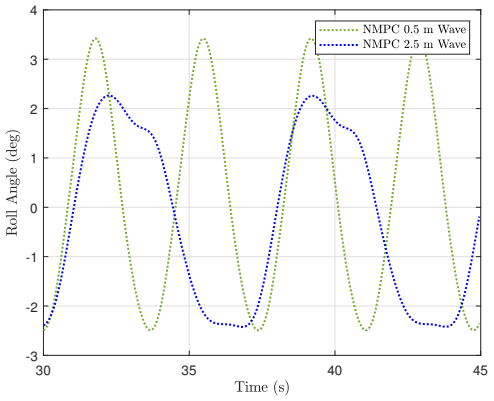

(a) Roll angle of the NMPC direct controllers with a desired heading of 180° for 0.5 and 2.5 meter waves.

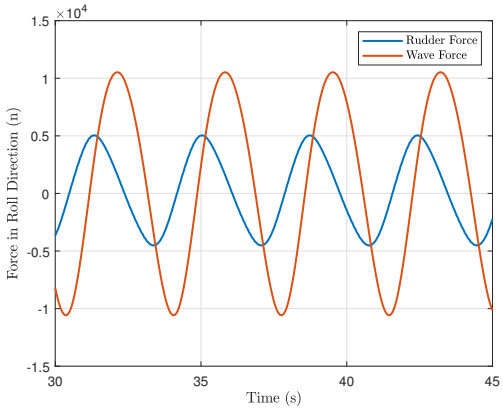

(b) Rudder and wave force in the roll direction for 0.5 meter waves.

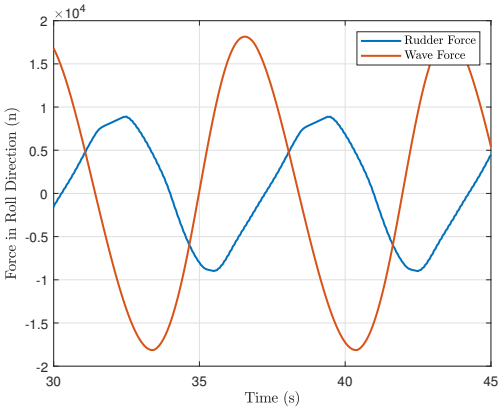

(c) Rudder and wave force in the roll direction for 2.5 meter waves.

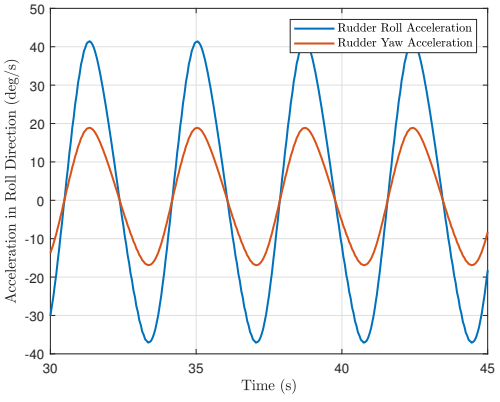

(d) Rudder induced roll and yaw accelerations for 0.5 meter waves.

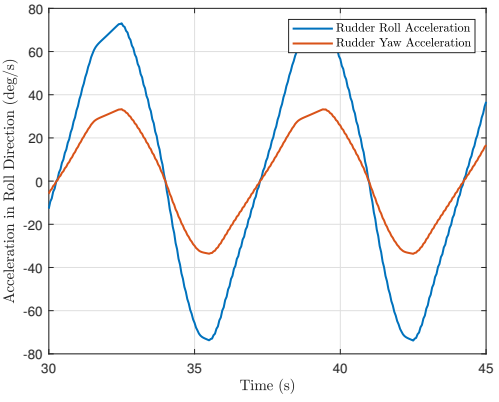

(e) Rudder induced roll and yaw accelerations for 2.5 meter waves.

FIGURE 8.5: Plots showing the influence of the rudder on total force in the roll direction and on the roll and yaw accelerations.

wave force, and the wave force for 2.5 meter waves is higher, but the roll angle is lower. Crucially, the difference for the two is the phase of the rudder actuation to the wave force. The controller can use the rudder to stabilize the roll angle, but this is balanced with the need to maintain the path. The maximum wave force in the sway, roll, and yaw occur near the same phase on the wave, so this poses a challenging scenario for the NMPC controller. The wave simultaneously forces the vessel off the path in the sway direction while inducing a moment in the roll and yaw direction, to which the controller can not remedy for all three as the required rudder for the sway and yaw wave forces, is the opposite of the roll wave forces. Turning into a wave as it induces a roll moment to satisfy the sway and yaw positions exacerbates the roll angle. Instead, the controller turns into the wave before it begins to induce a roll moment to offset the maximum roll force from the rudder and wave. The controller is performing the same small tacking maneuver seen in the head sea case, now to satisfy the roll angle penalty. However, the encounter frequency dictates how larger a tack can be performed as the rudder rate is limited. For the 2.5 meter waves with a slower encounter frequency, the controller is able to begin the turn earlier, shifting the rudder-induced roll force to mitigate some of the wave-induced roll force. For the 0.5 meter waves, the rudder response is not shifted by as much, resulting in the rudder contributing to the wave-induced rolling and resulting in a larger roll angle.

Figures 8.5(d) and 8.5(e) plot the rudder-induced roll and yaw accelerations for 0.5 and 2.5 meter waves. Though the rudder force in the yaw direction is higher than in the roll direction, the moment of inertia in the roll direction is 5 times lower than in the yaw direction, resulting in rudder-induced roll acceleration twice that of the yaw acceleration. In Sutton and Ag (1997) it was found that quick rudder movements, in conjunction with fin stabilizers, could stabilize a Royal Navy frigate without affecting steering due to the decade between the responses of the roll and yaw in a Bode plot. This was tried for the thesis, but because of a number of differences in the dynamics of a Navy frigate and the vessel in this thesis, and the relatively low wave force in the roll direction, performance was not much changed from the results presented.

Figure 8.6 plots the pitch and roll angles and their corresponding wave forces for the NMPC direct and PID controller with a 180° heading. Figure 8.6(a) shows the pitch angles of the two controllers, with the NMPC having slightly better negative pitch angles, and figure 8.6(b) shows the wave force in the pitch direction with the results nearly identical to the resultant pitch angles. Figure 8.6(c)

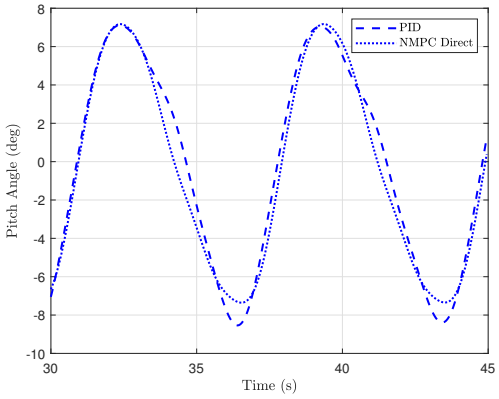

(a) Pitch angle of the NMPC direct and PID controllers in 2.5 meter waves with a desired heading of 180°

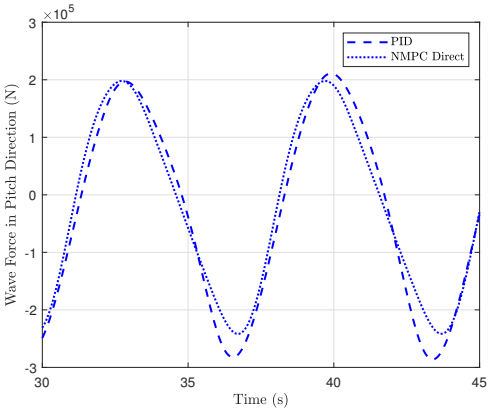

(b) Pitch wave force of the NMPC direct and PID controllers in 2.5 meter waves with a desired heading of 180°

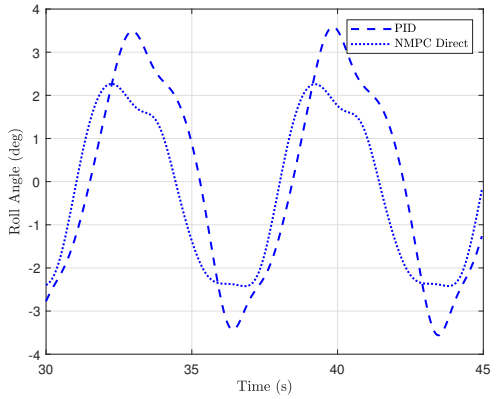

(c) Roll angle of the NMPC direct and PID controllers in 2.5 meter waves with a desired heading of 180°

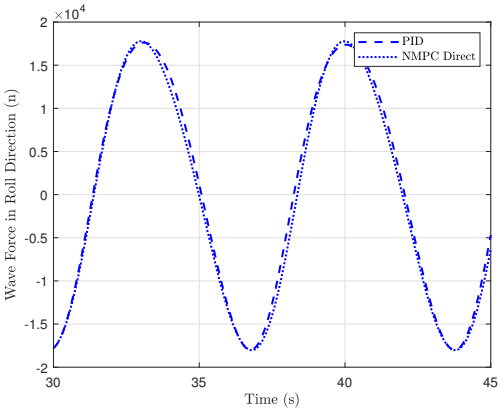

(d) Roll wave force of the NMPC direct and PID controllers in 2.5 meter waves with a desired heading of 180°

FIGURE 8.6: The wave force in the pitch and roll directions and the subsequent angles.

though, looks much different than figure 8.6(d). These figures show the roll angles and wave force in the roll direction, respectively. Owing to the large rudder acuation force in the roll direction, the NMPC direct controller is able to reduce the positive roll angle by 1.4° compared to the PID controller despite both experiencing the same wave force.

The actuation and path following of the PID and NMPC direct controllers are shown in figure 8.7. The propeller actuation is shown in 8.7(a). The wave force in the surge direction is low, so the range of propeller speeds is small, with the PID controller having very high-frequency changes, while the NMPC controller shows a smooth response. The NMPC controller also has a small deviation in surge velocity shown in figure 8.7(b). The NMPC employs large rudder angles in figure 8.7(c) to tack across the waves as discussed above, but as this is to counteract the wave-induced sway and yaw motions, the path following in figure 8.7(d) is not largely affected, with the NMPC only

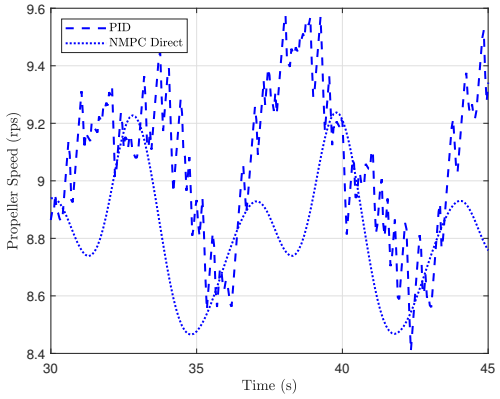

(a) The propeller response of the NMPC direct and PID controllers in 2.5 meter waves with a desired heading of 180°

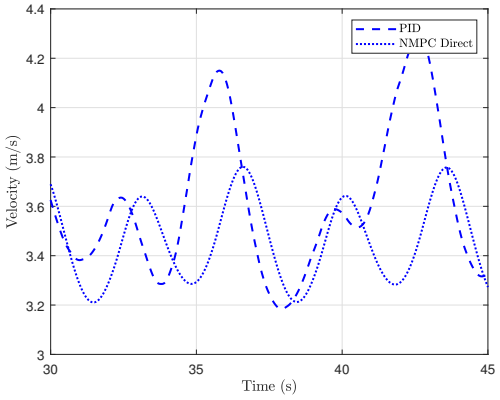

(b) The velocity profiles of the NMPC direct and PID controllers in 2.5 meter waves with a desired heading of 180°

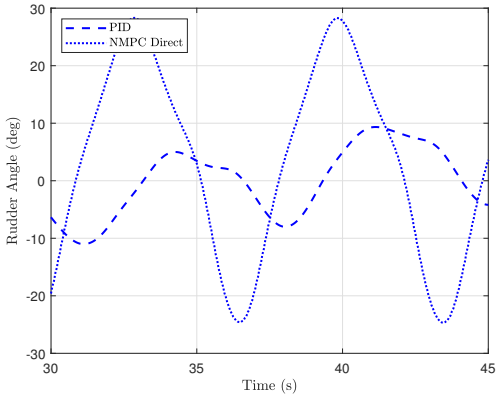

(c) The rudder response of the NMPC direct and PID controllers in 2.5 meter waves with a desired heading of 180°

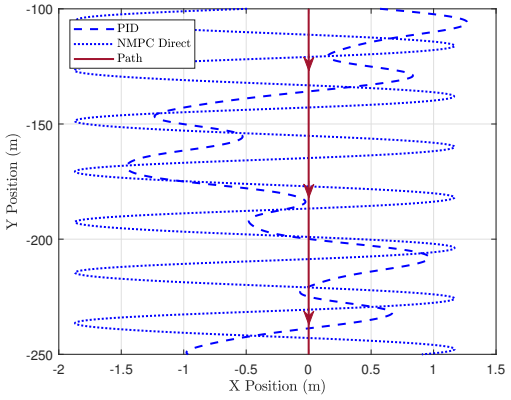

(d) The path following of the NMPC direct and PID controllers in 2.5 meter waves with a desired heading of 180°

FIGURE 8.7: Path following and actuation for NMPC and PID controllers in 2.5 meter waves with a desired heading of 180°

straying from the path by 0.5 meters more than the PID controller.

One other change was made to the NMPC tacking controller. Previously, the controller surveyed the final coordinates of the vessel in the prediction horizon to verify whether they violated the tacking boundary or not. If they did, the final reference in the prediction horizon was changed to the opposite tacking reference. The reference change would then propagate through the reference vector because of the receding horizon principle. This method is not ideal, as per Gros et al. (2016), the references should not have an abrupt change to ensure stability and optimality. The sharp change in heading reference would also cause the controller to deviate from other references, such as velocity as was seen with the early path following test of figure 7.1. This can cause higher wave forces during tacking. Also, for large differences in tacking angles, the reference change at

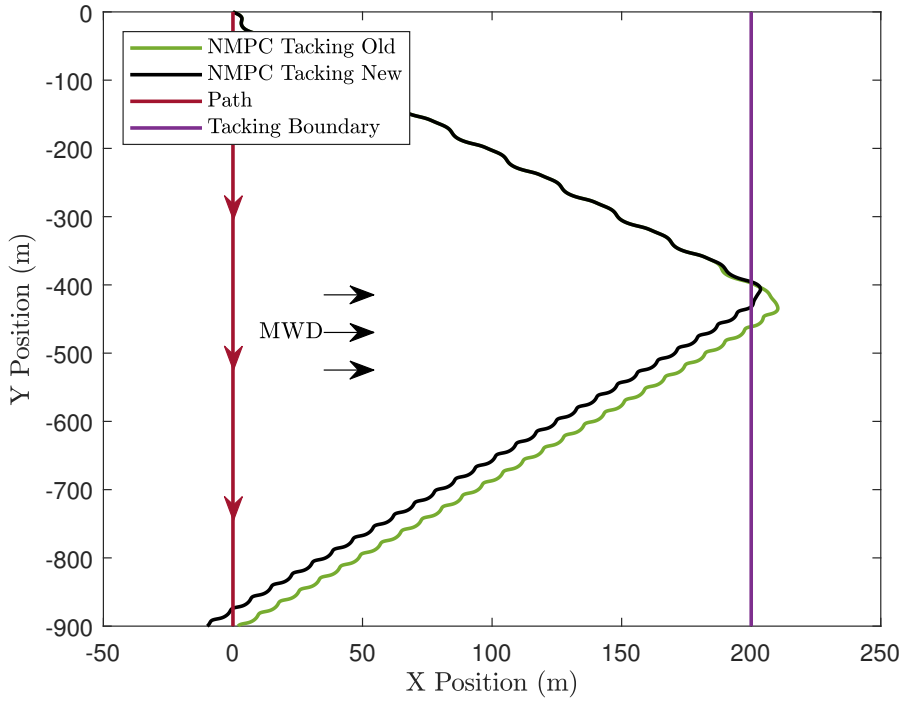

FIGURE 8.8: The original method of implementing a tacking maneuver compared to the new method.

the tacking boundary means there can be a large overrun of the boundary as seen in figure 7.3(a). To rectify this, when the last position in the prediction horizon violates the tacking boundary, the controller calculates the maximum turn rate of the vessel at the reference velocity, and the angle difference between the two tacks. With this, it calculates the time required to complete the turn. It then creates a smooth turning reference trajectory vector that is placed at the end of the prediction horizon. This new method is compared to the old in figure 8.8. This was performed in 2.5 meter waves with a desired heading of 180°. The waves cause the new method to still violate the boundary, as they are not factored into the trajectory, but the new method is able to reduce the overshoot by 65% from 10.3 meters past the boundary to 3.5 meters.

8.1.3 Beam Sea with SWEM

The NMPC direct and PID controller were simulated in the same, 2.5 meter single wave harmonic plus 1.5 meter full sea state, as the last chapter. For this test, the controllers had a desired heading of 180°. Figure 8.9 plots the pitch and roll angles and the path following performance of the two controllers. Figure 8.9(a) sees the NMPC controller with slightly lower positive pitch angles for

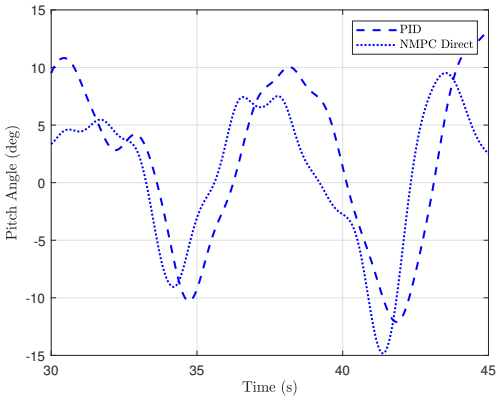

(a) The pitch angles of the NMPC direct and PID controllers in 2.5 meter waves with a 1.5 meter full sea state added.

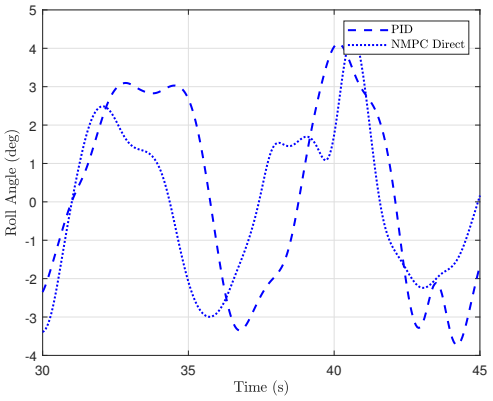

(b) The roll angles of the NMPC direct and PID controllers in 2.5 meter waves with a 1.5 meter full sea state added.

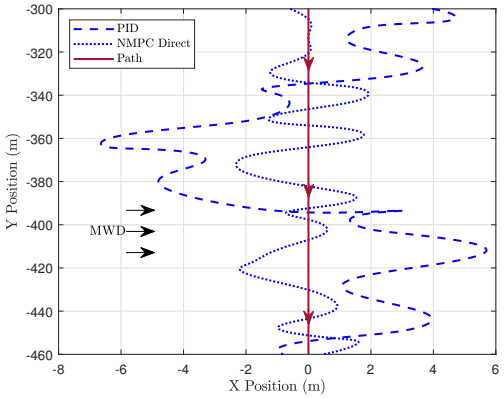

(c) Path following performance of the NMPC direct and PID controllers in 2.5 meter waves with a 1.5 meter full sea state added.

FIGURE 8.9: The performance of the NMPC direct and PID controllers in 2.5 meter waves with a 1.5 meter full sea state added in beam seas.

TABLE 8.5: Result of NMPC and PID in full sea state

Parameter	NMPC Direct (deg)	PID (deg)
RMS Pitch Angle	5.87	6.55
RMS Roll Angle	2.09	2.79
Pitch Peak Max Angle	11.13	13.51
Pitch Trough Max Angle	-14.82	-14.61
Roll Positive Max Angle	5.84	5.88
Roll Negative Max Angle	-5.07	-5.92

much of it, with some higher negative pitch angles. The roll angles of the two controllers in figure 7.12(b) are similar. The NMPC achieves better path following compared to the PID in 8.9(c).

Table 8.5 has some of the overall pitch and roll performance numbers for the two controllers. There were many more smaller peaks than the previous SWEM testing, making it difficult to automate

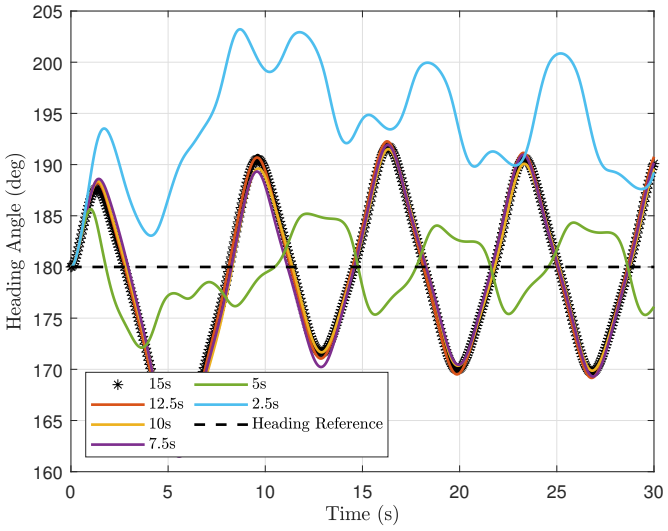

(a) Heading angle for various prediction horizon lengths in 2.5 meter waves. Original indicated by the '∗'.

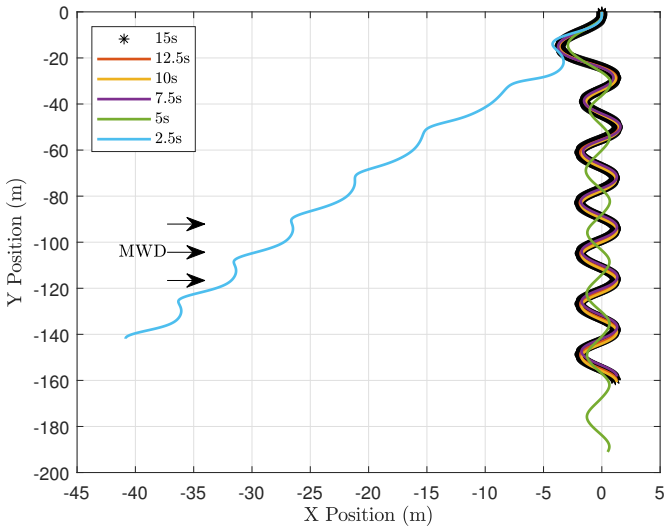

(b) Position for various prediction horizon lengths in 2.5 meter waves. Original indicated by the '∗'.

FIGURE 8.10: These figures show the performance of the NMPC in 2.5 meter waves with various prediction horizon lengths.

the calculation of the average peak values, even when accounting for prominence and threshold, so RMS was used in lieu of that. The NMPC controller had better performance for both the RMS pitch and roll angles, and had lower magnitudes for all of the maximum angles, except for the maximum negative pitch angle.

8.1.4 Beam Sea Prediction Horizon Tests

As before, the effect of prediction horizon length and and prediction step size is tested on the NMPC controller. The wave heights are the same 2.5 and 0.5 meters. The simulation involved the NMPC direct controller with a desired heading of 180°. Figure 8.10 shows the performance of the NMPC controller in 2.5 meter waves for the various prediction horizon lengths mentioned previously. For these simulations the vessel has an average wave encounter frequency of 0.9 rad/s or a 6.98 second period. This is the period of the wave. The performance is similar for prediction horizons 7.5 seconds and longer, with a large degradation below this point. This is seen in both the heading angles in figure 8.10(a) and the positions in figure 8.10(b). This holds up to the earlier finding that the prediction horizon should be at least one wave harmonic.

The original step size for the beam simulations was 0.1 seconds, so that is the baseline used in the step size comparisons. The amplitude of the heading angle reduces as the step size increases in figure 8.11(a), but the heading retains the same frequency and overall pattern until 0.35 second step sizes. A 0.25 to 0.3 second step size gives the controller 23 to 28 steps per encountered wave period, which is similar to previous findings.

Figure 8.12 looks at the effect of horizon length on the performance of the vessel in 0.5 meter waves. For this wave height, the average encounter frequency is 1.7 rad/s with a encounter period of 3.70 seconds. Again, because this is a beam sea, this is the encounter period of the wave. Previously, there was only slight degradation for a prediction horizon of 2.5 seconds as this was around the same length as the encounter period. However, now the encounter period is longer than 2.5 seconds, and there is severe degradation of the 2.5 second prediction horizon. The effect is most noticeable in the position plot in figure 8.12(b) though a slight performance loss can be seen in the heading plot figure 7.20(a).

The last figures in 8.13 show the effect of step size on the 0.5 meter wave case. Unlike last time, there are no large diverging paths. It is difficult to see any meaningful degradation in the heading plot in figure 8.13(a). In the position plot, figure 8.13(b), only the step sizes 0.2 seconds and below appear to even oscillate around the desired path of $x = 0$. The other step sizes appear shifted in the positive x direction. The results in the beam sea reinforce the earlier findings that the prediction

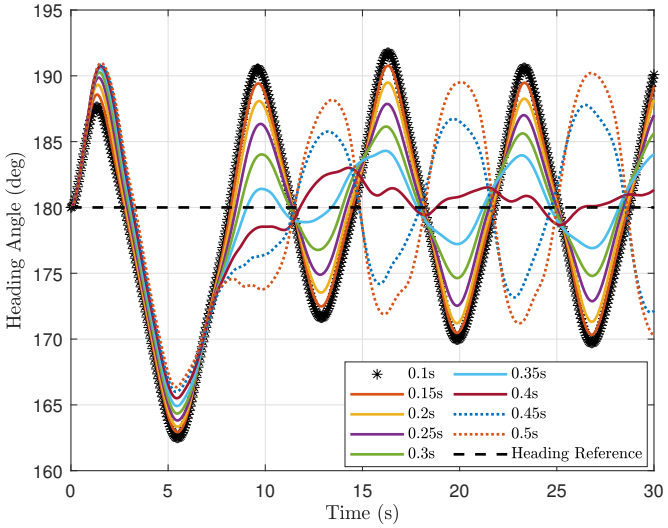

(a) Heading angle for various prediction horizon step sizes in 2.5 meter waves. Original indicated by the '∗'.

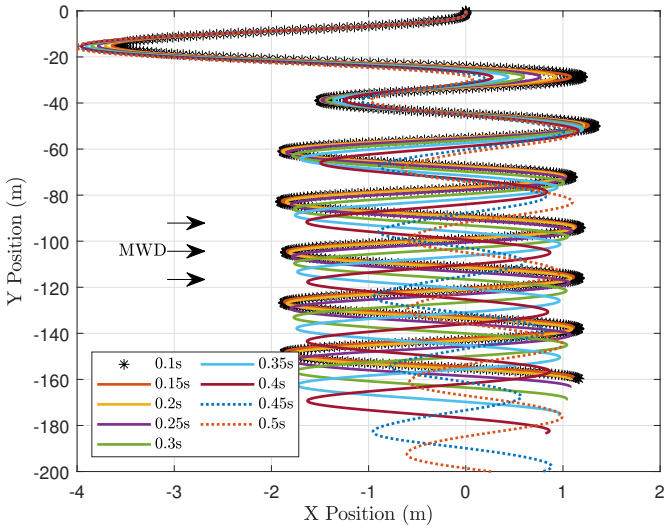

(b) Position for various prediction horizon step sizes in 2.5 meter waves. Original indicated by the '∗'.

FIGURE 8.11: These figures show the performance of the NMPC in 2.5 meter waves with various prediction horizon step sizes.

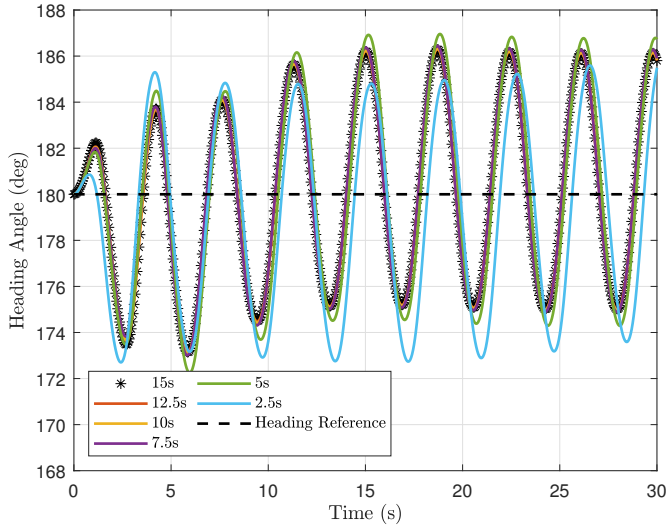

(a) Heading angle for various prediction horizon lengths in 0.5 meter waves. Original indicated by the '∗'.

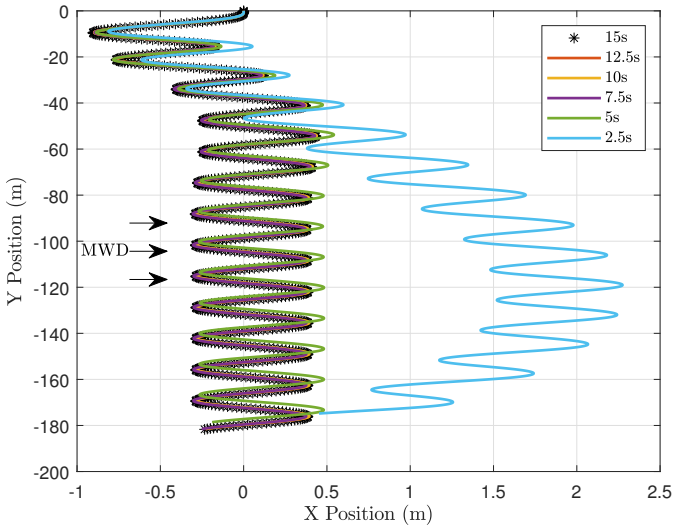

(b) Position for various prediction horizon lengths in 0.5 meter waves. Original indicated by the '∗'.

FIGURE 8.12: These figures show the performance of the NMPC in 0.5 meter waves with various prediction horizon lengths.

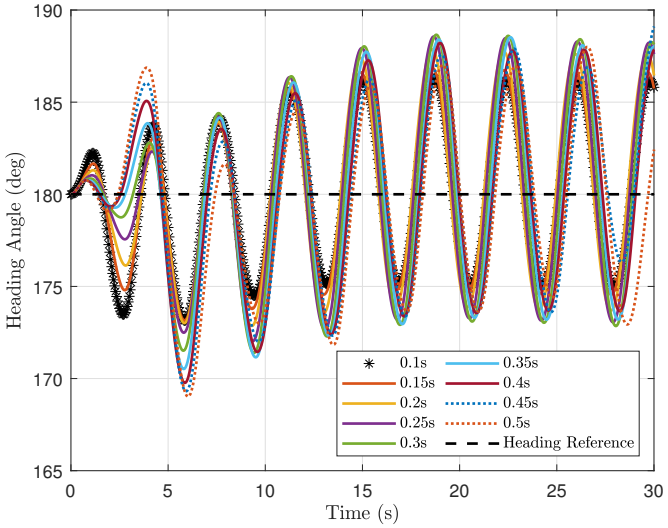

(a) Heading angle for various prediction horizon step sizes in 0.5 meter waves. Original indicated by the '∗'.

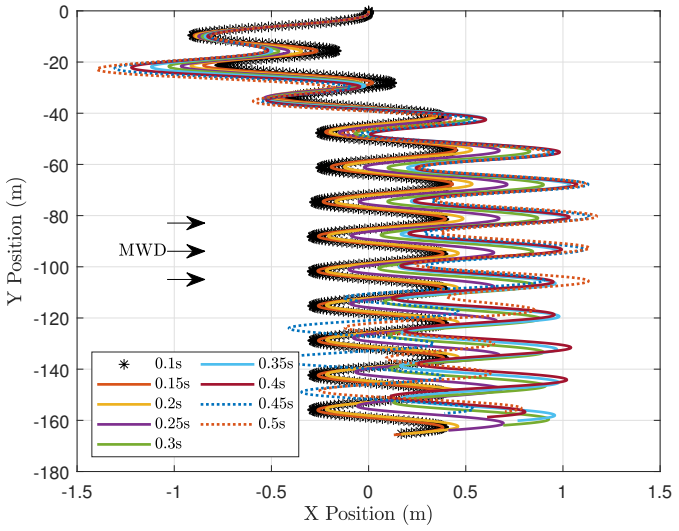

(b) Position for various prediction horizon step sizes in 0.5 meter waves. Original indicated by the '∗'.

FIGURE 8.13: These figures show the performance of the NMPC in 0.5 meter waves with various prediction horizon step sizes.

horizon should be at least as long as the encountered harmonic, and there should be at least 20 step sizes per encounter period.

8.2 Following Sea

Control of a vessel in following seas presents a difficult challenge owing to the dangerous phenomenon known as broaching. In this scenario, the vessel loses heading control, characterized by an abrupt change in yaw direction and often accompanied by a large roll moment. In Umeda and Hashimoto (2002), the criteria to determine a broach event is an angular yaw velocity in one direction despite an attempted counter steering by the rudder at its maximum angle. Many of the studies on broaching use captive models to quantify the forces responsible for broaching with the aims of improving modeling of the vessel-wave forces (Horel et al., 2014; Bonci et al., 2019; Bonci, 2019; Renilson, 1981). Others rely upon CFD methods to simulate the broach (Carrica et al., 2008, 2012) or high fidelity models (Araki et al., 2011). On methods of control and prevention, a common tactic is to drag a long rope behind the vessel to stabilize the yaw movements. This concept was adapted by Renilson (1986) with the Seabrake, which used actuated flaps of a towed platform behind the vessel for stability. Another concept was the use of extreme rudder to increase drag and improve stability using the Anti-Broaching Steering System (Umeda et al., 1999). There have been few studies investigating controller performance in following seas. One approach was the use of optimal control using the Covariance Matrix Adaption Evolution Strategy (CMA-ES) in Maki et al. (2021). The approach was successful and has advantages over more typical SQP methods of solving OCPs in that it is better able to find global minimums in highly nonlinear scenarios, such as in following seas. The disadvantage keeping the method from use on real ASV systems is the computation time for a single prediction step can take a day or longer. The CFD analysis in Carrica et al. (2012) provides a good walk through of the events during a broach. The following is a brief summary of the mechanics involved.

The velocity of the sea surface is not constant in presence of waves. The movement of the water in a wave is not linearly up and down, but is an orbital movement. The orbital mechanics of a wave produce different forces along the position of the wave (Thurman and Trujillo, 2001). Figure 8.14 shows the directions of these forces and velocities. At the trough of the wave, the relative velocity

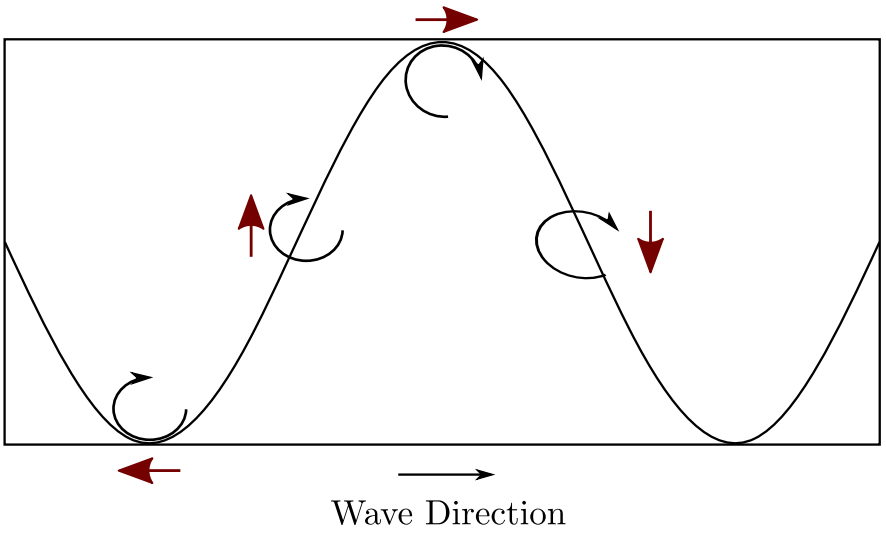

FIGURE 8.14: Orbital mechanics of a wave.

of the water on the surface is opposite of the wave direction. On the backside of the wave, the movement becomes perpendicular to the wave surface. At the crest, the surface velocity aligns with the wave direction, before pointing downward on the face of the wave.

This change in relative surface velocity has an impact of the actuation of the vessel, where near the crest of the wave, the relative velocity of the water flowing over the rudders slows down reducing their actuation force (Tupper and Rawson KJ, 2001). This reduces the ability to counter steer any wave-induced yaw effects. The variable relative velocity profile of the water in a wave can induce asymmetric periodic surging, Spyrou et al. (2016). For a vessel traveling at the wave speed or just above, the danger lies in becoming trapped on the face of the wave. At the trough, the surface forces push the vessel back towards the face of the wave until it reaches an equilibrium point where the forces of gravity balance with the wave and drag forces on the boat, resulting in the boat surfing down the wave. It can be difficult to escape the surf-riding condition. Near the crest of the wave, there is a risk of the propellers and rudders lifting out of the water, in which case all actuation is lost. As seen in Carrica et al. (2012), when the propellers and rudders leave the water, the controller increases their actuation in an effort to control the vessel, and when the propellers and rudders reenter the water, usually after the vessel slows down, there is a sudden actuation moment induced in the roll and yaw direction exacerbating any current broaching.

8.2.1 Following Sea Tacking Planner

The approach in this thesis is one based on avoidance. The exact conditions in which broaching occurs for the vessel in this thesis are not known, due to the need for a CFD or experimental analysis such as the ones cited above. Also, the simulation model does not contain all the necessary dynamics to accurately capture a broaching event as will be discussed below. However, there are studies which involve analogues of the vessel in this thesis (Bonci et al., 2019; Bonci, 2019). In these and others (Renilson, 1981), generalized conditions in which broaches are likely to occur can be drawn. Figure 8.15 shows these conditions. Broaching usually occurs in Froude numbers 0.3 and above. The Froude number is defined as:

$$Fr = \frac{U(t)}{\sqrt{gL}}, \tag{8.1}$$

where $U(t)$ is the forward velocity of the vessel, g is the acceleration due to gravity, and L is the vessel waterline length. For the vessel in this thesis traveling at the desired velocity that has been used throughout, 4 m/s, the Froude number is 0.38. Another criteria is the wave length to vessel length ratio $\frac{\lambda}{L}$ with the most dangerous ratio between 1-3.5. A wave steepness, H/λ, where H is the wave height, of 0.06 or higher is more likely to cause a broaching. Finally, as discussed above, the broaching typically occurs when the vessel is traveling just above the wave speed known as celerity, and surge forces push the vessel back to the equilibrium surf-riding zone on the front face of the wave. The risk of broaching reduces as the angle between the major wave direction and heading angle exceeds 30°, as the differential velocity between the wave increases to the extent that the wave passes the vessel without entrapping it in the surf-riding equilibrium point.

With the broach zone established, the task of the tacking planner is to provide a reference heading and velocity which avoids the broach zone, and the task of the controller is to adhere to these references. The search zone for the tacking planner is highlighted in blue in figure 8.16(a). As the dynamics of the vessel are once again symmetrical about the wave direction, only half of the following and quartering seas is used. The angle and path length definitions are provided in figure 8.16(b).

The same cost equations from chapter 6 are used for following seas, including the surge force and actuation terms. Since the primary objective of the tacking planner is to avoid references in the

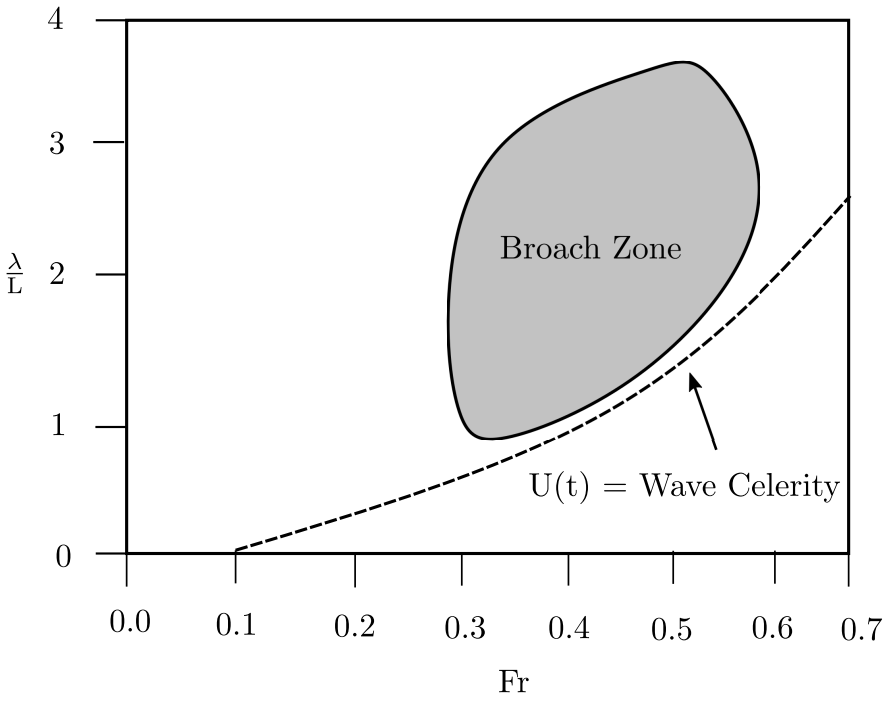

FIGURE 8.15: A plot showing the typical operating zone in which broaching is likely to occur.

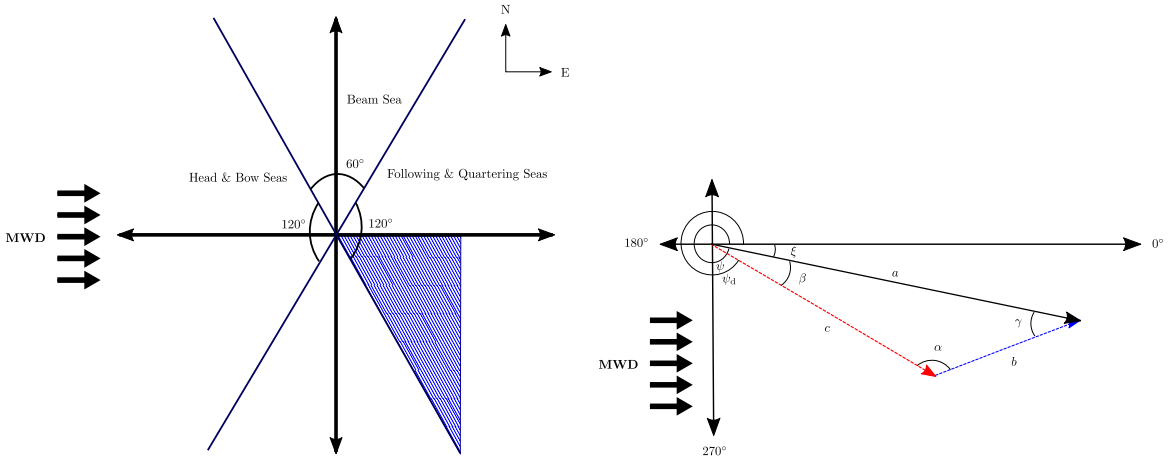

(a) The zone of following seas used in this section

(b) Tacking angles and path terms for following seas.

FIGURE 8.16: These figures show following seas and path and angle definitions for this section.

broach zone, several logical checks are implemented before the cost is calculated. The checks are:

1. Is the Froude number of the desired velocity $\geq$0.3? If no, then the tacking planner can calculate the optimal path on a restricted velocity interval of $u(t) \in [1, Fr]$.

2. If the Froude number of the desired velocity is ≥ 0.3, is the desired heading within 30° of the wave direction? If no, then the tacking planner can calculate the optimal path on a restricted heading interval of $\psi \in [\text{MWD} + 30°, \psi_{\text{MAX}}]$.

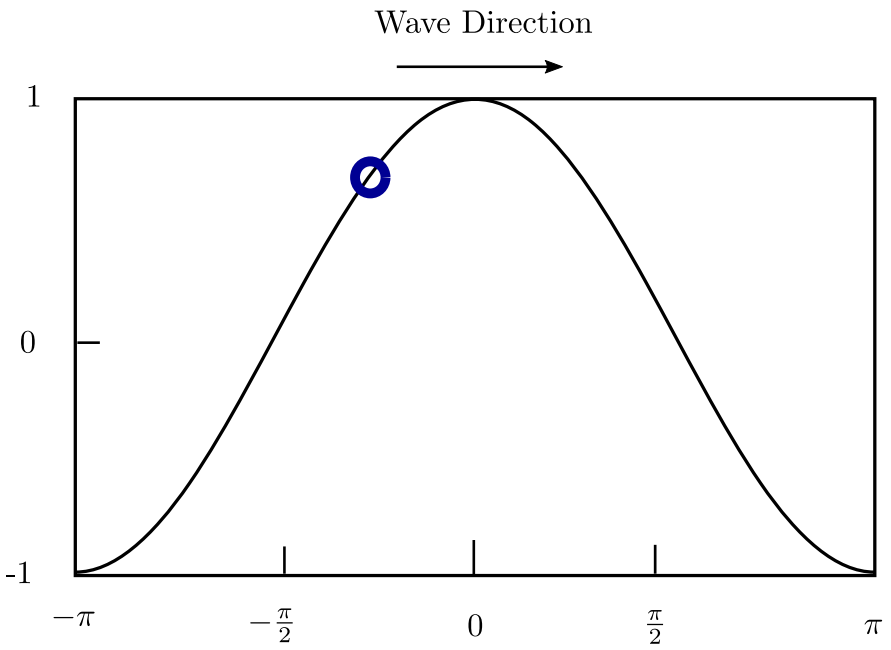

FIGURE 8.17: Ideal location upon the wave in a following sea.

3. If the desired heading and velocity are within 30° of the wave direction and above $Fr = 0.3$, then given the planar wave forces on the back of the wave, can the vessel match the wave velocity? If yes, travel at the wave velocity, if no, then the tacking planner can calculate the optimal path on a restricted velocity interval of half the wave velocity, $u(t) \in [1, 0.5u(t)_{\mathrm{w}}]$, where $u(t)_{\mathrm{w}}$ is the wave speed.

As mentioned in check 3, the tacking planner creates a reference for the vessel to travel on the back of the wave, if the vessel can match the wave velocity. In figure 8.17 the blue circle indicates the reference wave location, χ_{w}. The ticks on the bottom indicate the relative location upon the wave, with 0 being at the crest of the wave, $[0,\pi]$ is the front of the wave with $[0,\frac{\pi}{2}]$ being the surf-riding zone. The back of the wave is $[-\pi,0]$ with the tacking planner reference being at $-\frac{\pi}{4}$ or -45°. This location was chosen as it provides a good buffer length from going over the crest or slowing down into the trough. With the tacking planner defined, table 8.6 presents the results of the following sea tacking planner. When calculating the ability to travel at the wave velocity, (6.3d) is used to determine the required propeller speed which balances the wave and drag force to result in a steady velocity at the desired χ_{w}. This propeller speed is provided as a reference to the controller in, lieu of the previous method which calculated the propeller reference speed for calm water. These references are provided in the table. Note that for a heading of 120°, the reference velocity is above the stated operational velocity of the vessel, however, the propeller speed is below its maximum

TABLE 8.6: Tacking planner results for following seas. (Note: D=Direct, T=Tacking)

Wave Condition & Heading	Heading (deg)	Velocity (m/s)	Propeller Speed (rps)
0.5m 90°	90	5.77	7
0.5m 105°	105	5.97	7.91
0.5m 120°	120	6.66	10.23
0.5m 135°	135	4.3	-
1.5m 90°	90	8.92	12.7
1.5m 105°	105	9.23	13.5
1.5m 120°	120	10.3	16
1.5m 135°	135	5.8	-
2.5m 90°	90	10.9	15.18
2.5m 105°	105	11.28	16.18
2.5m 120°	120	12.59	19.49
2.5m 135°	135	6.5	-

range with the wave force providing additional forward acceleration to achieve the reference velocity with less propeller actuation. It should also be noted, for high wave and wave force scenarios, it may be unwise to try and travel near the operational limit of the engine, as there is little range left to mitigate any additional disturbances that may enter the system. At the 135° heading, the vessel can not match the wave velocity, as the angle between the wave direction and vessel heading is too steep, so the minimum cost of the tacking planner is used to determine the velocity and heading. In these scenarios, the propeller speed reference is calculated using the calm-water assumption again. For all wave conditions and headings, the tacking planner prescribes path following.

The tacking planner also provides the wave location, χ_{w}, reference. Two of the possible methods were considered for this. One is the reintroduction of the wave state into the state dynamics. As before, the wave state would be height agnostic, only varying between -1 and 1. The tacking planner wave reference of -45° would be converted to the height position of the wave, for example to 0.7071. As can be spotted, this is not sufficient information to locate the position along the wave as $\chi_{\mathrm{w}} = 45°$ also has a height of 0.7071. The derivatives or slopes of these two positions differ, so, theoretically, the velocity of the wave state could be used, however, this assumes a constant encounter frequency which may not be true. So another wave state would need to be added:

$$\eta(t) := -\sin\left(\omega t + \frac{\omega^2}{g} x(t)\right). \tag{8.2}$$

The negative value follows with the convention of using the derivative, but a positive sine works as well for giving the position along the wave. This method embeds the location along the wave

in the prediction horizon and the optimal control problem, but requires at least two extra states, and could be more difficult and computationally demanded in a multiple wave state environment. Additional research needs to be conducted to determine how the NMPC would handle a situation in which it is equidistant to two desired χ_w, either in terms of physical distance, or in cost to reach either one.

The second method, and the one used in this thesis, is to allow the tacking planner to create a trajectory of planar coordinates for the NMPC controller, turning the problem into one of trajectory tracking. Using the assumed wave velocity, and the previously determined optimal path, the tacking planner creates a set of (x, y) reference coordinates for each time step to maintain the vessel in the desired χ_w location. In a manner similar to initiating a tack, the position of the vessel in the prediction horizon is given to the tacking planner, however, it is now the entire predicted positions not just the last position. If at any point along the prediction horizon the vessel falls to a χ_w position of -90° or below, the reference χ_w is shifted back to the wave behind at that point in the prediction horizon and all points after. Previously, it was discussed how the abrupt change in references is not ideal for the NMPC, in this instance the sharp change in actuation typically seen caused by this method of reference change is the desired behavior. When the vessel begins to drift towards the trough of the wave, slowing down as much as possible to create the largest velocity differential between the vessel and the wave, helps to prevent the vessel from becoming entrapped in the surf-riding zone. Further investigation needs to be completed to determine if a different transition strategy provides the same benefits, while improving the robustness of the NMPC.

8.3 Following Sea Model Inaccuracy

Issues arose when trying to implement the PID and NMPC controllers in the simulation. The wave model, SWEM, uses fluid dynamics to create the sea surface, but the output is the physical parameters of the wave, such as height, frequency, and travel angle. SWEM outputs a current velocity, but it is a mean current velocity along a fixed direction, and does not vary among the phase or direction of the wave components, as the orbital dynamics suggest it should. The coefficients of the vessel dynamics are similarly found using CFD software, and accounts for the orbital dynamics in the planar degrees to an extent. The actuation of the vessel does not account for the orbital

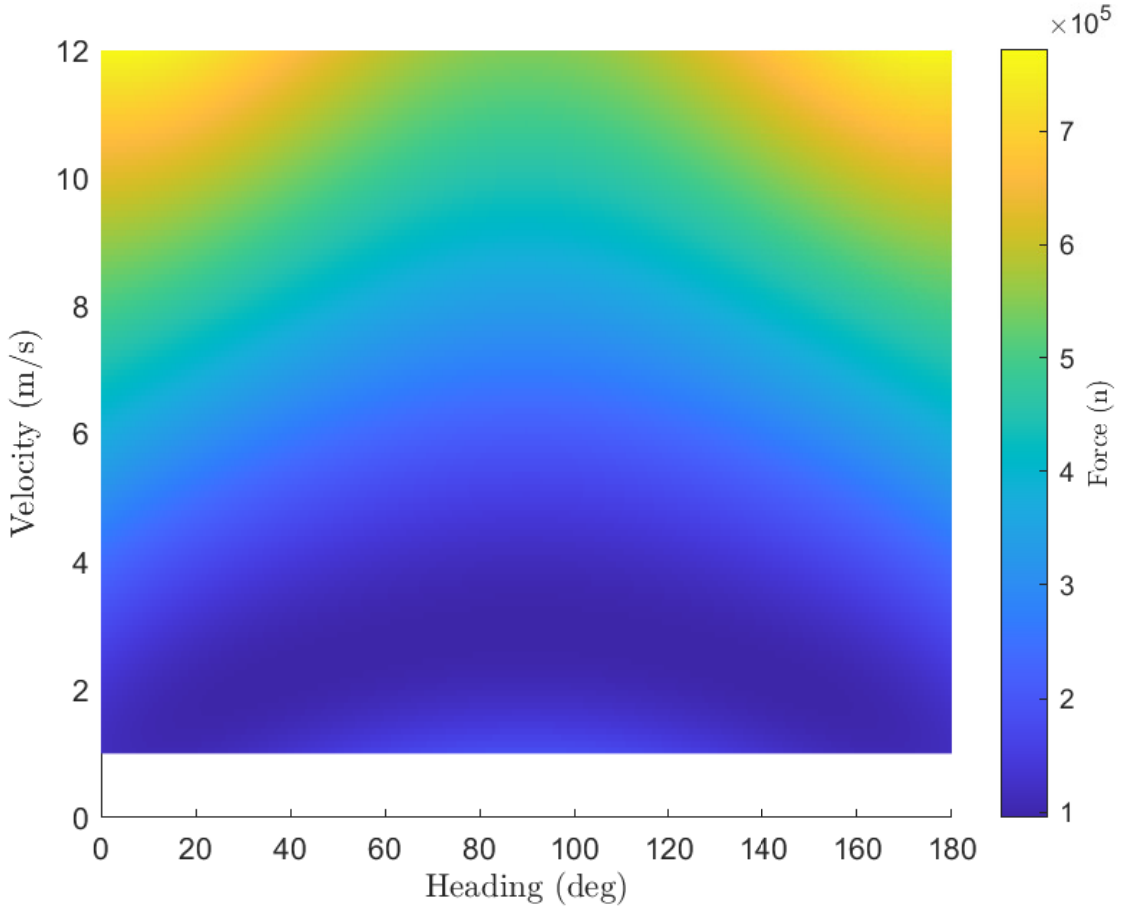

FIGURE 8.18: Wave force in the pitch direction for following seas.

dynamics and the relative fluid velocity along the wave. As such, given a specified vessel velocity, rudder angle, and propeller speed, the actuation forces are constant for all locations along the wave profile. More troublesome is the wave force in the pitch direction. Figure 8.18 plots the pitch wave force in the following sea direction for 2.5 meter waves. The velocity dependence of the pitch force, as implemented in the simulation, is based on the velocity of the vessel and not the relative velocity of the vessel and wave. For traveling at the wave velocity of 10.9 m/s with a heading of 90°, the maximum force in the wave direction is approximately 5.25×10^5 n.

To see what effect this has we first look at figure 8.19. In this figure, the PID controller travels at 90° at the wave velocity in 2.5 meter waves with a desired velcity of 0 m/s. The pitch angle reaches up to 40°, then oscillating before settling to about 28°. This occurs on the back of the wave at a location of 25°. For a constant position, and with all of the states reaching an equilibrium point, the primary forces acting in the pitch direction should be hydrostatic forces. In pitch and heave

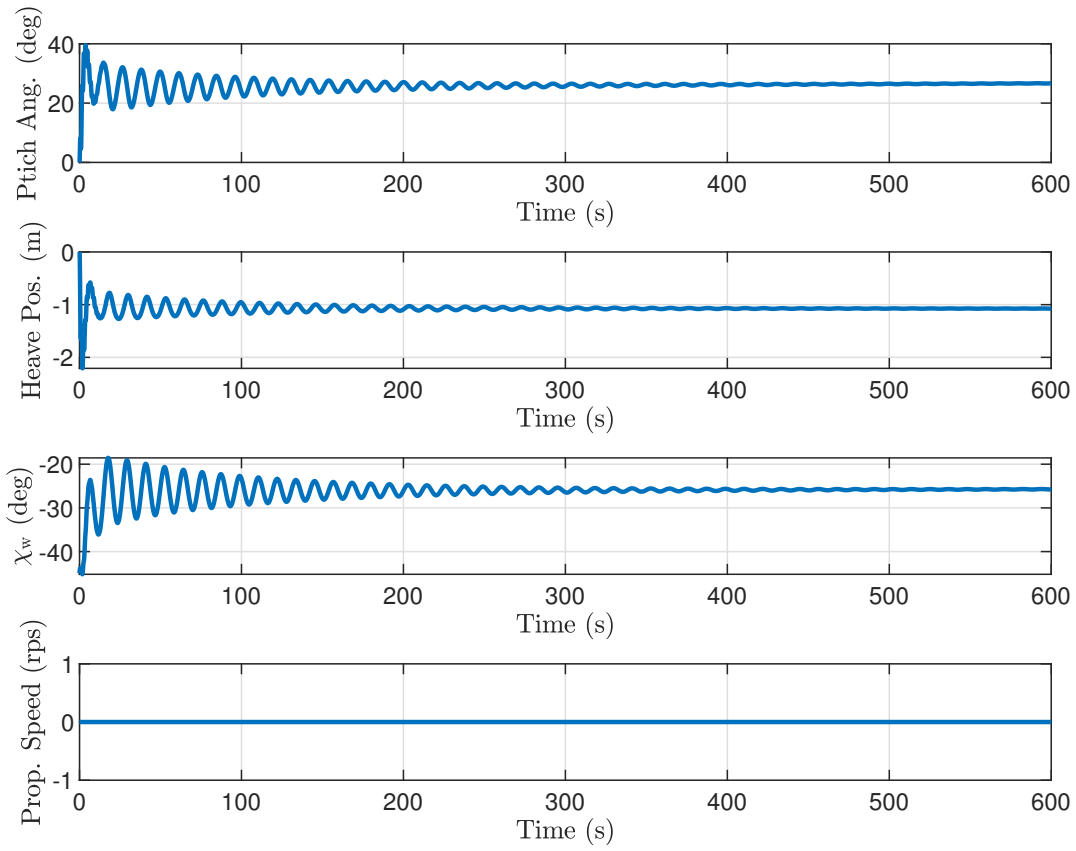

FIGURE 8.19: PID with 90° heading in 2.5 meter waves. Initial velocity of 10.9 m/s with a desired velocity of 0 m/s.

direction, the vessel should rest on the back of the wave at roughly the angle of the wave. The pitch angle in figure 8.19 is much higher than what would be expected. The wave steepness is 0.033, which is very shallow. Even if the bow was at the wave crest height and the stern was at the trough, this would only be 12.6 degrees. As Newton's laws tell us, the pitch angle is a result of the double integration of the pitch acceleration over time. With the wave force in the pitch direction, seen in figure 8.18, so high, and the fixed location upon the wave, the pitch angle continues to increase until the restoring forces bring it to an equilibrium. The heave position is what would be expected for this wave position. Note that the heave vector points down towards the earth so a negative heave value is actually up in more common vernacular. Also, note the zero propeller speed. This will be discussed further below.

The same simulation was run again, but instead of the vessel starting with a velocity of 10.9 m/s it is started at 0 m/s. The wave quickly forces the vessel up to speed and beyond the wave position

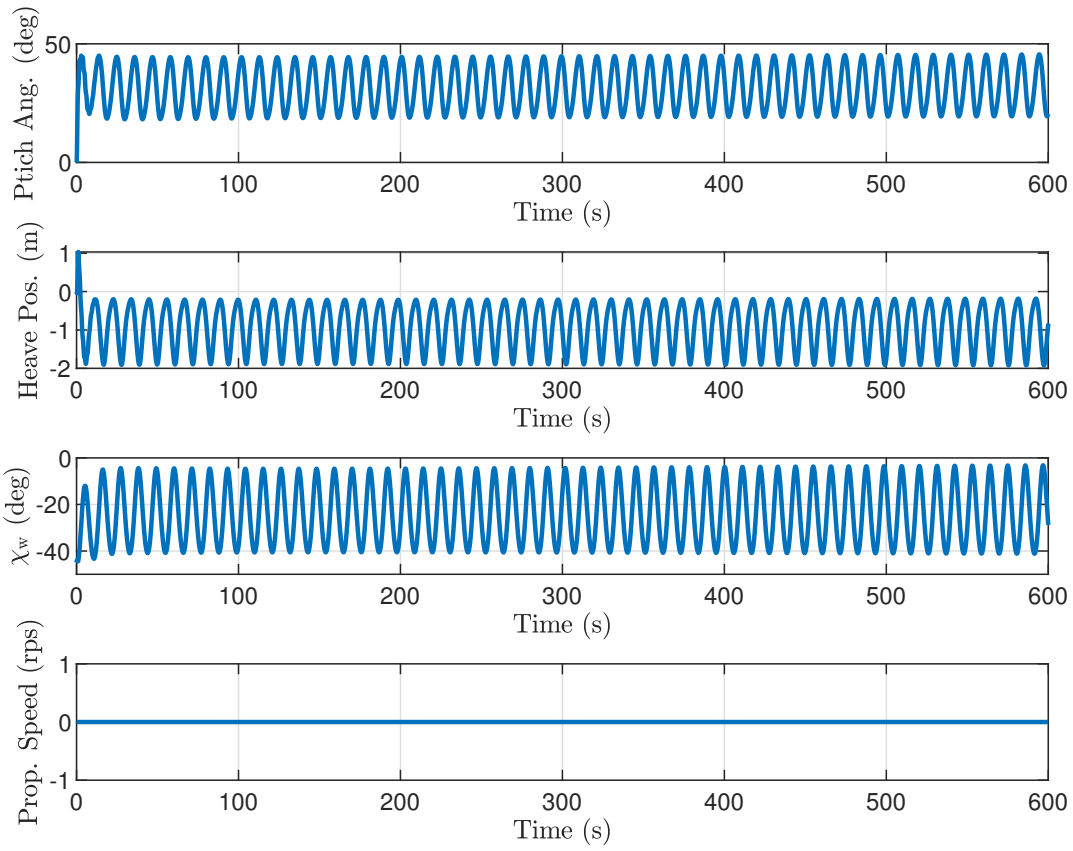

FIGURE 8.20: PID with 90° heading in 2.5 meter waves. Initial velocity of 0 m/s and desired velocity of 0 m/s.

seen in the previous example. Again there is no propeller actuation, the wave is surging the vessel forwards and backwards in what appears to be a limit cycle on the back of the wave. Now with the additional movement, hydrodynamic forces begin to influence the pitch angle, which is now oscillating between 25-45° with the heave position also varying from -2 to -0.25 meters. Again, the pitch angle appears much higher than would be expected, given that the vessel is traveling between -5° and -40° on the back of the wave. It also appears that there is some form of an equilibrium point of the back of the wave which, to the author's knowledge, is not a known phenomenon. The vessel settles around this point on the back of the wave.

To test if the vessel could travel out of the supposed equilibrium point on the back of the wave, the same simulation was ran again with a desired velocity of 12 m/s, figure 8.21. This time the vessel accelerates over the crest of the wave, before the actuation, wave forces, and gravity balance on the front of the wave with a wave position of about 18°. Then to test if this if the vessel would

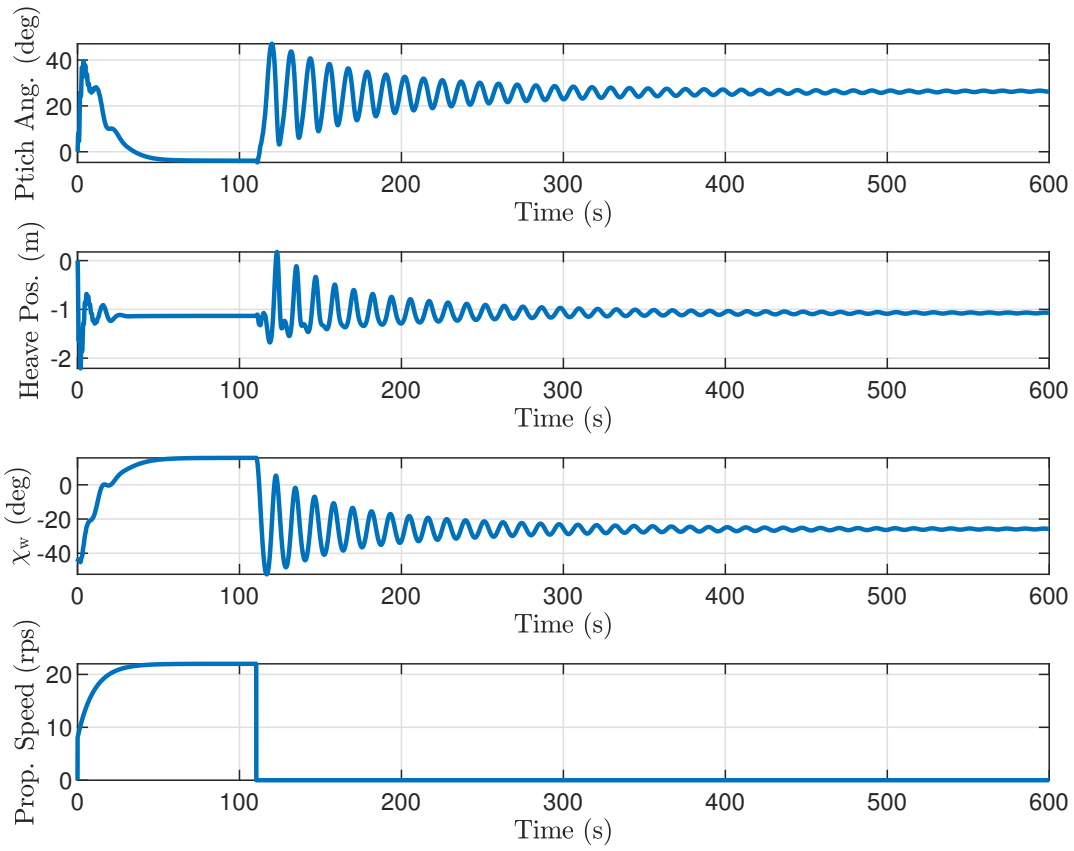

FIGURE 8.21: PID with 90° heading accelerating to the front side of the wave before slowing down with a desired velocity of 0 m/s to the backside of the wave.

stay in the surf-riding zone, the desired velocity was changed to 0 m/s at 110 seconds. The vessel quickly loses velocity, falling back to a wave position of -45° before showing similar behavior to the first example in figure 8.19. Interestingly, it does not exhibit the stable oscillation of the second example.

To test the stability while traveling at an angle to the wave direction, the vessel was simulated with a desired heading of 120° with a desired velocity of 12.59 m/s to match the wave velocity along the wave direction. The vessel has two events in which the roll angle peaks above 50°, but as the vessel accelerates it again finds a stable state at the crest of the wave. At 180 seconds, the desired velocity was changed to 10 m/s to determine if the vessel would move to the backside of the wave. Instead, the oscillation about the crest changed slightly, but remained. When the desired velocity was changed back to 12.59 m/s, a new more aggressive oscillation occurred in the surf-riding zone of the wave. The pitch angles varied by as much as 75° in this simulation.

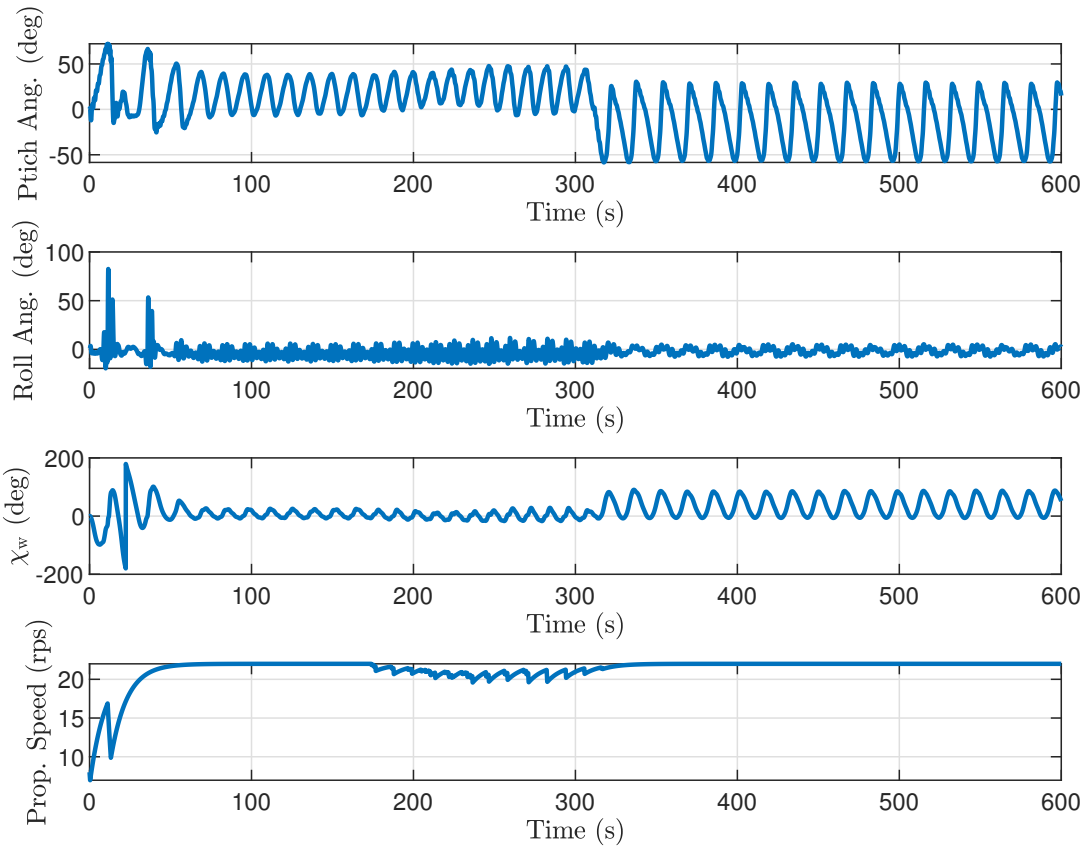

FIGURE 8.22: The PID controller with a heading of 120° with an initial desired velocity of 12.59 m/s, reduce to 10 m/s, then back up to 12.59 m/s.

Figure 8.23 plots the NMPC performance when traveling at a desired heading of 90° in 2.5 meter waves. The pitch angle greatly effects the NMPC controller. The NMPC model does not contain the Euler transformation equations to translate the body fixed velocities to NED positions. Instead, the positions of the NMPC model are the integration of the velocities. This means that when the vessel is at a 40° angle, a velocity in the body fixed surge direction is actually a velocity in both the surge and heave NED direction. This causes issues with the NMPC controller as the predicted values begin to diverge from the measured values it is being sent from the simulation. This is apparent, as the pitch angle settles to near zero at 32 seconds, the controller's behavior also settles and reaches a stable operation point on the front side of the wave.

It is apparent that the large pitch angle causes issues with the NMPC controller. It is also far larger than would be expected. In the other DOFs, the wave force is mostly independent of the vessel velocity, however, the pitch wave force increases as the vessel velocity increases. It could,

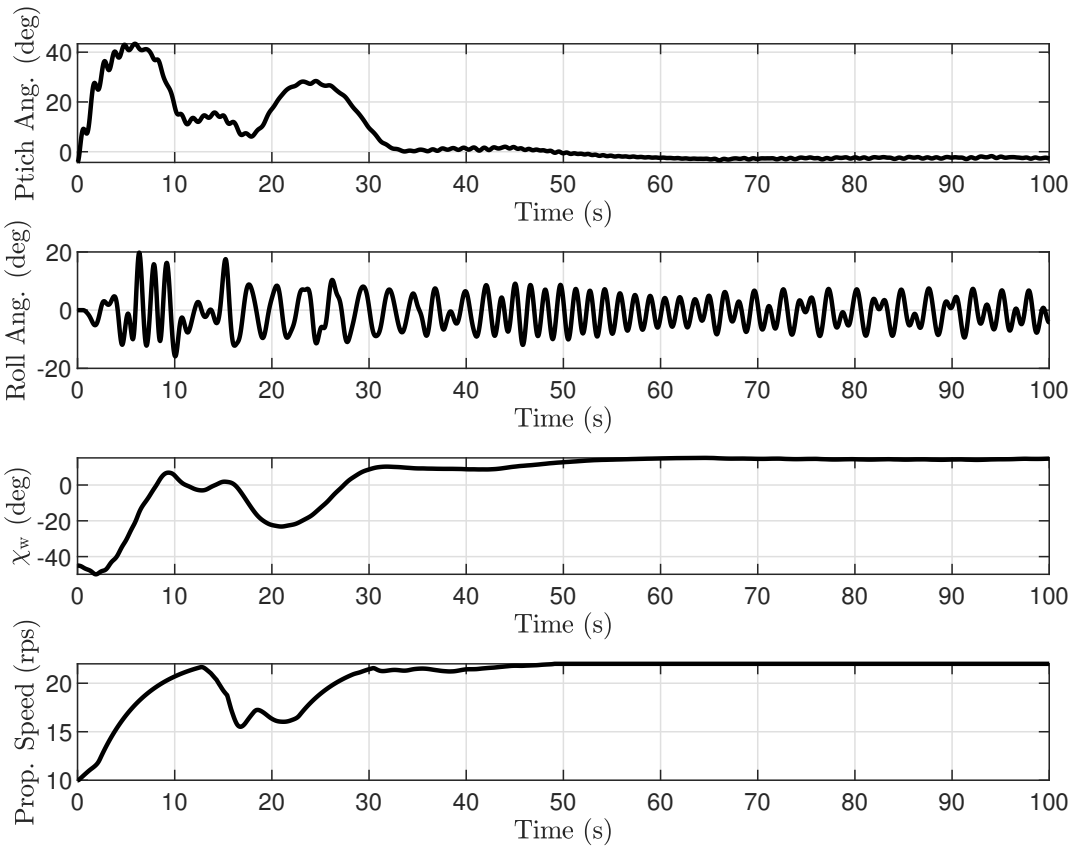

FIGURE 8.23: The NMPC direct controller with a heading of 90°. The controller struggles with the high pitch angle.

perhaps, be a case that the velocity axis in figure 8.18 should be the relative wave velocity, though this would not work in the head sea scenario. The figure shows that the minimum wave force in the pitch direction for a heading of 90° occurs at 3 m/s. To test if this was the case, the relative vessel-wave velocity was calculated as:

$$U_{\mathrm{r}}(t) = 7\cos(|\psi_{\mathrm{MWD}} - \psi|), \tag{8.3}$$

where the major wave direction is 90°. A velocity of 7 was chosen as this results in the wave force in the pitch direction being near its minimum, according to the pitch RAO. This relative velocity was then used to calculate the wave force in the pitch direction. The PID controller was simulated with a desired heading of 90° and the results are shown in figure 8.24. The pitch angle is smaller now, with the maximum reached at about -32° before settling to -10°. However, the wave position

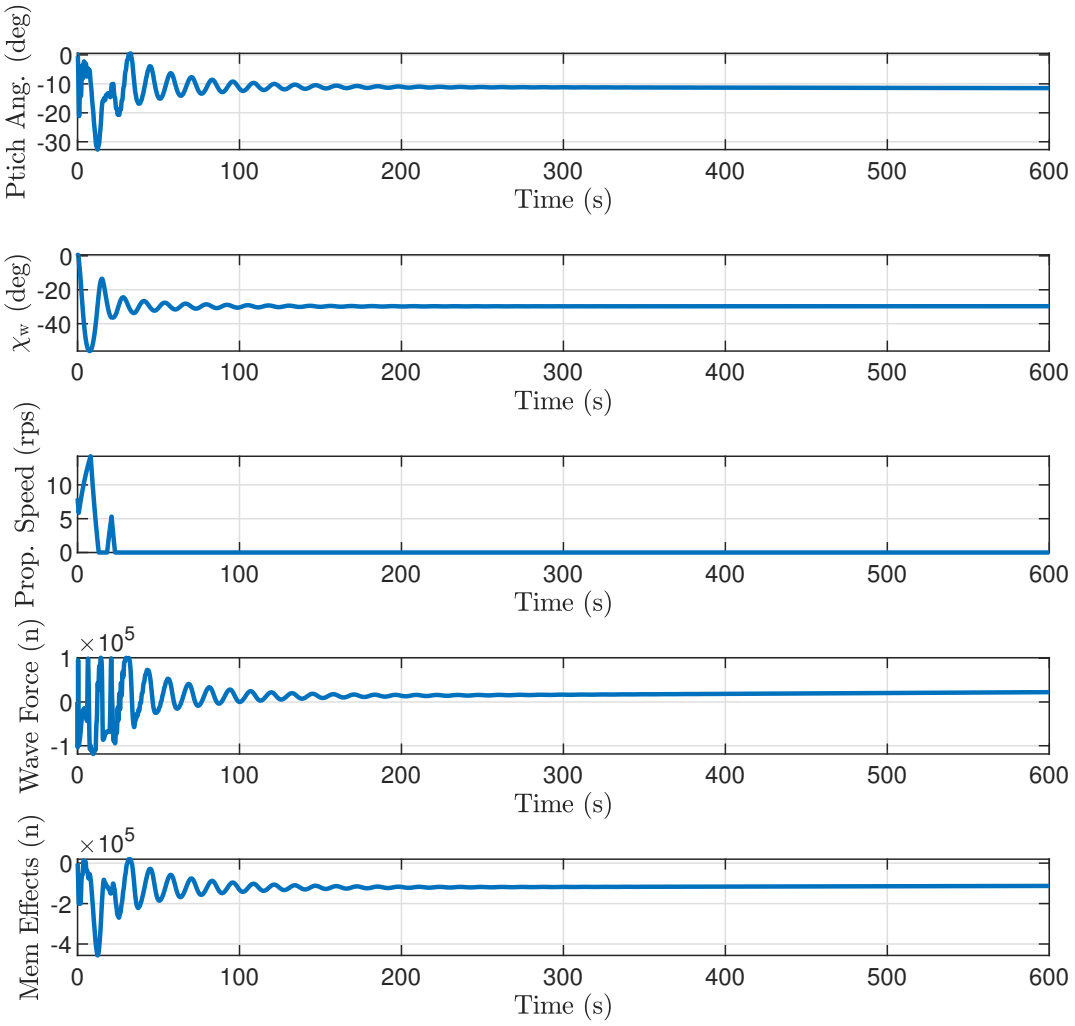

FIGURE 8.24: PID with 90° heading in 2.5 meter waves. Initial velocity of 10.9 m/s with a desired velocity of 10 m/s and pitch force reduced with new relative velocity term. Memory fluid effects cause the pitch angle to be negative on the back of the wave.

is -30° on the backside of the wave. The pitch angle should be positive in this wave position. To see why, the memory fluid effects in the pitch direction were plotted along with the wave force in the pitch direction. The wave force in the pitch direction is much lower than before and positive, but the memory fluid effect in the pitch direct is negative and has a larger magnitude than the wave force, resulting in an overall negative pitch angle.

The dynamics in the simulation model are highly coupled and balanced, and removing just one force from the equation does not work. Figure 8.25 shows what occurs when the memory fluid effect is

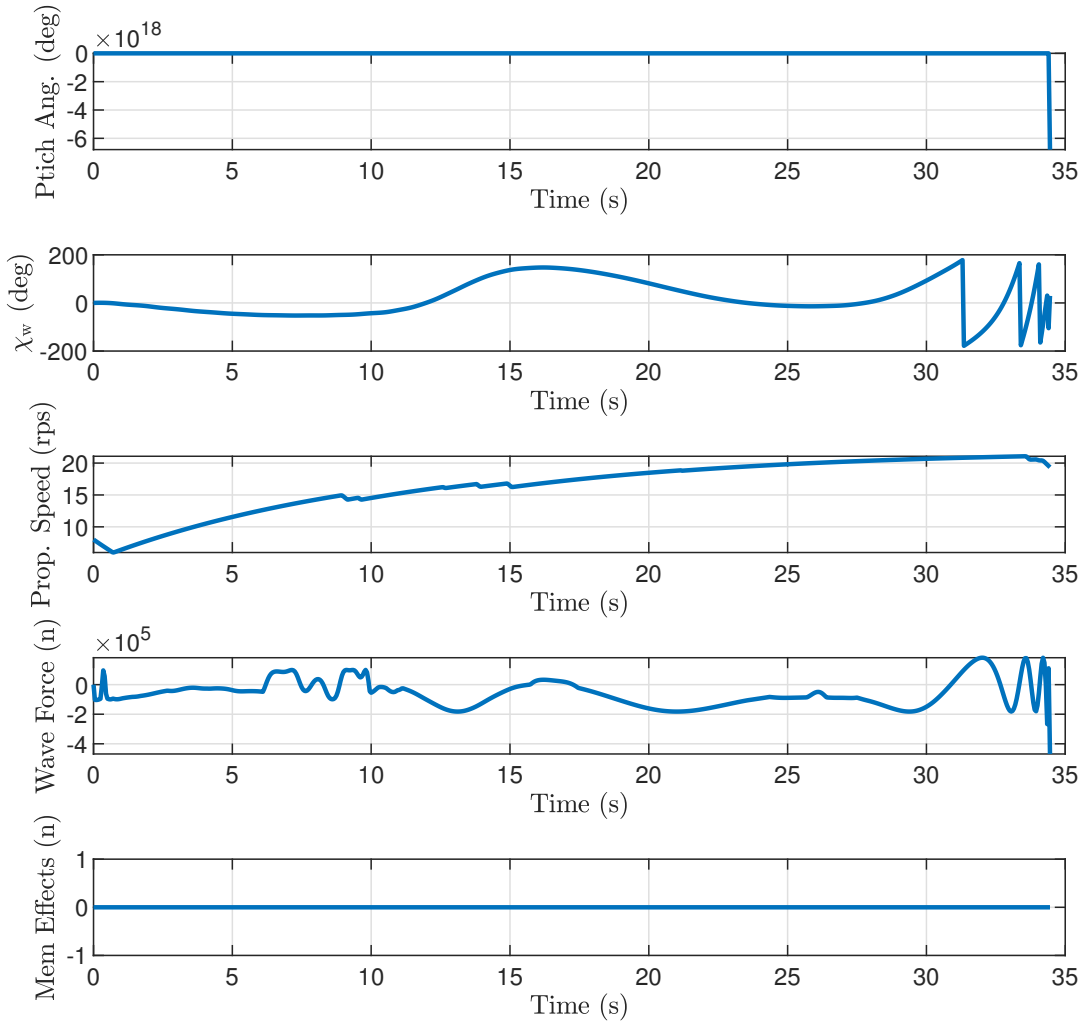

FIGURE 8.25: PID with 90° heading in 2.5 meter waves. Initial velocity of 10.9 m/s with a desired velocity of 10 m/s and pitch force reduced with new relative velocity term. No memeory fluid effects in the pitch direction causes the simulation to crash.

removed for only the pitch direction. The simulation crashes with the pitch and heave positions of the vessel going to infinity.

With the dynamics of the pitch direction in the simulation not amenable to modification, it was removed in order to ascertain if a 4 DOF simulation model could still give a reasonable indication of a controller's performance in a following sea. The heave direction was also removed because of the coupling between the pitch and heave directions. With this new simulation model, the PID controlled vessel was simulated with a desired heading of 120°, desired velocity of 12.59 m/s to

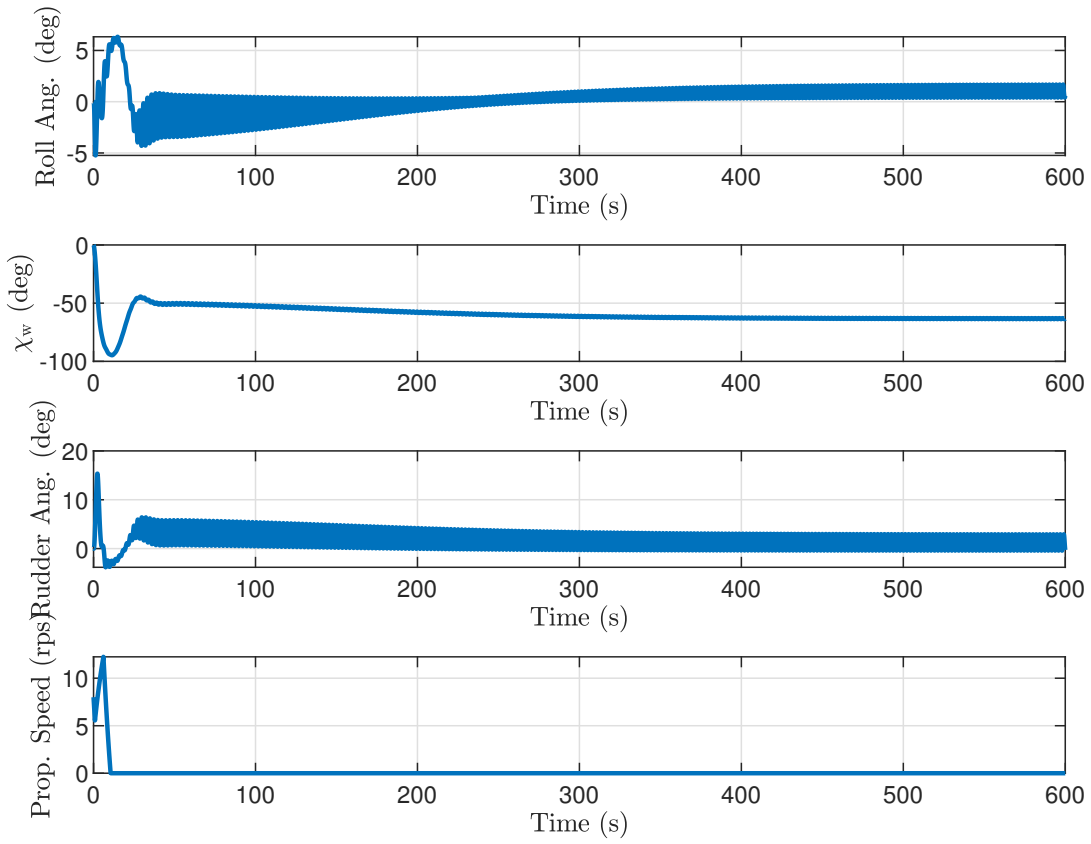

FIGURE 8.26: Reduced 4 DOF simulation model with a heading of 120° and 12.59 m/s desired velocity.

match the wave velocity, and an initial condition on the crest of the wave. This is plotted in figure 8.26. The vessel quickly falls back to the trough of the wave behind it before the propellers accelerate it part way back up the back of the wave, where the wave force in the surge direction becomes positive, and moves the vessel the rest of the way to the stable position on the wave of -60°. Then, like the other examples, it stays in the stable state. The rudder actuation angles are small and near zero.

On a wave with orbital mechanics, the performance of the propellers and rudders varies along the wave. To try to simulate this, and attempt to rid the simulation of the stability state, a relative water velocity was added to the actuation mechanics. This was the same relative velocity that was used to reduce the wave force in the pitch direction. Originally, the vessel was tested with a fixed velocity along the wave profile. With no significant changes, this was changed to reflect the different

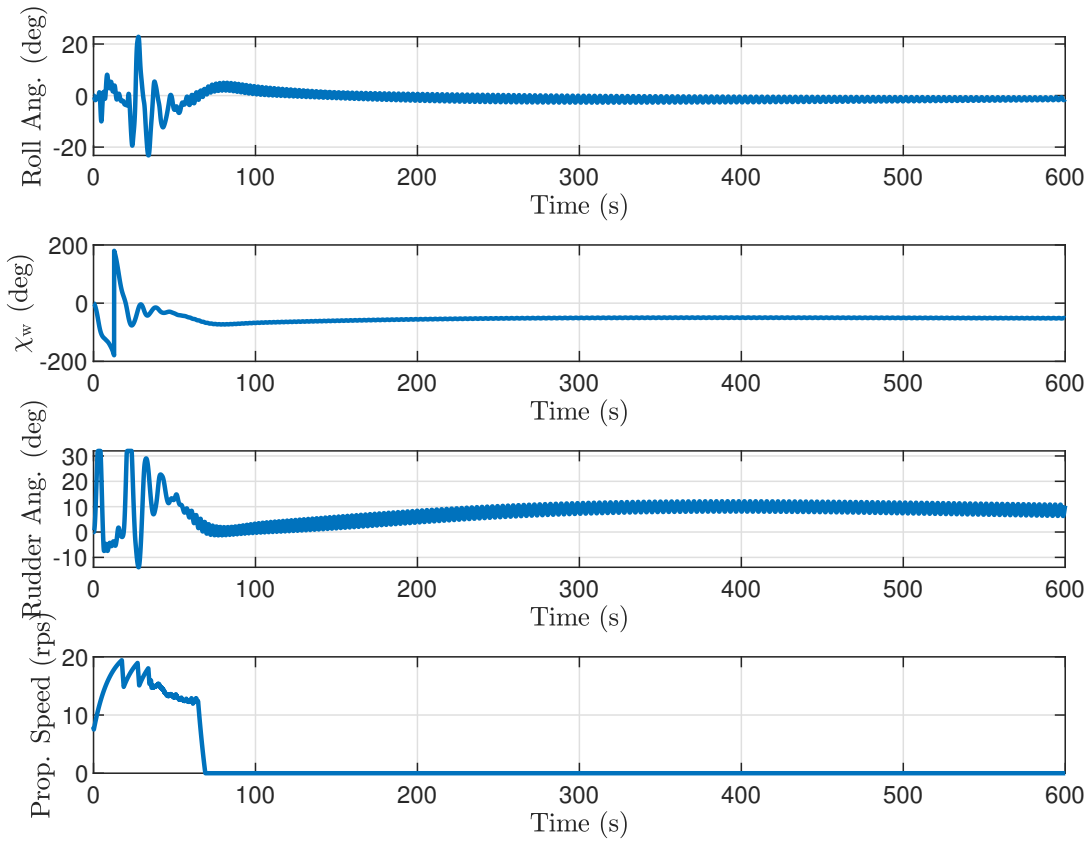

FIGURE 8.27: Reduced 4 DOF simulation model with a heading of 120° and 12.59 m/s desired velocity. The actuation performance is modified to simulate the orbital mechanics of the wave.

velocities of the water along the wave profile. To calculate this (8.4) was modified to:

$$U_r(t) = 7\cos(\chi_w)\cos(|\psi_{MWD} - \psi|). \tag{8.4}$$

Now, as the vessel travels at the wave velocity with a heading on 90°, on the crest of the wave, the relative water speed over the propellers and rudders is 3.9 m/s, while in the trough it is 17.9. The vessel can now produce a large yaw actuation force in the troughs, while the propeller actuation is limited, and on the crest, the rudder actuation is limited, but the propeller can produce more force in the surge direction. This was simulated with the same conditions as the previous example and the results are shown in figure 8.27. This time, with the reduced force in the surge direction from the propellers when the vessel nears the trough at the beginning of the simulation it is unable to accelerate back up the wave so the vessel falls back to the wave behind. After this, however, it

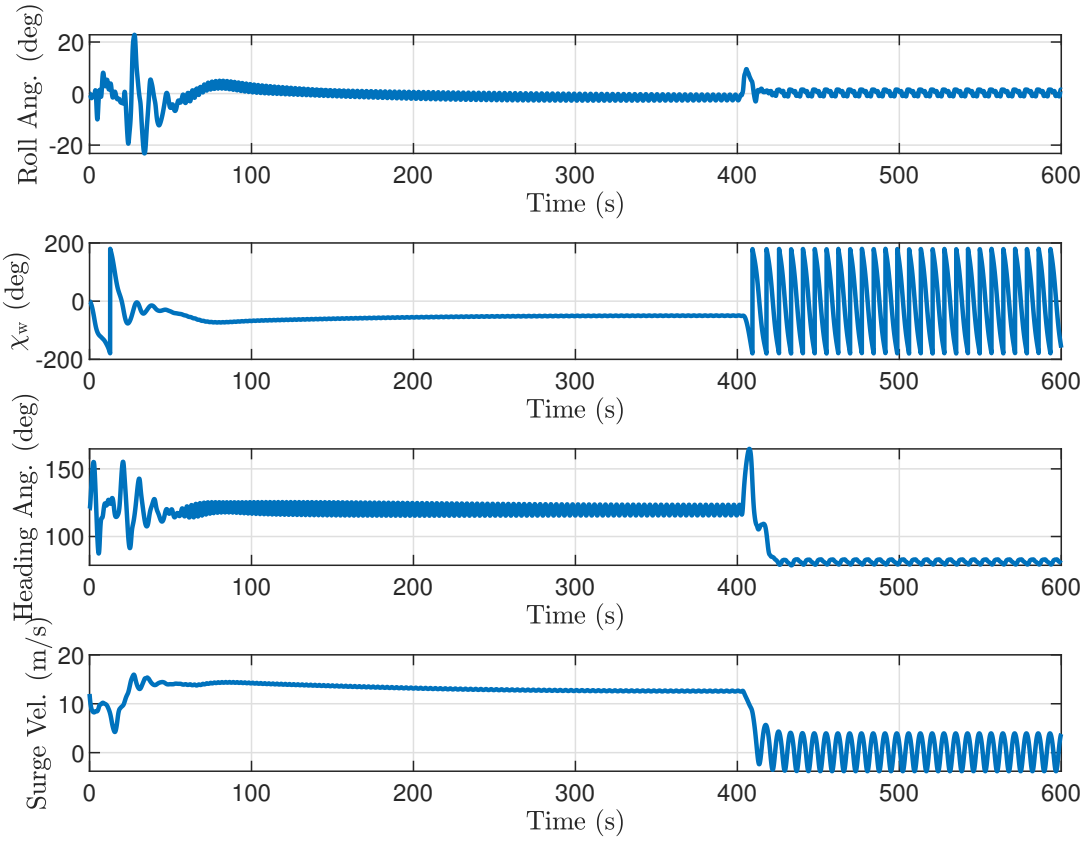

FIGURE 8.28: Reduced 4 DOF simulation model with a heading of 120° and 12.59 m/s desired velocity. At 400 seconds the actuation is cut off and the vessel returns to a heading of 90° and oscillates among the waves.

reaches the same stability point where it remains for the rest of the simulation. The only difference at this stability point is due to the reduced actuation force from the rudders. The rudder angle increases from near zero to around 10°, but this is well within the range of the capable rudder angles.

To determine how stable the vessel is in these steady state conditions a variety of simulations were run, wherein arbitrary disturbances were added, or a small full sea state was superimposed. Open loop rudder control was also used and, finally, total loss of actuation tested. With the disturbances added, the PID mitigates them, which is the designed purpose of feedback control. In open loop control, with the heading near the direction of the wave, the vessel remains stable, with no propeller actuation necessary to maintain the steady state. For larger heading angles, the oscillations in the yaw direction slowly grow until the steady state is lost and the wave passes the vessel. The worse

case scenario is the total loss of actuation. Again, if the initial heading angle is near the wave direction, the vessel maintains a steady state of moving at the wave velocity on the backside of the wave. Figure 8.28 shows the results of a large heading angle. The vessel is traveling at an angle of 120 degrees on the back of the wave when actuation is cut at 400 seconds. The heading angle increase to 165 degrees as the vessel moves down to the trough of the wave before the next wave rights the heading to 90 degrees where the vessel settles into an oscillatory motion as the waves continue to move past the vessel. The average forward velocity at this point is just above 0 m/s.

With the wave stabilizing the surge velocity, and the heading when the yaw angle is near the wave direction, it becomes difficult to assess the performance of the controllers. Even a non-actuated vessel is able to maintain the same steady state as the controllers in some scenarios. Additionally, the larger surge force on the back of the wave can make it impossible for the NMPC controller to reduce the tracking error to zero. If the stable location on the wave is above -45° for a given heading, with the constraint on the controller that the propeller speed must remain at zero or above there is no way for the controller to satisfy the tracking reference. Every effort was made to have the simulation model reflect the known behavior in following seas to ascertain the performance of the controllers, unfortunately, no useful data on the performance of a PID or NMPC controller can be produced for following seas. Also, the larger than expected pitch angle when traveling with the wave may indicate that the previous pitch results in the beam section for headings that traveled with the wave, may be higher than they should be.

8.4 Summary

This chapter investigated the performance of the controller in beam and following seas. Roll penalization was added to the controller, due to the concern of excessive roll angles in beam seas. The tacking planner was modified to reflect the reduced forces in the surge direction, and an iterative method was introduced for the tacking planner owing to the asymmetrical cost surface. The differing velocities of the tacking NMPC made direct comparisons to the PID and NMPC direct controllers difficult. Even in beams seas, the wave force in the roll direction remained small enough, that often the rudder force in the roll direction was larger. This was reflected in the lower roll angles for the NMPC direct controller in 2.5 meter waves compared to 0.5 meter waves. The NMPC direct

controller still managed general improvements in the roll angle over the PID controller, but the pitch results were mixed. The NMPC direct controller also saw general improvements in performance when the full sea state was added. A modification of the tacking initiation by the tacking planner reduced the tacking boundary over shoot for the NMPC tacking controller. Testing of the impact on performance for various step sizes and horizons lengths reinforced the previously found results. The topic of control in following seas was introduced in the second half of the chapter. The difficulty of this task, and the subsequent tacking planner for following seas were laid out. Methods for maintaining a defined position upon the waves were presented, with the method of the tacking planner handling the references chosen. Unfortunately, the performance of the controllers in following seas could not be discovered. Modifications to the simulation were made to better reflect the vessel behavior in following seas, including mimicking the effects the wave orbital mechanics have upon actuation, however, there remained a strong stable point on the back of the wave that, for certain conditions, even non-actuated vessels remain stable at.

Chapter 9

Conclusions

This work was aimed at producing a controller which having knowledge of the sea-state could reduce the wave force, or wave induced motions to reduce the risk of capsizing. To meet this aim the following was performed:

- The previously developed Halcyon and SWEM models were modified. For the simulation models themselves, changes were made to the interpolation methods used for better accuracy in single harmonic environments. The equations of motions were modified, and some simplifications were made such as removing the memory fluid effects for the model used in the controller.
- It was shown that the encounter frequency is not suitable to be linearized without loss of knowledge of the vessel's position upon the wave. This required the use of a nonlinear control method, and with its fast computation, natural constraint handling, and predictive nature, the Real Time Iteration scheme for Nonlinear Model Predictive Control was chosen.
- The task of path following and wave mitigation was formulated as an optimal control problem. This was done first as a 1 DOF simulation, and increased up to a full 6 DOF simulation.
- The solution to the 6 DOF optimal control problem showed that tacking on two time-scales, that is, a small high frequency tack on each wave, along with a larger drift tack to increase the average encounter angle and decrease the average wave force, was the optimal navigation method.

- The previously found optimal solution is not conducive to a single NMPC controller due to the disparate time-scales to the two control objectives. Thus a time independent tacking controller was developed to be the outer control loop, presenting the inner NMPC controller a tacking path to follow.

- This tacking method proved to be superior in head seas when compared to a more conventional LOS PID path following method which ignores the wave induced motions. This performance held even when presented with an unknown full sea-state. The performance advantage in beam seas was less clear due to the minimal roll caused by the waves.

- Finally, practical aspects of the controller were tested such as prediction horizon length, and RAO surface use. For prediction horizon length, it was found that the length should be about 1.3 times the encounter period to ensure the prediction captures the full dynamics of the harmonics. For step size, they should be chosen to have about 25 steps by encounter period for a high enough resolution of the wave curve. This hints at the use of an adaptive controller to change parameters based on wave conditions and heading to ensure the most efficient controller use. For the RAO surface, it appears for now that using the RAO surface of larger waves on calmer sea-states allows for adequate performance, but the opposite is not true. More research into these findings need to be done.

9.1 Future Work

Much work is yet needed to be able to implement the NMPC controller on a real vessel. This thesis began work testing on the use of the RAOs of a single wave height. This would be the simplest implementation based on the assumption that RADAR or LiDar measurements of the sea surface are unlikely to capture individual wave harmonics, but instead relay only the total wave heights. Initial results appear promising with using the RAOs of a 2.5 meter wave on 1 meter wave simulation. More simulations in more environments are needed to determine if this is viable for all conditions. In addition, it needs to be tested against a controller which knows all of the individual wave harmonics. Another method for multiple waves could be the reformulation of the RAOs not as 3D surfaces based upon heading and velocity, but as 4D surface which is dependent on heading, velocity, and wave height.

Another area which needs further research that was introduced in this thesis is the step size and prediction horizon lengths for different sea states. For high-frequency waves, small step sizes are needed, while for slower wave frequency, larger prediction horizons are needed. Static prediction parameters, which satisfy both of these, are inefficient in both. Instead, an adaptive prediction horizon needs to be investigated for use in all wave conditions.

In the literature, many of the MPC controllers were used with LOS heading controllers. This thesis used the NMPC as a reference tracker. One area of interest to the author is the performance difference between the two implementations, as well as the implications of dividing the tasks of heading and velocity control up. Examinations could include LOS MPC, in which the heading is geometrically assigned and the velocity is dynamically altered, or the lookahead distance is dynamically varied by the MPC and the velocity is constant. A geometrically assigned heading eliminates the need for the prediction horizon to capture the entire trajectory back to the path.

Further research which would be more involved is the inclusion of wave forecasting based on measured data instead of the presumed known wave data. The inclusion of a high level COLREG planner, and a hybrid tacking and path planner, which accounts for curved paths around objects, is also needed to complete the controller. Lastly, rebuilding the vessel model and simulating in an CFD program would help to verify the NMPC and PID controllers' ability in following seas.

Appendix A

Publications

Available online at www.sciencedirect.com

ScienceDirect

IFAC PapersOnline CONFERENCE PAPER ARCHIVE

IFAC PapersOnLine 53-2 (2020) 14692–14697

Towards Control of Autonomous Surface Vehicles in Rough Seas

Daniel R. McCullough * **Bryn L. Jones** *
Oscar J.G. Villarreal * **J.A. Rossiter** *

* *Department of Automatic Control and Systems Engineering, University of Sheffield, Sheffield United Kingdom.*

Abstract: This paper addresses the problem of controlling an Autonomous Surface Vehicle (ASV) in rough sea-states, with a view towards minimising wave-induced forces, whilst maintaining headway. This is a challenging control application since, and as is derived in the paper, the interaction between the vessel and the wave disturbance is nonlinear and coupled. This subsequently motivates the novel application of the Real Time Iteration Scheme (RTI) for Nonlinear Model Predictive Control (NMPC) of the ASV. Analysis of the resulting control signal provides an important insight into the role of the wave encounter frequency. Specifically, by actuating at twice the average wave encounter frequency, the nonlinear controller is able to reduce the wave forces, compared to an open-loop controller that achieves the same average velocity.

Keywords: Nonlinear and optimal marine system control, autonomous surface vehicle, nonlinear model predictive control, real time optimization.

1. INTRODUCTION

With the potential to replace manned vessels for dirty operations such as cleaning up oil spills, (Kim et al., 2012), dangerous ones, like those found in mine sweeping, or dull monotonous tasks like patrolling, (Oleynikova et al., 2010), the need for autonomous surface vehicles is increasing. This growth in use necessitates an increase in the ability of the Autonomous Surface Vehicle (ASV) to handle more extreme ocean environments, such as rough seas, in a similar or superior manner as human pilots.

Traditional path following controllers may neglect ocean disturbances, (Lekkas and Fossen, 2014; Oh and Sun, 2010; Çimen and Banks, 2004), or consider only ocean drift forces, (Paliotta et al., 2019; Peymani and Fossen, 2013). Larger vessels, such as container ships can often assume ocean disturbances to be planar for most conditions in sea state 3 or below on the Douglas Scale. For larger vessels in the presence of waves, constraining roll is important for reducing sea-sickness and damage to cargo (Li et al., 2009, 2010).

However, smaller sea going vessels of the magnitude of tens of meters or smaller are greatly impacted by waves. Reinhart et al. (2010) use a priori optimized control path templates to find that tacking in littoral waves reduces bow diving. This behavior is used in a path planning algorithm which, when the angle between desired direction of travel and the main wave direction is smaller than a predefined threshold a secondary point is added to the path to increase the angle and to create this tacking behaviour. A PID controller is used to maintain the planned path without knowledge of the ocean environment which reduces the bow diving but does not eliminate it. With a set maximum pitch and roll constraint, Ono et al. (2014), calculates feasible safe velocity regions for use in path planning in rough seas. The model used a direct input, that is the input is the velocity of the system, allowing it to move from one safe velocity region to the next in one time step. On a boat this would not be possible, and the boat would have to move through unsafe velocity regions and potentially capsize or bow dive. Therefore, in this work we propose an optimal control strategy that is based upon a first-principles model of the ASV and wave interaction dynamics, with a view towards minimising wave induced forces whilst maintaining headway.

The rest of the paper is organized as follows; section 2 presents the derivation of a low-order state space model that describes the coupled dynamics between the ASV and a wave, section 3 introduces the control problem formulation, section 4 presents the results and discussion from the simulations, and section 5 concludes the paper, and discusses future work.

2. SYSTEM MODEL

2.1 ASV Dynamics

The ASV model is based upon a simplified description of the Halcyon ASV: more details of the 6 degrees of freedom (DOF) model can be found in (Heins et al., 2017). For the purpose of developing initial control strategies this paper examines the 1 DOF scenario, with the changes and simplifications from the full model noted below. The simplification is based upon the following assumptions.

- The model degrees of freedom are restricted to forwards (surge) motion only. The state space model developed in this paper can be augmented with addi-

10.1016/j.ifacol.2020.12.1832

tional states to describe the other degrees of freedom and will be studied in future work.
- There are no water-current or wind-induced forces. Again, these can be included in the model but the focus of the present work is upon wave-induced forces.
- Actuation is restricted to the propeller input only. Future work will include steering once roll and yaw dynamics are included.
- The wave induced forces arise from a single wave harmonic, corresponding to regular waves, and the controller has full information of this. In practice, the sea surface is more complex and wave forecasting is an active research area (see: Merigaud and Ringwood (2019))
- The vessel is heading directly into the oncoming waves. This assumption will be relaxed in future work when steering inputs are considered.

The equations of motion of the boat in the surge direction are as follows:

$$\dot{\chi}(t) = \nu(t), \tag{1a}$$

$$\dot{\nu}(t) = \frac{D(\nu(t)) + \tau_{\mathrm{p}}(\nu(t), \zeta(t)) + \tau_{\mathrm{w}}^{\nu}(\nu(t), \eta(t))}{M}, \tag{1b}$$

$$\dot{\zeta}(t) = \frac{-1}{\kappa}\zeta(t) + \frac{1}{\kappa}u(t). \tag{1c}$$

The system has five states, $x = [\chi, \nu, \zeta, \eta, \dot{\eta}]^T$, with $\chi(t)$ being the position in the boat reference frame at time t, $\nu(t)$ is the surge velocity of the boat, $\zeta(t)$ is the propeller speed, $u(t)$ is the propeller control input, and $\eta(t)$ and $\dot{\eta}$ are wave states defined in the following section. In the above equations $D(\nu(t))$ is the drag term, $\tau_{\mathrm{p}}(\nu(t), \zeta(t))$ is the propulsion from the propellers, κ is the propellor time constant, and $\tau_{\mathrm{w}}^{\nu}(\nu(t), \eta(t))$ is the wave force in the surge direction, derived in the next section. Table A.1 in the appendix list the parameters employed in this paper. The surge drag force equation is as follows:

$$D(\nu(t)) = -\frac{1}{2}\rho S C_f^*(\nu(t))\nu(t)^2, \tag{2}$$

where S is the wetted hull surface area and ρ is the density of water. The modified resistance curve, $C_f^*(\nu(t))$,is approximated by the following 6th order polynomial:

$$D(\nu(t)) = -\frac{1}{2}\rho S(p_1\nu(t)^6 + p_2\nu(t)^5 + p_3\nu(t)^4 + p_4\nu(t)^3 + p_5\nu(t)^2 + p_6\nu(t) + p_7)\nu(t)^2, \tag{3}$$

where p_x are constant coefficients defined in appendix A.2. The thrust from the dual propellers is modelled by:

$$\tau_{\mathrm{p}}(\nu(t), \zeta(t)) = 2K_\tau \rho d^4 \zeta(t)^2, \tag{4}$$

where d is the propeller diameter and where the thrust parameter K_τ is given by:

$$K_\tau(J) = K_\tau^{\{1\}}J^2 + K_\tau^{\{2\}}J + K_\tau^{\{3\}}, \tag{5}$$

where, $K_\tau^{\{i\}}$ are thrust polynomial constants defined in appendix A.3, and the advance ratio, J, is:

$$J = \frac{\nu(t)}{\zeta(t)d}. \tag{6}$$

2.2 Wave Environment and Forces

The force exerted on the boat by the wave is calculated using a Response Amplitude Operator (RAO) (Fossen, 2011). The full model uses look-up tables to find the values dependent on the conditions. In the case of the surge direction, the force RAO is appoximately an affine function of the surge velocity and wave frequency, as shown in Figure 1. The phase RAO is assumed to be constant for all boat velocities at a specific wave frequency. For the force RAO, the force is linearly dependent on the velocity, as well as linearly dependent on the wave frequency. Selecting a wave frequency, the dimensionalized force RAO can be approximated by the following equation:

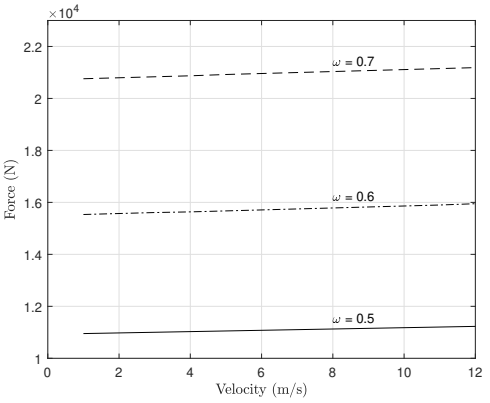

Fig. 1. Surge RAOs at various wave frequencies and surge velocities. The plot is dimensionlized with ρ and g

$$\rho g|F^{\nu}(\nu(t))| \approx a\nu(t) + b, \tag{7}$$

where $a = 23.18$, $b = 10845$, for the wave frequency, ω, of 0.5 rad/s. Note, the force RAO magnitude, $|F^{\nu}(\nu(t))|$, typically uses a subscript to indicate first order wave forces or second order drift forces. This paper only discusses first order wave forces so the subscript is excluded.

Wave Environment The force imparted on the boat from the wave is dependent upon the wave height and boat position. For a single harmonic in the surge direction the wave elevation is defined as:

$$\xi(\chi_{\mathrm{e}}, t) = a_h \cos(k\chi_{\mathrm{e}} - \omega t + \epsilon), \tag{8}$$

where a_h is the wave amplitude, ϵ is an arbitrary added phase, and $\chi_{\mathrm{e}} \in \mathbb{R}$ is the boat's position in an inertial reference frame. Assuming the boat's χ-axis coincides with the fixed reference frame χ_{e}-axis, χ_{e} can be described in the boat's body fixed frame by (Pérez and Blanke, 2002):

$$\chi_{\mathrm{e}} = \chi_0 + \int \nu(t)\, dt. \tag{9}$$

Inserting (9) into (8) and setting $\chi_0 = 0$ results in the wave elevation described in the boat's reference frame:

$$\xi(\chi, t) = a_h \cos\left(\int \nu(t)\, dt - \omega t - \epsilon\right). \tag{10}$$

With the deep water dispersion relation $k = \omega^2/g$ is assumed, the wave force term in (1b) is a function of the force RAO (7) and the wave elevation (10):

$$\tau_{\mathrm{w}}^{\nu}(\nu(t), \eta(t)) = -\rho g|F^{\nu}(\nu(t))|a_h \cos\left(\omega t + \frac{\omega^2}{g}\int \nu(t)\, dt + \phi_{\mathrm{RAO}} + \epsilon\right), \tag{11}$$

where g is the acceleration due to gravity, $|F^{\nu}(\nu(t))|$ is the force RAO, and ϕ_{RAO} is the phase RAO which is assumed

constant at 1.502 radians. Note, typical notation for the wave frequency ω, wave amplitude a_h, and ϵ include a k subscript to indicate each wave component, however, to avoid confusion with the discrete time indices later, and since this paper only concerns a single wave component, the subscript has been dropped.

Next, the wave harmonic is decoupled from the height and force RAO to simplify use in state space form and is redefined as:

$$\eta(t) := \cos\left(\omega t + \frac{\omega^2}{g}\int \nu(t)\,dt + \phi_{\text{RAO}} + \epsilon\right). \tag{12}$$

The dynamics of $\eta(t)$ are obtained by differentiating (12) with respect to time. The resulting expressions are somewhat involved, but can be simplified significantly by performing an order of magnitude analysis to retain only the leading-order terms under the following set of assumptions:

- $\omega \in [0.30, 0.75]$ rad/s. This is justified by observing that the vast majority of wave energy in a typical wave energy spectrum is concentrated in this band.
- $\nu(t) \in [0, 10]$ m/s. This is the typical operating range in surge velocity for the ASV studied.
- $\frac{\omega^2}{g}\dot{\nu}(t) \ll \omega + \frac{\omega^2}{g}\nu(t)$ so it is neglected.

With these assumptions the first derivative is:

$$\dot{\eta}(t) \approx -\left(\omega + \frac{\omega^2}{g}\nu(t)\right)\sin\left(\omega t + \frac{\omega^2}{g}\int \nu(t)dt + \phi_{\text{RAO}} + \epsilon\right). \tag{13}$$

The second derivative is:

$$\ddot{\eta}(t) \approx -\left(\omega + \frac{\omega^2}{g}\nu(t)\right)^2 \eta(t). \tag{14}$$

The term $\omega + \frac{\omega^2}{g}\nu(t)$ is the encounter frequency of the boat to a wave in a head sea.

2.3 Combined State Space Model

The combined surge and wave dynamics can be expressed in linear time varying form as shown in (Tomás-Rodríguez and Banks, 2010). Here, in (15), it is clear to see the coupling between the boat velocity and the wave state. The force of the wave imparted on the boat in the (2,4) term is dependent on both the velocity of the boat and the wave state, while in the (5,4) term, the square of the encounter frequency can be seen. Linearization of this system about a fixed velocity loses this coupling. This motivates the use of a nonlinear control technique.

3. CONTROLLER DESIGN

The following section presents the design of a Nonlinear Model Predictive Controller based on a condensed single-shooting approach. The optimisation is implemented within the Real Time Iteration Scheme (RTI) (Diehl et al., 2005) which is a popular method to achieve real-time performance.

3.1 NMPC Controller

Considering a discrete-time representation of the general nonlinear system (15), the objective is to minimize a cost function of the form,

$$J = (Y_r - \hat{Y})^T Q (Y_r - \hat{Y}) + (U_r - \hat{U})^T R (U_r - \hat{U}) \tag{16a}$$

$$s.t.$$

$$x_k = x_0 \tag{16b}$$

$$x_{k+1} = f(x_k, u_k), \tag{16c}$$

$$y_k = g(x_k, u_k), \tag{16d}$$

$$U_{min} \le \hat{U} \le U_{max} \tag{16e}$$

$$Y_{min} \le \hat{Y} \le Y_{max} \tag{16f}$$

where $x_k \in \mathbb{R}^{n_x}$ are the states of the system at time k, $u_k \in \mathbb{R}^{n_u}$ are the inputs, and $y_k \in \mathbb{R}^{n_y}$ are the outputs. Moreover, $Q > 0 \in \mathbb{R}^{N_p n_y \times N_p n_y}$ and $R > 0 \in \mathbb{R}^{N_p n_u \times N_p n_u}$ are positive definite matrices for penalizing output and input errors, respectively; $Y_r, \hat{Y}, U_r, \hat{U}$ are column-vectors containing future output references, output predictions, input references and input predictions, respectively; and the optimisation subject to initial condition (16b), state dynamics (16c), state-output function (16d), and input and output constraints (16e) and (16f).

Cost function (16) is a Nonlinear Programming Problem (NLP), which is in general difficult to solve. Popular alternatives are Sequential Quadratic Programming (SQP) methods which form a linearized Convex Quadratic Program to find an optimal search direction which eventually drives the solution towards a local optimum. In predictive control, the linearization of the cost function is only defined after the future inputs and states trajectories are defined. To address this, single-shooting methods use an initially guessed nominal input trajectory $\bar{U} = [\bar{u}_k^T, \bar{u}_{k+1}^T, \cdots, \bar{u}_{k+N_p-1}^T]^T$ which can be used to obtain the nominal state and output trajectories, $\bar{X} = [\bar{x}_{k+1}^T, \bar{x}_{k+2}^T, \cdots, \bar{x}_{k+N_p}^T]^T$ and $\bar{Y} = [\bar{y}_{k+1}^Y, \bar{y}_{k+2}^T, \cdots, \bar{y}_{k+N_p}^T]^T$, respectively, by propagating the input through the state dynamics (16c) and obtaining the respective outputs through output function (16d).

By taking a first order Taylor approximation, with a slight abuse of notation, all future inputs and outputs can then be obtained starting from an initial condition mismatch δx_0 related to the Real-Time Iteration Scheme as,

$$\hat{U} = \bar{U} + \delta\hat{U} \tag{17a}$$

$$\hat{Y} = \bar{Y} + \delta\hat{Y} = \bar{Y} + G\delta x_0 + F\delta\hat{U} \tag{17b}$$

where matrices G and F are defined as

$$\begin{bmatrix} \dot{\chi}(t) \\ \dot{\nu}(t) \\ \dot{\zeta}(t) \\ \dot{\eta}_k(t) \\ \ddot{\eta}_k(t) \end{bmatrix} = \begin{bmatrix} 0 & 1 & 0 & 0 & 0 \\ 0 & -\frac{D(\nu(t))}{M} & \frac{\tau_p(\nu(t),\zeta(t))}{M} & -\frac{\rho g |F^u(\nu(t))| a_h}{M} & 0 \\ 0 & 0 & -\frac{1}{\kappa} & 0 & 0 \\ 0 & 0 & 0 & 0 & 1 \\ 0 & 0 & 0 & -\left(\omega + \frac{\omega^2}{g}\nu(t)\right)^2 & 0 \end{bmatrix} \begin{bmatrix} \chi(t) \\ \nu(t) \\ \zeta(t) \\ \eta_k(t) \\ \dot{\eta}_k(t) \end{bmatrix} + \begin{bmatrix} 0 \\ 0 \\ \frac{1}{\kappa} \\ 0 \\ 0 \end{bmatrix} u(t) \tag{15}$$

$$G = \begin{bmatrix} C_1A_0 \\ C_2A_1A_0 \\ \vdots \\ C_{N_p}A_{N_p-1}\cdots A_1A_0 \end{bmatrix}, \tag{18a}$$

$$F = \begin{bmatrix} C_1B_0 & \mathbb{O} & \cdots & \cdots \\ C_2A_1B_0 & C_2B_1 & \mathbb{O} & \cdots \\ C_3A_2A_1B_0 & C_3A_2B_1 & C_3B_2 & \cdots \\ \vdots & \vdots & \vdots & \ddots \\ C_{N_p}A_{N_p-1}\cdots A_1B_0 & C_{N_p}A_{N_p-2}\cdots A_2B_1 & \cdots & \cdots \end{bmatrix}. \tag{18b}$$

and,

$$A_k = \left.\frac{\partial f(\hat{x}_k,\hat{u}_k)}{\partial \hat{x}_k}\right|_{\substack{\hat{x}_k=\bar{x}_k \\ \hat{u}_k=\bar{u}_k}} \quad B_k = \left.\frac{\partial f(\hat{x}_k,\hat{u}_k)}{\partial \hat{u}_k}\right|_{\substack{\hat{x}_k=\bar{x}_k \\ \hat{u}_k=\bar{u}_k}} \tag{19a}$$

Moreover, this paper focuses on regulating the average boat velocity and minimizing the wave forces defined as:

$$\tau_w = \bar{\tau}_w + \frac{\partial \tau_w(\bar{\nu}_k,\bar{\eta}_k)}{\partial \nu_k}\delta\nu_k + \frac{\partial \tau_w(\bar{\nu}_k,\bar{\eta}_k)}{\partial \eta_k}\delta\eta_k. \tag{20}$$

thus, resulting in the output matrix defined as:

$$C_i = \begin{bmatrix} 0 & 1 & 0 & 0 \\ 0 & \frac{\partial \tau_w(\bar{u}_k,\bar{\eta}_k)}{\partial \nu_k} & 0 & \frac{\partial \tau_w(u_k,\eta_k)}{\partial \eta_k} \end{bmatrix}. \tag{21}$$

The wave force in the surge direction does not vary by a large amount with a change in velocity which can be seen in Figure 1. Using an additional tuning parameter in the force RAO equation, (7) can be rewritten as:

$$|F_k^{\nu}(\nu_k)| = \alpha(a\nu_k) + b, \tag{22}$$

where α is the additional tuning weight which can be used to virtually increase the change in the wave force with respect to the boat velocity.

To obtain a desired average velocity, the rows of the linearized prediction model (17b) related to the velocity are averaged over the prediction horizon.

Optimization Substituting input and output linearised prediction models (17a) and (17b) in the original cost function (16), and rearranging the cost in terms of the decision variable $\delta\hat{U}$ (condensing approach) results in the standard QP form:

$$J = \frac{1}{2}\delta\hat{U}^T H\delta\hat{U} + \delta\hat{U}^T f + C \tag{23a}$$

s.t.

$$M\delta\hat{U} \le \gamma \tag{23b}$$

$$H = F^TQF + R \tag{23c}$$

$$f = -\left[F^TQ(Y_r - \bar{Y} - G\delta x_0) - R(\bar{U} - U_r)\right] \tag{23d}$$

$$M = \begin{bmatrix} I \\ -I \\ F \\ -F \end{bmatrix} \quad \gamma = \begin{bmatrix} U_{max} - \bar{U} \\ -(U_{min} - \bar{U}) \\ Y_{max} - \bar{Y} - G\delta x_0 \\ -(Y_{min} - \bar{Y} - G\delta x_0) \end{bmatrix} \tag{23e}$$

Having defined this, any QP solver of choice can be used to solve (23a). Once the optimal input deviation, $\delta\hat{U}$, is obtained, equation (17a) is used to recover the actual input. Only the first input is applied to the system, and the process is then repeated, which is the well known receding horizon strategy.

3.2 Real Time Iteration Scheme

The Real Time Iteration (RTI) scheme, is a strategy that enables real-time performance for Nonlinear Optimal Control. The following is a brief explanation of the procedure.

Initial Value Embedding (IVE) It uses the solution found in the previous step in a shifted version, typically duplicating the last input variable $u_{k+N_p|k+1} = u_{k+N_p-1|k}$, to obtain the nominal trajectory over which the formulation will linearise and optimise.

Single SQP To further reduce the computational burden and achieve predictable timings, only a single step of the SQP is performed. This is reasonable given that the solution is "hot-started" from the previous solution, which is expected to be close to the optimal solution, provided no significant unknown/unexpected disturbances have entered the system.

Computation Separation Separates the computations into preparation and feedback phases to avoid the computation delay related to the preparation of the QP. Diagrams showing the timings of these phases can be found in Gros et al. (2016).

(1) Preparation Phase: In between sampling times, the preparation phase uses a predicted nominal state for the next sampling time $\bar{x}_0 = \hat{x}_{k|k-1}$ as a starting point obtained from the last state $x_{k-1|k-1}$ and last input $u_{k-1|k-1}$ which allows the preparation of the QP main matrices $H, M, F, etc.$, and partially, vectors f and γ.
(2) Feedback Phase: Once the current state measurement becomes available the feedback phase calculates the state mismatch $\delta x_0 = x_0 - \bar{x}_0$, finishes the calculation of f and γ, and solves the QP. In some cases, it may be beneficial to run the QP prior to the state measurement assuming $\delta x_0 = 0$ to obtain an estimate of the Lagrange multipliers, λ, related to the inequalities constraints. In this strategy, the optimal solution obtained from the RTI can be shown to have the form as presented in Wang (2011):

$$\hat{U} = \bar{U} - H^{-1}\left[\overbrace{\underbrace{-(F^TQ(Y_r - \bar{Y}) - R\bar{U})}_{\text{Unconstrained}}}^{\text{Preparation Phase}} \overbrace{\underbrace{+M^T\lambda}_{\text{Constrained}}}^{\text{Preparation Phase}} \overbrace{\underbrace{+F^TQG\delta x_0}_{\text{Feedback Phase}}}^{\text{Feedback Phase}}\right] \tag{24}$$

4. SIMULATION RESULTS

The boat was simulated heading directly into oncoming waves with the propellers being the only actuation. The wave was a single harmonic with a wave height of 1 meter and a frequency of 0.5 rad/s. The NMPC had a prediction horizon of 200 steps ahead, with the sample period 0.08 seconds resulting in a prediction window of 16 seconds which captures just over one complete harmonic. The simulation was run for 30 seconds. The weights of the NMPC were $Q_u = 10$ for penalizing deviations of the average velocity from the desired average, $R_u = 1.4 \times 10^{-7}$ penalizing deviations from U_r, and the tuning weight in (22) is set as $\alpha = 100$. The following shows a comparison

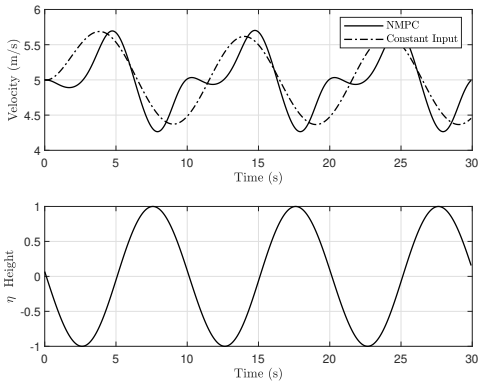

Fig. 2. The top plot shows the velocity profiles of the two controllers. The bottom plot shows the wave state η. The velocity profile shows a global minimum for the NMPC controlled boat when η is maximum and a local minimum when η is minimum.

between a constant propeller input which produces an average 5 m/s velocity and the NMPC controller with a desired average velocity of 5 m/s.

Figure 2 shows the velocity profiles of the open loop controller and the NMPC controller compared to the wave state, η. A clear difference in the velocity profiles can be seen. The open loop controller has an oscillating, single harmonic velocity resulting from changes only in the wave force, while the NMPC scenario has a more complex velocity profile. A global minimum of velocity for the NMPC controller occurs when the wave state is at its maximum, while a local minimum velocity for the NMPC controller occurs at the minimum of the wave state. Both the local and global maximum velocity occurs when the wave state is at zero. This behavior allows the boat to maintain the desired average velocity while reducing peak wave forces.

The resulting force on the boat can be seen in Figure 3. This figure shows the weighted wave force as calculated from (22). The base force, that which the boat would experience at 0 m/s, is subtracted from this figure to better show the difference in the two scenarios. Figure 4 shows the input for both controllers as it compares to the wave state. The NMPC input frequency appears to be twice that of the wave. This double harmonic is confirmed when looking at Figure 5. This figure shows the amplitude spectrum of the input signal to the propeller for NMPC. In the simulation, with an average velocity of 5 m/s the average encounter frequency of the boat is 0.628 rad/s, which has a small peak in the amplitude spectrum, while a much larger peak in seen at 1.256 rad/s or double the average encounter frequency. This can be explained by the fact that for each wave period, the minimal wave force occurs twice. NMPC exploits this by having the velocity profile shown in Figure 2, with peaks during the minimal wave force time.

5. CONCLUSION AND FUTURE WORK

This paper formulated and solved the problem of minimizing wave-induced forces upon an ASV heading into

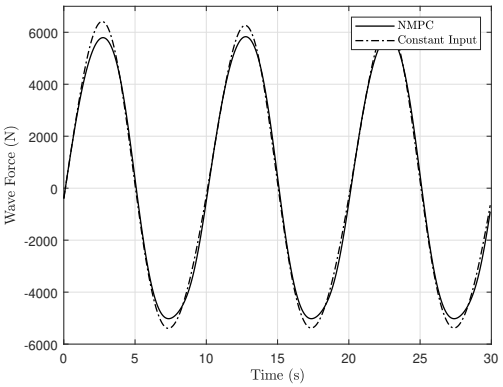

Fig. 3. Wave force comparison between the two controllers. Note: The base wave force is subtracted to more clearly show the difference in the two controllers.

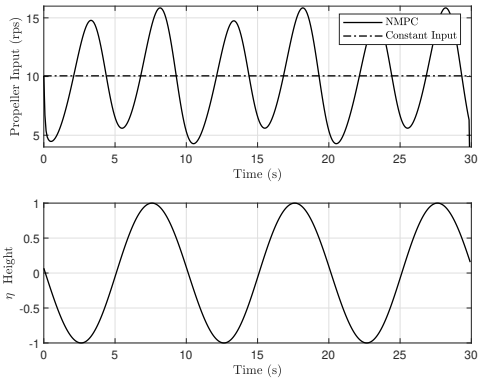

Fig. 4. The top plot shows the propeller input profiles of the two controllers. The bottom plot shows the wave state η.

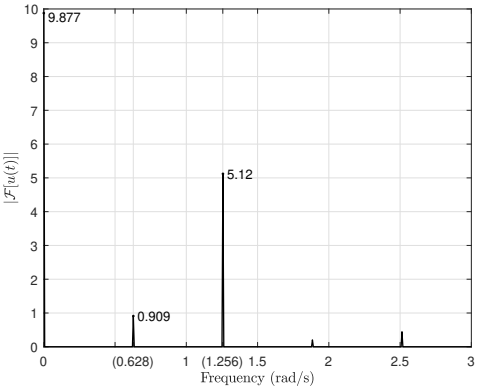

Fig. 5. An amplitude spectrum of the NMPC controller input

ocean waves. Because of the velocity-dependent encounter frequency, linearization of the dynamics removes the important coupling between the vessel and the wave, hence motivating the use of a NMPC which can benefit both, from the future prediction of the wave, as well as the ability to handle nonlinear dynamics and constraints. Moreover, a key finding of this study was observed in the velocity and input profiles required to minimize wave forces which resulted in twice the average encounter frequency. Further studies will seek to use this coupling concept to explore other degrees of freedom such as pitch and roll as well as the additional input of steering, and use NMPC's ability to reduce forces and satisfy constraints to handle more complex sea states.

REFERENCES

Çimen, T. and Banks, S.P. (2004). Nonlinear optimal tracking control with application to super-tankers for autopilot design. *Automatica*, 40(11), 1845–1863.

Diehl, M., Bock, H.G., and Oder, J.P.S. (2005). A real-time iteration scheme for nonlinear optimization in optimal feedback control. 43(5), 1714–1736.

Fossen, T.I. (2011). *Handbook of marine craft hydrodynamics and motion control*. John Wiley & Sons.

Gros, S., Zanon, M., Quirynen, R., and Bemporad, A. (2016). From linear to nonlinear MPC : bridging the gap via the real-time iteration. 7179.

Heins, P.H., Jones, B.L., and Taunton, D.J. (2017). Design and validation of an unmanned surface vehicle simulation model. *Applied Mathematical Modelling*, 48, 749–774.

Kim, Y.H., Lee, S.W., Yang, H.S., and Shell, D.A. (2012). Toward autonomous robotic containment booms: Visual servoing for robust inter-vehicle docking of surface vehicles. *Intelligent Service Robotics*, 5(1), 1–18.

Lekkas, A.M. and Fossen, T.I. (2014). Minimization of cross-track and along-track errors for path tracking of marine underactuated vehicles. In *2014 European Control Conference, ECC 2014*.

Li, Z., Sun, J., and Oh, S. (2009). Path following for marine surface vessels with rudder and roll constraints: An MPC approach. *Proceedings of the American Control Conference*, 3611–3616.

Li, Z., Sun, J., and Oh, S. (2010). Handling roll constraints for path following of marine surface vessels using coordinated rudder and propulsion control. *Proceedings of the 2010 American Control Conference*, 6010–6015.

Merigaud, A. and Ringwood, J.V. (2019). Incorporating Ocean Wave Spectrum Information in Short-Term Free-Surface Elevation Forecasting. *IEEE Journal of Oceanic Engineering*, 44(2), 401–414.

Oh, S.R. and Sun, J. (2010). Path following of underactuated marine surface vessels using line of sight based model predictive control. *Ocean Engineering*, 37(2-3), 289–295.

Oleynikova, E., Lee, N.B., Barry, A.J., Holler, J., and Barrett, D. (2010). Perimeter patrol on autonomous surface vehicles using marine radar. *OCEANS'10 IEEE Sydney, OCEANSSYD 2010*, 1–5.

Ono, M., Quadrelli, M., and Huntsberger, T.L. (2014). Safe maritime autonomous path planning in a high sea state. In *Proceedings of the American Control Conference*, 4727–4734.

Paliotta, C., Lefeber, E., Pettersen, K.Y., Pinto, J., Costa, M., and De Figueiredo Borges De Sousa, J.T. (2019). Trajectory Tracking and Path following for Underactuated Marine Vehicles. *IEEE Transactions on Control Systems Technology*, 27(4), 1423–1437.

Pérez, T. and Blanke, M. (2002). Simulation of Ship Motion in Seaway. 1–13.

Peymani, E. and Fossen, T.I. (2013). 2D path following for marine craft: A least-square approach. In *IFAC Proceedings Volumes (IFAC-PapersOnline)*, volume 9, 98–103. Toulouse, France.

Reinhart, R.F., Steil, J.J., Huntsberger, T.L., and Stoica, A. (2010). Tacking reduces bow-diving of high-speed Unmanned Sea Surface Vehicles. In *Proceedings - EST 2010 - 2010 International Conference on Emerging Security Technologies, ROBOSEC 2010 - Robots and Security, LAB-RS 2010 - Learning and Adaptive Behavior in Robotic Systems*, 177–182.

Tomás-Rodríguez, M. and Banks, S.P. (2010). *Linear, time-varying approximations to nonlinear dynamical systems: With applications in control and optimization*, volume 400. Springer Verlag.

Wang, L. (2011). *Model Predictive Control System Design and Implementation Using MATLAB*. Springer.

Appendix A. MODEL PARAMETERS

Table A.1. Halcyon Parameters

Name	Symbol	Value
Mass	M	11000 kg
Max Surge Velocity	$\nu^{\max}$	10 m/s
Propeller Diameter	d	0.622 m
Propeller Time Constant	κ	1.8 s
Wetted Surface Area	S	36.36 m^2
Water Density	ρ	1025 kg/m^3
Wave Amplitude	a_h	1 m
Wave Frequency	ω	0.5 rad/s
Acceleration due to Gravity	g	9.81 m/s^2
Phase RAO	ϕ_{RAO}	1.502 radians
Force RAO Slope	a	23.18 N/(m/s)
Force RAO Intercept	b	10845 N
RAO Tuning Weight	α	100

Table A.2. p Constant Coefficients

p_1	-9.22×10^{-7}	p_5	-5.52×10^{-3}
p_2	3.14×10^{-5}	p_6	2.49×10^{-3}
p_3	-4.00×10^{-4}	p_7	1.70×10^{-2}
p_4	2.31×10^{-3}		

Table A.3. $K_\tau^{\{i\}}$ Thrust Polynomial Constants

$K_\tau^{\{1\}}$	0.0041
$K_\tau^{\{2\}}$	-0.5002
$K_\tau^{\{3\}}$	0.6008

Bibliography

Mohamed Abdelaal, Martin Franzle, and Axel Hahn. Nonlinear model predictive control for tracking of underactuated vessels under input constraints. In *Proceedings - EMS 2015: UKSim-AMSS 9th IEEE European Modelling Symposium on Computer Modelling and Simulation*, pages 313–318, 2016. ISBN 9781509002061.

Mohamed Abdelaal, Martin Fränzle, and Axel Hahn. Nonlinear Model Predictive Control for trajectory tracking and collision avoidance of underactuated vessels with disturbances. *Ocean Engineering*, 160(December 2017):168–180, 2018. ISSN 00298018.

Craig H. Allen. The seabots are coming here: Should they be treated as vessels? *Journal of Navigation*, 65(4):749–752, 2012. ISSN 03734633.

Carlos Almeida, Tiago Franco, Hugo Ferreira, Alfredo Martins, Ricardo Santos, José Miguel Almeida, João Carvalho, and Eduardo Silva. Radar Based Collision detection developments on USV ROAZ II. *OCEANS '09 IEEE Bremen: Balancing Technology with Future Needs*, 2009.

J Alves, P Oliveira, R Oliveira, A Pascoal, M Rufino, L Sebastiao, and C Silvestre. Vehicle and Mission Control of the DELFIM Autonomous Surface Craft. In *14th Mediterranean Conference on Control and Automation*, 2006.

A S Annamalai, A Motwani, R Sutton, C Yang, S Sharma, and P Culverhouse. Integrated navigation and control system for an uninhabited surface vehicle based on interval Kalman filtering and model predictive control. *IET Conference on Control and Automation 2013: Uniting Problems and Solutions, 4 - 5 June*, pages 1–6, 2013.

A. S. K. Annamalai, R. Sutton, C. Yang, P. Culverhouse, and S. Sharma. Robust adaptive control of an uninhabited surface vehicle. *Journal of Intelligent & Robotic Systems*, 78(2):319–338, 2015.

Motoki Araki, Naoya Umeda, Hirotada Hashimoto, and Akihiko Matsuda. An Improvement of Broaching Prediction with a Nonlinear 6 Degrees of Freedom Model. *Journal of the Japan Society of Naval Architects and Ocean Engineers*, 14(February):85–96, 2011. ISSN 1880-3717.

Dennis Belleter, Mohamed Adlene Maghenem, Claudio Paliotta, and Kristin Y. Pettersen. Observer based path following for underactuated marine vessels in the presence of ocean currents: A global approach. *Automatica*, 100:123–134, 2019. ISSN 00051098.

Dennis J.W. Belleter, Roberto Galeazzi, and Thor I. Fossen. Experimental verification of a global exponential stable nonlinear wave encounter frequency estimator. *Ocean Engineering*, 97:48–56, 2015. ISSN 00298018.

Michael Richard Belmont, J. M.K. Horwood, R. W.F. Thurley, and J. Baker. Shallow angle wave profiling lidar. *Journal of Atmospheric and Oceanic Technology*, 24(6):1150–1156, 2007. ISSN 07390572.

Michael R Benjamin and Joseph A Curcio. COLREGS-Based Navigation of Autonomous Marine Vehicles. pages 32–39, 2004.

Marco Bibuli, Massimo Caccia, and Lionel Lapierre. Path-following algorithms and experiments for an autonomous surface vehicle. In *IFAC Proceedings Volumes (IFAC-PapersOnline)*, volume 7, pages 81–86, 2007. ISBN 9783902661623.

Glenn Bitar, Morten Breivik, and Anastasios M. Lekkas. Energy-Optimized Path Planning for Autonomous Ferries. *IFAC-PapersOnLine*, 51(29):389–394, 2018. ISSN 24058963.

Glenn Bitar, Bjørn-olav H Eriksen, Anastasios M Lekkas, and Morten Breivik. Energy-Optimized Hybrid Collision Avoidance for ASVs. pages 2522–2529, 2019a.

Glenn Bitar, Andreas B Martinsen, Anastasios M Lekkas, Morten Breivik, Glenn Bitar, and Andreas B Martinsen. Docking and of ASVs of ASVs with. *IFAC PapersOnLine*, 53(2):14488–14494, 2020. ISSN 2405-8963.

Glenn Bitar, Vegard N Vestad, Anastasios M Lekkas, and Morten Breivik. Warm-Started Optimized Trajectory Planning for ASVs. In *IFAC-PapersOnLine*, volume 52, pages 308–314. Elsevier Ltd, 2019b.

Chris E. Blenkinsopp, Ian L. Turner, Michael J. Allis, William L. Peirson, and Luke E. Garden. Application of LiDAR technology for measurement of time-varying free-surface profiles in a laboratory wave flume. *Coastal Engineering*, 68:1–5, 2012. ISSN 03783839.

H. G. Bock and K. J. Plitt. Multiple Shooting Algorithm for Direct Solution of Optimal Control Problems. *IFAC Proceedings Series*, 17(2):1603–1608, 1985. ISSN 07411146.

Paul T. Boggs and Jon W. Tolle. Sequential Quadratic Programming. *Acta Numerica*, 4:1–51, jan 1995. ISSN 14740508.

M. Bonci, P. De Jong, F. Van Walree, M. R. Renilson, and R. H.M. Huijsmans. The steering and course keeping qualities of high-speed craft and the inception of dynamic instabilities in the following sea. *Ocean Engineering*, 194(July):106636, 2019. ISSN 00298018.

Matteo Bonci. *The Manoeuvrability of High-Speed Craft in the Following Sea*. PhD thesis, 2019.

E. Bouws, H. Gunther, W. Rosenthal, and C. L. Vincent. Similarity of the wind wave spectrum in finite depth water 1. Spectral form. *Journal of Geophysical Research*, 90(C1):975–986, 1985. ISSN 01480227.

Thomas L. Bradley, Stephen P., Hax, Arnoldo C., Magnanti. *Applied Mathematical Programming*. Addison-Wesley Publishing Company, 1977.

Mark Briggs. Innovation and the mid-victorian royal navy: The case of the whitehead torpedo. *Mariners Mirror*, 88(4), 2002. ISSN 2049680X.

Elisabeta Burlacu, Leonard Domnisoru, and Dan Obreja. Seakeeping prediction of a survey vessel operating in the caspian sea. *Proceedings of the International Conference on Offshore Mechanics and Arctic Engineering - OMAE*, 11A:1–10, 2018.

Massimo Caccia, Marco Bibuli, Riccardo Bono, and Gabriele Bruzzone. Basic navigation, guidance and control of an Unmanned Surface Vehicle. *Autonomous Robots*, 25(4):349–365, 2008. ISSN 09295593.

Massimo Caccia, Riccardo Bono, Gabriele Bruzzone, Giorgio Bruzzone, Edoardo Spirandelli, Gianmarco Veruggio, Angela Maria Stortini, and Gabriele Capodaglio. Sampling sea surfaces with SESAMO: An autonomous craft for the study of sea-air interactions. *IEEE Robotics and Automation Magazine*, 12(3):95–105, 2005. ISSN 10709932.

Walter Caharija, Kristin Y. Pettersen, Marco Bibuli, Pedro Calado, Enrica Zereik, Jose Braga, Jan Tommy Gravdahl, Asgeir J. Sorensen, Milan Milovanovic, and Gabriele Bruzzone. Integral line-of-sight guidance and control of underactuated marine vehicles. In *IEEE Transactions on Control Systems Technology*, volume 24, pages 1–20, 2014.

S. Campbell, W. Naeem, and G. W. Irwin. A review on improving the autonomy of unmanned surface vehicles through intelligent collision avoidance manoeuvres. *Annual Reviews in Control*, 36(2):267–283, 2012. ISSN 13675788.

Pablo M. Carrica, Kwang Jun Paik, Hamid S. Hosseini, and Frederick Stern. URANS analysis of a broaching event in irregular quartering seas. *Journal of Marine Science and Technology*, 13(4): 395–407, 2008. ISSN 09484280.

Pablo M. Carrica, Hamid Sadat-Hosseini, and Frederick Stern. CFD analysis of broaching for a model surface combatant with explicit simulation of moving rudders and rotating propellers. *Computers and Fluids*, 53(1):117–132, 2012. ISSN 00457930.

Ioannis K. Chatjigeorgiou. *Analytical Methods in Marine Hydrodynamics*. Cambridge University Press, 2018.

Joseph Curcio, John Leonard, and Andrew Patrikalakis. SCOUT - A low cost autonomous surface platform for research in cooperative autonomy. *Proceedings of MTS/IEEE OCEANS, 2005*, 2005: 725–729, 2005.

Anil W. Date. *Introduction to computational fluid dynamics*, volume 9780521853. 2005.

Moritz Diehl, Hans Georg Bock, Holger Diedam, Pierre-brice Wieber, Moritz Diehl, Hans Georg Bock, Holger Diedam, Pierre-brice Wieber Fast, and Direct Multiple. Fast Direct Multiple Shooting Algorithms for Optimal Robot Control. *Fast Motions in Biomechanics and Robotics*, page 28, 2005a.

Moritz Diehl, Hans Georg Bock, and Johannes P. Schlöder. A real-time iteration scheme for nonlinear optimization in optimal feedback control. *SIAM Journal on Control and Optimization*, 43 (5):1714–1736, 2005b.

David Eager, Ann Marie Pendrill, and Nina Reistad. Beyond velocity and acceleration: Jerk, snap and higher derivatives. *European Journal of Physics*, 37(6), 2016. ISSN 13616404.

T. Elfouhaily, B. Chapron, K. Katsaros, and D. Vandemark. A unified directional spectrum for long and short wind-driven waves. *Journal of Geophysical Research C: Oceans*, 102(C7):15781–15796, 1997. ISSN 01480227.

Bjørn Olav H. Eriksen and Morten Breivik. MPC-Based mid-level collision avoidance for ASVs using nonlinear programming. In *1st Annual IEEE Conference on Control Technology and Applications, CCTA 2017*, volume 2017-Janua, pages 766–772, 2017. ISBN 9781509021826.

Hubert Fay. *Dynamic Positioning Systems*. Editions Technip, 1989. ISBN 978-2710805809.

H. Ferreira, R. Martins, E. Marques, J. Pinto, A. Martins, J. Almeida, J. Sousa, and E. P. Silva. SWORDFISH: An autonomous surface vehicle for network centric operations. *OCEANS 2007 - Europe*, pages 1–6, 2007a.

Hugo Ferreira, C. Almeida, A. Martins, J. Almeida, N. Dias, A. Dias, and E. Silva. Autonomous bathymetry for risk assessment with ROAZ robotic surface vehicle. *OCEANS '09 IEEE Bremen: Balancing Technology with Future Needs*, pages 1–6, 2009.

Hugo Ferreira, A. Martins, A. Dias, C. Almeida, J. Almeida, and E. Silva. ROAZ Autonomous Surface Vehicle Design and Implementation. *Robótica Controlo, Automação, instrumentação*, (October 2015), 2007b. ISSN 0874-9019.

Hugo Miguel Ferreira, Carlos Almeida, Alfredo Martins, José Miguel Almeida, André Dias, Guilherme Silva, and Eduardo Silva. Environmental modeling with precision navigation using ROAZ autonomous surface vehicle. *IROS 2012-IEEE/RSJ International Conference on Intelligent Robots and Systems*, (November 2015):1–6, 2012.

Thor I. Fossen. A nonlinear unified state-space model for ship maneuvering and control in a seaway. *International Journal of Bifurcation and Chaos in Applied Sciences and Engineering*, 15(9):2717–2746, 2005. ISSN 02181274.

Thor I. Fossen. *Handbook of Marine Craft Hydrodynamics and Motion Control*. John Wiley & Sons, 2011. ISBN 9781119991496.

Thor I Fossen, Morten Breivik, and Roger Skjetne. Line of sight path following of underactuated marine craft. *IFAC Proceedings Volumes*, 36(21):211–216, 2003.

Thor I. Fossen and Anastasios M. Lekkas. Direct and indirect adaptive integral line-of-sight path-following controllers for marine craft exposed to ocean currents. *International Journal of Adaptive Control and Signal Processing*, 31(4):445–463, apr 2017. ISSN 10991115.

Thor I Fossen, Kristin Y Pettersen, and Roberto Galeazzi. Line-of-sight path following for dubins paths with adaptive sideslip compensation of drift forces. *IEEE Transactions on Control Systems Technology*, 23(2):820–827, 2015. ISSN 10636536.

Oscar Julian Gonzalez Villarreal and Anthony Rossiter. Shifting strategy for efficient block-based non-linear model predictive control using real-time iterations. *IET Control Theory and Applications*, 14(6):865–877, 2020. ISSN 17518652.

G J Grigoropoulos, S Harries, D P Damala, L Birk, and J Heimann. Seakeeping Assessment for High-Speed Monohulls – a Comparative Study. *8Th Intl. Marine Design Conf.*, (September 2016): 1–12, 2003.

Sébastien Gros, Mario Zanon, Rien Quirynen, Alberto Bemporad, and Moritz Diehl. From linear to nonlinear MPC: bridging the gap via the real-time iteration. *International Journal of Control*, 93(1):62–80, 2016. ISSN 13665820.

Svein Olav Hegerland. *An Experimental Study of a Redundant Position System for the Autonomous Ferry Milliampere Utilizing Ultra Wide- Band Radio Frequencies.* PhD thesis, Norwegian University of Science and Technology, 2018.

Peter H. Heins and Bryn Ll Jones. SWEM: A multiphysics sea-surface simulation environment. *2016 UKACC International Conference on Control, UKACC Control 2016*, (1), 2016.

Peter H. Heins, Bryn Ll Jones, and Dominic J. Taunton. Design and validation of an unmanned surface vehicle simulation model. *Applied Mathematical Modelling*, 48:749–774, 2017. ISSN 0307904X.

Voigt R. Hodgson, Herbert R. Lissner, and Lawrence M. Patrick. Response of the Seated Human Cadaver to Acceleration and Jerk with and without Seat Cushions. *Human Factors: The Journal of Human Factors and Ergonomics Society*, 5(5), 1963. ISSN 15478181.

B. Horel, P. Guillerm, J. Rousset, and B. Alessandrini. Experimental Database for Surf-Riding and Broaching-to Quantification based on Captive Model Tests in Waves. *ISSW 14th proceedings*, (October):94–104, 2014.

Boris Houska, Hans Joachim Ferreau, and Moritz Diehl. ACADO toolkit - An open-source framework for automatic control and dynamic optimization. *Optimal Control Applications and Methods*, 32(3):298–312, 2011. ISSN 01432087.

D Hudson. User manual for program suite THARBM, three-dimensional analysis of rigid body motions. Technical report, School of Engineering Sciences, Ship Science, University of Southampton., 2000.

Jan Jankowski and Andrzej Laskowski. Capsizing of small vessel due to waves and water trapped on deck. In *Proceedings of the 9th International Conference on Stability of Ships and Ocean Vehicles*, pages 1–7, 2006.

Aaron Kandel, Chu Xu, David Cardona, and Carey Whitehair. Fuel and Time Optimal USV Trajectory Planning under Flexible Refueling Constraints. *arXiv*, pages 1–6, 2020.

Fuat Kara. Time domain potential and source methods and their application to twin-hull high-speed crafts. *Ships and Offshore Structures*, pages 1–14, 2022. ISSN 17445302.

Nikolaos D. Katopodes. *Free-surface flow: Computational methods*. 2018.

Peter Kimball, John Bailey, Sarah Das, Rocky Geyer, Trevor Harrison, Clay Kunz, Kevin Manganini, Ken Mankoff, Katie Samuelson, Thomas Sayre-McCord, Fiamma Straneo, Peter Traykovski, and Hanumant Singh. The WHOI Jetyak: An autonomous surface vehicle for oceanographic research in shallow or dangerous waters. In *2014 IEEE/OES Autonomous Underwater Vehicles, AUV 2014*. IEEE, 2015. ISBN 9781479943449.

C. Kirches, L. Wirsching, H. G. Bock, and J. P. Schlöder. Efficient direct multiple shooting for nonlinear model predictive control on long horizons. *Journal of Process Control*, 22(3):540–550, 2012. ISSN 09591524.

Wilhelm B. Klinger, Ivan R. Bertaska, Karl D. Von Ellenrieder, and M. R. Dhanak. Control of an Unmanned Surface Vehicle with Uncertain Displacement and Drag. *IEEE Journal of Oceanic Engineering*, 42(2):458–476, 2017. ISSN 03649059.

P. Krata. Total Losses of Fishing Vessels Due to the Insufficient Stability. *TransNav : International Journal on Marine Navigation and Safety of Sea Transportation*, 2(March):311–315, 2008. ISSN 2083-6473.

Yoshiaki Kuwata, Michael T Wolf, Dimitri Zarzhitsky, Terrance L Huntsberger, and Senior Member. Safe Maritime Autonomous Navigation With COLREGS , Using Velocity Obstacles. 39(1):110–119, 2014.

L3Harris. private communication, mar 2016.

Jacoby Larson, Michael Bruch, and John Ebken. Autonomous navigation and obstacle avoidance for unmanned surface vehicles. 623007(May 2006):623007, 2006.

Taehwan Lee, Hanguen Kim, Hyun Chung, Yuseok Bang, and Hyun Myung. Energy efficient path planning for a marine surface vehicle considering heading angle. *Ocean Engineering*, 107:118–131, oct 2015. ISSN 00298018.

Anastasios M. Lekkas and Thor I. Fossen. Minimization of cross-track and along-track errors for path tracking of marine underactuated vehicles. In *2014 European Control Conference, ECC 2014*, pages 3004–3010, 2014. ISBN 9783952426913.

Zhen Li, Jing Sun, and Soryeok Oh. Path following for marine surface vessels with rudder and roll constraints: An MPC approach. In *Proceedings of the American Control Conference*, pages 3611–3616, 2009. ISBN 9781424445240.

Zhen Li, Jing Sun, and Soryeok Oh. Handling roll constraints for path following of marine surface vessels using coordinated rudder and propulsion control. In *Proceedings of the 2010 American Control Conference, ACC 2010*, pages 6010–6015, 2010. ISBN 9781424474264.

Liquid Robotics. Wave Glider.

Lu Liu, Dan Wang, Zhouhua Peng, and Hao Wang. Predictor-based LOS guidance law for path following of underactuated marine surface vehicles with sideslip compensation. *Ocean Engineering*, 124:340–348, sep 2016a. ISSN 00298018.

Shukui Liu, Florian Sprenger, Apostolos Papanikolaou, George Dafermos, and George Zaraphonitis. Experimental and numerical studies on linear and nonlinear seakeeping phenomena of the DTC ship in regular waves. *Ship Technology Research*, 68(1):41–61, 2021. ISSN 20567111.

Zhilin Liu and Chao Geng. Model predictive controller design with disturbance observer for path following of unmanned surface vessel. pages 1827–1832, 2017.

Zhixiang Liu, Youmin Zhang, Xiang Yu, and Chi Yuan. Unmanned surface vehicles: An overview of developments and challenges. *Annual Reviews in Control*, 41(May):71–93, 2016b. ISSN 13675788.

Atsuo Maki, Naoki Sakamoto, Youhei Akimoto, Yuki Banno, Sreenath Maniyappan, and Naoya Umeda. On broaching-to prevention using optimal control theory with evolution strategy (CMA-ES). *Journal of Marine Science and Technology (Japan)*, 26(1):71–87, 2021. ISSN 09484280.

J E Manley and M Frey. Development and operation of the autonomous surface craft ARTEMIS. *MIT Sea Grant Undergraduate Summer Research Program*, 1994.

Justin E. Manley. Development of the autonomous surface craft 'ACES'. *Oceans Conference Record (IEEE)*, 2:827–832, 1997. ISSN 01977385.

Justin E. Manley, Aaron Marsh, Whitney Cornforth, and Colette Wiseman. Evolution of the autonomous surface craft AutoCat. *Oceans Conference Record (IEEE)*, 1:403–408, 2000. ISSN 01977385.

Alfredo Martins, Hugo Miguel Ferreira, Carlos Almeida, Hugo Silva, José Miguel Almeida, and Eduardo Silva. ROAZ and ROAZ II Autonomous Surface Vehicle Design and Implementation. *International Lifesaving Congress 2007*, 2007.

Andreas B Martinsen, Anastasios M Lekkas, and Sebastien Gros. Autonomous docking using direct optimal control. In *IFAC-PapersOnLine*, volume 52, pages 97–102. Elsevier Ltd, 2019.

Andreas B Martinsen, Anastasios M Lekkas, Sébastien Gros, Jon Arne Glomsrud, and Tom Arne Pedersen. Reinforcement Learning-Based Tracking Control of USVs in Varying Operational Conditions. 7(March), 2020.

Daniel R. McCullough, Bryn L. Jones, Oscar J.G. Villarreal, and J.A. Rossiter. Towards Control of Autonomous Surface Vehicles in Rough Seas. In *IFAC-PapersOnLine*, volume 53, pages 14692–14697. Elsevier Ltd, 2020.

Rian Mehta, Scott R Winter, Stephen Rice, and Maarten Edwards. Are passengers willing to ride on autonomous cruise-ships ? *Maritime Transport Research*, 2(October 2020):100014, 2021. ISSN 2666-822X.

Alexis Merigaud and John V. Ringwood. Incorporating Ocean Wave Spectrum Information in Short-Term Free-Surface Elevation Forecasting. *IEEE Journal of Oceanic Engineering*, 44(2): 401–414, 2019. ISSN 03649059.

P. Mishra, U. K. Pradhan, U. S. Panda, S. K. Patra, M. V. RamanaMurthy, B. Seth, and P. K. Mohanty. Field measurements and numerical modeling of nearshore processes at an open coast port on the east coast of India. *Indian Journal of Geo-Marine Sciences*, 43(7):1272–1280, 2014. ISSN 09751033.

Signe Moe and Kristin Y. Pettersen. Set-Based line-of-sight (LOS) path following with collision avoidance for underactuated unmanned surface vessels under the influence of ocean currents. In *1st Annual IEEE Conference on Control Technology and Applications, CCTA 2017*, volume 2017-Janua, pages 241–248, 2017. ISBN 9781509021826.

W. Naeem, R. Sutton, and J. Chudley. Modelling and control of an unmanned surface vehicle for environmental monitoring. In *UKACC International Control Conference*, Glasgow, 2006.

J. N. Newman. *Marine Hydrodynamics*. The MIT Press, 1977. ISBN 9780262280617.

Karol Niklas and Artur Karczewski. Determination of Seakeeping Performance for a Case. 27(108): 4–16, 2020.

Frédéric Nouguier, Stéphan T. Grilli, and Charles Antoine Guérin. Nonlinear ocean wave reconstruction algorithms based on simulated spatiotemporal data acquired by a flash LIDAR camera. *IEEE Transactions on Geoscience and Remote Sensing*, 52(3):1761–1771, 2014. ISSN 01962892.

Okey Nwogu. Effect of steady currents on directional wave spectra. In *Proceedings of the International Conference on Offshore Mechanics and Arctic Engineering - OMAE*, volume 1, 1993.

Elena Oleynikova, Nicole B. Lee, Andrew J. Barry, Joseph Holler, and David Barrett. Perimeter patrol on autonomous surface vehicles using marine radar. *OCEANS'10 IEEE Sydney, OCEANSSYD 2010*, pages 1–5, 2010.

Masahiro Ono, Marco Quadrelli, and Terrance L. Huntsberger. Safe maritime autonomous path planning in a high sea state. In *Proceedings of the American Control Conference*, pages 4727–4734, 2014. ISBN 9781479932726.

Ronald L O'Rourke. Navy Large Unmanned Surface and Undersea Vehicles: Background and Issues for Congress [Updated March 30, 2020] R45757. Technical report, 2020.

Claudio Paliotta and Kristin Y. Pettersen. Geometric path following with ocean current estimation for ASVs and AUVs. In *Proceedings of the American Control Conference*, volume 2016-July, pages 7261–7268. American Automatic Control Council (AACC), 2016. ISBN 9781467386821.

António Pascoal, Paulo Oliveira, Carlos Silvestre, Luis Sebastião, Manuel Rufino, Victor Barroso, João Gomes, Gerard Ayela, Pascal Coince, Marcus Cardew, Anne Ryan, Hugh Braithwaite, Nicholas Cardew, Jonathan Trepte, Nicolas Seube, J. Champeau, P. Dhaussy, V. Sauce, R. Moitié, Ricardo Santos, Frederico Cardigos, Marc Brussieux, and Paul Dando. Robotic ocean vehicles for marine science applications: The european ASIMOV project. *Oceans Conference Record (IEEE)*, 1:409–415, 2000. ISSN 01977385.

Thomas Pastore and Vladimir Djapic. Improving autonomy and control of autonomous surface vehicles in port protection and mine countermeasure scenarios. *Journal of Field Robotics*, 27(6), 2010. ISSN 15564959.

Alexey Pavlov, Håvard Nordahl, and Morten Breivik. MPC-based optimal path following for underactuated vessels. *IFAC Proceedings Volumes (IFAC-PapersOnline)*, pages 340–345, 2009.

Ann Marie Pendrill and David Eager. Velocity, acceleration, jerk, snap and vibration: Forces in our bodies during a roller coaster ride. *Physics Education*, 55(6), 2020. ISSN 13616552.

Tristan Perez and Thor I. Fossen. Kinematic models for manoeuvring and seakeeping of marine vessels. *Modeling, Identification and Control*, 28(1):19–30, 2007. ISSN 03327353.

Tristan Perez and Thor I. Fossen. A Matlab toolbox for parametric identification of radiation-force models of ships and offshore structures. *Modeling, Identification and Control*, 30(1):1–15, 2009. ISSN 03327353.

Ehsan Peymani and Thor I. Fossen. 2D path following for marine craft: A least-square approach. In *IFAC Proceedings Volumes (IFAC-PapersOnline)*, volume 9, pages 98–103, Toulouse, France, 2013.

F. Prini, S. Benson, R. W. Birmingham, R. S. Dow, L. J. Ferguson, P. J. Sheppard, H. J. Phillips, M. C. Johnson, J. Mediavilla Varas, and S. Hirdaris. Full-scale seakeeping trials of an all-weather

lifeboat. *RINA, Royal Institution of Naval Architects - SURV 9 - Surveillance, Search and Rescue Craft, Papers*, 2018.

Federico Prini, Simon Benson, Richard Birmingham, Robert S. Dow, H.J. Phillips, P.J. Sheppard, and J. Mediavilla Varas. Seakeeping Analysis of a High-Speed Search and Rescue Craft by Linear Potential Theory. *International Conference on Lightweight Design of Marine Structures*, (November), 2015.

Federico Prini, R. W. Birmingham, Simon Benson, H.J. Phillips, P.J. Sheppard, J. Mediavilla Varas, M. C. Johnson, and Robert S. Dow. Seakeeping Analysis of a High-Speed Search and Rescue Craft by Linear Potential Theory. In *24th International HISWA Symposium on Yacht Design and Yacht Contstruction*, number November, pages 1–12, Amsterdam, 2016. ISBN 9789461867490.

R. Felix Reinhart, Jochen J. Steil, Terrance L. Huntsberger, and Adrian Stoica. Tacking reduces bow-diving of high-speed Unmanned Sea Surface Vehicles. In *Proceedings - EST 2010 - 2010 International Conference on Emerging Security Technologies, ROBOSEC 2010 - Robots and Security, LAB-RS 2010 - Learning and Adaptive Behavior in Robotic Systems*, pages 177–182, 2010. ISBN 9780769541754.

M. R. Renilson. *The broaching of ships in following seas.* PhD thesis, 1981.

M. R. Renilson. THE SEABRAKE - A DEVICE FOR ASSISTING IN THE PREVENTION OF BROACHING-TO. In *Third Intl. Conf. on Stability of Ships and Ocean Vehicles*, page 6, 1986.

G. N. Roberts and R. Sutton. *Advances in unmanned marine vehicles.* Institution of Engineering and Technology, 2006.

Rolls Royce. Rolls-Royce and Finferries demonstrate world's first Fully Autonomous Ferry, 2018.

Sintef. ShipX, 2022.

Renato Skejic and Odd M. Faltinsen. A unified seakeeping and maneuvering analysis of ships in regular waves. *Journal of Marine Science and Technology*, 13(4):371–394, 2008. ISSN 09484280.

Roger Skjetne. *The Maneuvering Problem.* PhD thesis, Norwegian University of Science and Technology, 2005.

Roger Skjetne, Thor I. Fossen, and Petar V. Kokotović. Robust output maneuvering for a class of nonlinear systems. *Automatica*, 40(3):373–383, 2004.

Geor Smith, Cristina Huertas-olivares, Frank Neumann, Tim Stallard, Claudio Bittencourt Ferreira, Jonathan Flinn, Thomas Boehme, Andrew Grant, Cameron Johnstone, and Hans Christian Sorensen. Commision of The Equitable Testing and Evaluation of Marine Energy Extraction Devices in terms of Performance, Cost and Environmental Impact. Technical report, 2011.

Timothy C Smith and Kevin M Silva. Linear seakeeping high sea state applicability. *International Ship Stability Workshop*, (June):111–116, 2017.

SNAME The Society of Naval Architects and Marine Engineers. Nomenclature for Treating the Motion of a Submerged Body Through a Fluid. Technical Report Technical and research bulletin NO.1-5, 1950.

Asgeir J Sørensen. Annual Reviews in Control A survey of dynamic positioning control systems. 35:123–136, 2011.

K. J. Spyrou, N. Themelis, and I. Kontolefas. Numerical statistical estimates of ship broaching-to. *Journal of Ship Research*, 60(4), 2016. ISSN 15420604.

R Sutton and A I Ag. Robust control methodology applied to the design of a combined steering stabiliser system for warships. 144(2), 1997.

Yusuke Tahara, Satoshi Tohyama, and Tokihiro Katsui. CFD-based multi-objective optimization method for ship design. *International Journal for Numerical Methods in Fluids*, 52(5):499–527, 2006. ISSN 02712091.

Atul Thakur, Petr Svec, and Satyandra K. Gupta. GPU based generation of state transition models using simulations for unmanned surface vehicle trajectory planning. *Robotics and Autonomous Systems*, 60(12):1457–1471, 2012. ISSN 09218890.

Harold Thurman and Alan Trujillo. *Essentials of Oceanography*. Prentice Hall, 7th editio edition, 2001. ISBN 9780130652355.

Alan Trevennor. A Brief History of Microcontrollers. In *Practical AVR Microcontrollers*, chapter Chapter 1. Technology in Action, 2012.

E. C. Tupper and Rawson KJ. *Basic Ship Theory*. Elsevier Science, 2001.

Naoya Umeda and Hirotada Hashimoto. Qualitative aspects of nonlinear ship motions in following and quartering seas with high forward velocity. *Journal of Marine Science and Technology*, 6(3), 2002. ISSN 09484280.

Naoya Umeda, Akihiko Matsuda, and Matao Takagi. Model Experiment on Anti-Broaching Steering System. *Journal of the Society of Naval Architects of Japan*, 1999(185):41–48, 1999. ISSN 0514-8499.

Systems Inside Unmanned. Hyundai Heavy Tests Fully Autonomous Passenger Ship.

U.S. Coast Guard. 2020 Recreational Boating Statistics. Technical report, 2020.

U.S. Navy. The Navy Unmanned Surface Vehicle (USV) Master Plan. Technical Report July, 2007.

Thomas W. Vaneck, Claudia D. Rodriguez-Ortiz, and Mads C. Schmidt. Automated bathymetry using an autonomous surface craft. In *Proceedings of the Annual Meeting - Institute of Navigation*, 1996.

Oscar J.G. Villarreal. *Efficient Real-Time Solutions for Nonlinear Model Predictive Control with Applications*. PhD thesis, University of Sheffield, 2021.

WAMIT. Wamit User Manual, 2013.

Ning Wang, Chunjiang Qian, Jing Chao Sun, and Yan Cheng Liu. Adaptive robust finite-time trajectory tracking control of fully actuated marine surface vehicles. *IEEE Transactions on Control Systems Technology*, 24(4):1454–1462, 2016.

Wei Wang, Tixiao Shan, Pietro Leoni, David Fern, Drew Meyers, Carlo Ratti, and Daniela Rus. Roboat II : A Novel Autonomous Surface Vessel for Urban Environments. In *International Conference on Intelligent Robots and Systems*, pages 1740–1747, 2020. ISBN 9781728162126.

A H Wertheim, J E Bos, and W Bles. Contributions of roll and pitch to sea sickness. *Brain Research Bulletin*, 47(5):517–524, 1998.

Martin S. Wiig, Kristin Y. Pettersen, Else Line M. Ruud, and Thomas R. Krogstad. An Integral Line-of-Sight Guidance Law with a Speed-dependent Lookahead Distance. In *2018 European*

Control Conference, ECC 2018, pages 1269–1276. Institute of Electrical and Electronics Engineers Inc., nov 2018. ISBN 9783952426982.

Bing Zhang, Changfu Zong, Guoying Chen, and Guiyuan Li. An adaptive-prediction-horizon model prediction control for path tracking in a four-wheel independent control electric vehicle. *Proceedings of the Institution of Mechanical Engineers, Part D: Journal of Automobile Engineering*, 233 (12):3246–3262, 2019. ISSN 09544070.

Zhiwei Zhang and Xiao Ming Li. Global ship accidents and ocean swell-related sea states. *Natural Hazards and Earth System Sciences*, 17(11), 2017. ISSN 16849981.